Focused Ion Beam-induced Fluorescence Spectroscopy: Mechanisms, Characterization, Instrumentation, and Application

by Garrett Budnik

Thesis submitted in fulfillment of the
requirements for the degree of
Doctor of Philosophy

School of Mathematical and Physical Sciences
University of Technology Sydney
Australia
August 2022

Certificate of original authorship

I certify that the work in this thesis has not previously been submitted for a degree nor has it been submitted as part of requirements for a degree except as part of the collaborative doctoral degree and/or fully acknowledged within the text.
I also certify that the thesis has been written by me. Any help that I have received in my research work and the preparation of the thesis itself has been acknowledged. In addition, I certify that all information sources and literature used are indicated in the thesis.

Signature of Student:

Production Note:
Signature removed prior to publication.

Date: 15 August 2022

This research is supported by an Australian Government Research Training Program Scholarship.

Acknowledgments

The work presented in this dissertation was carried out under a joint collaboration between the Microstructural Analysis Unit in the School of Mathematical and Physical Sciences of the University of Technology Sydney, Sydney, NSW, Australia and the Advanced Technology department of Thermo Fisher Scientific in Hillsboro, OR, USA. I wish to thank Professor Milos Toth, my principal supervisor, for his guidance, support, and supervision throughout this project. I sincerely wish to thank Dr. Mostafa Maazouz, the manager of the FIB group in Advanced Technology, who recognized the potential of the technology developed within this thesis from its earliest stage and spear-headed the support of the project at Thermo Fisher Scientific. Without the intellectual, financial, and material support from Thermo Fisher Scientific by Dr. Maazouz, none of this work would have happened. I would also like to thank Dr. Marcus Straw not only for setting up the collaboration grant between UTS and TFS, but for being a role model and encouraging me to pursue this endeavor.

In order to produce the highest quality results in this dissertation, access to state-of-the-art tools and systems only available at the Thermo Fisher Scientific campus in the USA was necessary. I would like to thank Professor Toth and the School for supporting my many trips back and forth between Australia and the USA. As a result of these travels, I was able to collaborate with different groups both at UTS and at TFS. I would like take this opportunity to explicity ackowledge the work of those individuals.

On the UTS side, I would like to thank Dr. John Scott for his mentorship, friendship, and support. There were many experiments that were designed and performed with his help that did not make it into this dissertation, but laid the foundation for the results that came later. Those days of our long arguments over electron transfer and excitation theories framed the discussions in Chapter 6, while his deft editing and deep literary knowledge and manuscript oversight led to him becoming my co-supervisor. Similarly, I'd like to thank Dr. James Bishop and Dr. Johannes Fröch for the many experimental ideas and discussions, particularly Dr. Bishop and his help setting up the gas chemistry in the Ga FIB lab. Although these results did not make this report, their contributions are significant

nonetheless. My sincerest thanks to technical staff Katie McBean and Dr. Mark Lockrey for their lab oversight and tool upkeep as well as machinist Greg Dalsanto for machining the support components for the optics.

In the USA, I would like to thank Galen Gledhill, Dr. Rich Swinford, and Dr. Jorge Filevich. Galen Gledhill and Dr. Rich Swinford developed the software that allows the camera to interface with the FIB. Galen provided the intial idea and GIS concept for the mini-lens optic that I was able to modify, optimize, and implement onto the system. Myself, Galen Gledhill, Dr. Jorge Filevich, and Dr. Mostafa Maazouz designed the elliptical mirror setup along with mechanical engineers Keith Ragsdale and Tom Nichols who made it a reality. A special thanks to Tom Nichols, who carried the sub-stage design across the finish line with thorough and deligent tolerance stack analysis, safety checks for collisions, and communicating with vendors, as well as for providing me with CAD drawings for many system components throughout the project and for being a great friend. I would like to thank Joe Christian for his help with various hardware integration onto the systems and modifications. Whether I needed to lift a column, install a new power supply, or change a detector configuration, Joe was always there to assist (or do it outright) and is a great friend. I would like to also thank the Thermo Fisher interns Suzanna Officer and Michelle Salem who continued many of my experiments during my intervals in Australia, sending me data. Specifically, Suzanna performed the Si-C anode imaging and Michelle collected the images of the elliptical mirror for field of view characterization.

Lastly, and above all, a special thanks to the one that was by my side through this entire process - the one that was by my side every day. Throughout the extensive travelling, the COVID-19 epidemic, the late nights, loss of loved ones, and physical ailments experienced during this candidacy, you were the one I could always depend on to get me through it. Your dedication, devotion, and unconditional love goes beyond what any words of thanks can express on these pages. So thank you, Carson, you're a good dog.

Oh, and my girlfriend Katie. She was pretty great too.

Contents

List of Figures

List of Tables

Abstract

This dissertation provides an investigation into the physics of photon emission as a result of energetic ion bombardment on material surfaces and the development of a novel technique in the form of Focused Ion Beam-induced Fluorescence Spectroscopy (FIB-FS) capable of performing 2D and 3D elemental analysis from these signals at the nanoscale. It details the engineering and design of highly sensitive, versatile prototype instrumentation that detects these photons and provides methods and workflows developed to characterize, optimize, and extract various forms of information from the specimen using FIB-FS. Characterization of the technique's fundamental limits are included in the first recorded measurements of lateral resolution and depth resolution on calibrated certified standards. A lateral resolution of 15.5 nm, a depth resolution of 12.8 nm, parts-per-million trace concentration detection sensitivity, and the ability to detect light elements such as Li and H are reported along with a demonstration of its application to Li-ion battery research and development. The results are benchmarked against well-established techniques of energy-dispersive X-ray spectroscopy (EDX) and secondary ion mass spectrometry (SIMS) to show FIB-FS as both complementary and competitive. Furthermore, the technique is used to investigate materials under various chemical environments and bombardment conditions, elucidating the physical nature behind the mechanisms of sputtered atom excitation and photon emission. Photon yields from excited sputtered atoms with different charge states under various oxygen environments are reported that are not explained with existing models, laying the groundwork for a new mechanistic description. FIB-FS is demonstrated as a high-resolution, sensitive, multifaceted analytical technique for multidimensional elemental analysis at the nanoscale and is poised for the advancement of fundamental insights into atomic excitation processes.

Chapter 1

Introduction

Material characterization techniques underpin progress in nanoscale science and technology [1–4]. Elemental and chemical analysis techniques are particularly important, and their prevalence and usefulness are determined not only by basic performance metrics such as resolution, accuracy and sensitivity, but also by their applicability to methods used to fabricate and process nanostructured materials and devices. The breadth of these requirements has led to regular use of numerous analysis methods as varied as atom probe tomography, XPS, SIMS and electron-beam techniques such as EELS, Auger electron spectroscopy (AES), EBSD and EDX [5–17]. In all cases, however, exceptional achievements in specific performance metrics are accompanied by drawbacks such as a highly restrictive sample geometry (e.g., in atom probe tomography and EELS), poor lateral resolution at high excitation energies (e.g. in EDX), the need for an ultra-high vacuum environment (e.g., in AES), or the inability to detect common elements such as hydrogen (e.g., in EDX, XPS). Consequently, there is continued interest in new characterization techniques [18–20] that have a high 3D spatial resolution (limited only by the fundamental particle interactions themselves) and can detect most elements in the period table - particularly light elements such as lithium and hydrogen and trace element concentrations, which are either challenging or impossible by complementary electron beam techniques.

Spectroscopy and the detection of optical signatures from atoms remains one of the most powerful forms of elemental identification due to the electronic structure and energy transitions unique to each element. Additionally, in recent years focused ion beam (FIB) techniques have matured into versatile, high-resolution methods for direct-write fabrication and processing of nanostructured materials and devices [21–26]. Here, a focused ion beam analysis technique based on in-flight fluorescence spectroscopy (FS) of atoms sputtered by energetic ions [27–32] is introduced with the aim to enable light element and trace element detection at the nanoscale in the FIB-SEM system. The FIB-FS technique combines the best properties of the FIB performance with the power of spectroscopic analysis and fundamental limitations of ion-solid interactions through the design and operation of an ultra-sensitive, novel optical detection scheme. These characteristics are demonstrated through nanoscale 3D tomography of GaAs/AlGaAs quantum wells, nanoscale lateral resolution of semiconductor heterostructures, and detection of trace-level impurities. Through high 3D spatial resolution and sensitivity coupled with a proclivity for hydrogen and lithium detection, FIB-FS is found to enhance and complement existing analytical techniques for a variety of applications, while offering a competitive advantage for other applications such as Li-ion battery analysis.

Furthermore, the mechanisms that govern the fundamental process of electronic excitation of the detected sputtered atoms of the FIB-FS technique remains unknown and as such, the results that establish FIB-FS as a premiere nanoscale analysis technique are only the initial steps in realizing its full potential. Therefore, a second goal of this work is to elucidate the fundamental interaction that leads to the emission of photons from the sputtered atoms in order to advance the understanding of charged particle interactions as well as to guide new methodologies with the FIB-FS technique. In other words, not only can FIB-FS enable fundamental insight to atomic excitation processes, but these very discoveries will further advance the capabilities of FIB-FS. To this end, FIB-FS stands before a rich and open potential application space where it can be seen as both a solution that greatly enhances the nanoanalysis capabilities of focused ion beam systems and as a means for exploring the complex fundamental interactions of ions and matter.

1.1 Thesis Structure

To lay the foundation for discussion of FIB-FS, understanding of ion-solid interactions and photon emission is first provided. Chapter 2 begins with an overview of ion-solid interactions and the basics of sputtered particles that lead to photon emission. It continues with a historical background review of the relevant literature and existing models used to describe the excitation and ionization of sputtered atoms. Since knowledge of the excitation mechanisms coincided with the development of new techniques and experiments, these methods are discussed concurrently to the insights they provided. It concludes with the current state of technology, its limitations, and the existing knowledge of the excitation mechanism.

Chapter 3 picks up from this conversation to discuss the FIB-FS instrumentation and hardware development responsible for the high efficiency detection chain that enables nanoscale detection and eliminates the limitations of the prior technology. Over the course of the work in this dissertation, various optical detection systems were developed to collect light under different environments and to enable wide-range versatility in applications. The discussion is broken into collection, detection, and data analysis with the necessary background optics theory being provided as needed. For collection, the design and operation of (i) an elliptical mirror and (ii) an insertable mini-probe that capture light at the point of emission under the charged particle columns and transfer it out of the vacuum chamber are reviewed first. Once the photons make it out of the chamber, they can be detected with either a camera or a photomultiplier tube. Each of these has different pros and cons depending on the desired experiment, which are reviewed thoroughly in the detection section. Lastly, a discussion of workflows and methods is given that reviews how the strengths of the different detectors and optics configurations can be used to optimize characterization processes through different modes of operation and analysis methods.

As with any new technique, FIB-FS must be characterized, and its limitations explored and understood. In Chapter 4, the technique's performance enabled by the designs in Chapter 3 is characterized in the context of nanoscale tomography and compared to those of modern techniques. The lateral resolution and depth resolution are investigated and demonstrated through fundamental limitations of ion-solid interactions and FIB performance. Detection limits are presented and found to be consistent with the high sensitivities found with prior methods. Together, these features position FIB-FS favorably as a prime technique for nanoscale characterization of surfaces and materials.

As an example of its versatility and application, a demonstration of the FIB-FS technique on a modern FIB-SEM system to characterize lithium ion batteries is provided in Chapter 5, marking the first use of FIB-FS to provide 2D and 3D chemical maps in microscopy. Li-ion battery analysis is chosen due to its pertinence in today's microscopy research and its widespread application. It is a particularly challenging field due to the requirements to detect trace metal dopants, Li and H distributions - materials that are critical for development. Detection of trace metals, H, and Li in this application showcases the FIB-FS technique's versatility and sensitivity, making it a viable technique for analyzing challenging samples compared to other microscopy techniques. In the demonstration, a novel method of analysis is developed in the coupling of traditional EDX with FIB-FS that enables full battery characterization.

Once familiar with the FIB-FS technique and its application, the discussion returns to the complex topic of ion-solid interactions and how FIB-FS and its multiple modes of operation can be used to explore excitation mechanisms and gain insight to unanswered questions about photon emission. Chapter 6 brings the discussion back to the principal of photons emitted from sputtered atoms and the investigations performed with FIB-FS to elucidate the nature of the emission. It begins with a brief introduction of where the current knowledge of secondary ion and photon emission stands and the motivation for the investigation. It follows with a simple experiment that measures the photons emitted by sputtered excited magnesium atoms (Mg I), photons from sputtered excited magnesium ions (Mg II), and magnesium secondary ions (Mg SI).

Despite the experiment's simplicity, the photons emitted by sputtered excited secondary ions have rarely been studied in the prior body of literature, which almost exclusively reviews photon emission or metastable state detection from sputtered neutral particles. By recording the response of the Mg I, Mg II, and Mg SI signals and through analysis of the absolute photon yields, these trends are compared to the existing models introduced in Chapter 2. The results demonstrate that analysis of photons from sputtered particles requires corrections to photons yields [photon/sputtered atom] and removal of artifacts from the ion-solid interactions to accurately describe the nature of excitation. In doing so, a new conversation is formed around the mechanism of excitation and ionization and its impact on analytical applications, made possible by investigations with the FIB-FS technique.

The results in Chapter 6 are suggestive and are by no means absolute or conclusive. There is much more work needed to be done to fully understand the source of excitation of such a dynamic system. Nevertheless, the knowledge gained from Chapter 6 is coupled with the development of the instrumentation in Chapters 3 and 4 to deliver a novel nanoscale analytical technique in FIB-FS. The dissertation is concluded with final remarks and the outlook of FIB-FS, where future directions and projects are considered, particularly those directed towards quantification, mechanistic understanding, and detection of isotopic and molecular particles.

Chapter 2

FIB-FS Background and Principles

2.1 Introduction

The delivery of charged particles to a specimen's surface results in a vast range of unique and complicated interactions with the substrate atoms, each of which has its own application, field of research, and extensive body of literature surrounding it. The photons emitted by sputtered particles and subsequently detected with the FIB-FS technique are a natural consequence of these collision processes that evolve from ion-matter interactions. As such, the detection of sputtered particles with FIB-FS and even the excitation mechanism itself will be directly influenced by the augmentation of the substrate atomic surface under irradiation. Because of these dependences, the purpose of this chapter is to present a background to some well-known ion-sample interactions that will develop under any energetic ion irradiation of a substrate surface. The discussion puts into context the mechanism of excited state formation under the same circumstances, which is reviewed in the second half of the chapter.

Despite many aspects of ion-matter interactions being well-understood, excited state formation is not one of them. Various models have been proposed over the years attempting to quantify and describe the nature of the formation, but a comprehensive model that explains the large body of experimental data has yet to be put forth. These models, as well as the experimental data they intend to describe, are discussed in a historical literature review. In this review, various methods, equipment, and hardware were developed to study photon emission from sputtered atoms which are discussed concurrently. All operate in broad ion beam settings or with probe sizes focused to the mm range and under stationary irradiation, thereby limiting the range of experimental designs to extract information and setting the stage for FIB-FS to enable new insights into the excitation mechanism.

2.2 Ion-Matter Interactions

Remaining within the scope of physics involved in FIB-FS, the phenomena associated with the irradiation of ions on solids discussed in this text is limited to regimes in which the projectile possesses the energy well above the minimum amount of kinetic accelerating energy to displace an atom from its lattice location (a few hundred of eV) and an upper limit such that the interaction is contained in the near-surface regime (few 10s of keV). The phenomena observed in these regimes is a fundamental process of the interaction of massive ions that transfer energy to surface atoms through violent inelastic and elastic collisions that result in modification of the substrate matrix. These modifications, while not limited, can be grouped into a handful of general categories and are depicted in Figure 2.1:

1. Ion implantation - the bombarding particle is incorporated into the substrate at an interstitial or lattice site following collision and recoil of lattice atoms.

2. Recoiled atom damage - substrate atoms are dislocated from their original location as a consequence of the bombarding particle's collision cascade, forming new defects, mixed interstitials for multi-chemical samples (also known as collisional mixing), amorphization, and energy dissipation in the bulk.

3. Sputtering - substrate atoms or molecules at the surface receive enough kinetic energy with a perpendicular velocity component along the surface normal from an ion-atom or atom-atom collision to overcome the surface binding energy and are ejected from the surface into the vacuum.

4. Excitation - substrate atoms and backscattered bombarding ions may be electronically excited or ionized through energy and electron transfer mechanisms.

Coupled with the delivery of the ions in a probe size less than 10 nm in diameter determined by the FIB optics (see Appendix A), these processes provide the framework for countless significant technological advances including direct maskless implantation and doping [33–35], nanoscale surface characterization [16, 36–38], ion beam lithography [39, 40], thin film deposition [41–44], nanoscale circuit edit, fabrication, and machining [45–47], and transmission electron microscope (TEM) lamella preparation [46, 47]. Such advancements have been made and are supported through the development of analytical expressions and simulations that describe sample modification under ion bombardment. The formalism that describes these mechanisms is extensive and rich with detail, such

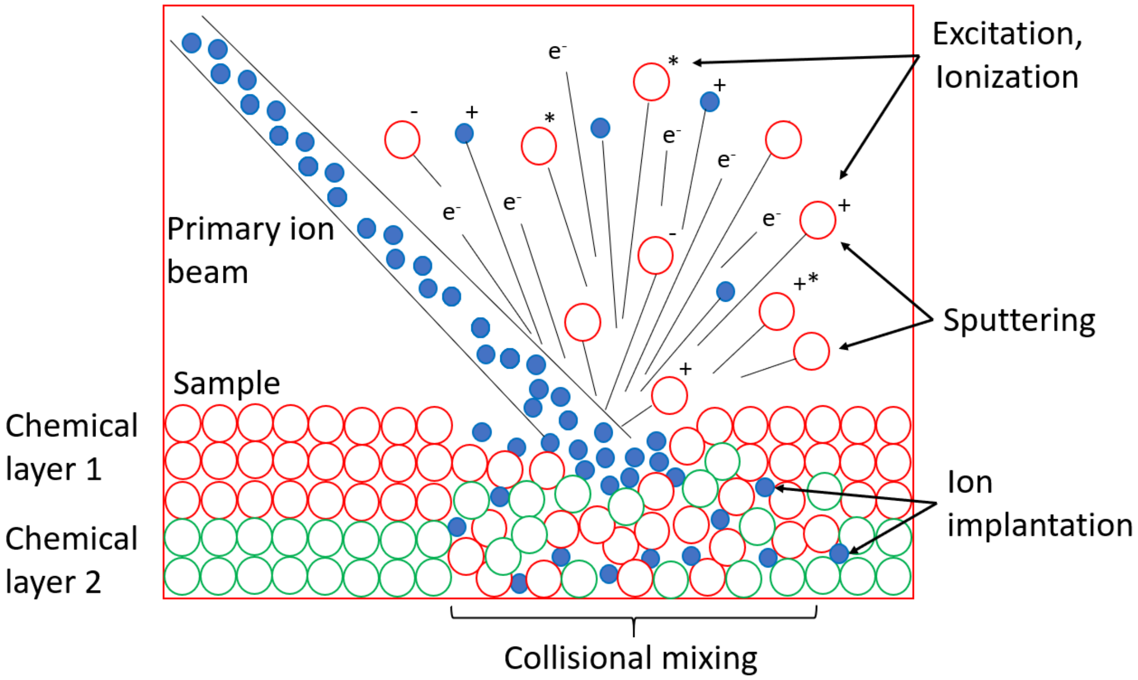

Figure 2.1: Schematic of some of the many dynamic processes that occur during ion beam irradiation. The primary ion beam bombards the surface atoms and transfers kinetic energy, resulting in secondary electron emission, ion implantation, collisional mixing, sputtering, and excitation.

that a complete review is not even remotely possible here. Since the subject of this thesis is inherently convolved with the modification of the sample atoms under ion irradiation, however, a general understanding of how these mechanisms evolve and behave as a function of experimental conditions is required. Therefore, the expressions that provide representation of the core physical concepts while allowing for simple and coherent descriptions of their dependencies on tangible experimental parameters are provided in the following paragraphs. For a full derivation of these formalisms, the reader may refer to the texts cited throughout as well as these review texts [48–58].

2.2.1 Energy Loss and Stopping of Ions in Solids

The 4 processes mentioned above are closely correlated and evolve naturally from the energy transfer of the incident projectile to the lattice atoms. This kinetic energy transfer is dissipated through either elastic collisions (nuclear collisions) or inelastic collisions (electronic collisions) in what is commonly referred to as nuclear stopping and electronic stopping, respectively. The differential energy loss is a sum of these stopping powers [49, 54, 55, 58]:

$$\frac{\mathrm{d}E}{\mathrm{d}x} = \left(\frac{\mathrm{d}E}{\mathrm{d}x}\right)_{\mathrm{n}} + \left(\frac{\mathrm{d}E}{\mathrm{d}x}\right)_{\mathrm{e}} = -N[S_{\mathrm{n}} + S_{\mathrm{e}}] \tag{2.1}$$

where N is the number density of atoms, with S_{n} and S_{e} being the nuclear and electronic stopping crossing sections, respectively.

Determination of these stopping powers have been explored extensively by Sigmund [49], Lindhard [51, 52], and Ziegler [56, 57] building on the foundations of Bohr [59] and Rutherford [60, 61]. The nuclear stopping cross section follows directly from the Coulombic potential and energy transfer T from the ion of energy E to an atom at rest:

$$S_{\mathrm{n}}(E) = \frac{1}{1-m} C_m \gamma^{1-m} E^{1-2m} \tag{2.2}$$

where

$$C_m = \frac{\pi}{2} \lambda_m a^2 \left(\frac{M_1}{M_2}\right)^2 \left(\frac{2Z_1Z_2e^2}{a}\right)^{2m}. \tag{2.3}$$

Here γ is the fraction of energy transferred in elastic collisions from momentum conservation $\gamma = 4M_1M_2/(M_1 + M_2)^2$ of bombarding ion M_1 and target atom M_2, noting that $T_{\mathrm{max}} = \gamma E$, while a is the screening length $a = 0.885a_0(Z_1^{2/3} + Z_1^{2/3})^{-1/2}$ with Bohr radius $a_0 = 0.0529$ nm. Arguably the most important factor m characterizes the power potential to describe the interaction between atoms, ranging from $m \approx 0$ at low energies and $m = 1$ at high energies, with λ being a dimensionless fitting function of m. In short, the stopping cross section increases approximately linearly at low bombarding energies $E, (m \sim 0)$ and decreases at high energies $E, (m \sim 1)$ converging to Rutherford scattering with small energy transfers.

The electronic stopping power cross section is less exact:

$$S_{\mathrm{e}}(E) \approx 8\pi e^2 a_0 Z_1^{1/6} \frac{Z_1 Z_2}{\left(Z_1^{2/3} + Z_2^{2/3}\right)^{3/2}} \frac{v}{e^2/\hbar} \tag{2.4}$$

being proportional to the ion's velocity v. This electronic stopping doesn't cause scattering of the ion, but results in energy loss and slowing down. Unlike nuclear stopping, electronic stopping dominates at high energies, however, both depend on ion and sample mass so there exists regimes of nuclear stopping and electronic stopping power based on bombarding conditions. For heavy ions like Xe, electronic stopping is almost negligible until energies in the MeV range, while lighter ions like N and O may be dominated by electronic stopping at landing energies near 20 keV shown in Figure 2.2.

The nuclear and electronic stopping cross sections can then be used to find the finite range of the ion's path length in the target from equation (2.1):

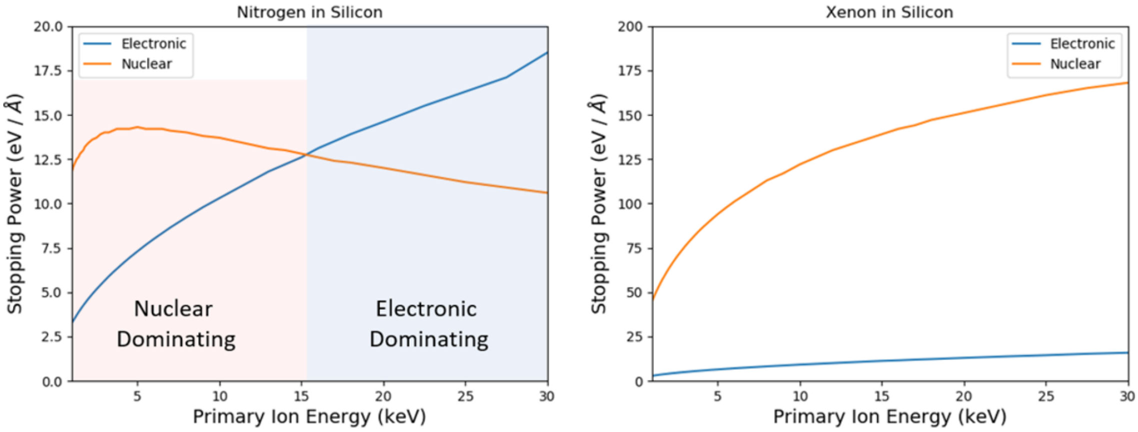

(a) **(b)**

Figure 2.2: Nuclear and electronic stopping powers for various energies of N^+ **(a)** and Xe^+ **(b)** into Si calculated with Monte Carlo simulations in SRIM [57, 62].

$$R(E) = \int_E^0 \frac{\mathrm{d}E}{\mathrm{d}E/\mathrm{d}x} = -\frac{1}{N}\int_E^0 \frac{\mathrm{d}E}{S_\mathrm{n}(E) + S_\mathrm{e}(E)}. \tag{2.5}$$

While an extensive amount of ion range data has been found to be in close agreement with this description [56, 57, 62, 63], discrepancies arise for ions incident on crystalline materials or for ions that react chemically with the sample upon implantation. If an ion travels along the axis of the crystal plane of a crystalline material, it will travel much further than the range described by (2.5) due to a “steering” effect along the channels, resulting in less collision and less energy loss than an amorphous target in a process known as channeling [64–66]. Therefore, care must be taken when considering data collected from crystalline structures and under chemically active ion species.

Owing to the energy losses described above, the recipient substrate atoms of the energy transfer from bombarding ions will be displaced and begin their own sub-collision cascade sequence. These atoms are known as recoiled atoms and their subsequent collisions after primary ion impact determine the proceeding process of recoil atom damage and defect generation in the substrate bulk. For most metals and semiconductors, the minimum amount of energy to displace a substrate atoms is between 15-40 eV [67, 68]. The displacement will produce an interstitial atom and subsequent vacancy, and for ion-atom collisions with energy transfers orders of magnitude larger than this minimum recoil energy, massive amounts of interstitial-vacancy pairs may form within the region described by the ion range $R(E)$ in (2.5). As a result, a large zone of disordered states in the center of collision cascade is formed surrounded by interstitial atoms extended a few nanometers from $R(E)$.

It is important to note that the mass dependencies of the scattering cross sections identified in equation (2.2) can lead to preferential dislocation or relocation distances of one chemical species over others in compound targets. This can create profound changes in the collisional mixing of multicomponent targets and along interstitial boundaries, complicating depth analysis of layered samples and boundary resolution of heterostructures. The bulk damage and mixing along these boundaries is the subject of many studies and will be discussed later in this text as it relates to signal transients and artifacts from this evolution during ion irradiation.

2.2.2 Sputtering

Also owing to the energy losses described above are the recoiled atoms that end up travelling towards the surface with enough kinetic energy to overcome the surface binding energy and be ejected from the surface. It is straightforward to see that collecting and identifying the removed atoms from the surface of the sample allows for important chemical and structural information to be obtained, and that the FIB probe size enables this capability at the nanoscale. Therefore, it becomes necessary to develop a formalization of sputtering in order to understand quantitative yields, statistics, and behavior characteristics of sputtering under different ion conditions.

There are three regimes used to describe sputtering as a result of the different displacement cascades that develop under various ion-sample energy and mass conditions [48, 50, 55, 58]. The near-threshold, or single-knockon regime, is used to describe light ions with low energies which produce only a handful of isolated recoiled atoms (e.g. He^+ with energy of a few hundred eV to 1 keV). The non-linear or spike cascade regime is used to describe cascades that produce so many frequent collisions that linear models break down, such as in the case with high energy and heavy ion (e.g. U^+) or cluster ion bombardment. The most widely applicable formalization is the linear collision cascade regime, developed by Peter Sigmund [48–50]. It describes a binary collision model that treats each moving ion and stationary atom collision individually and most accurately describes the interactions occurring for the majority of modern FIB energies and ion species. It is the only one considered here.

According to Sigmund, the sputtering yield Y scales linearly with the energy deposited at the surface:

$$Y(E,\theta) = \Lambda F_{\text{D}}(E,\theta,x=0) \tag{2.6}$$

where Λ is a material-specific constant and $\int F_{\text{D}}(E,\theta,x)\text{d}x$ is the energy available in the cascade to create recoiled atoms. The factor Λ was explored by Sigmund and related to the material's planar surface barrier. If the recoiled atom has enough energy to overcome the surface binding energy U - i.e. the probability of the atom i escaping the surface at angle θ_i is equal to 1 if $E_i\text{cos}^2\theta_i \geq U$ - then the factor Λ is derived from the recoil density and stopping power cross section:

$$\Lambda = \frac{\Gamma_m}{8(1-2m)NC_mU^{1-2m}} \tag{2.7}$$

where N is the atomic density of the substrate, $\Gamma_m \approx 0.4$, and C_m is defined in (2.3). When $E_i \sim U, m = 0$, 2.7 reduces to:

$$\Lambda = \frac{3}{4\pi^2}\frac{1}{NC_0U}. \tag{2.8}$$

The energy deposited by the ion to the surface F_D is defined by the landing energy E, incident angle θ (relative to surface normal), and the primary ion nuclear stopping power S_n:

$$F_\text{D}(E, \theta, x = 0) = \alpha N S_\text{n}(E) \tag{2.9}$$

where alpha is a dimensionless function of θ and mass ratio M_2/M_1. Combining (2.6), (2.8), and (2.9), the sputter yield becomes:

$$Y(E, \theta) = \frac{\Lambda\alpha S_\text{n}(E)}{U} \tag{2.10}$$

Equation (2.10) is one of the most widely used and cited equations in ion-solid literature, however, it is important to note that it attributes too strong of an interaction potential at low energies and a discrepancy arises.

Early results by Sigmund [48] used $C_0 = 0.0181\text{nm}^2$ (owing to the Born-Mayer screening length a), showed that (2.10) reduces to

$$Y(E, \theta) = 0.042\frac{\alpha S_\text{n}(E)}{U} \tag{2.11}$$

and a factor of 2 discrepancy between experimental data was consistently seen. Since then, corrections to the low energy regime have been made by various authors [69–71], but accurate measurements of sputtering at low energies remains difficult. Therefore, the energies explored in later chapters remain above 1 keV landing energy.

Despite the low energy convergence, (2.10) remains powerful at predicting sputter yields for atoms at higher energies and provides a simple description of the yield as a function of the ion incident angle, energy, mass, and sample parameters like surface binding energy, density, and mass. A highly influential parameter to the sputter yield is the term α. Historically, α values were extracted from experimental data, but absolute values now exist after decades of research. In

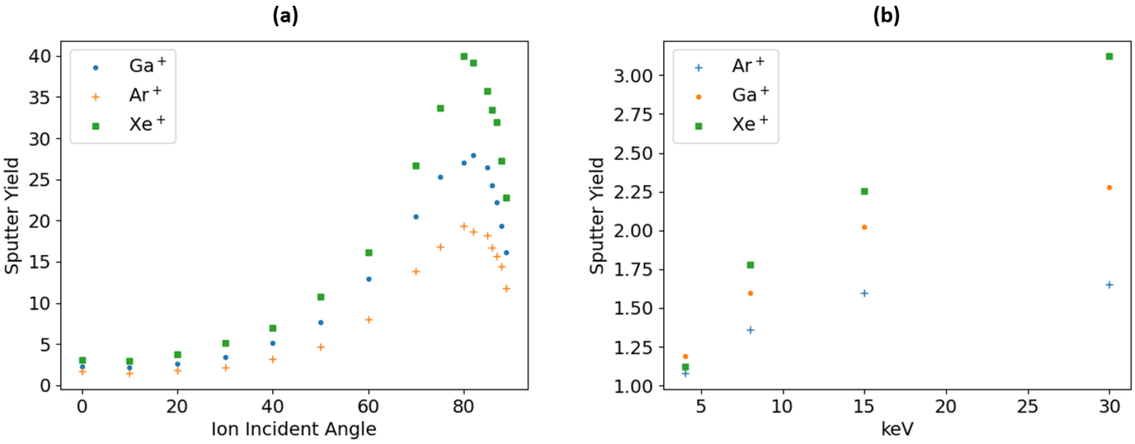

Figure 2.3: Sputtering yield results calculated using the Monte Carlo program SRIM. **(a)** shows the behavior of the sputtering yield in units of sputtered atom/ion for various ions at 30 keV landing energy on Si at multiple primary ion incident angles θ in degrees (0 = surface normal), highlighting the strong dependency of sputtering yield on incident angle. **(b)** shows the behavior of the yield for various ions on Si at multiple landing energies, showing the strong dependency on ion-atom mass ratio and landing energy, owing to the nuclear scattering cross section according to (2.10).

short, α depends on the mass ratio of the primary ion and sample atom and the primary ion incident angle θ. It remains fairly constant for mass ratios (ion/atom) less than 0.5, but increases rapidly for ratios above 0.5 and increases exponentially with increasing θ until near-glancing angle irradiation where it takes a steep dive. Figure 2.3 shows how these parameters affect the sputtering yield for ion irradiation of Si.

There are two significant consequences of this mass-ratio and incident angle dependence for a given ion mass that affect any FIB-based experiment or analytical technique. The first is that the elements comprising of a compound or multicomponent target will be sputtered at different rates in a process called preferential sputtering. If one element is preferentially sputtered at a higher rate than another element in the same sample target, then different perceived concentrations of the respective elements will be interpreted when a population of atoms are collected from the same sputter acquisition. In a more dynamic sense, this process will also actively change the stoichiometry of the surface under irradiation. Changes in the chemical structure of the surface can create a perpetual feedback loop until a steady state is reached: preferential sputtering causes changes to surface chemistry, which induce changes to surface binding energy, which cause changes to the sputtering rate... Thus, for compound samples, time-resolved or transient measurements will always involve a dynamically evolving

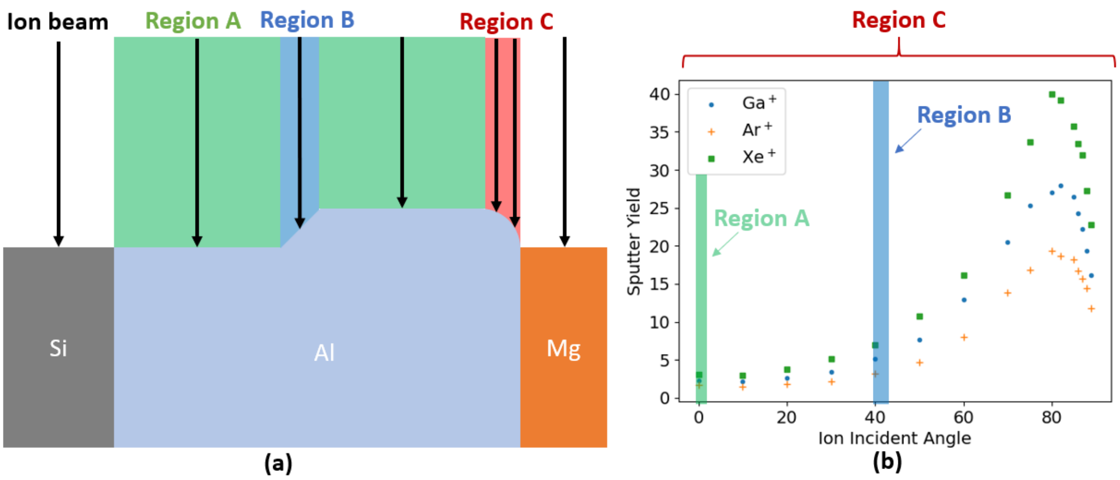

Figure 2.4: Depiction of how artifacts arise from relative sputter yield changes due to sample topography. **(a)** shows a cross section of an arbitrary multicomponent sample with varying surface topography defined by different ion incident angles in Regions A, B, and C. As the ion beam scans across the different regions, atoms of the respective chemical composition will be removed in accordance with the rate defined by **(b)**. Despite no chemical or stoichiometric changes between regions A, B, or C, more atoms will be removed in regions C and B than region A. As a result, the concentration of Al atoms may be perceived to be higher in these regions.

surface with variable, element-specific, atom removal rates.

The second consequence is the impact of the surface topography on the sputtered atom yield. Even at the nanoscale, a target surface will naturally have geographical variations in its structure such that increased sputter yields will be observed around edges and features. In other words, the contours of a feature change the primary ion incident angle and result in a relative increase in the sputtering rate at the contour. Figure 2.4 shows how in these areas more atoms will be sputtered compared to the rest of the area of interest and how they can result in misleading concentration ratios despite a consistent chemical profile. This manifests as an artifact when the collection of the atoms or signals are mapped to spatial locations to form images, chemical maps, or depth profiles. Not only will increased counts be observed laterally around edges and boundaries, but as the ion beam continues to mill, these regions will be removed faster and expose target substrate atoms at varying depths for a given 2D scan. This type of non-planar delayering and recession of the surface easily causes confusion and misleading spatial information for a given image or profile with signals coming from mixed depth locations.

2.2.3 Stopping Range of Ions in Matter (SRIM)

It's clear that any ion-sample irradiation experiment contains a significant amount of dependencies and complex interactions and that a strong grasp of these behaviors is needed before interpreting any secondary signals that arise from ion bombardment. The preceding formalism has been expanded upon by many authors in order to spatially characterize the magnitude of ion implantation, collisional mixing, sputtering, and excitation as a function of experimental parameters like bombarding energy, ion mass, and substrate mass with a fair degree of certainty. As a result, the localized information can be leveraged to interpret the signals arising from ion bombardment like secondary ions and photons to draw conclusions and make corrections from the known sample modification and response to the ion beam. These corrections are particularly significant for transient acquisitions involving a dynamic and evolving sample under irradiation.

Open-access simulation programs like the Stopping Range of Ions in Matter (SRIM) [56, 62, 72] are used to provide estimates of spatial locations where the different interactions will contribute such as energy loss vs depth, tracking of implanted atoms and recoiled atoms, and surface locations of departing atoms. The program uses a Monte Carlo approach to launch ions into a sample defined by its atom density, surface binding energy, lattice displacement energy, and lattice binding energy. It launches one ion at a time and calculates each interaction along

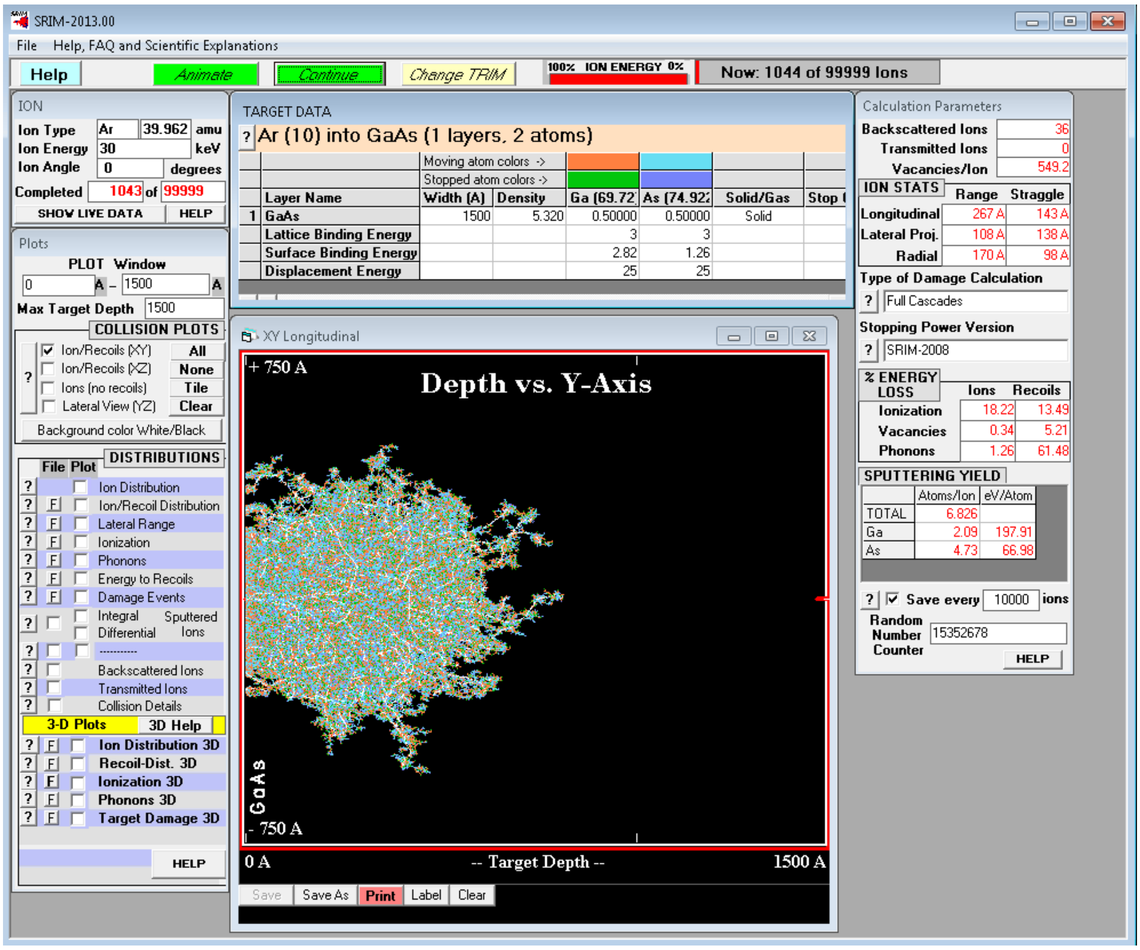

Now: 1044 of 99999 Ions

ION
Ion Type: Ar 39.962 amu
Ion Energy: 30 keV
Ion Angle: 0 degrees
Completed 1043 of 99999

Plots
PLOT Window: 0 A – 1500 A
Max Target Depth: 1500
☑ Ion/Recoils (XY)
☐ Ion/Recoils (XZ)
☐ Ions (no recoils)
☐ Lateral View (YZ)

TARGET DATA
Ar (10) into GaAs (1 layers, 2 atoms)

		Moving atom colors ->		🟧	🟦		
		Stopped atom colors ->		🟩	🟪		
	Layer Name	Width (A)	Density	Ga (69.72	As (74.92	Solid/Gas	Stop
1	GaAs	1500	5.320	0.50000	0.50000	Solid	
	Lattice Binding Energy			3	3		
	Surface Binding Energy			2.82	1.26		
	Displacement Energy			25	25		

Calculation Parameters
Backscattered Ions: 36
Transmitted Ions: 0
Vacancies/Ion: 549.2

ION STATS	Range	Straggle
Longitudinal	267 A	143 A
Lateral Proj.	108 A	138 A
Radial	170 A	98 A

Type of Damage Calculation: Full Cascades
Stopping Power Version: SRIM-2008

% ENERGY LOSS	Ions	Recoils
Ionization	18.22	13.49
Vacancies	0.34	5.21
Phonons	1.26	61.48

SPUTTERING YIELD

	Atoms/Ion	eV/Atom
TOTAL	6.826	
Ga	2.09	197.91
As	4.73	66.98

☑ Save every 10000 ions
Random Number Counter: 15352678

Figure 2.5: The SRIM program window used for estimates and visualization of the many ion-sample interactions for an example of 30 keV Ar$^+$ bombardment on GaAs. The graphical window shows the Ar ion trajectories and recoiled atoms Ga and As in the sample bulk while the tabular data shows the calculated ranges, energy loss, and sputtering yields.

the collision cascade, tracking energy loss and each individual recoiled atom subcascade, allowing for quantification and visualization of ion range, recoil atom displacements, and energy loss. Figure 2.5 shows the graphical user interface of the program during a simulation of 30 keV Ar ions into a sample of GaAs, depicting the ion trajectories, preferential sputtering yields, atom recoil locations and more. Even more detailed information such as energy loss of the recoiled atoms, phonon generation, and ionization yields can be tracked and analyzed from an exported text file from the program that records every detail of every interaction. The SRIM program and calculations on the output disk data are used throughout the analysis in this document to investigate contributions from different aspects of the ion-sample interaction to the emission of secondary ions and photons.

2.3 Photon Emission

When a beam of charged atoms bombards the surface of a material, a variety of particles will be ejected from the surface as a result of the principals discussed above. Elastic collisions between the incident ions and substrate surface atoms may cause some of the incident ions to be backscattered, while inelastic collisions will cause the ejection of electrons (secondary electrons or SEs) and substrate atoms via sputtering. The vast majority of sputtered substrate atoms will be ejected in the form of ground state neutral atoms, however, a fraction of the population may be ejected in an ionized state or excited state as a consequence of the collision, energy transfer, or electron transfer occurring during the interaction volume or just above the surface.

Since each element has a unique, quantized electronic structure and mass, the population of atoms can be collected and identified. A handful of techniques have been developed to capture and identify these sputtered atoms for direct elemental analysis. Some methods are based on the excitation that happens inherently in the bombardment processes, such as secondary ion mass spectrometry (SIMS) [16, 36–38], while others rely on an *ex situ* source of excitation, such as laser induced fluorescence (LIF) [73–75], laser induced resonance ionization spectroscopy (RIS) [76, 77], or multiphoton ionization techniques [78–81].

A lessor known signal that is emitted during the ion bombarding process are photons, which can be analyzed through spectroscopic means to perform elemental analysis [27–29, 31, 32]. The photons emitted during ion irradiation come in two forms depicted in Figure 2.6 – atomic line emission from an excited sputtered atom, and broadband emission from electron-hole recombination across a bandgap in the bulk. Both types of photonic emission reveal unique information that is characteristic of the sample and inherent to its process.

The source of the broadband emission is believed to be attributed to the recombination of electron-hole pairs in the bulk of the material [82–85] – an analogue to the cathodoluminescence (CL) phenomena and the basis of its etymology: ionoluminescence (IL). As the ion penetrates into the sample, it will excite electrons across the material's bandgap via inelastic collisions. Once the electron is excited across the bandgap, it will return to its valence band or another electron will recombine with the newly-formed hole. Because defects and variations in the crystal lattice structure exists in the bulk, the energy of the gap that the electron crosses may vary. Combining this with the initial energy level of the electron, which could be greater or less than the bandgap of the material, results in a broad range of energies in which the electron may de-excite, yielding a continuous broadband curve. The spectrum resulting from this emission can be used to identify defects, crystal structures and impurities [85, 86].

While electron-hole recombination is certainly possible within the interaction volume of many ion-solid experiments, care must be taken in the interpretation of the source of the signal. The existence of the defect or band gap that is required to generate the recombination will not have an overlapping valance-conduction band and will therefore be subject to surface charging induced by the energetic probe ions. As the surface continues to charge with ion irradiation, the secondary electrons emitted by the ions will be attracted back towards the sample, being accelerated by the potential at the surface (which can easily reach keV locally). In these conditions, it is impossible to discern if the continuum emission is a result of ion collision or electron collision (IL vs CL). Because of these complications and that the same information can be gained by the non-destructive CL technique, IL has not attracted much popularity outside of a few He ion microscope applications [82, 85] and mostly remains a source of background and spectral contamination for the more valuable atomic line emission.

The source of the atomic line emission has been attributed to the excitation of a sputtered atom, occurring shortly after its collision with the incident ion. The mechanism of the excitation has been proposed to happen through multiple avenues [27, 28, 87, 88]:

1. a ground state atom may collide inelastically with another atom on its way out of the solid and become excited

2. the initial collision with the incident ion leaves the struck atom in an excited or ionized state

3. perturbations from the collision cascade deposit energy and create a lo-

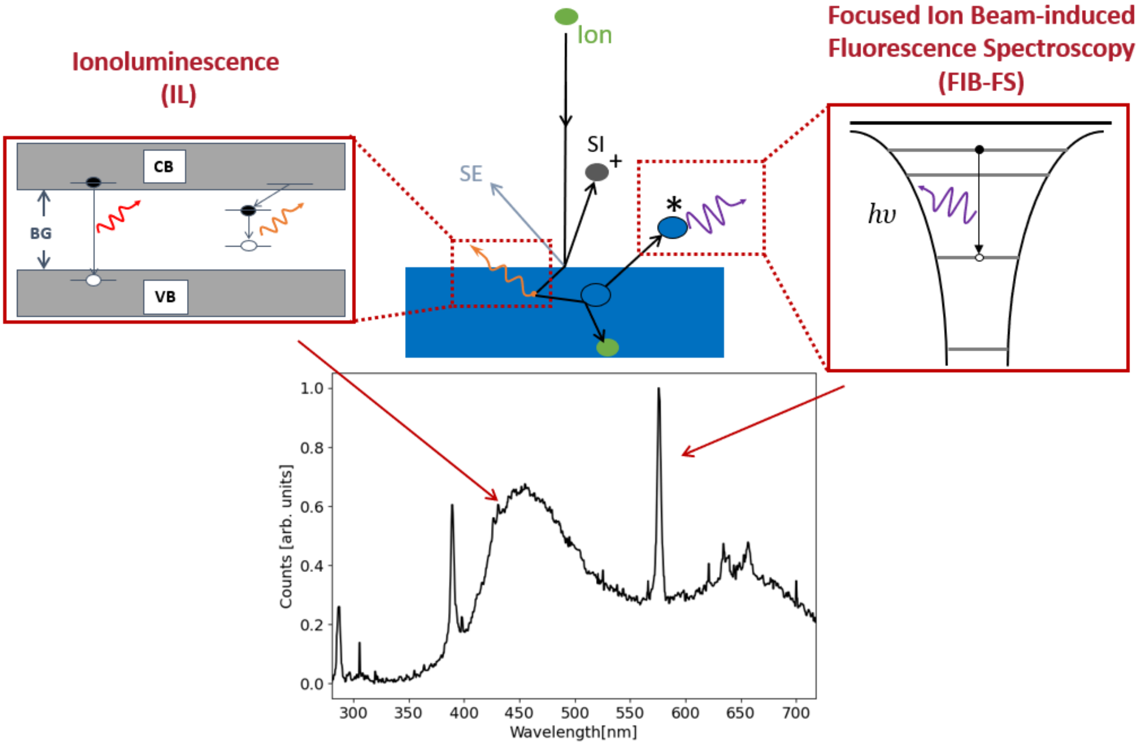

Figure 2.6: Depiction of the two types of photon emission mechanisms from a SiO_2 sample under 30 keV Xe^+ bombardment and the resulting spectra. When the ion contacts the surface of the sample, collisions cause the emission of secondary electrons, sputtered atoms, and sputtered ions. Some of the sputtered atoms are emitted into an excited state and deexcite above the surface releasing a photon with energy $h\nu$, indicative of its elemental electronic structure. Collection and diffraction of these photons results in Si atomic line detection shown in the spectrum, the core process for FIB-FS. As the ion continues along the collision cascade, excitation of electrons across the SiO_2 bandgap occurs. These electrons can relax directly across the bandgap, or through pathways with many defect or virtual states of lower energy, resulting in broad emission spectrum of continuum energy, the core process for ionoluminescence.

cal thermodynamic equilibrium (LTE) at an elevated temperature which the atom passes through

4. an initially sputtered diatom or molecule breaks apart and the dissociation of the molecule results in a charge exchange of an electron into an excited state

5. an initially ionized atom captures an electron into an excited state during its departure

Explanation of the excitation mechanism is only half the battle; once the particle has left the surface of the sample in an excited state by any mechanism, it may return to its ground state by means of either radiationless deexcitation or photon emission. A competition for the deexcitation pathway may exist between excited electrons tunneling directly into vacant states in the sample, Auger deexcitation, and photon emission, making conclusions on the excitation mechanism of the sputtered species even more complicated in addition to the dynamic changes to the surface inherent to ion-solid interactions.

A large body of literature dating back almost 100 years offers extensive studies on ion bombardment and sputtered atoms trying to discern the nature of the excitation and deexcitation. Much experimental data has been accumulated to study the effect of yields, velocity distributions, angular distributions, and population distributions of the ejected particles on a variety of substrates and surfaces. The processes have been shown to be highly dependent on primary ion beam conditions of current, angle, and energy [87, 89–94], as well as target and sputtered atom characteristics such as target atom and bulk electron configuration [95–99], surface chemistry [100–104], and proximity of the sputtered particle to the target surface [105–109]. Various models have been proposed in these reports including resonant electron tunneling, binary collision, molecular bond-breaking, quantum mechanical and thermodynamic. Owing to the influence of dynamic physical-chemical properties and transients of the surface and its influence on the probability of excitation of the ejected species, however, a unified understanding of the mechanisms that govern the ionization and excitation processes of sputtered atoms has yet to come forward.

2.3.1 Binary Collision and Resonant Ionization

Effects of matter under charged particle irradiation have been long studied from scattering experiments of Thomson and Rutherford and like any other field, discoveries tend to occur concurrently in different parts of the world. Thus, it is hard to pin-point the first descriptions of light emitted by atoms under ion bombardment or develop a linear timeline of the progress in understanding. What is clear is that perplexing behavior of photon intensities under different conditions were observed even in the earliest reports studying the excitation. One very noticeable observation is that neutral atoms from metal-oxide substrates emit photons with intensity up to a factor of 10 or more compared to their pure metal counter-parts. Snoek and van der Weg provide models in the early 1960s [105, 110] that describe the discrepancy as a result of excitation from an initial collision followed by radiationless deexcitation processes above the surface.

The initial excitation is assumed to result from a constant rate of atom-atom or atom-ion binary collisions at the surface, however, the photon yield is determined by the interaction of the atom with the surface of the substrate at close distances along its departure. For a metal defined by a square potential well with electrons populating up to the Fermi level, they theorize two electron tunneling processes in a resonant ionization process and an Auger deexcitation process. Depiction of the processes are shown in Figure 2.7. They describe the probability P of photon emission from a sputtered atom as a function of its departing perpendicular velocity $v_\perp$:

$$P(v) = \text{exp}\left[-\frac{A}{av_\perp}\right] \tag{2.12}$$

where A and a are constants for transition rates of radiative transfer above the surface. Constant a is determined by the overlap of the atomic and bulk metallic electron wave functions with A being constant rate. When used to describe the neutral excited atom enhancement from oxides, non-radiative transfer is blocked by the existence of a forbidden band gap shown in Figure 2.7 process **C**, thereby forcing the excited atom to deexcite by photon emission and resulting in greater intensities.

The model proposed by van der Weg was successful in describing the obvious differences between metals and oxides, so validation with other experiments followed. Based on the perpendicular velocity component of the probability of emission, one would expect that the relationship could be probed through changes in the primary landing energy and incident angle. In these situations, the sputtered atom's probability to escape without losing its excited electron through nonradiative transfer is greater if the atom is moving away from the surface faster or if the atom has less time to interact with the surface and can escape the region. Therefore, sputtering atoms at high incident angles could eject atoms at more parallel trajectories to the surface, while ions bombarding at lower energies might eject atoms with slower velocities and result in lower yields.

Light-versus-distance (LvD) and Doppler broadening measurements were de-

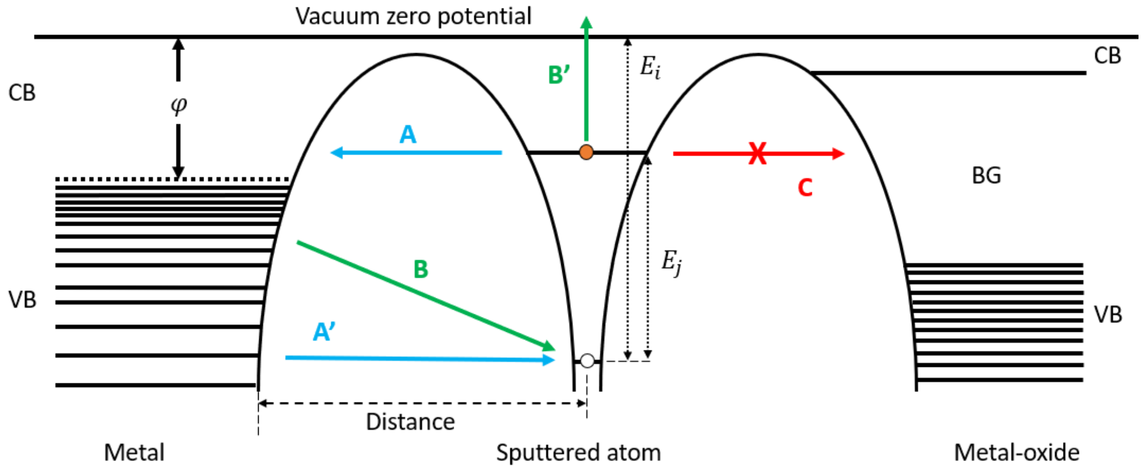

Figure 2.7: Resonant ionization and neutralization electron transfer mechanisms for excited atoms depicted on the potential energy diagram of a sputtered atom leaving the surface of metal and metal-oxide. Resonant ionization and neutralization occur via process **A** and **A'** where the excited state of energy E_j is in resonance with empty states in the conduction band near work function φ. The electron may tunnel into the bulk, leaving the sputtered atom in an ionized state, which may or may not be populated through resonant neutralization in **A'**. Auger emission shown in **B** may also occur, where a valence electron with higher energy tunnels to the ground state atom, with the excess energy transferred to the excited state electron resulting in its emission in **B'** with energy of difference in the ionization energy E_i and excited state energy E_j. For oxides, any electron transfer is blocked by the existence of a forbidden energy bandgap, forcing radiative photon emission with energy $E_j = h\nu$.

veloped as early techniques to measure these velocities by observing the decay of the photon yield as a function of the perpendicular distance from the surface. As the name suggests, the intensity I is found by taking measurements of the intensity of distances and fitting the decay curve to:

$$I = I_o \exp\left[\frac{-x}{v_\perp \tau}\right] \tag{2.13}$$

where I_o is the intensity from a particular transition, x is the distance of the measurement, and τ is the lifetime of the excited atoms defined by the Einstein coefficient of the transition. Mean lifetimes of excited states from sputtered atoms of various elements were reported early on by Andersen [111–115], Braun [116], Harvey [117], and others [118] and found to be in good agreement with expectations from short lived atomic excited states with lifetimes in the nanosecond range.

Doppler shifts are performed by measuring the line shape of the spectral signal:

$$f = \left(\frac{c \pm v_r}{c \pm v_s}\right) f_o \tag{2.14}$$

where c is the propagation speed of waves in the medium, v_r is the speed of the detector, v_s is the speed of the source, and f_o is the original frequency from the source.

The results that followed were mixed. Some results suggest that only fast particles with energy higher than 100 eV are responsible for the radiation [109, 110, 119], while other results suggest only slow particles are responsible [95, 120, 121], that a mix of fast and slow particles are present [116], that it depends on the surface chemistry [122] or the energy of the level [123], or that in some cases no broadening is observed whatsoever [30].

Doppler broadening and LvD measurements are difficult to interpret under the experimental conditions provided at the time. Compared to the charged particle microscopes of today, the hardware used for these experiments was somewhat rudimentary, typically consisting mainly of an ion source, a single Einzel lens, a vacuum chamber, fixed or limited sample/foil holders, and a monochromator to observe the light through a sapphire or quartz window. Some examples of the apparatuses used in the 1970s are shown in Figure 2.8. These devices were capable of delivering µA's of ion current into spots of diameter in the mm range over a range of energies from a few hundred eV to tens or hundreds of keV. The limitations imposed on the optical setup by the charged particle apparatus in these conditions restricted detection schemes to geometries where all particles emerging from the surface may contribute to the radiation observed at the detector. In a calculation where both the spatial distribution of the emitted light and the photon

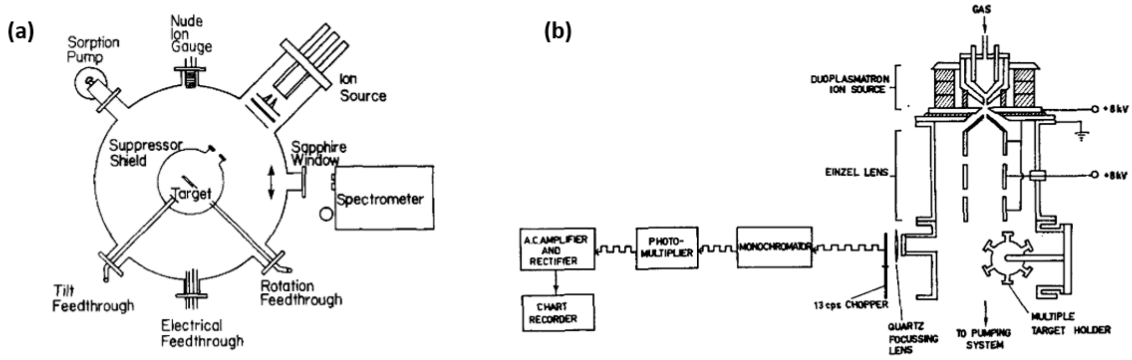

Figure 2.8: Some apparatuses used in the 1970s to study light emission from ion bombardment. **(a)** System in 1972 used by MIT researchers Martel and Olson [87], **(b)** Schematic of apparatus used by Tsong in 1975 [124].

yield are coupled to the velocity of the atom like LvD, reflections from the sample surface, cascading photon emission from higher excited states, and atoms with out-of-plane velocity vectors can contribute greatly to the interpreted signal.

Nevertheless, decreasing photon intensity with lower bombardment energies [87, 91–94] and continued reporting of high yields from of metal-oxides [93, 95–97, 125] continued to build support for this model with similar arguments being made even in more recent studies [99, 126–128].

It wasn't until adsorption experiments that studied photon emission under different gaseous environments that the model began to be challenged. Experiments that introduced a slight background pressure of oxygen and other reactive gases to the sample chamber during irradiation sought to elucidate the mechanism of the so called “oxygen effect.” The oxidation of metal surfaces provides a unique approach to the mechanisms in Figure 2.7 in that monolayer and small coverage adsorption of oxygen doesn't immediately form a bandgap in the metal's electronic structure. Rather, the dissociation of oxygen molecules on the surface will interact with the electron density, raising the occupied states near the Fermi level and act as a dipole layer pointing normal to the surface. Measured through a decrease in the work function, variations up to 1 or 2 eV can occur as the thickness of the oxide layer increases. While this doesn't produce a forbidden gap, the rise in the bound states should effectively block resonant ionization transfer mechanisms previously available in the conduction band.

Despite reductions in sputtering yield that come from the oxidation of the surface atoms, even small exposures to low oxygen pressures could lead to large photon yield enhancement. It was not uncommon to see enhancements orders of magnitude with oxygen exposure compared to clean metal surfaces throughout the 1970s [96, 125, 129–132]. While the large photon yield enhancements seem to qualitatively agree with the model, focused experiments revealed this was not the case. Most notable of these are the experiments of oxygen coverage on titanium surfaces performed by Loxton et al. [104] and those performed with cesium coverage on metals by Thomas [133] and Yu [134].

Loxton took a targeted approach to the problem by closely observing the emission of three different titanium atomic lines from different environments of pure Ti and Ti oxidation conditions. Two of the lines originated from excited states with energy above the Fermi level of the substrate while one excited state was below. The electronic structures of Ti, Ti with oxygen gas exposure, TiO_2, and TiO_2 with oxygen gas exposure will have different work functions that cause only one of the excited states being observed to go in and out of resonance with the conduction band. According to the model proposed by van der Weg, only the one state should see large relative enhancement or quenching compared to the other two lines with the increased or decreased work function in each environment. Instead, all three levels were enhanced with oxygen presence, regardless of the state.

Thomas took a different approach by lowering the work function with cesium adsorption. Cesiation of metal surfaces drastically lowers the work function such that if resonant ionization were occurring, then the relative shift in the energy levels would be enough to block the non-radiative electron transfer and enhance photon emission. The added benefit of using Cs or Li over oxidation with O_2 is that any chemical or molecular bonding contributions from oxygen are removed. In the case of fractional monolayers of cesium deposition on Cu and Al surfaces, Thomas did not see any significant photon intensity change. Even more striking, were the results from Yu who followed up with a similar experiment in 1983 showing direct evidence of electron tunneling *to sputtered ions* shown in Figure 2.9. Although Yu was studying secondary ion emission from Au and Al films and not photons, the crossing of the Fermi level with the $6s$ empty valence shell of the departing ion resulted in two orders of magnitude decrease in ion emission through resonant neutralization, effectively showing the inverse process is more likely than that proposed by van der Weg.

Kelly had proposed in 1982 [135] that the prerequisite of the van der Weg model, a binary collision, may be enough to adequately describe the variety of results. A pure statistical model, Kelly bases the excitation on random inelastic energy transfer $\Delta E = KE$ where K is a proportionality constant defined by the electronic energy loss and no interaction between the free atom and surface take place. For all excited state energy levels with energy E_i less than ΔE, the state may be populated with a probability proportional to its multiplicity g_i. He derived the following expression for the absolute yield for a sputtered atom in excited state

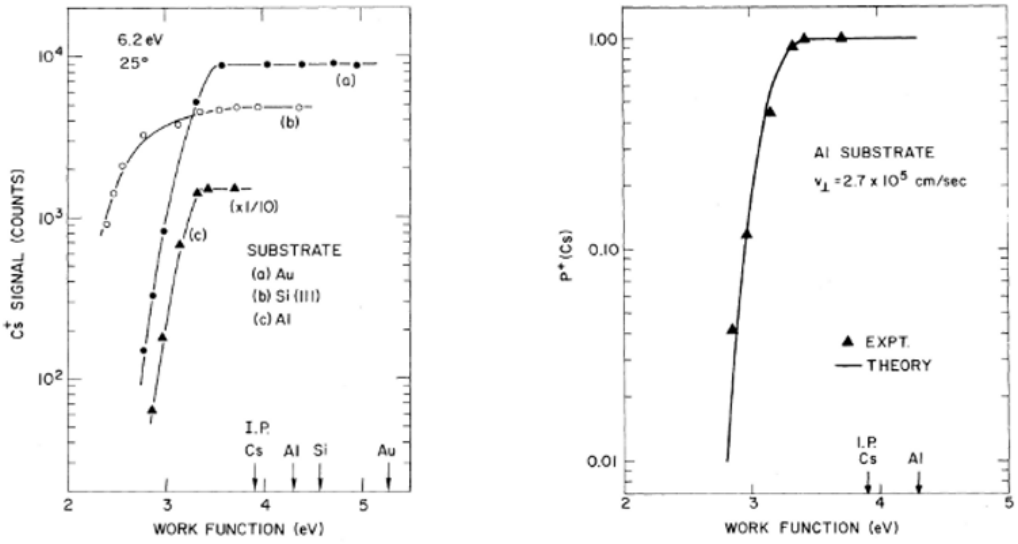

(a) **(b)**

Figure 2.9: Results of from Yu [134] showing direct evidence of electron tunneling neutralization of secondary ions during lithium adsorption on different substrate surfaces. The results show over an order of magnitude decrease in Cs secondary ion emission with reduced work function on different substrates. Both experiments used a Cs primary ion beam. The substrates used in **(a)** are labeled on the plot while **(b)** shows the Al data and model prediction.

i:

$$Y_i = 2g_i Y_T U_o K \frac{\sum_{k=i}^{\infty} G_k^{-1}(E_k^{-1} - E_{k+1}^{-1})}{\sum_j^k g_j} \tag{2.15}$$

where Y_T is the total sputtering yield, U_o is the surface binding energy, G_k is the cumulative degeneracy of states k. Comparing to a list of absolute photon yields given by Tsong and Yusuf [136] published a few years earlier, Kelly finds reasonable agreement within a factor of 3 for about a dozen elements. A consequence of the agreement in the model, however, is that the excited atoms required average kinetic energies on the order of a few hundred eV from the collision and the floor was opened again for velocity distribution measurements.

By the 1980s, laser technology had empowered techniques like laser induced fluorescence spectroscopy (LIF). LIF is based on the excitation of the atoms in the radiation field of the incident laser photons for which Bay [73] and Betz [101] provide good reviews. A high powered tunable dye laser is positioned roughly 45° from the sputtered atom plume, with the spectrometer or monochromator positioned orthogonally (see Figure 2.10). The narrow bandwidth and tunability of the dye laser allows the user to scan the wavelength of the incident beam over a range of wavelengths to resonantly excite two and three-level excited state systems of the sputtered atoms. Doppler shifts to measure velocity distributions of

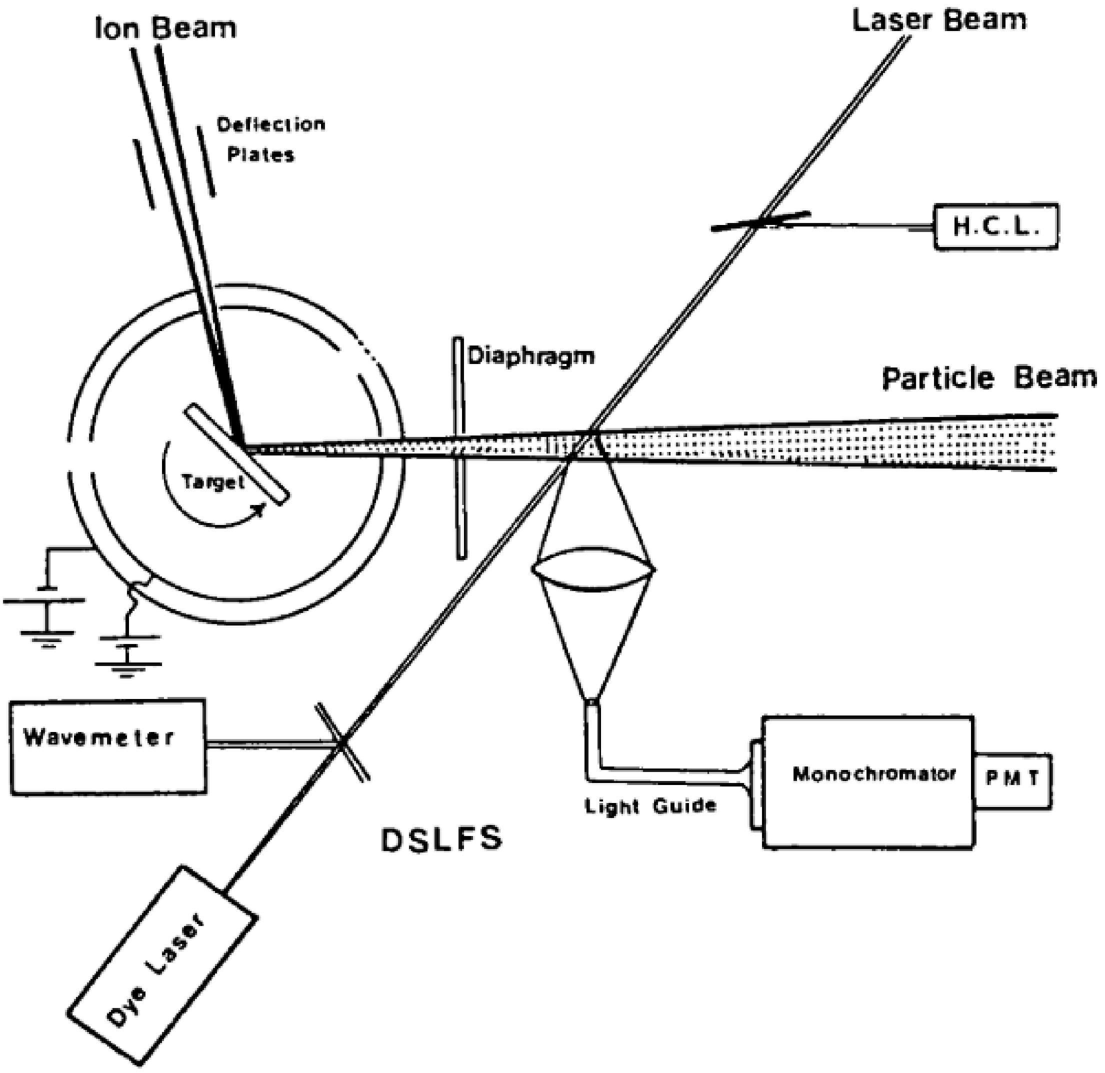

Figure 2.10: Laser induced fluorescence spectroscopy setup used by Bay [73] and Betz [101] to enable the study of velocity distributions of short lived and metastable excited states of sputtered atoms.

the atoms can be performed by observing the emission lines from the spontaneous emission of the resonantly excited atoms or more directly by measuring the absorption linewidth of the incident laser beam on the back end.

The addition of LIF technique provides multiple benefits over the prior LvD methods used. The first benefit is that the velocity measurement is decoupled from the excitation mechanism of ion beam, allowing for the energy levels to probed at distances far away from the influence of the surface electronic structure. Optical components and geometry of the setup can be modified to further reduce any artifacts from light reflections and out-of-plane atom's photon emission. Cascading photon emission artifacts from excitation of higher energy levels of the atoms are also ignored since the laser discriminates against all other levels except the resonant absorption state. The biggest opportunity enabled by LIF, however, is the detection and excitation of metastable excited states which were previously impossible to observe. These metastable states differ from the short-lived excited states in that they maintain their excitation at distances far from the surface, preserving any information generated during the sputtering event. As a result, several studies returned velocity distributions of ground state, excited state, and metastable state sputtered atoms with velocity distributions peaking at energies no more than 10 eV using LIF [73–75, 101, 137–143], much less than those required by binary collisions alone, so researchers began to look elsewhere.

2.3.2 Local Thermodynamic Equilibrium

An alternative mechanism to the electron transfer model was a local thermodynamic model (LTE) developed by Andersen and Hinthorne [144], which describes the existence of a plasma at the surface region as a potential source of the excitation. The model arose from the observation that the population of excited states N_i over the ground state N_o could be fit to a Boltzmann distribution for system in thermal equilibrium:

$$\frac{N_i}{N_o} = \frac{g_i}{g_o} \exp\left[\frac{-E_i}{kT}\right] \tag{2.16}$$

where g_i and E_i are the degeneracy and energy of the excited state, respectively. To test for the existence of a plasma from the short lived sputtered species spectra, Martin [102] derives that the population distributions can be found by the intensity I of the transition from excited state i to state j by:

$$I_{ij} = A_{ij}\; h\nu_{ij}\; N\; g_i\; Z^{-1} \exp\left[\frac{-E_i}{kT}\right] \tag{2.17}$$

where A_{ij} is the transition probability, ν_{ij} is the photon frequency of the transition, N is the total number of atoms, and Z is the electronic partition function. Thus, the "reduced intensity" plot of ln$(I_{ij}/g_i A_{ij} hv_{ij})$ as a function of excited state energy E_i should yield a straight line if the source is a plasma in LTE.

Sure enough, population distributions of the transitions from a wide range of elements returned remarkably straight lines (see Figure 2.11) and good fits suggesting the existing of such a plasma [73, 101, 102, 106, 146–148]. The results were promising and indicated the potential for quantitative analysis to be performed using the sputtered atoms.

Closer examination of the results, however, revealed many holes in the theory. First was the reporting of a wide variety of "temperatures" for the supposed plasma. Ranges of temperatures in the above reports were routinely

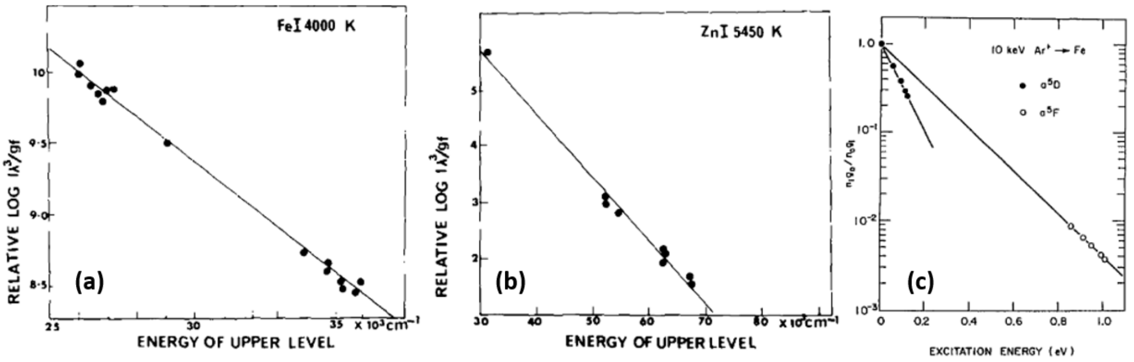

Figure 2.11: Reduced intensity plots from [102] **(a)-(b)** and [145] **(c)** showing good and bad agreement with local thermodynamic equilibrium, respectively. **(a)** and **(b)** show straight line fits with a temperature of 4000K and 5450K from 50 keV Ar$^+$ bombarding Fe and Zn found from equation (2.17), suggesting the presence of a plasma. **(c)** also returns straight line fits using the same method on data from 10 keV Ar$^+$ bombarding Fe, however, two different temperatures are found depending on which ground state multiplet the transition lands (a^{5}D vs a^{5}F).

$\sim 3000 - 10000$K, however, temperatures differing by thousands of K where being reported for the same elements by different authors (e.g. Ar$^+$ bombardment on Fe returns $T \simeq 2800$K reported by Tsong [106] and $T \simeq 4300$K from MacDonald [146]). While these differences were initially disregarded due to different experimental conditions or environments, the idea took a serious blow to its validity when different temperatures were reported for the same material in the same sputtering site. Specifically, Yu reports transitions to different ground state multiplets of Fe [145] and found $T \simeq 980$K for the a^5D multiplets and $T \simeq 2000$K for the a^5F multiplets. Tsong also reported $T \simeq 4220$K for Fe and $T \simeq 5350$K for Ni coming from the same steel sample in the same acquisition [149].

The evidence of multiple plasmas at the same surface, some of them requiring temperatures up to 10000K to deliver the observed population distributions, had mounted a justifiable skepticism for the local thermodynamic equilibrium model. Snowdon evaluated the validity of the LTE model in a fundamental analysis [150] and showed that the foundation of the model in Equation (2.17) was incorrect, but coincidentally leads to the same populations of the right approach. In a series of papers following the analysis, Snowdown backed the work showing equally impressive fits using different equations as well as showing that the secondary electrons yields are impossibly small for the existence of a plasma required by LTE [151–153], removing any physical basis for such a model. Thus, all that can be said is that the population distribution of excited states follows a Boltzmann-like distribution.

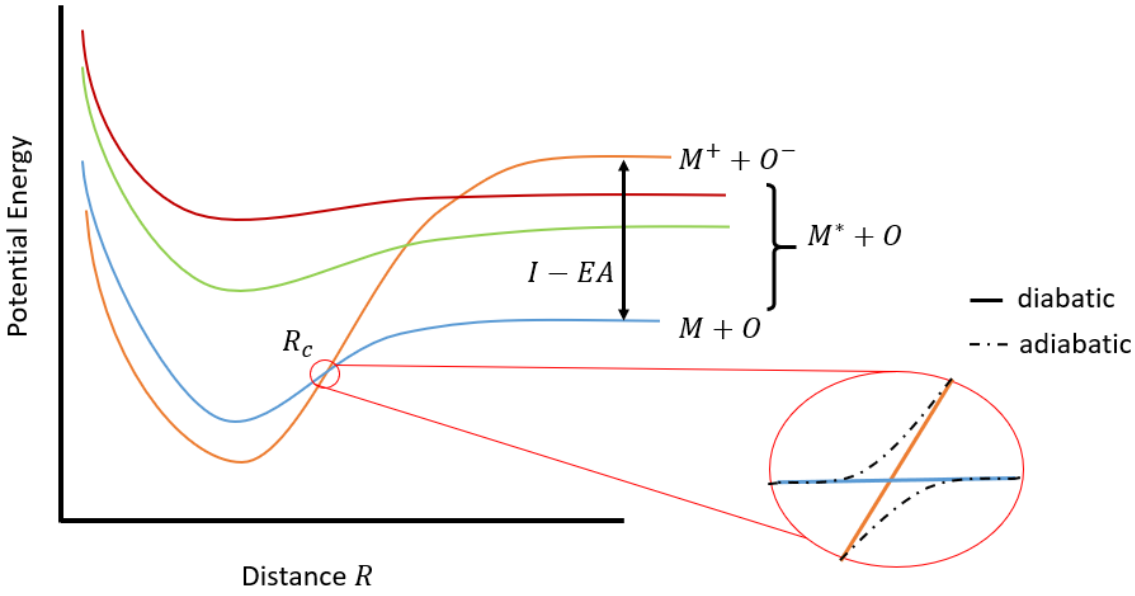

Figure 2.12: Schematic energy diagram of the molecular bond-breaking mechanism for excited state formation. At close inter-nuclear distances, the metal oxygen molecule is defined by the diabatic ionic curve $M^+ + O^-$. As the atom separates, the system may follow the adiabatic curve at crossing point R_c and result in $M + O$ neutral atom state or it can jump the gap with some probability P and continue on the ionic curve resulting in secondary ion emission $M^+ + O^-$. Many systems of excited state atoms $M^* + O$ exist between the covalent and ionic curves at various distances R_i, each with a probability P_i of following the adiabatic transition.

2.3.3 Molecular Bond-Breaking

A couple of authors [118, 133, 154] had mentioned a molecular bond-breaking model as a potential alternative explanation to their early results. Offered as more of an abstract discussion to generate ideas in those reports, they considered the formation of excited states as a result of the evolution of the electronic structure during the dissociation of molecules in the sputtering event. Blaise [155] used the model to look at a metal-oxygen bonding system to explain the enhancement in photon yield with oxygen. Supposing that the system could be treated on an individual level of metal (M) and oxygen (O) bonding, then potential energies of the metal-oxide are a function of the inter-nuclear distance R shown in Figure 2.12. At an infinite distance R, the system is described by the ground state covalent diabatic potential curve of neutral atoms $M + O$. As the two atoms approach each other, electron transfer to the electronegative atom occurs at distance R_c across the adiabatic potential energy curve and the system is defined by the ionic potential energy curve $M^+ + O^-$ at inter-nuclear distances $< R_c$.

The process is considered in reverse for excitation. At the surface, the atoms are initially defined by the ionic potential energy curve of the $M^+ + O^-$ system at close inter-nuclear distances. During the sputtering process, the metal and oxygen atom begin to separate following the diabatic potential energy curve of the ionic system to the cross-over point R_c. If the atoms are moving away with enough speed and energy, then it is possible that the gap is jumped and the adiabatic to diabatic transition is skipped. The electron is kept by the electronegative species O^- and the system continues along the ionic diabatic potential curve, resulting in positive metal ion M^+ and negative ion O^- at an energy above the ground state neutral system defined by the difference in ionization energy I of the metal atom and electron affinity of the oxygen atom EA. Since many states of excited metal atom M^* exist between the neutral curve and ionic curve with multiple curve-crossing points, Blaise qualitatively describes the enhancement of emission with increased oxygen coverage.

Later, Yu formalized the bond-breaking model and uses the concept to first predict the probability of secondary ion emission with and without oxygen coverage [156]. In the case of pure metals, it is assumed that a cation vacancy X is created on the surface during the sputtering of metal M. This cation vacancy can trap an electron with an electron affinity EA in a similar curve-crossing process as the dissociation of a metal-oxide atom, except here the inter-nuclear distance is treated in regards to the surface vacancy–sputtered metal atom distance ($M + X$ instead of $M + O$). The Landau-Zener curve-crossing formula is used to calculate the probability of ionization:

$$P^+ = G \exp\left(-\frac{2\pi H_{12}^2}{v|a|}\right)_{R=R_c} \tag{2.18}$$

where G is the ratio of the degeneracies of the ion and ground state M^+ and M^0, v is the escape velocity, and $|a|$ is the difference in the first derivatives of the potential curves. H_{12} is the transition-matrix element defined by the normalized wavefunctions of the electron in the metal atom M and cation vacancy site X:

$$H_{12} = \frac{R_c}{8}\psi_1\left(\frac{R_c}{2}\right)\psi_2\left(\frac{R_c}{2}\right) \tag{2.19}$$

Yu uses a hydrogen-like wavefunction for ψ_1 since the outermost electrons for the metals being considered were s electrons:

$$\psi_1(r) = 2\alpha^{3/2}\exp(-\alpha r) \tag{2.20}$$

where $\alpha^2 = 2I$, I being the ionization potential.

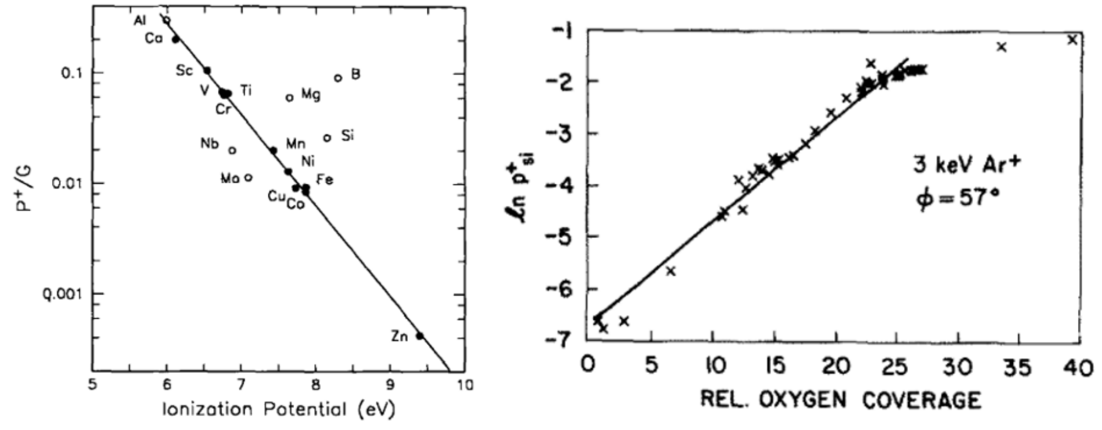

(a) **(b)**

Figure 2.13: Application of the molecular bond-breaking model of ionization probability developed by Yu for secondary ion emission. **(a)** Theoretical ionization probability for 17 elements plotted as a function of their ionization potential [156]. **(b)** Ionization probability of Si as a function of oxygen concentration [157].

Not much is known about the state of the cation site X, so Yu approximates ψ_2 as a negative ion in the field of M^+:

$$\psi_2(r) = \left(\frac{R}{R-r}\right)^{1/\gamma} C\frac{\sqrt{2\gamma}}{r}\text{exp}\left(-\gamma r - \frac{r}{R\gamma}\right) \tag{2.21}$$

where $\gamma^2 = 2EA$ and C is an amplitude fitting parameter to correct for the fact that ψ_2 is a solid-state cation vacancy.

Using the ionization model above, Yu predicted the secondary ion yields of roughly a dozen metals from their ionization energy I and the electron affinity of oxygen EA with great accuracy [156]. The model also agreed well for secondary ion emission under increasing oxygen adsorbate coverage (see Figure 2.13).

Yu later extends the model to photon emission [145], describing the excitation probability P_i:

$$\begin{aligned} P_i &= g * \frac{1-p}{(1-p)g_0 + pg_+}, \qquad \text{where} \\ p &= \text{exp}\left(\frac{-2\pi H_{23}^2}{v|a|}\right)_{R=R_{ci}} \end{aligned} \tag{2.22}$$

but the model didn't see as much success as it did describing secondary ion emission. One reason is because a consequence of the molecular bond-breaking model is that the maximum excitation energy allowed by the curve-crossing is $I - EA$, yet excited states and metastable states were routinely reported with energies well above this limitation [96, 118, 125, 155]. Additionally, velocity distributions from LIF measurements began to report the slow speeds of the excited atoms [73–75, 101, 137, 138, 141–143], with some being emitted at slower velocities than the ground state atoms being sputtered [139, 140], contradicting the proposed curve-crossing theory.

2.3.4 Resonant Electron Transfer

Considering that the electron neutralization model proposed by van der Weg can be seen as early as 1965, it is odd that the reverse process wasn't proposed until almost 20 years later. Perhaps it took the growing evidence of secondary ion neutralization by Yu and discoveries with SIMS to spark the idea, but the appearance of a model that describes the resonant transfer of an electron into an excited state of a departing sputtered atom first appears in 1981 by Veje [158]. In contrast to the models inspired by van der Weg, Kelly, and Gruen described in 2.3.1 which ascribe to a process that begins with an excitation source from binary atom-atom or ion-atom collisions followed by a yield determined by the interaction of the atom with the surface, Veje proposes that atoms are emitted in the same state that they exist in the solid (i.e. as ionic cores) and that the excitation of the neutral atoms is determined by the population of excited states of the departing ion in a resonant neutralization from the band structure of the surface.

Veje begins with a description of the atoms in the metal that follows the Sommerfeld picture in which the atoms are sitting as ionic cores within an electron gas [159]. The valence electrons will be delocalized in a pure metal, sitting at a potential described by the Fermi energy. Thus, as an ionic core sputtered from its lattice site passes through the electron gas, it may be effectively neutralized through pickup of an electron into the ground state. For excitation, ions that survive the neutralization will then be subject to a time-dependent evolution of the valence-shell orbital or outer-shell orbital becoming a free atomic eigenstate at some finite distance nanometers away from the solid where interactions with the surface field no longer disturb the orbital. Since electrons will tend to preserve their original orbital energy, orbitals with final atomic binding energies close to the binding energies of the valence electrons in the solid may be populated by an electron tunneling process during this transition to a free atom. Consequently, orbitals that have final states that lie at higher energies or that are bound more tightly will be less likely to be populated than ones whose final states more closely resemble the electron's original energy.

In series of reports from 1981 to 1990, Veje used this model to describe the population distribution and respective photon emission from excited states of neutral and ionic metals [29, 89, 90, 103, 108, 158–160]. In each of these studies, Veje observed significantly more emission from excited ions than for excited neutrals, particularly for Al, Mg, and Be metals. By comparing the electronic energy structure of the free atom energy levels that the transitions were coming from, Veje found that the states being populated were very close to the work function of the metal under bombardment. When observing the same states under oxygen exposure, he found that states laying above the Fermi level were enhanced, which he attributed to a decrease in the work function and an increase in resonant transfer that preferentially populates the higher states at the new condition [103, 108].

Unfortunately, Veje's model didn't gain much attention until a resurgence in studying the excited sputtered species occurred in the late 1990's. A number of profound studies on sputtered excited metastable states were conducted which resurfaced many questions regarding excitation mechanisms [79, 80, 161–174]. Aimed at providing population and velocity distributions of excited states, resonant multiphoton ionization spectroscopy is coupled to a time-of-flight (ToF) mass spectrometer in these studies to ionize and then detect metastable and excited states. An example of such a setup is shown in Figure 2.15.

Berthold and Wucher particularly call upon Veje's model to describe the fact that velocities the metastable states of sputtered silver atoms drop-off by an order of magnitude compared to the neutral ground state silver atoms and vary as a function of incident angle [79, 169, 170]. Namely, that the excitation probability P scales as:

$$P(v) \propto 1 - \text{exp}\left(\frac{-A}{v_{\perp}}\right) \tag{2.23}$$

where A is a parameter related to the electronic properties of the sputtered atom, much like Equation (2.12). Vandeweert provides a good illustration of the process in [165] after observing similar phenomena from sputtered Co and Ni, it is shown in Figure 2.14.

Vandeweert [165, 166], Wucher [174], Bastiaansen [167, 168], Cortona [163], Lievens [164], and Tan [173] follow up with reports of high populations of metastable states from sputtered atoms. The population of the states is preferential for states that resemble valence band configurations of the bulk. The populations of the metastable states in these experiments were consistently in the several percent of the total sputtered population (and in one case [173] a complete population inversion over the ground state population), such that the only explanation could be a resonant electron transfer.

Just when it seemed as though the question had finally been answered, Staudt [80] and Sroubek [171] report abnormally high populations of silver atoms into the $4d^9 5s^2 (^2\text{D}_{5/2})$ state. The result is alarming since this state lies at an excitation energy of 3.75 eV, well above the Fermi level of silver, and thus could not be populated by resonant electron transfer from the band states of the solid to the

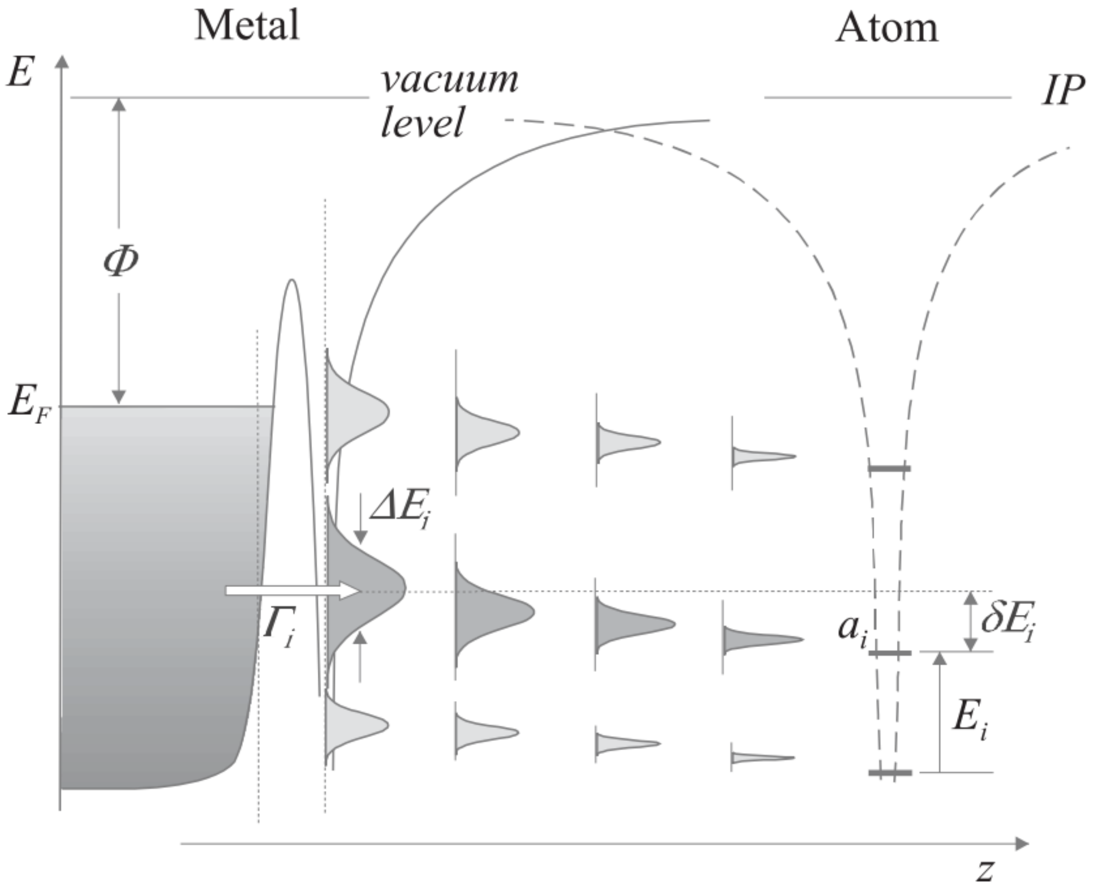

Figure 2.14: Schematic of the resonant electron transfer model provided by Vandeweert [165]. During sputtering, the excited state wavefunctions of the departing atom have some overlap with valence band states at close distances to the sample surface. At greater distances, only those with strong resonance are populated.

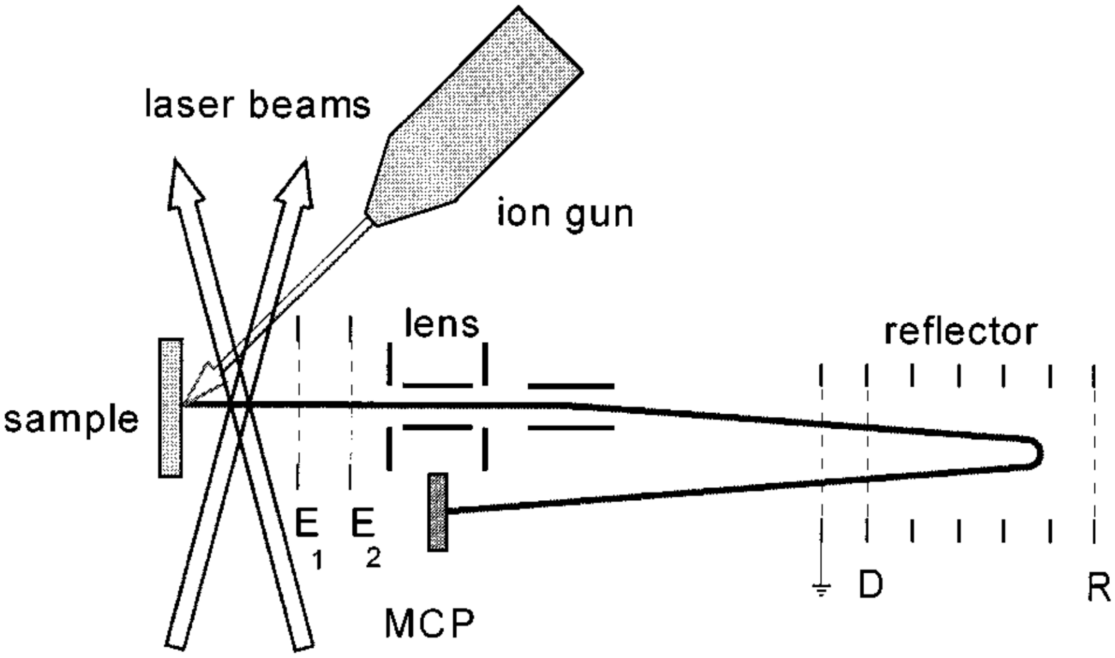

Figure 2.15: Example of the multiphoton resonant ionization and mass spectrometer experimental setup used by Berthold and Wucher [79] and popular throughout the 1990s and early 2000s to study excited metastable states from sputtered atoms.

outgoing particles. In addition, the angular models developed by their coworkers Wucher [174] did not match the new data. Thus, the familiar cloud of doubt was once again cast upon the mechanism of excitation, however, with new questions and ideas that these newer studies have surfaced [172].

2.4 Analytical Techniques

Despite a lack of understanding of the physical nature of the process, a couple of scientists appreciated the potential for analytical capabilities in photon emission. Aside from the apparatuses assembled to perform techniques of LIF and multiphoton ionization mass spectrometry, a couple of dedicated systems were developed to use the photon emission from sputtered atoms to try and deliver meaningful chemical information throughout the 1900s. One such technique is called Ion Beam Spectrochemical Analysis (ISBCA), developed by Tsong and McLaren in early 1970 [106, 124, 175], which uses a duoplasmatron source to deliver a 1 mm diameter Ar^+ beam to a target surface at 20 µA/mm^2. A quartz lens is mounted on the side of the specimen vacuum chamber that couples the light into a grating system and onto a photomultiplier for wavelength detection. A figure of the system is shown in Figure 2.8.

A second technique is called Surface Composition by Analysis of Neutral and Ion-Induced Radiation (SCANIIR) developed by White, Simms and Tolk in the early 1970s [31, 32]. The SCANIIR method is mostly identical to the IBSCA method, with the exception of a charge exchange chamber and deflection plates located above the specimen chamber which enable the formation and delivery of a neutral primary beam to the surface. The ion beam passes into the charge exchange chamber where the pressure of the exchange gas is regulated to produce roughly 30% neutralization of the ion beam. These atoms continue on their trajectory past the chamber where a dipole deflector deflects the remaining ions out of the beam and into a dump, leaving the neutral atoms undeflected and free to pass into the specimen chamber and onto the target surface.

Studies with the SCANIIR and IBSCA techniques demonstrated the potential for the photon emission to be used in analytical experiments, however, these techniques were not widely characterized outside of some detection sensitivities [31, 32, 106, 124]. Tsong and Yusuf [136] are among the very few to attempt to quantify absolute photon yields, reporting values ranging from 10^{-2} to 10^{-6} photons/sputtered atom for various metals under 20 keV Ar^+ bombardment. While these reports show the detection sensitivity of some materials down to 1 parts-per-million (ppm) or lower, the SCANIIR and IBSCA techniques fell out of popularity and into a niche experimental field of broad ion beam bombardment and mechanistic studies through the 1980s and 1990s. Conversely, ion beam technology branched out and advanced at an exponential rate such that these techniques are now completely obsolete for modern nanoscale environments that FIBs routinely operate in.

2.5 Conclusion

It is clear that the field of ion irradiation is no closer to a consensus on describing the nature of the emission than it was decades ago. Many of the questions that haunted researchers since its discovery are unanswered. One might even conclude that this confusion has been a critical point in the lack of success of photons being used in analytical techniques or the absence of any photon detectors on modern day FIBs. On the other hand, the mechanisms that govern secondary ion emission are equally complicated by matrix effects and conflicting discussions on ion formation during sputtering continue to this day. Nevertheless, SIMS is established as a premier nanoscale analytical technique that has seen its success cultivate alongside the advances of the FIB systems. Considering that the photon yields and sensitivities determined from prior rudimentary methods are similar to SIMS yields (and in some cases, better), it is reasonable to reassess the valuation of photons from sputtered atoms as a beneficial and convenient means to extract elemental information in modern microscopy. Additionally, if there's one trend that can be extracted from the prior literature, it is that more clarity is gained as more data is brought forth. Perhaps it was easy to describe mechanisms early on with simple concepts from a small batch of data taken with techniques limited by the technology of the day. As new avenues are opened with new instruments and advances in technology, however, these simple concepts become inadequate and the richness of the data increases.

The following chapters present and characterize a new technique based on these principals in the hopes of continuing this trend and by providing solutions for new applications more suited for modern FIB applications. In doing so, FIB-FS is developed as premier technique for nanoscale 3D tomography with widespread application, capable of delivering new insights into these mechanisms and propelling it from the obscurity of its foundations.

Chapter 3

FIB-FS Design and Development

3.1 Introduction

The combined FIB-SEM system is a well-established technology that has a profound breadth of application space that touches almost all areas of science. The combination of the powerful imaging and analytical techniques available from the SEM and the modification capabilities provided by the FIB, allow users to image and process both surface and internal structures of samples at the nanometer and micrometer scale on a single platform. The two charged particle beams are mounted at fixed positions with an angle of 52° and co-focused at a geometrically optimized single point such that modification and imaging can be done *in situ*, additively, iteratively, and reductively. An example of a FIB-SEM combined system is the Thermo Fisher Scientific Helios 5 Small DualBeam™ in Figure 3.1. This system is one of the main systems used for the work throughout this project.

For any technique to have success on the FIB-SEM platform, it must be:

1. geometrically compatible with the primary configuration
2. maintain a versatile workflow that can be integrated with other charged particle processing methods
3. produce novel or unique information that can be easily interpreted or analyzed
4. be acquired at a reasonable price or cost of ownership

While collection of photons from charged particle irradiation is nothing new and has been done for both electron beam irradiation and ion beam radiation for decades, construction of a highly efficient photon collection system that is integrated on a FIB-SEM combined system, is. The prior techniques of IBSCA and SCANIIR discussed in Chapter 2 are highly inefficient, requiring microamps or milliamps of current to collect enough signal. Since the spot size of the ion probe scales with the primary ion beam current (see Appendix A), small currents are required to enter the nanoscale analytical regime. FIB-FS is based on sputtered atoms, which will scale proportionately with the current, meaning that only the most efficient photon detection systems will be able to detect the signal at small currents (pA to nA). At this scale, every photon counts.

Over the course of this research, a considerable amount of effort was made to develop the FIB-FS technique that meets the above criteria. Creation of such hardware requires deep and experienced knowledge of FIB-SEM architecture, vacuum systems, optical design, analog and digital signal control sequencing, and detector operation. This chapter reviews both the physical concepts and mechanical challenges faced in order to deliver an optimized system that transmits photons emitted from the charged particle bombardment point, through vacuum barriers, and into a detector to produce spectroscopic information. The result is a material characterization technique compatible with nanoscale fabrication and processing methods that can be deployed on any FIB-SEM platform.

3.2 Overview

The FIB-FS technique can be broken down into sections: collection optics of the emission, transmission of the signal, detection of the signal, and operation modes. Figure 3.2 shows a schematic outline of each of these categories as they are manifested on a charged particle system. The overall design is meant to be modular, allowing for different collection optics, fiber optics, and detectors to be easily swapped and interchanged depending on the experiment to be performed. When approaching a detection chain design from scratch, it is helpful to either start with the collection point and optimize the path through to the detection point, or vice versa. In reality, the design progressed as an iteration between detection and collection, however, for readability, the chapter beings with the former with discussion of the transmission chain when appropriate.

3.3 Collection Optics

A consequence of having two different particle beams coincident at a single point in space is that real estate in the area around that point is severely limited. Coupled with the requirements for versatility and compatibility with all the minimum necessary secondary electron and ion detectors, gas injection systems (GIS), and analytical hardware like EDX, the optical collector in FIB-FS needed to be

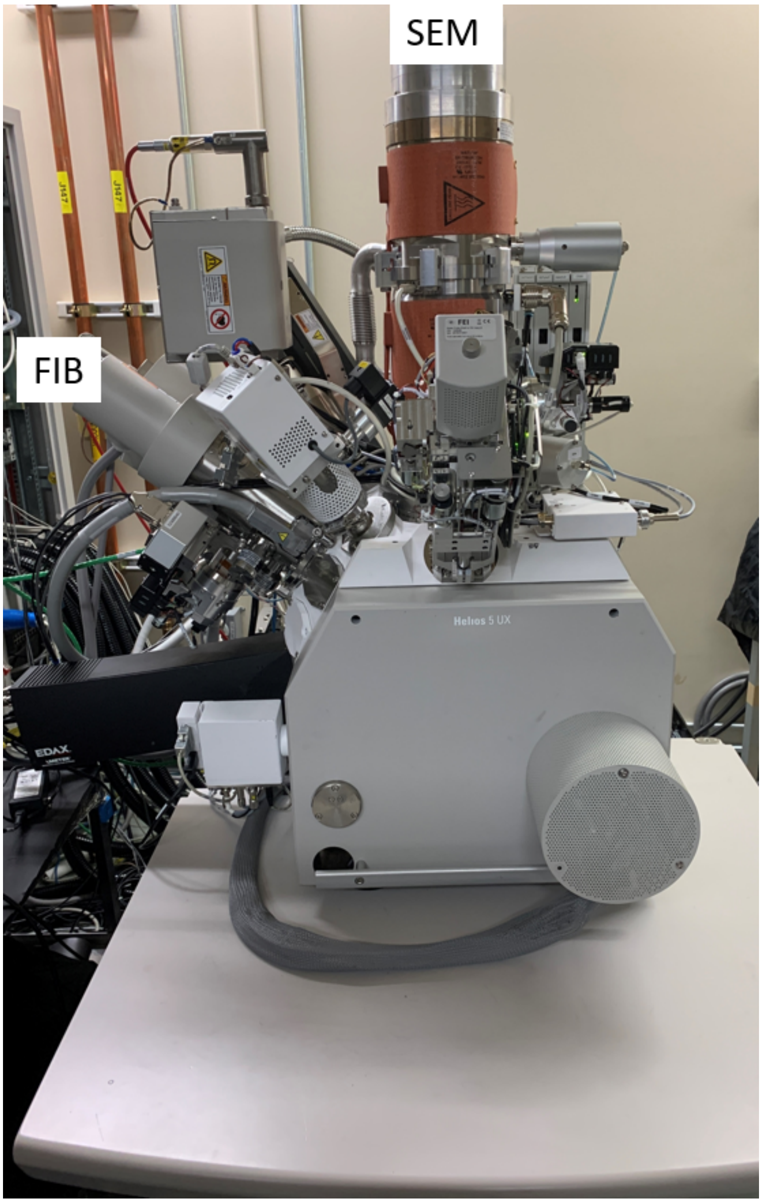

Figure 3.1: Thermo Fisher Scientific Helios 5 Small DualBeam system. The system consists of a coincident SEM and Ga^+ FIB, along with various particle detectors, and analytical and processing tools.

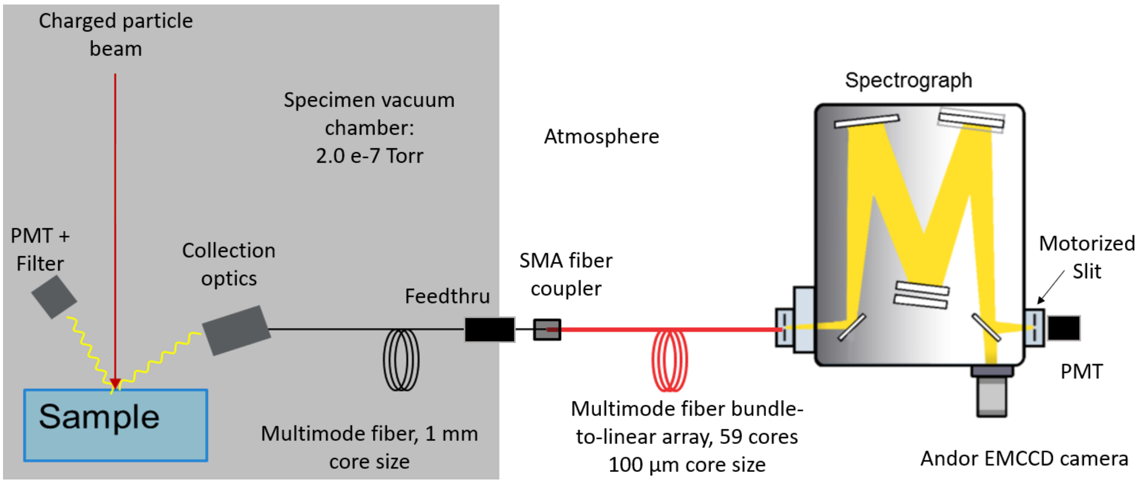

Figure 3.2: FIB-FS detection chain outline showing the various modular transmission and detection components.

low profile. On the other hand, photon emission yields for many materials are extremely low [31, 32, 106, 136], demanding that a high collection efficiency be met in order to produce meaningful results.

The first and most straightforward way to increase collection efficiency is to increase the surface area of collected signal via the solid angle. Since the photons emitted by sputtered atoms are emitted by excited atoms in free space, there is no preferential directionality and the emission is isotropic [110, 120, 145]. Therefore, the total collection efficiency CLE is defined as the product of the solid angle collection efficiency SA, the coupling efficiency CE, and the quantum efficiency QE of the entire chain:

$$CLE = SA * CE * QE \tag{3.1}$$

The solid angle of an arbitrary surface S subtended at a point P is equal to the solid angle of the projection of that surface onto a sphere with the same point center, which is found as the surface integral in spherical coordinates:

$$\Omega = \iint_S \text{sin}\theta \; \text{d}\theta \text{d}\phi \tag{3.2}$$

which for 2π emission around zenith angle θ is

$$\Omega = \int_0^{2\pi} \int_0^{\theta_0} \text{sin}\theta \; \text{d}\theta\text{d}\phi = 2\pi(1 - \text{cos}\theta_0) \tag{3.3}$$

Here, for some spherical surface S with radius r, the angle θ_0 is found by the inverse tangent of the ratio of the surface radius r and its distance d from point P (see Figure 3.3). The solid angle efficiency is simply the percentage of this surface over hemispherical 2π coverage so $SA = \Omega/2\pi$.

Combining equations (3.3) and (3.1), we see that the total collection efficiency CLE scales according to the proximity of the collector surface to the emission

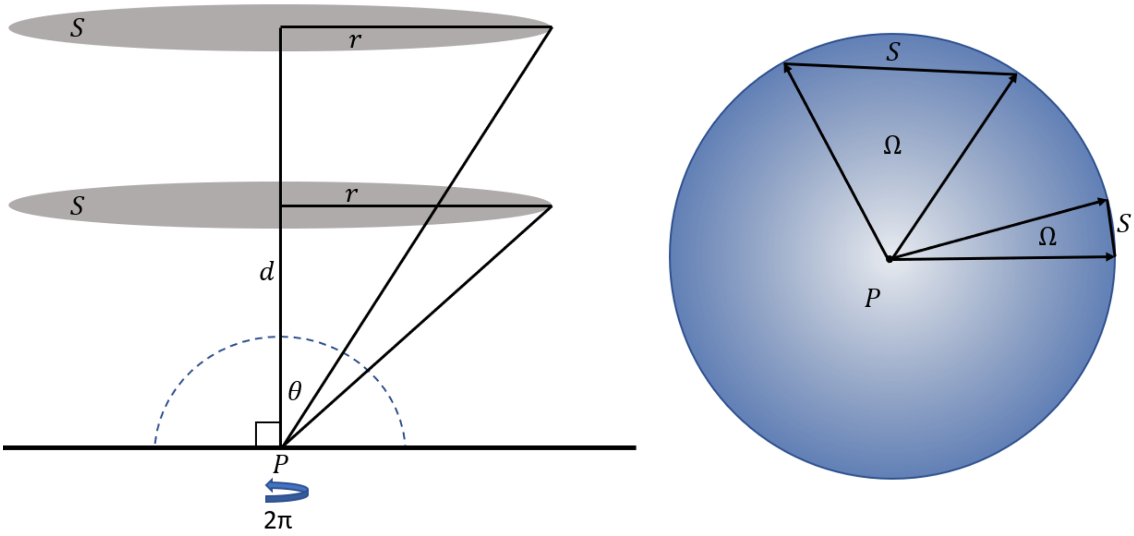

Figure 3.3: Solid angle for collection optics showing how efficiency scales with inverse tangent of collector surface area radius r over proximity d. The solid angle of complete hemisphere is 2π according to equation (3.3) for ϕ from 0 to 2π and θ from 0 to $\frac{\pi}{2}$.

point by tan$^{-1}(r/d)$. In other words, the solid angle blows up at short distances for the same collector surface size. For optical collection systems where the quantum efficiency is a constant of the material's reflectance and absorbance losses, that leaves collector surface size and distance as the first variable to optimize.

Naturally, the dependence of the collection efficiency on the solid angle conflicts with both the geometry of the two charged particle columns as well as compatibility with other probes trying to achieve the same goal. If a FIB-FS collector is positioned too close to the sample, it may collide with one of the columns or if it covers too much surface area, then it will block and obstruct other devices and detectors. To remedy this quagmire, two collection devices were developed for FIB-FS: a low-profile insertable mini probe consisting of a mini-lens fiber coupling system, and a high-solid angle elliptical mirror collection system.

3.3.1 Insertable Mini Probe

A gas injection system (GIS) is a tool that comes standard on almost any FIB or SEM system. It consists of a small crucible, in which some gas chemistry is stored, with a small needle (outer diameter $\sim$ 500-800 µm) attached to the end. The crucible and needle are mounted to a body that is bolted onto a port of the main specimen vacuum chamber. The body of the GIS is pneumatically inserted and retracted to allow for gas delivery at the FIB-SEM coincident point, allowing for the high gas flux density and surface coverage needed for processes like gas-assisted milling, deposition, or etching [176–178]. Since the insertable pneumatic system was already in place and with the high availability of chamber port flanges designed for mounting of this device, the GIS framework was chosen as basis to design a low profile photon collector.

A GIS module was emptied of its gas chamber and modified to be equipped with a mini-lens and multimode fiber optic cable collection system. The modifications consist of an aluminum dummy crucible of the same dimensions of the standard GIS gas crucible, except for large bore through the middle that allows for a lower diameter extending rod to be inserted. The extending rod also has a 1.5 mm hole drilled all the way through to the imaging end to allow a fiber optic cable to be fed through the rod. A 1 mm core size, multimode step index fiber of UV-VIS or VIS-NIR transmission with a 0.22 NA can be used as the light guide to maximize the coupling efficiency based on spectral response while the large core size allows for the largest field of view collection. The total transmission distance between collection and detection is 3 meters, so losses from transmission of the step index fiber are small. The fiber is fed through the GIS body, crucible, and extending rod so that it reaches the imaging distal end of the rod. The distal end of the extension rod was designed to fit a mini-lens system that couples light from a diverging point source to a fiber optic cable.

There are many different lenses and orientations that one could use to achieve optimal coupling. Given the space restrictions and knowing that close proximity to the emission point is necessary, only fused silica lenses with outer diameter less than 3 mm are considered. A variety of these types of lenses are readily available and stocked at most retail optics suppliers such as Edmond Optics and Thorlabs. Some common lenses provided in these dimensions are: ball lenses, half-ball lenses, drum lenses, and half-drum lenses.

Ray tracing optics simulations of these lenses at multiple orientations were performed in Zemax OpticStudio [179], an optical design software. For each configuration, a diverging point source was defined to launched 1000 rays over an emission cone angle defined by the solid angle which is determined by the diameter and position of the first lens. The image plane can be defined as a multimode fiber with core size 1 mm, such that the efficiency reported will be recorded as the percent % number of rays coupled to the fiber optic from total number of launched rays. A total of 6 different configurations were simulated: ball lens, double ball lens, half-ball lens, reverse half-ball lens, half-drum lens, and reverse half-drum lens. Figure 3.4 shows the ray tracing simulations for each configuration.

The position of the lens is varied from 0.1 mm to 4 mm and the emission cone angle is adjusted accordingly, so that an accurate percentage of transmitted rays reaches the image plane. Varying the fiber position reveals tolerance of the coupling efficiency from the focal length of each lens. The results are shown in Figure 3.5, showing that the most efficient coupling system is the half-drum lens with roughly 62% coupling efficiency. Since this configuration requires a larger working distance, however, the overall collection efficiency is similar to the half-ball lens, which has a maximum coupling efficiency of roughly 40%. Considering the tolerance of the fiber placement, the half-drums lens also makes mounting and positioning easier.

Each of these systems is unique from a standard fiber optic and lens coupling system in that the fiber core size and the lens are of similar sizes. Here, the lens diameter is 2 mm and fiber core is 1 mm, so the incoming rays approach relatively collimated as opposed to highly focused in the case of a 1 inch lens with a 100 µm core fiber. The shallow angles are well within the acceptance cone of the fiber for total internal reflection at the fiber core and cladding boundary, so high coupling efficiency of multiple modes and wavelengths is achieved without having a second focusing lens, saving space.

With the lens system optimized, the extending rod was modified accordingly. The outer diameter is tapered down to the mini-lens outer diameter for the absolute smallest profile allowed in order to enable its optimized positioning roughly 2.5 mm from the FIB-SEM coincident point (see Figure 3.5 **(a)**). There are 3 set screws to allow for fiber tilt position adjustment for optimal coupling, which is achieved using a power meter to take throughput measurements into and out of the optical system. A purge hole is tapped at the half-drum focal length to both allow the assembly to be efficiently pumped under vacuum and to allow a visual inspection of the fiber in the rod so that it can be placed approximately 2 mm from the end of the lens according to Figure 3.5 **(b)**.

Figure 3.6 shows the mini-lens hardware assembly with the mounting, extending rod, and distal end hardware designs and how they fit together. A set screw is placed at the distal end of the mounting crucible to keep the extending rod in place. A small amount of silver paste is used along the sidewall of the imaging end of the rod to keep the lens in place. A viton o-ring between the mounting crucible and the GIS body keeps the vacuum contained within the inner tube of the device, while the end of the body is sealed with vacuum grade epoxy Torr Seal to allow the fiber optic cable to feed through while maintaining vacuum.

Alignment of the optic is controlled by manipulation of the body at the main chamber bracket shown in Figure 3.7. The entire body sits on a large viton o-ring that provides both a vacuum seal and a cushion for the body to be manipulated for alignment. The axial position is controlled with a lock ring stop that sets the distance to be inserted when the pneumatic line is activated. Pitch and yaw alignment is performed with a 3 mm hex key that applies pressure at 4 points of the

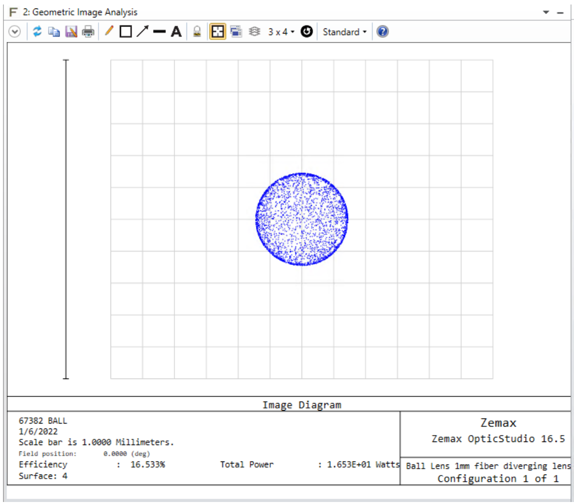

```
Image Diagram
67382 BALL
1/6/2022
Scale bar is 1.0000 Millimeters.
Field position:      0.0000 (deg)
Efficiency         :  16.533%          Total Power         : 1.653E+01 Watts
Surface: 4

Zemax
Zemax OpticStudio 16.5
Ball Lens 1mm fiber diverging lens
Configuration 1 of 1
```

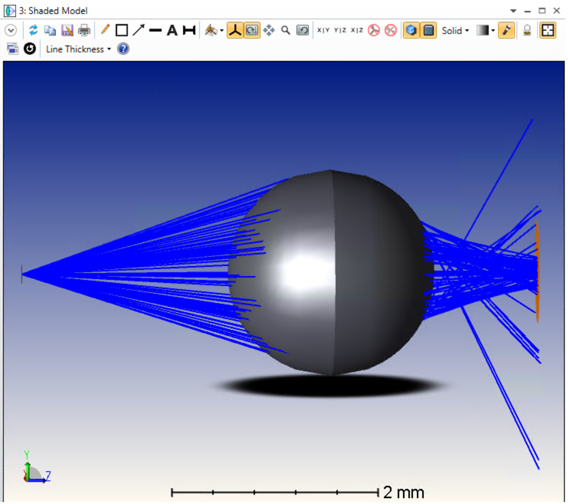

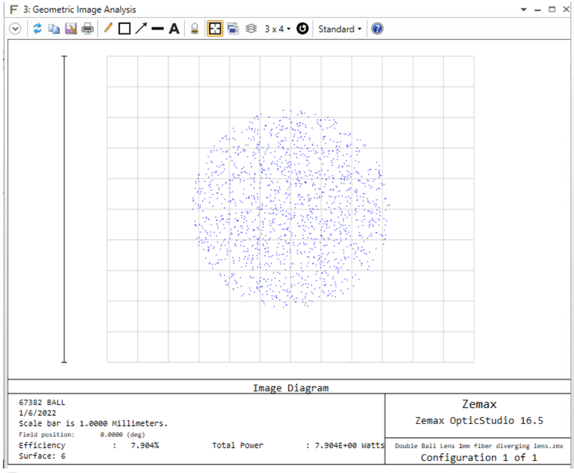

```
Image Diagram
67382 BALL
1/6/2022
Scale bar is 1.0000 Millimeters.
Field position:      0.0000 (deg)
Efficiency         :   7.904%          Total Power         : 7.904E+00 Watts
Surface: 6

Zemax
Zemax OpticStudio 16.5
Double Ball Lens 1mm fiber diverging lens.zmx
Configuration 1 of 1
```

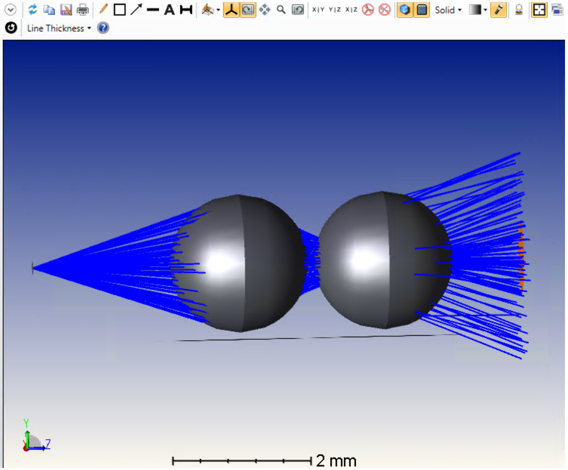

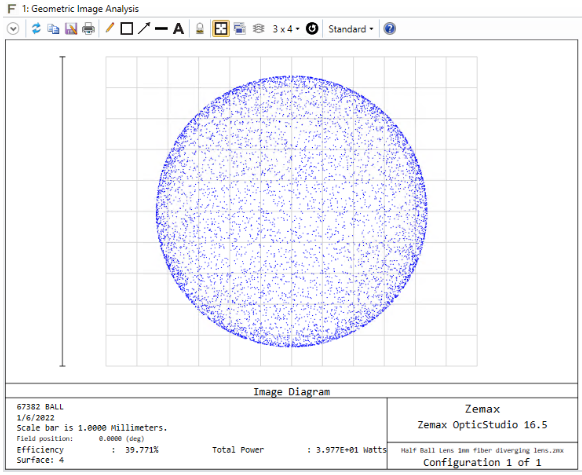

```
Image Diagram
67382 BALL
1/6/2022
Scale bar is 1.0000 Millimeters.
Field position:      0.0000 (deg)
Efficiency         :  39.771%          Total Power         : 3.977E+01 Watts
Surface: 4

Zemax
Zemax OpticStudio 16.5
Half Ball Lens 1mm fiber diverging lens.zmx
Configuration 1 of 1
```

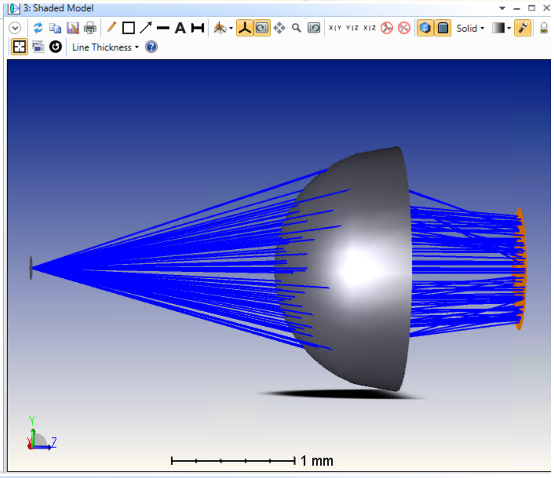

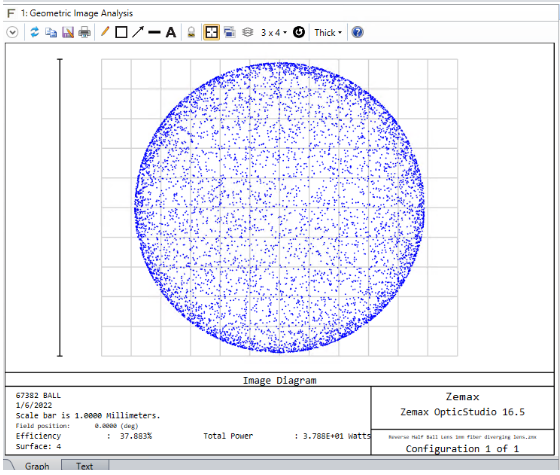

```
Image Diagram
67382 BALL
1/6/2022
Scale bar is 1.0000 Millimeters.
Field position:      0.0000 (deg)
Efficiency         :  37.883%          Total Power         : 3.788E+01 Watts
Surface: 4

Zemax
Zemax OpticStudio 16.5
Reverse Half Ball Lens 1mm fiber diverging lens.zmx
Configuration 1 of 1
```

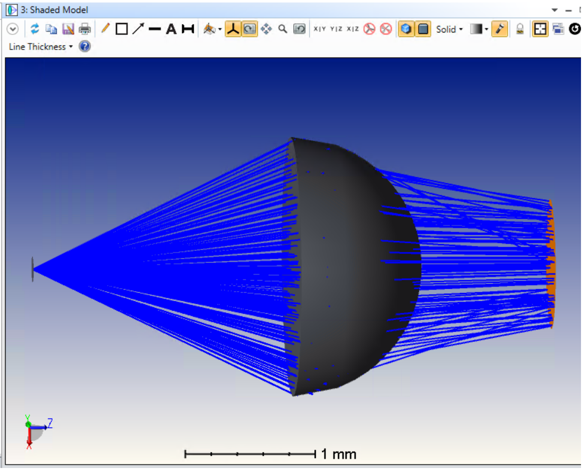

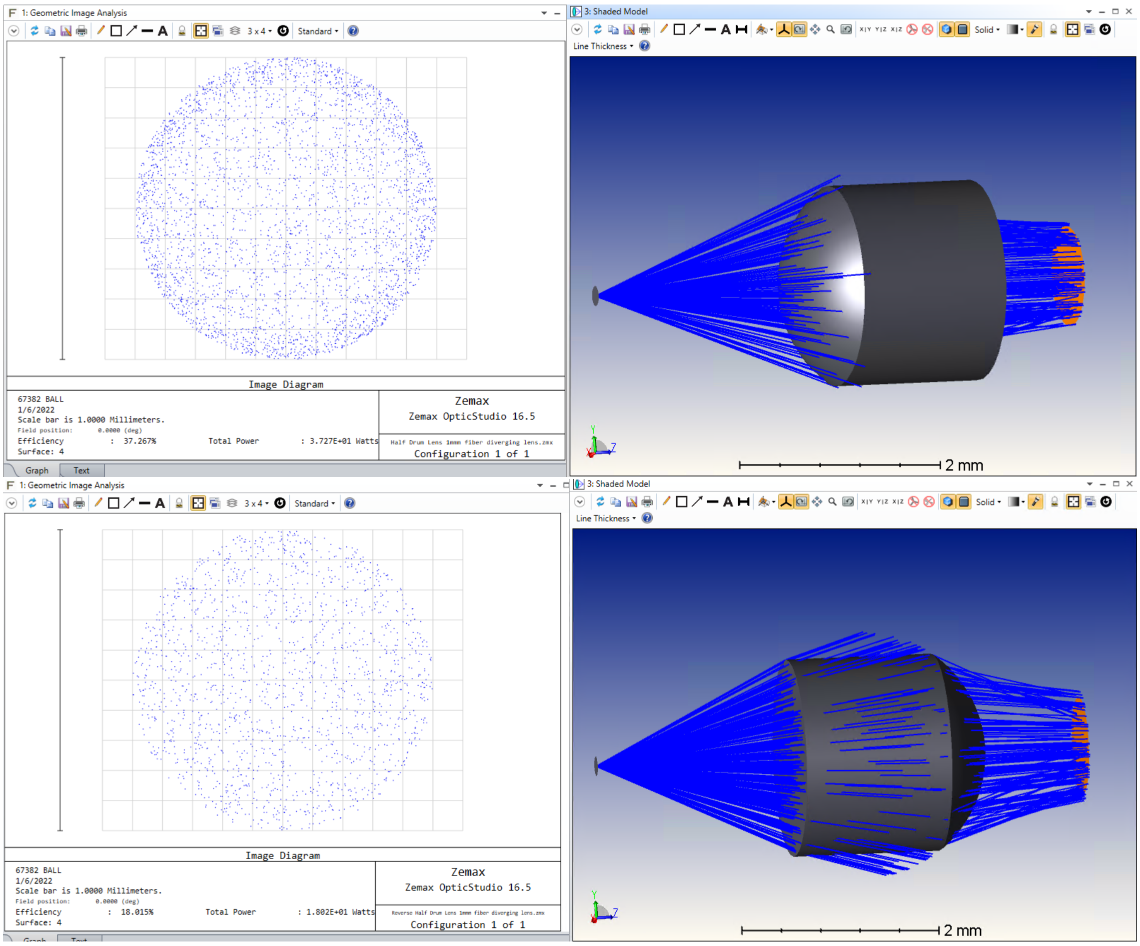

```
Image Diagram
67382 BALL
1/6/2022
Scale bar is 1.0000 Millimeters.
Field position:       0.0000 (deg)
Efficiency          :  37.267%          Total Power        : 3.727E+01 Watts
Surface: 4

Zemax
Zemax OpticStudio 16.5
Half Drum Lens 1mmm fiber diverging lens.zmx
Configuration 1 of 1
```

```
Image Diagram
67382 BALL
1/6/2022
Scale bar is 1.0000 Millimeters.
Field position:       0.0000 (deg)
Efficiency          :  18.015%          Total Power        : 1.802E+01 Watts
Surface: 4

Zemax
Zemax OpticStudio 16.5
Reverse Half Drum Lens 1mmm fiber diverging lens.zmx
Configuration 1 of 1
```

Figure 3.4: Zemax ray tracing simulation for each of the mini-lens collection optics designs. From top to bottom: ball lens, double ball lens, half-ball lens, reverse half-ball lens, half-drum lens, and reverse half-drum lens. The best configuration is the half-drum lens, which allows for high coupling efficiency and a low profile.

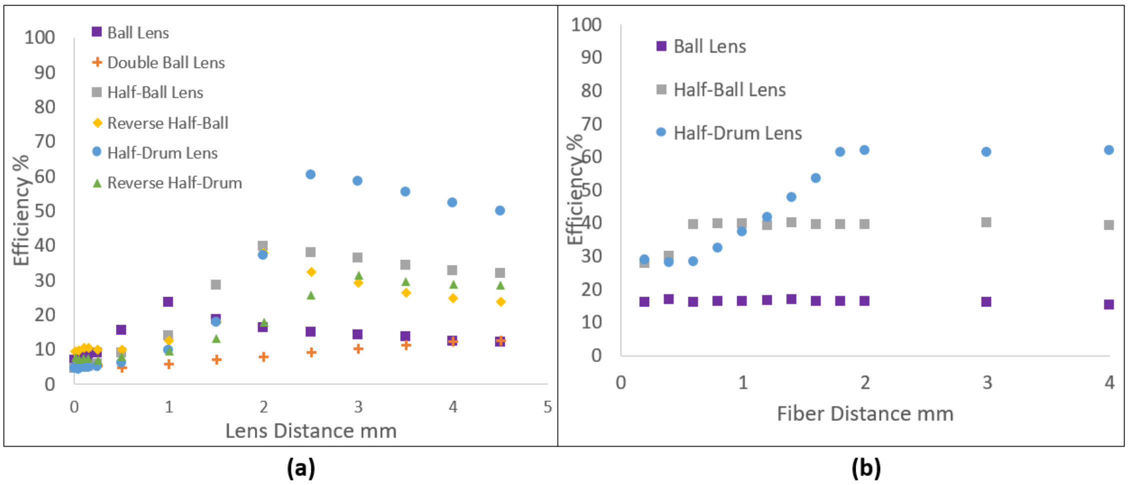

Figure 3.5: Coupling efficiencies of each mini-lens system as function of distance from emission point **(a)** and its respective fiber positioning tolerance at the focal point **(b)**.

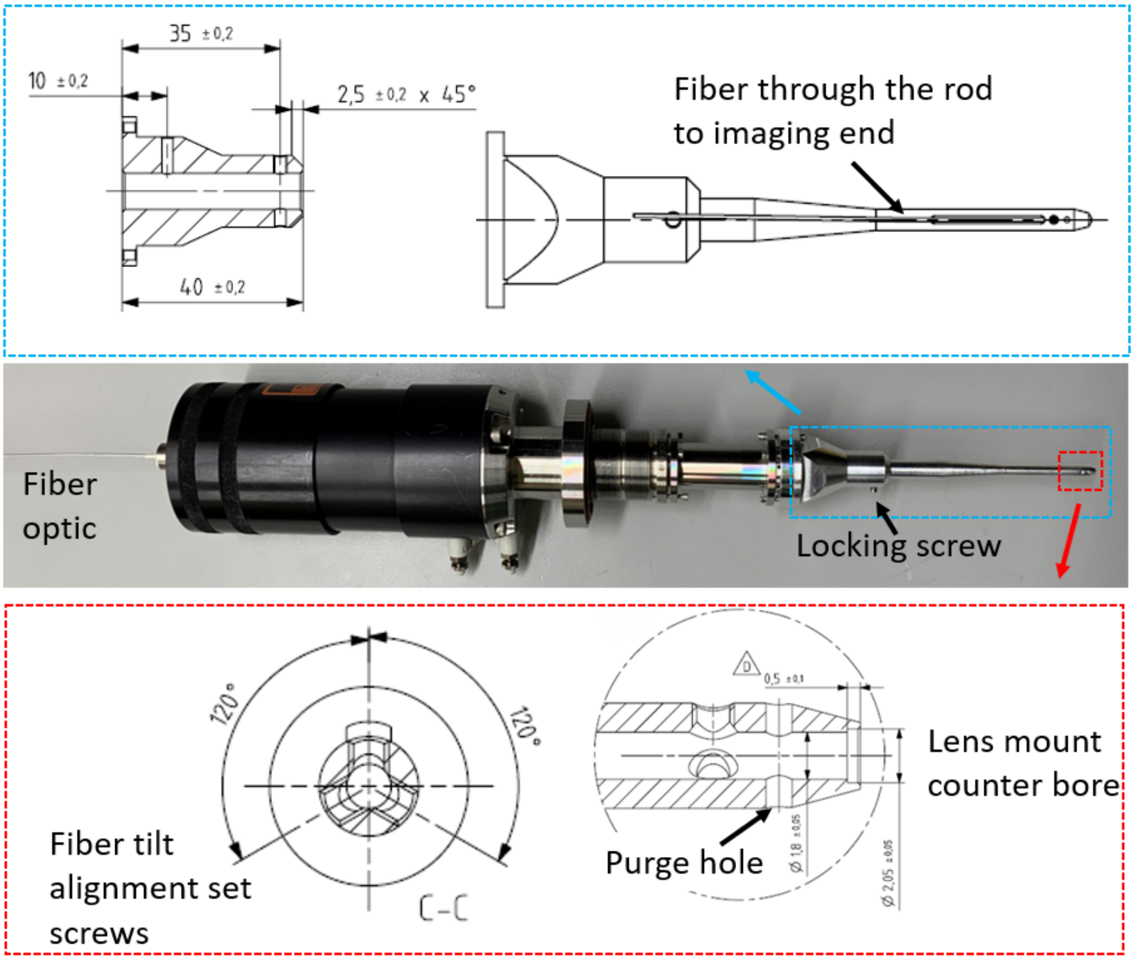

Figure 3.6: GIS modifications for the mini-lens optical probe, showing the mounting hardware, lens design and assembly.

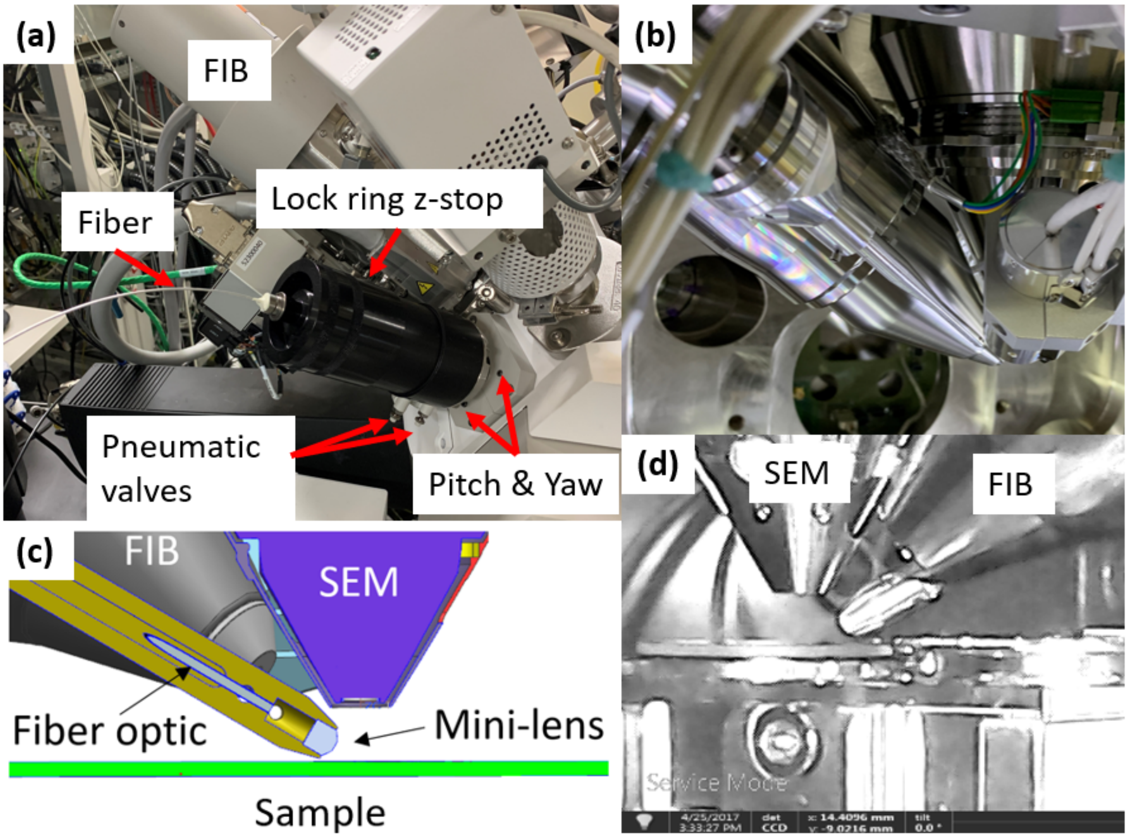

Figure 3.7: Mini-lens optic assembly and operation on a Thermo Fisher Scientific Small DualBeam system. **(a)** The main specimen vacuum chamber mounting and alignment mechanisms of the probe. **(b)** Inside view of the specimen chamber showing the retracted optic and its line of sight. **(c)** Cross-section schematic of the inserted probe with the sample the FIB-SEM coincident eucentric height at normal SEM incident angle. **(d)** In-chamber camera photograph of the inserted optic under vacuum and in use with a sample at the eucentric height.

flange body. The alignment procedure is straightforward: a sample (typically an Al standard stub) is irradiated with the ion beam in a box centered at the FIB-SEM coincident point, while the body is adjusted until the FIB-FS signal is maximized. The procedure is easiest when started at large z distance to align the transverse component and then the axial position is aligned with fine tuning of the pitch and yaw performed at the final z step.

Once aligned, the optic can be inserted and retracted instantly. The alignment is robust, landing within about 100 micrometers through multiple activation cycles. The specimen chamber port mounting also allows for full sample and main stage movement (0-52° tilt, 360° rotation, full x-y range) without obstruction or contact with the insertable probe at the eucentric coincident position. Since the probe operates at coincident eucentric, SEM-CL detection is also available and can be performed iteratively between FIB-FS operations. Additionally, the low profile allows for additional tools to be used concurrently such as: additional GIS nozzles, EDX, and EBSD detectors. Note, however, that unlike the isotropic emission of FIB-FS, the Lambertian emission of the CL signal [180] will mean that the collection efficiency will vary with the SEM incident angle and the probe line of site angle.

The total collection efficiency according to equation (3.1) for this setup with a half-drum at 2.5 mm from the emission point corresponds to a $SA = 7.15\%$ and a $CE = 62\%$ with only the spectral response left to be measured. Throughput of the setup was measured from the lens through to the fiber optic to test for QE and found to have negligible loss of only a few percent at the high spectral response wavelength of 635 nm. These losses are attributed to fused silica transmission and the reflection at each air-silica media transition. Thus, the total efficiency of the collection within the collection area is roughly 4.4%. The same analysis of the half-ball lens gives $SA = 10.5\%$ and $CE = 40\%$ for a total efficiency of 4.2%.

It is important to note that the maximum allowable collection area for the setup is limited by the fiber core size, the lens diameter, and distance to the bombardment point. As the ion beam scans a region outside of the optical axis set by the lens alignment, the rays emitted by sputtered atoms will approach the lens off-axis and the coupling efficiency to the fiber will be reduced in a vignetting effect. For the current setup with a half-drum lens positioned at 2.5 mm from the coincident point, the maximum field of view (FOV) is about 200 µm before off-axis coupling losses and vignetting occur, dropping the signal exponentially at the edges.

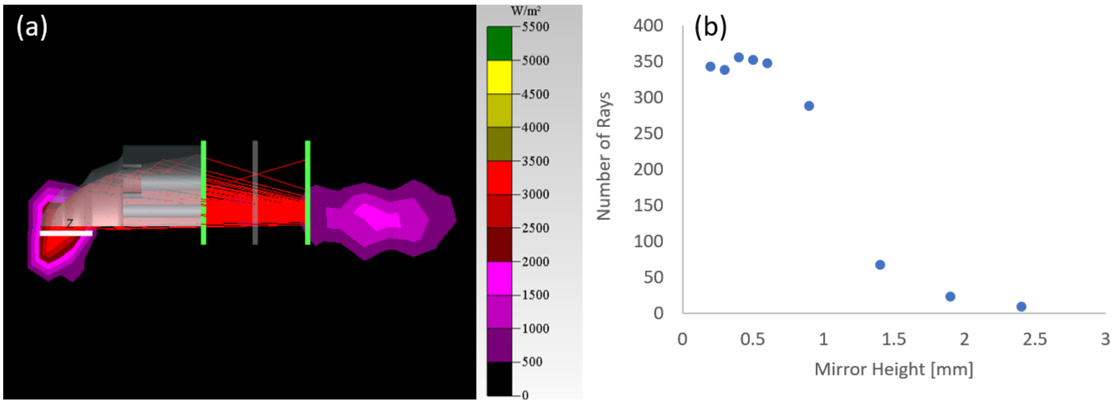

Figure 3.8: Ray tracing of the elliptical mirror to explore the coupling efficiency as a function of mirror height above the surface of the sample. **(a)** Irradiance maps and geometric setup in TracePro to model the mirror. **(b)** Ray tracing statistics of the number of rays captured by the fiber optic at the opposing focal point as a function of mirror height. The best collection is roughly 550 µm above the sample, capturing about 350 out of 500 launched rays.

3.3.2 Elliptical Mirror

While the insertable mini-probe allows for versatility and ease of operation, there is still much more improvement to be added by increasing the surface area of the collected region. Historically, ellipsoidal and parabolic mirrors have been used to approach the limits of collection from a point source emission and have been used routinely in single-beam SEM cathodoluminescence systems in the past [180–182]. Implementing a mirror-based approach on a charged particle microscope, however, has rarely been explored for ions [183] and has not been performed on a combined SEM-FIB system.

Design

Owing to the space restrictions imposed by the 2 columns, fitting a complete mirror between the sample surface and the pole tip is extremely difficult. The prior renditions mentioned are easily able to accommodate or relax the restriction by dropping the stage height (increase the working distance). While this approach allows for larger mirrors and ease of operation, it does not allow for eucentric operation of the two beams and comes at a cost of performance from the working distance. In order to allow for coincident and eucentric FIB and SEM operation along with full stage and sample positioning, considerable effort went towards developing a new mirror and mounting hardware.

The best possible solid angle collection efficiency would completely cover the

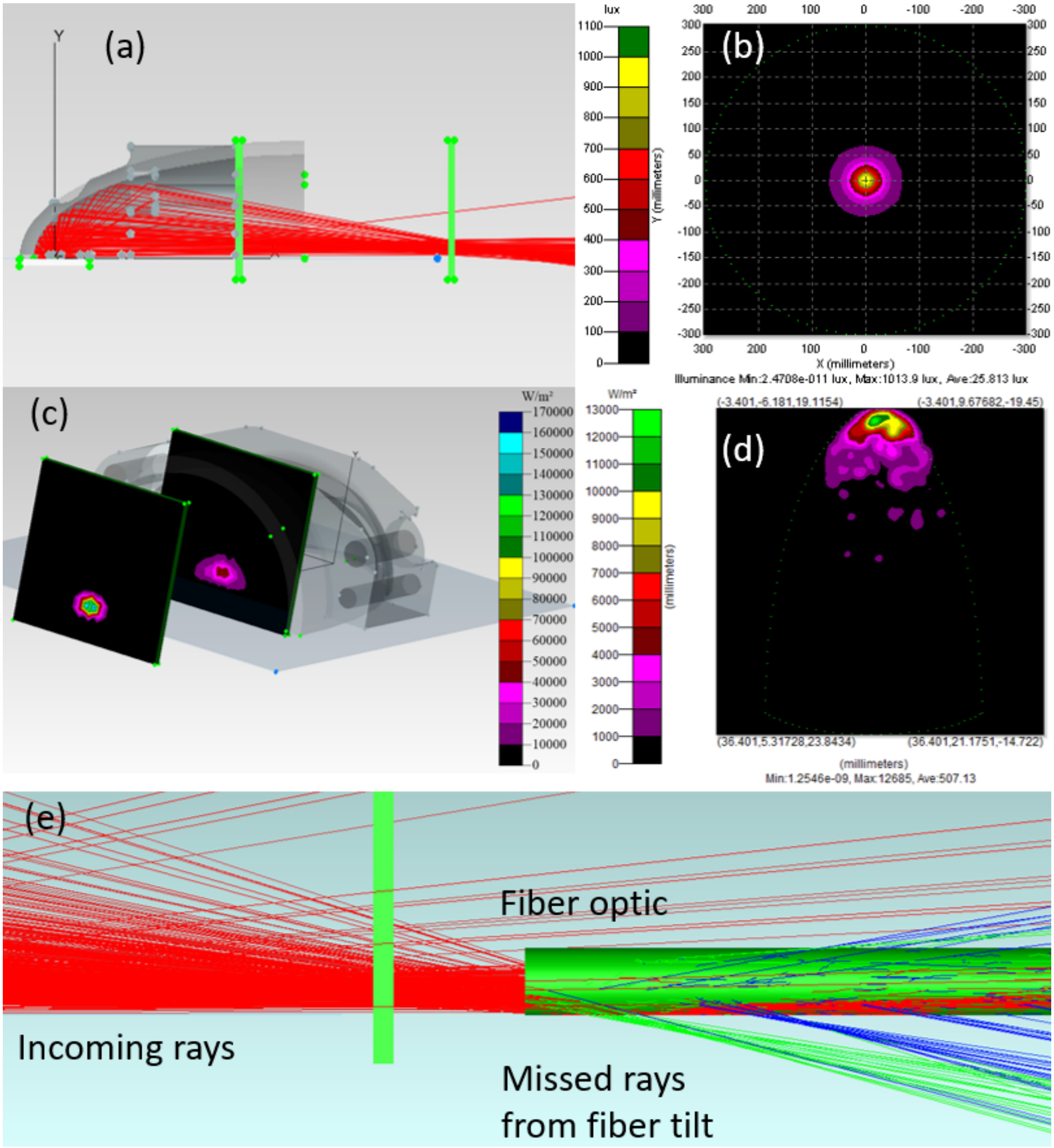

Figure 3.9: Ray tracing simulation of the fiber position tolerance. **(a)** Two screens are defined in space after the mirror placement and uniform diverging source. **(b)** Lux colormap of the rays at the fiber core. **(c)** Visualization of the convergence of the rays from the back of the mirror towards the focal point. **(d)** Irradiance colormap on the inside surface of the mirror positioned over the source, showing the high density of the reflections at the emission focal point. **(e)** TracePro ray tracing showing the uncollected rays with the fiber positioned parallel to the sample plane.

entire 2π steradian angle around the emission point. Completely covering the sample with a metal structure, however, makes secondary electron (SE) collection impossible. To increase the optical SA collection and maintain SE collection, an aluminum elliptical mirror was designed with dimensions to couple light from its focal point under the FIB-SEM coincident eucentric point to a UV-VIS or VIS-NIR fiber optic located at the opposing focal point. One side of the ellipsoidal mirror is left open to allow secondary electron and secondary ion escape for imaging when placed over the sample, while a slotted 500 µm aperture on the column end surface was drilled from 0 to 53 degrees from the zenith to allow for both FIB and SEM particle beams to pass through the mirror. The mirror is cut to achieve a 73% solid angle collection efficiency when placed 600 µm above the sample surface according to the mirror dimensions and is diamond-turned to a scratch/dig of 80/50 and 10 nm RMS for the highest reflective surface. The outer surface is cut to provide a contour of the SEM nose cone to allow for the closest fit under the SEM.

A simple geometric model was used to project the surface area of the mirror set by the fiber optic acceptance cone onto a suspended surface within the confines of the SEM working distance. It was found that an ellipse with a semi-major, semi-minor, and focal length of 39 mm, 15 mm, and 36 mm respectively. Like the lens design, ray tracing optimization was performed in Zemax and TracePro to confirm the dimensions. A spherical surface with uniform distribution was defined as the emitter and both ray tracing and illuminance simulations were performed to optimize the mirror position above the sample as well as the fiber position. Figure 3.8 shows the irradiance collected and the number of rays (out of 500) as function of the mirror distance to the surface simulated in TracePro, while Figure 3.9 shows the irradiance density plots of two different screens for optimized fiber position. The largest loss of coupling is from the open face of the mirror, accounting for roughly 25-30% ray loss, however, the loss is necessary to allow for SE detection. Also shown in Figure 3.9 is the irradiance density plot on the surface of the mirror and how, despite the high loss of the open area for SE collection, it is not as much as expected since the majority of emitted rays are captured in the nose of the mirror shown by the flux map on the top portion of the mirror's semi-major axis.

One metric which was not appreciated by the simple geometric model is the tolerance fiber optic tilt angle at the opposing focal point on the collection efficiency. Initially, the fiber was placed horizontal to the opposing focal point such that the surface area projection defined by the NA of the fiber mapped to the mirror's inner surface. Since the bottom half of the mirror was cut to allow for sample height clearance, a small tilt of the fiber core of 5° re-center's the core acceptance cone on the incoming ray axis, resulting in roughly 25% increase in the coupling efficiency, see Figure 3.9 (e).

Substage and Hardware

With an optimized mirror design, the next step was to design a system that would be able to place the mirror over the sample in the vacuum chamber. Such a system would need to be able to:

1. have 3 independent degrees of freedom from the main stage for mirror alignment over the emission point
2. allow for sample rotation and tilt between SEM and FIB normal
3. sub-micron reliable positioning
4. travel at a reasonable speed
5. have a safe homing sequence
6. have a safe parking position to allow for unobstructed microscope operation
7. have a safe path from the parking position to acquisition position
8. make moves that correspond (negatively) to the main stage movements in order to keep the mirror in the same location relative to the SEM-FIB while the sample effectively moves below it (i.e. maintain alignment)
9. break up large moves into smaller iterative steps of moving main stage and substage so as to never allow the mirror assembly to get too far out of “nominal” position where it would collide with detectors or the SEM pole piece

To meet these demanding requirements, 3 linear piezo translation stages from German-based company Smaract were chosen to mount the mirror to. The assembly included one 49 mm, one 21 mm, and one 12 mm travel stages – all non-magnetic and high vacuum-compatible. All corresponding air-to-vacuum cabling was purchased along with the sensor module and benchtop control system. A mounting sub-assembly was built so that the stages could be stacked on top of each other to give x-y-z linear translation. The substage assembly was then mounted to the main specimen chamber stage with a custom platform. Mounting to the main stage allows for the mirror to tilt along with the main specimen tilt, while the platform suspension above the rotation plate allows for the sample to rotate underneath. Figure 3.10 shows the mirror assembly and its operation in the chamber.

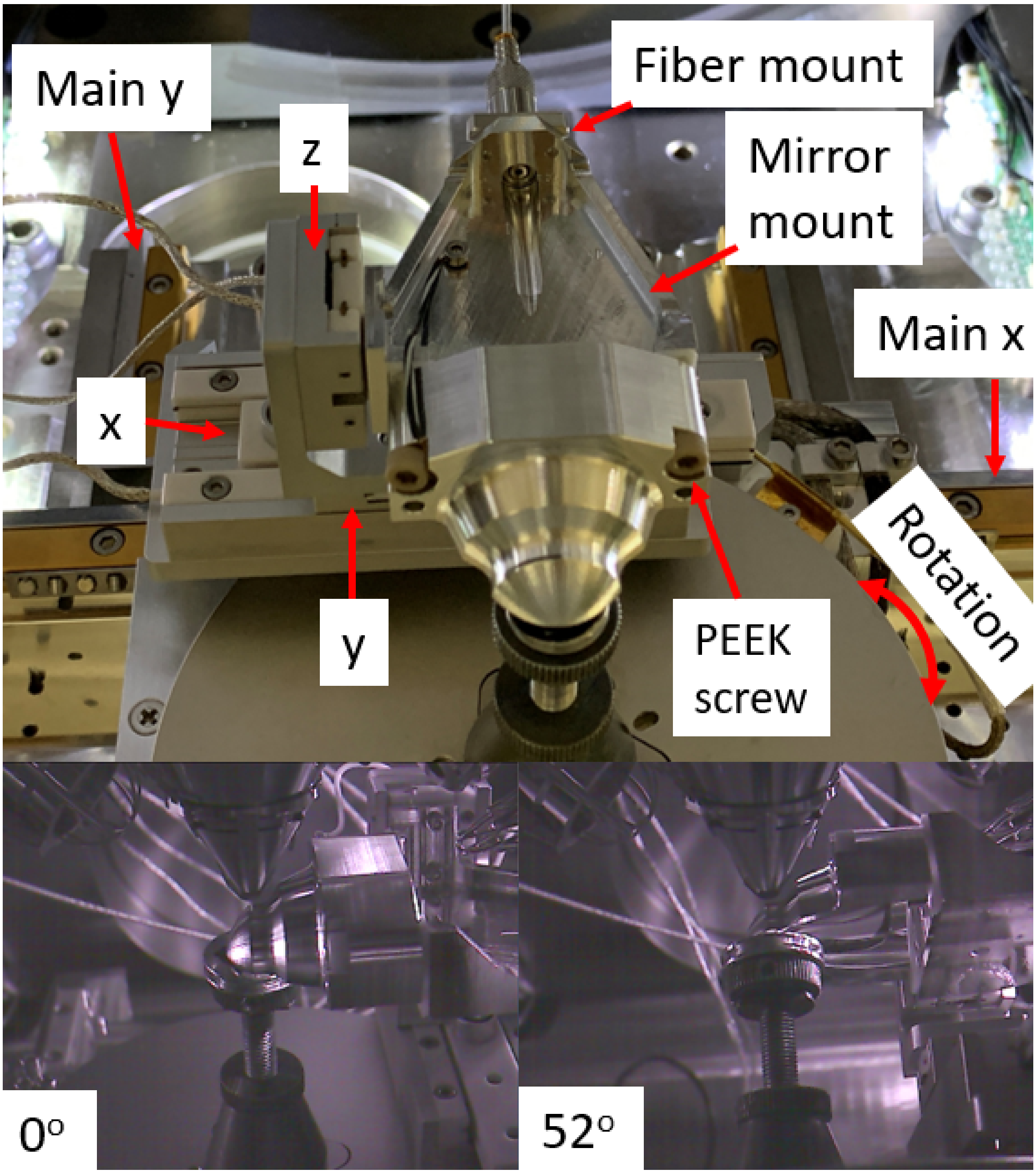

Figure 3.10: The elliptical mirror and substage system installed on the Helios. The design allows for 3 axis independent motion of the mirror along with tilt axis symmetry with the mainstage and free sample rotation.

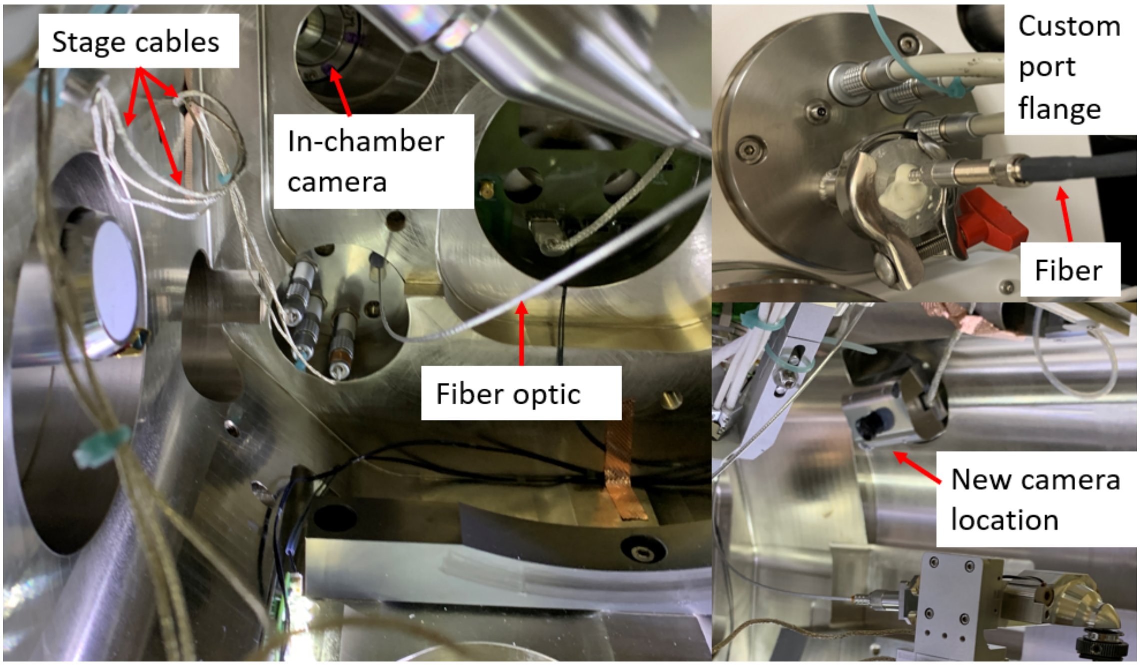

Figure 3.11: Elliptical mirror substage assembly and hardware showing cable routing and custom flange. A new camera is positioned on the opposite side of the standard camera to allow for unobstructed line of sight.

Alignment is done similar to the insertable mini-probe, where a sacrificial region of the sample is irradiated with the ion beam while the mirror position is fine-tuned using the signal response feedback. Once the alignment is optimized, any stage main stage sample movement will cause the entire mirror setup to move out of alignment position, so a python code was written to track the microscope stage movements and command an inverse movement on the piezo substage encoders. Thus, once aligned, any main stage movement will be countered with an opposing substage movement and the mirror is kept in alignment.

Lastly, two more additions were needed to complete the setup. First, a custom vacuum multi-element feedthrough flange was designed to deliver the substage and fiber optic cabling into the chamber from a rear port. Shown in Figure 3.11, the substage encoder lines are routed up along the chamber sidewall while the fiber optic cable is routed towards the roof to be clear of any main stage tangles. The cables end at the custom flange that provides a vacuum-atmosphere interface for the wires to pass through. The second was the addition of an in-chamber CCD camera to view the hardware. Since the line of site of the standard in-chamber camera is completely blocked, a new bracket was built to mount the camera in a new location on the opposite side of the SEM. This provides an unobstructed view of the hardware relative to the SEM and FIB nose cones, so that the user can avoid any accidental collisions.

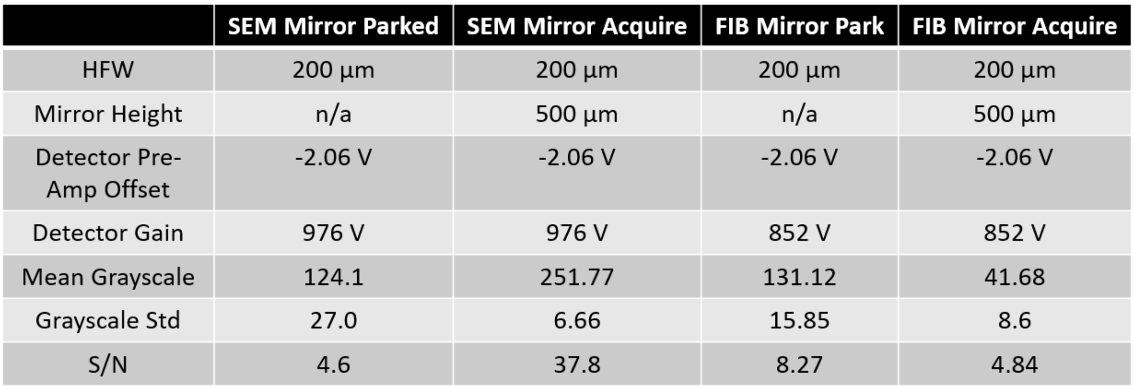

	SEM Mirror Parked	SEM Mirror Acquire	FIB Mirror Park	FIB Mirror Acquire
HFW	200 µm	200 µm	200 µm	200 µm
Mirror Height	n/a	500 µm	n/a	500 µm
Detector Pre-Amp Offset	-2.06 V	-2.06 V	-2.06 V	-2.06 V
Detector Gain	976 V	976 V	852 V	852 V
Mean Grayscale	124.1	251.77	131.12	41.68
Grayscale Std	27.0	6.66	15.85	8.6
S/N	4.6	37.8	8.27	4.84

Table 3.1: Table of SEM-SE and FIB-SE detector values with and without the elliptical mirror in the acquisition position.

Characterization

On-tool characterization to compare and validate the simulation was performed. There are obvious limitations to detector use with the mirror inserted – the in-chamber electron detector (ICE) is unusable (although usable with the mini-probe). The Everhart-Thornley detector (ETD), however, showed enhancement of the SE detection during SEM imaging with the mirror underneath. A consistent 8x average improvement in the S/N of the SE signal is found at mirror positions up to 1.6 mm above the sample surface and at imaging horizontal field widths (HFW) ranging from 50um to 200um. An example of this improvement is shown in Table 3.1.

SE detection for the FIB, on the other hand was shown to be much worse with the mirror inserted, dropping almost half the S/N. FIB SE detection was tested over the same HFW and mirror height offsets and demonstrated the same consistency. This contrasting behavior is not entirely understood and was not extensively explored. Considering that the SEM SE yield of Al is roughly 2x more than that of Si [184], the enhancement can be explained backscattered electrons (BSE) from the SEM hitting the mirror directly above the surface which are not present with ion irradiation. The BSE will cause an increase in SE production from the Al surface, which will then be directed to the same ETD.

One way to combat the loss of SE signal in the FIB is to bias the mirror with a small negative voltage. When an -1.5 V electrical bias is be placed on the mirror's aluminum surface, it will direct the SE trajectories out towards the ETD grid and result in roughly 18.5% SE collection improvement. To accommodate this, a thin PEEK dividing plate and PEEK mounting screws replace the standard Al screws to electrically isolate the mirror, and a small wire is snaked in to provide the small negative voltage (see Figure 3.10).

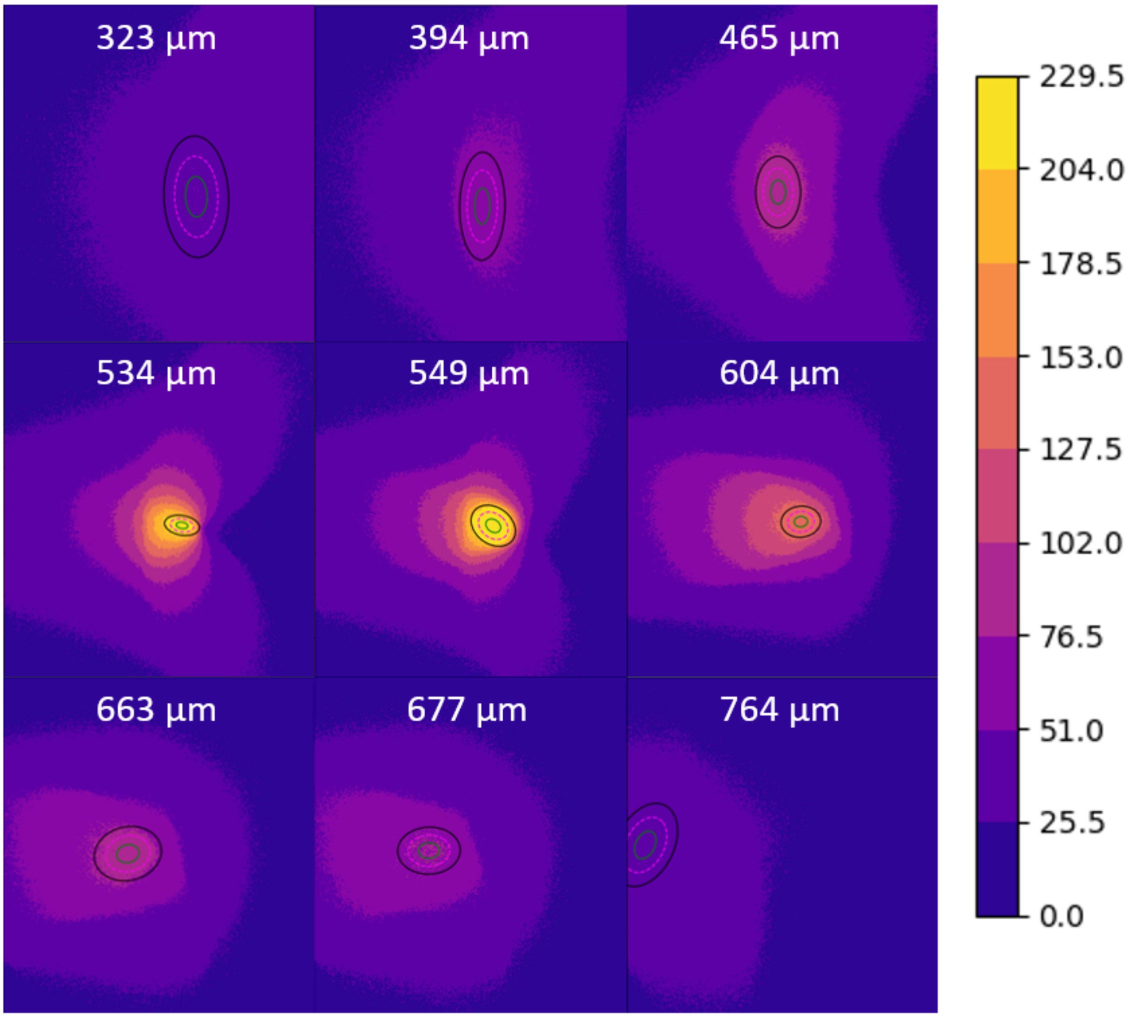

Figure 3.12: FIB-FS photon images from sample surface showing the aberration contributions for off-axis ray collection and the reduced signal observed at large collection angles as the mirror is moved above the sample. The values are reported in grayscale value from a raw PMT photon count. The green, pink, and black contours contain 1σ, 2σ, and 3σ of the entire counts in the image, respectively.

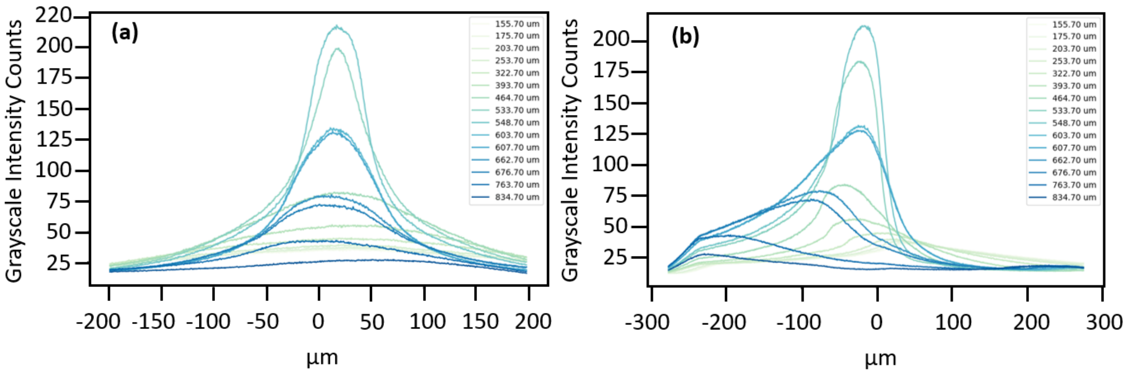

Figure 3.13: Line intensity profiles of mirror aberration characterization from the above images. **(a)** Vertical line profiles. **(b)** Horizontal line profiles. The results show that roughly 80 x 80 µm maximum FOV at the optimized height at 550 µm.

While the elliptical mirror designed here (and elliptical mirrors in general) are free from chromatic aberration [185, 186], off-axis rays will be subject to strong coma and astigmatism aberration and reduce the coupling efficiency at the fiber end. The focusing properties of elliptical and parabolic mirrors can be readily found [186–188], but these wavefront approximations are only valid for aperture angles less than π and do not apply for the case here. An apodization function has been developed for elliptical mirrors to attempt to describe the energy distribution in the spherical wavefront on the exit pupil [189], however, the function is not analytic and the simulation based on the expression is limited. Therefore, empirical measurements were performed on an Al sample to collect the light with a PMT and the subsequent images were processed to determine limits to the collection and serve as a baseline for qualitative aberration limitations.

With the mirror centered under the beam, a series of images at increasing mirror-sample heights reveals the collection losses associated with off-axis rays. The ion beam scans across the sample at different mirror heights and the image generated shows the grayscale values from the raw photon maps (see Figure 3.12). Vertical and horizontal line profiles are taken to summarize the measurement and are shown in Figure 3.13. The optimized height of 548 µm above the sample surface shows roughly 80 x 80 µm maximum FOV for the focal point of the mirror before losses up to 50% are introduced. Variation of the mirror height by 100 µm results in even larger losses for both the overall count value and the transverse component, emphasizing the requirement for sub-micron mirror stage strokes listed in item 3. Nevertheless, even with some losses from the aberrations, the elliptical mirror routinely yields close to 10x better signal than the mini-probe.

This relation between the off-axis emission and collection efficiency means that the maximum acquisition field of view is also dependent on the fiber optic core size. In other words, as photons are emitted from areas outside of the focal point, they will be focused at both a different location and at different angles at the opposite focal point where the fiber is. The choice for a large core 1 mm diameter sized fiber makes sense to minimize these losses and allow for a larger collection region at the sample surface. This choice in fiber optic for the transmission has impacts when it comes to the detection end, affecting diffraction and resolution so a discussion on the choice of detectors follows.

3.4 Detection

Once the photons have been coupled to the fiber optic in the chamber through either the elliptical mirror or the mini-probe, they are transferred through the vacuum chamber wall and can be delivered to any number of possible detectors. Whether the light is to be dispersed for spectral analysis or if it should pass directly to a sensor for specular detection will determine if a spectrometer or other optical components are needed. Since the primary goal of most FIB-FS is spectroscopy, the former is considered first.

3.4.1 EMCCD

Decomposition of polychromatic light requires two things: a spectrograph and a sensor/camera. The purpose of the spectrograph is to take the light from a source and diffract it onto a sensor. The diffraction of the light from the grating is defined by the grating equation:

$$m\lambda = \mathrm{d} * (\mathrm{sin}\theta_{\mathrm{i}} + \mathrm{sin}\theta_{\mathrm{d}}) \tag{3.4}$$

where m is the diffracted order, λ is the wavelength, d is the grating groove density, and θ_{i} and θ_{d} are the angle of the incident and diffracted light, respectively. By this equation, a polychromatic light source incident on a grating at the same angle will result in the different wavelengths being reflected at different angles. This operation is typically enhanced using a collimating mirror to direct the light towards the grating, followed by a focusing mirror to increase the separation of diffracted light at the sensor end. When an array of pixel sensors are placed at the diffracted end to collect the light simultaneously, all the wavelength components of the light source are collected according to the pixel location in which they land in a single snapshot. Thus, the sensor options to enable full spectrum acquisition are either charged coupled devices (CCD) or complementary metal-oxide semiconductor (CMOS) cameras.

Both CCD and CMOS cameras are used throughout the field of optics and have their own unique pros and cons. The CMOS sensor is a digital device that converts the charge from the photon impact on the pixel to a voltage at the pixel. The signal is then combined via multiple on-chip digital-to-analog converters, allowing for fast readout and framerate speeds, low noise, and are overall significantly cheaper than their CCD counterparts. While major improvements have been made to the technology in recent years, these cameras are not as sensitive as CCDs.

Unlike CMOS cameras, CCDs are analog devices that convert charge to electrons at the photosensitive pixel site. This fundamental difference is what allowed the development of the electron multiplying CCD (EMCCD), which is an on-chip improvement that enhances the gain in the readout register. When the image area is exposed to light, an electron is created from the photon impact and the charge is moved vertically into the readout register. When moving the charge through a register, there is a small probability that the charge transfer can create an additional charge by a process of impact ionization. This occurs when the charge is clocked and it has sufficient energy to create another electron-hole pair, effectively creating an amplification of the original signal when the new electron is read out. EMCCD's enhance this process by using two electrodes in the readout section and keeping them at different voltages, such that the electric field generated between them is high enough for electrons to cause impact ionization [190]. The result is amplification of the signal up to 1000x over the read noise since it occurs on-chip before the A/D converter, although at the cost of readout rate and charge transfer speeds. This technology combined with the inherently higher quantum efficiencies of CCD over CMOS, make the EMCCD the best choice for low-signal and single photon applications, and it is chosen here.

The purpose of any imaging system is to take the object and project it onto the image plane, only here the object image is projected at different locations based on its wavelength. An important aspect of this behavior is the ability to distinguish signal from two different wavelengths, or in other words, ensure that the angle of diffraction θ_{d} is large enough that the two different wavelengths can be resolved at the image plane. A simple way to quantify this is by the linear dispersion:

$$L = \frac{\partial \lambda}{\partial \theta_{\text{d}} * f} \tag{3.5}$$

where f is the focal length of the focusing mirror. It is easy to see by equation (3.4) and equation (3.5) that for a fixed grating groove density d and incident angle θ_{i}, the size of the detector will determine the overall bandwidth of wavelengths collected in a single frame, and that the subsequent pixel size and density will determine the ability resolve $\partial\lambda$.

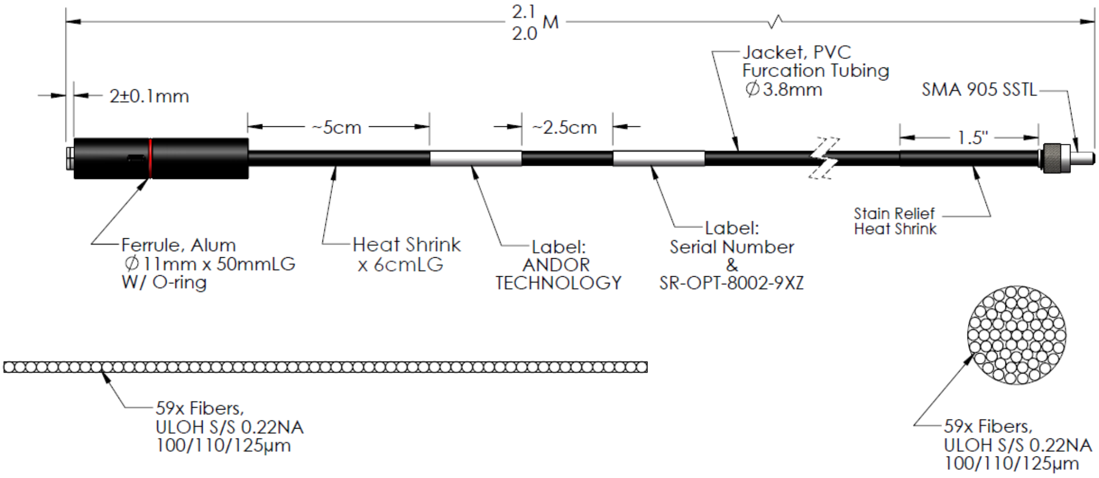

Figure 3.14: Custom fiber bundle-to-linear-array design used to improve spectral resolution of the spectrometer by taking the 1 mm core collection fiber and converting it to a linear array of 59 fibers with 100 µm core size. Two cables of this design were built: one with fused silica cores for UV-VIS transmission and one with VIS-NIR transmission cores. Since the fibers are of the same dimensions, they are easily interchanged.

This returns the question of fiber core size as equation (3.4) and (3.5) fail to tell the entire story. Since the spectrograph is inherently projecting the object image onto the sensor, the object itself will become a spectral resolution limitation if it is larger than the linear dispersion. In other words: if the linear dispersion of the system is 10 nm/mm, but the object has a diameter of 1 mm, then the images will overlap even if they differ by 5 nm in wavelength.

The benefits of a large core fiber optic on the detection end have been shown in prior sections so to avoid the losses at the collection end and to minimize the tradeoff between spectral resolution and fiber core size, a custom fiber bundle-to-linear-array was designed to connect to the 1 mm core fiber output at the chamber. Figure 3.14, shows the design of fiber. One end of the cord consists of 59 fibers, each with 100 µm core size in a bundle of diameter $\sim$ 1.1 mm. On the other side, the fibers are aligned vertically so that the width of the image into the spectrometer is defined by the 100 µm core size and not the 1 mm diameter. The vertical length of the fiber is roughly 7.4 mm, requiring that the detector be at least 7.5 mm high in order to not lose any photons.

The detector that was chosen to meet these specifications is the iXon 888 Ultra EMCCD camera from Andor, mounted to the Andor Kymera spectrograph. The camera is a back-lit, EMCCD, with a 1024 x 1024 pixel array - each pixel measuring 13 µm - resulting in a 13.3 x 13.3 mm image area. A number of gratings are used to deliver high-resolution, low bandwidths (1200 grooves/mm

Array Size	Minimum Exposure Time	Frame Rate
1024 x 1024	38 ms	26
512 x 1024	5 ms	200
128 x 1024	0.75 ms	1,333
64 x 1024	0.25 ms	4,000

Table 3.2: Minimum EMCCD exposure times and frame rate capable of maintaining -60°C CCD temperature with Frame Transfer and chiller.

$\sim$ 47 nm) or low resolution, high bandwidth (150 grooves/mm $\sim$ 430 nm) onto the large camera. A high QE and electron multiplication (EM) gain provide the best signal to noise enhancement in camera technology. A critical component is the ability to vertically bin charge in the readout register so that the vertical component of the fiber array can be read as a single column whilst maintaining the horizontal wavelength space. In other words: instead of 1024 x 1024 pixel readout, the charge on each pixel is shifted vertically and binned as a single column to create 1 x 1024 readout and results in higher signal to noise ratio.

A major limitation of such a large sensor is the readout and framerate. The fastest frame rate for a full frame readout is 26 fps, which corresponds to roughly 38 ms exposure time. These time frames can be too long for time-resolved or mapping measurements which will be discussed later on. When the camera is pushed past these limits with shorter exposure times, the charge shift is not fast enough to keep up with the readout and charge builds up on the sensor until saturation. Additionally, the sensor will heat up and cause the background level to rise.

The readout rate can be drastically reduced through two methods. The first is by using a ”Frame Transfer” mode of operation, which uses a masked frame storage area underneath the image area sensor. The signal hits the camera sensor and the charge is shifted to the storage section. Since charge transfer is faster than the readout, this step happens quickly and frees up the original image area for new exposure. Thus, time is saved by combining readout and exposure times by using the storage area to hold charge during readout while the imaging area is exposed. The second way to increase the framerate is to the reduce the total number of pixels read. Since the fiber array only consumes about 7.4 mm of the 13 mm sensor, light is not falling on the entire sensor. By moving the fiber image to the bottom of the sensor (closer to the readout), the top rows of pixels can be ignored in the readout, saving time and reducing read noise. Figure 3.15

and Table 3.2 shows how reducing the image area readout impacts the noise and maximum frame rate achievable. In both cases, a water chiller can be used to keep the chip temperature lower at faster rates. Since the maximum amount of signal throughput is required at the lowest background and fasted speed, only the minimum array that captures the fiber image is used. In this case 512 x 1024 allows the whole array to be imaged and is used as the base readout array (vertically binned as 1 x 1024).

A couple notes on the fiber image in Figure 3.15: not all fiber cores are illuminated in the array and gaps can be seen between cores. This is due to the geometric mismatch between the 1 mm fiber core and the 1.1 mm fiber bundle at the mating junction and the fiber packing fraction in the bundle. Since the bundle is slightly larger in diameter than the collection fiber, there are cores on the outer rim of the bundle that will not collect light. Furthermore, part of the surface area on the fiber bundle will consist of the cladding or gaps between the circular fibers and light is not transmitted (see Figure 3.14). The order of the fiber positioning on the linear end is random, so there are intermittent gaps in the fiber image. Second, the top of the fiber array appears slightly out of focus compared to the center of the array. This is field curvature aberration imposed by the focusing mirror on spectrograph. The focal length of this mirror is roughly 193 mm, and the depth of field is unable to focus tall object images. Unfortunately, the fiber array was a custom build so this artifact was not noticed during the demo of the spectrograph and was only discovered after purchasing the hardware. While other, larger focal length spectrographs provide a marginal improvement, it is not enough to justify the cost and the artifact remains a spectral resolution limitation.

3.4.2 PMT

Another common detector used in spectroscopic techniques is the photomultiplier tube (PMT). A PMT operates on the concept of turning photons into electrons that are then sent into a series of dynodes to generate a cascade of secondary electrons, effectively amplifying the gain of the original photoelectron (see Figure 3.16). Unlike the EMCCD, the PMT consists of a photocathode instead of the pixel array. The benefit of these technology is the high signal amplification from the dynode (can be up to 1 million times) and the fast readout rates (down to 10s of nanoseconds), however, spectroscopy with a PMT is handled differently from the EMCCD since the photocathode is not an array.

Whatever light that falls on the PMT photocathode will be counted as a signal, regardless of its wavelength (subject to the photocathode quantum efficiency). Therefore, in order to distinguish different wavelengths from a polychromatic light

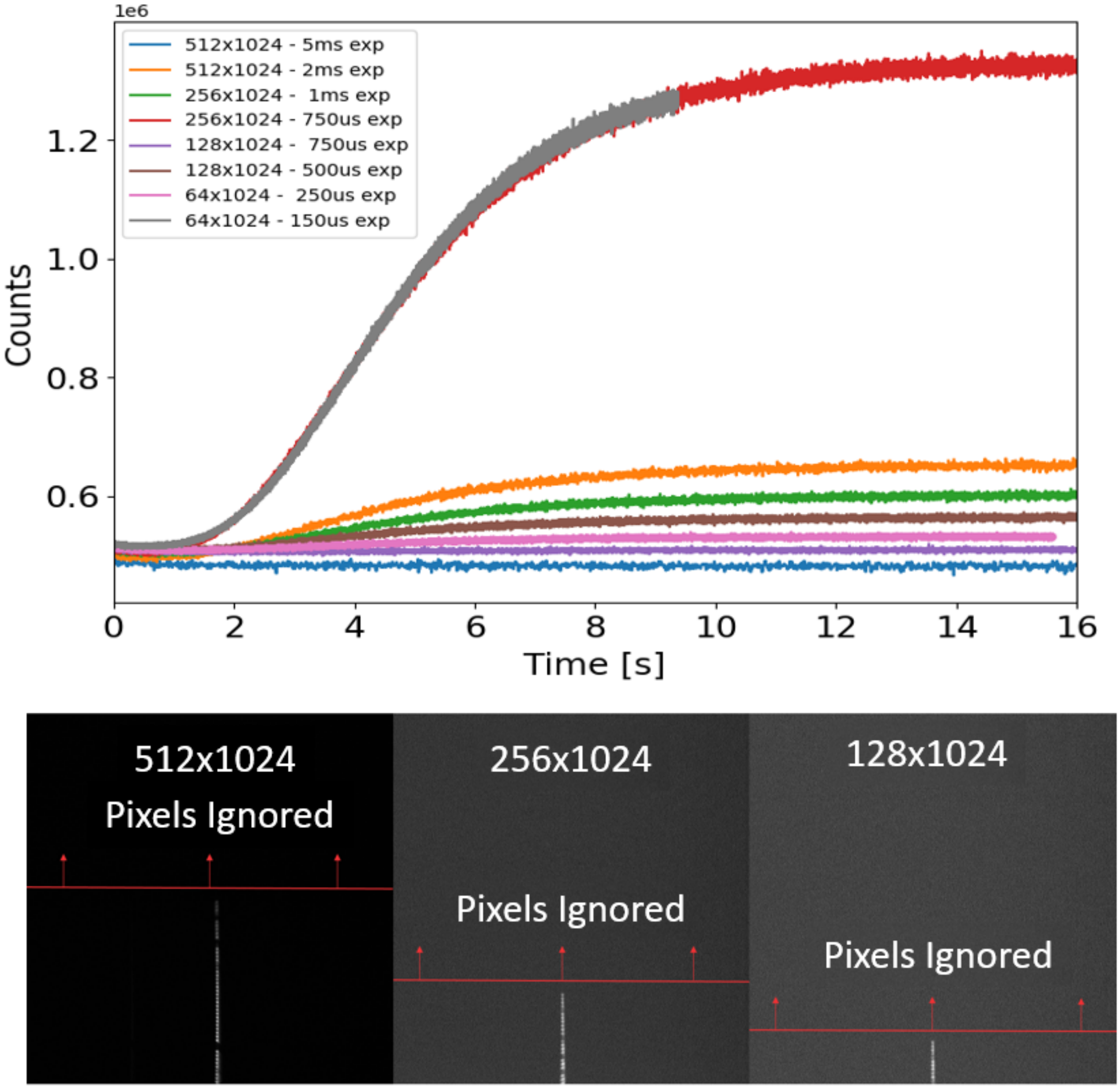

Figure 3.15: EMCCD binning and impact on background noise level. As the image of the fiber is moved towards the bottom of the image frame and the pixels are not read out, the camera is able to achieve lower noise and faster frame rates without charge buildup or overheating, making experiments with faster exposure times possible in smaller readout regions.

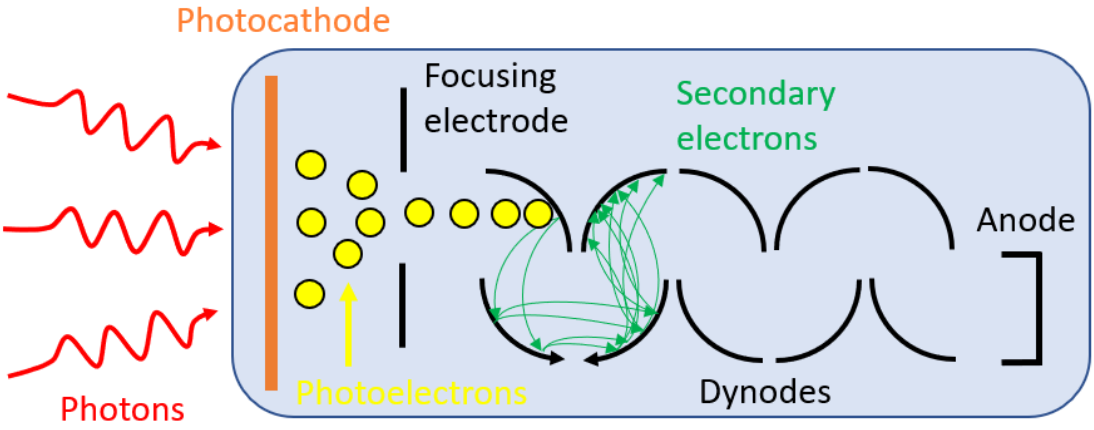

Figure 3.16: PMT structure and mechanism. Photons are converted to electrons at a photocathode, followed by an amplification process across multiple dynodes before readout.

source, one must ensure that the diffraction angle only delivers light of the desired wavelength onto the sensor with the other wavelengths blocked or deflected elsewhere. In a standard monochromator setup, the PMT is placed behind a slit that blocks light of other wavelengths while the grating is scanned across a range of angles to build a full spectrum. Alternatively, the slit can be set to a gap size that corresponds to a wavelength range or bandpass shown in Figure 3.17.

There are two possible conditions of operation: the user wants to know the bandpass transmitted for a given output slit width or the user desires specific bandpass onto the PMT and needs to know what to set the slit width to. For light of wavelength λ_c brought into the entrance of spectrograph at the half-angle $\varphi = 15.044°$ determined by the acceptance cone of the spectrograph, the incident angle θ_i of the ray that hits the edge of the grating is:

$$\theta_i = \sin^{-1}\left(\frac{\lambda_c * \mathrm{d}}{2\varphi}\right) \tag{3.6}$$

where d is the grating groove density. The angle α that hits the edge of the output slit is then geometrically set by the focal length f of the focusing mirror and slit width Δx:

$$\alpha = \tan^{-1}\left(\frac{\Delta x}{2 * f}\right) \tag{3.7}$$

The light will be dispersed according the grating equation (3.4). Since all rays are fixed at incident angle θ_i by the collimating mirror, the wavelength that hits the outer edge of the output slit becomes:

$$\lambda_{edge} = \mathrm{d} * (\sin(\theta_i - \varphi) + \sin(\theta_i + \varphi + \alpha)) \tag{3.8}$$

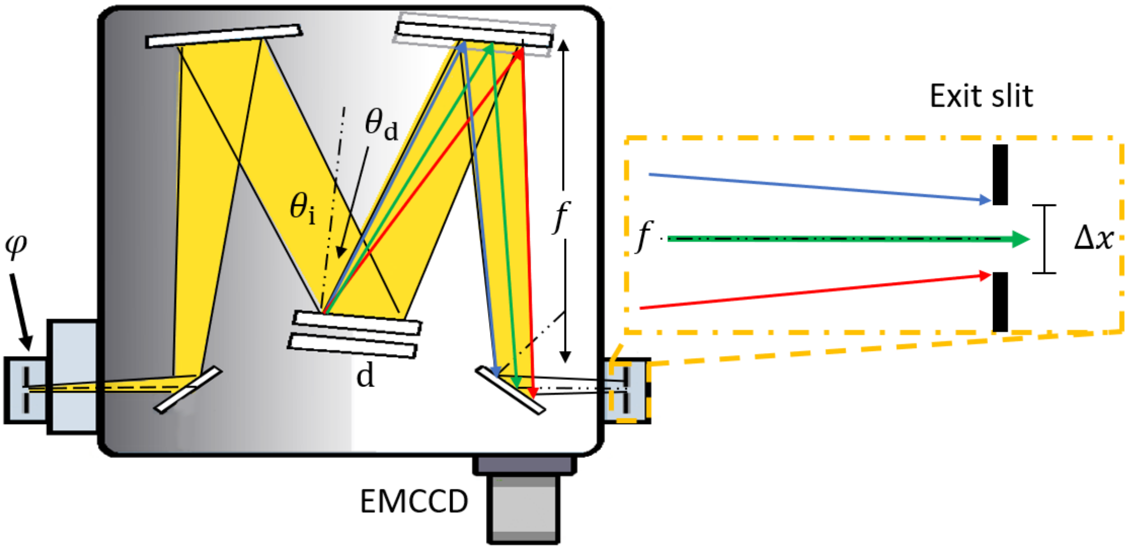

Figure 3.17: Spectrograph geometry.

The bandpass is simply the difference between the center wavelength λ_c and the wavelength λ_{edge}:

$$\text{bandpass} = 2 * (\lambda_{edge} - \lambda_c) \tag{3.9}$$

A small tilt correction is needed due to the focal plane tilt correction at the exit port (Andor, personal communication, 31 July 2018):

$$\text{bandpass} = \frac{2 * (\lambda_{edge} - \lambda_c)}{\cos 4.4^\circ} \tag{3.10}$$

In the latter case where a specific bandpass bp (designated in nm) is desired, the problem is solved in reverse:

$$\Delta x = 2 * f * \tan\left(\sin^{-1}\left(d * \left(\frac{1}{2} * \text{bp} * \cos(4.4)^\circ + \lambda_c\right)\right) - \sin\left(\theta_i - \varphi\right) - \theta_i - \varphi\right) \tag{3.11}$$

There are a couple ways to check the answer. A specific bandpass equal to a published value by Andor for a specific grating and camera sensor size is plugged in and compared to the bandpass in the specification of the setup. For example, with a grating with 150 lines per mm centered at 500 nm ($\theta_i = 2.225^\circ$ from equation (3.6)) on a camera that is 13.3 mm wide, the bandpass is listed as 436.52 nm. Plugging 436.52 nm $=$ bp into equation (3.11) yields a slit width $\Delta x =$ 13.275 mm. Similarly, with a 1200 lines per mm grating centered at 500 nm on the same detector, the bandpass is 47.69 nm quoted by Andor and the slit width determined by equation (3.11) in this case is$\Delta x =$ 13.309 mm. This operation can be combined with a various filters at the entrance port to further clean up or filter the desired wavelength or bandpass. Additionally, PMTs with

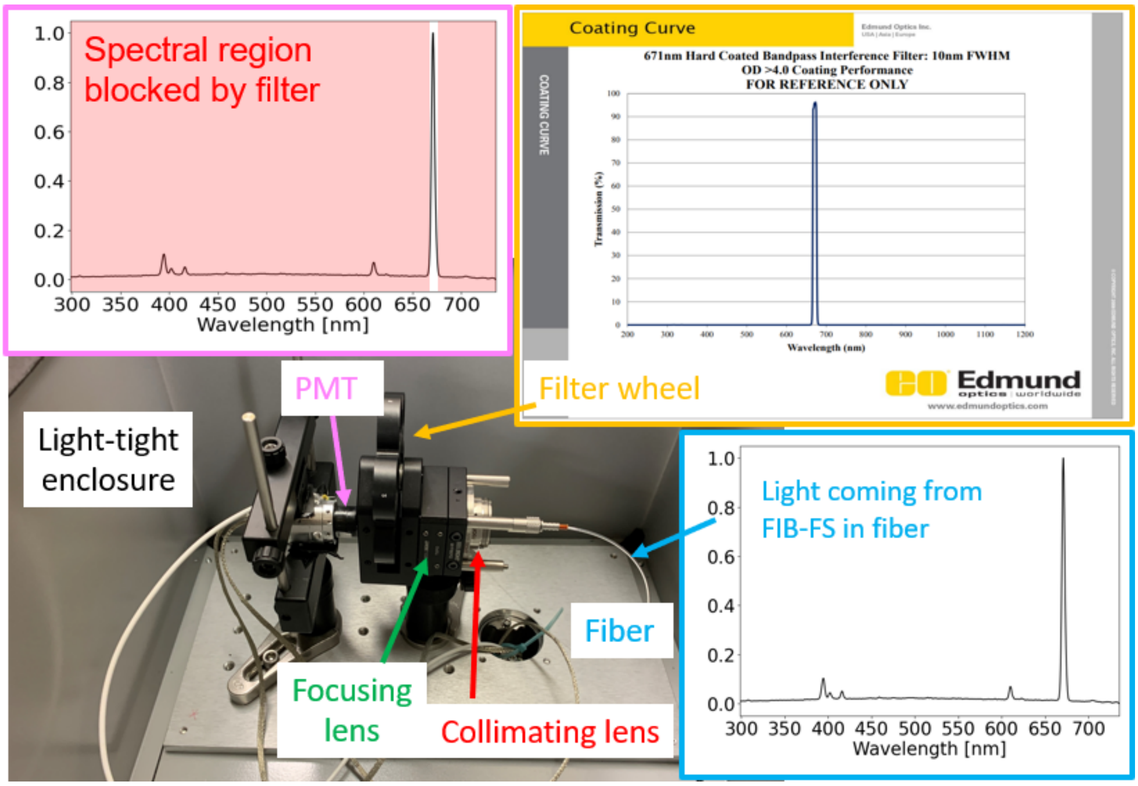

Figure 3.18: PMT and narrow-bandpass filter module used to collect photons at fast acquisition rates. The fiber optic carries a polychromatic signal from the microscope into a light-tight enclosure. A collimating lens and focusing lens direct the signal through a narrow bandpass filter onto a PMT, such that only signal of a specific atomic transition pass through for detection.

different spectral responses can be easily interchanged if a better performance in the UV or IR is desired.

A detection quantum efficiency study was carried out to characterize the performance between the two detectors. The total throughput of the system at the PMT output was measured less than 35%. Four MgF_2 coated aluminum mirror reflections of the spectrograph each with ∼90% reflectance for a compounded 65% throughput, combined with the largest loss coming from the grating which has a reflectance of roughly 55% at 632 nm and dispersion into higher order modes.

In the interest of better signal, a separate PMT module was designed to house the PMT along with a motorized filter wheel and optics shown in Figure 3.18. While the dispersion offered by the grating was no longer available, narrow bandpass filters with bandwidths of 5 nm and 10 nm are readily available, allowing similar atomic transition detection capabilities as the grating-slit-bandpass method. Since the light only passes through a filter, however, all the reflections and diffraction losses are bypassed. From the moment the light leaves the fiber, the spectrograph gives about 40% total detection efficiency under the best possible configuration (500 nm light with 500 nm blazed grating). When compared to the PMT module with a high throughput narrow bandpass filter, close to 95% detection efficiency can be achieved by going from the fiber straight into the PMT. With optional collimating and/or focusing optics, this will slightly decrease to $\sim$85%-90%.

3.5 Data Collection and Analysis

Both the EMCCD and the PMT detector provide advantages when employed in different operation modes in the FIB-FS technique. These modes of operation can be used in various orders and iterations to collect different information from the sample or to perform an optimized workflow. The following sections discuss the development of each of these different modes, how they are operated, the environments in which they are best suited for, and the analysis methods required to process the data that comes from them.

3.5.1 Survey Mode

The first and most straightforward mode of operation is termed Survey Mode. In this mode, the FIB scan is operated independently while the EMCCD camera and spectrometer acquires a spectrum over a designated exposure time. Since the exposure time and FIB scan are decoupled, an average spectrum of a region of interest is acquired with no spatial information. The FIB is free to perform any sort of cut or pattern within the limitations set by the electronics of the column. In this condition, low doses can be used to minimize damage at the surface and gain a quick elemental signature of the sample. Here, low resolution/large bandwidth gratings are used to maximize the spectral range to get an idea of what signals may be available for closer inspection or to be targeted later on with higher resolution gratings or more sensitive conditions. This mode is typically the first step in analysis with FIB-FS and provides a basic foundation on which the technique operates.

This mode can be can repeated to collect multiple successive spectra in a kinetic series, or Kinetic Survey Mode. A set number of total spectra or frames is chosen to collect with each spectrum having the same exposure time. The spectra are then ordered by their timestamp of acquisition, allowing for time-resolved spectral analysis of the sample at the minimum frame rates available (see Table 3.2).

3.5.2 Hyperspectral Mode

The next mode is a mode in which the FIB scan and EMCCD camera acquisition time are clocked in sequence such that the pixel dwell time of the FIB equals the exposure time of the camera. This mode is called Hyperspectral Mode, and it results in a full spectrum collected at every pixel that are then processed to generate elemental maps (see Figure 3.19). The process can be repeated multiple times, allowing for the ion beam to mill through the surface and into the bulk of the sample. When the data is stacked by layers, a 4-D (x-y-z-λ) data structure is formed which can be parsed by wavelength to produce an elemental volume map or depth profile.

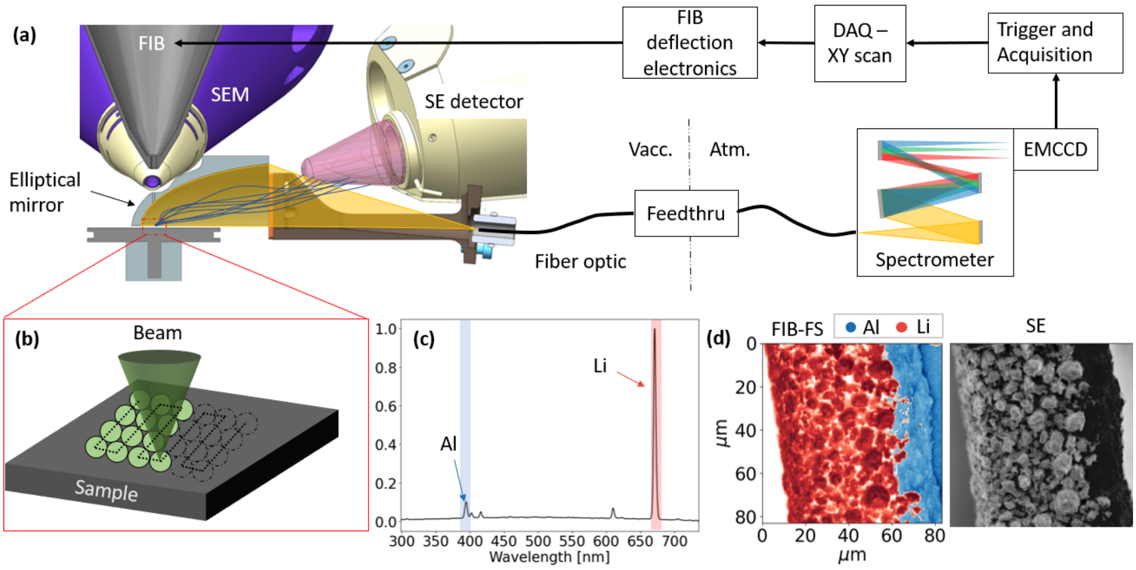

Figure 3.19: Schematic of FIB-FS Hyperspectral Mode acquisition. **(a)** The exposure time of the spectrometer is coupled to the dwell time of the FIB through a data acquisition card to the FIB deflection electrons to produce a series of spectra at every pixel scanned by the FIB **(b)**. The spectra **(c)** can be parsed by spectral bins to produce maps of the spectra line count values **(d)**.

In order to make this type of elemental data acquisition possible, timing sequences between the spectrometer and the FIB as well as data formatting are critical. A software was developed to sync the FIB and the spectrometer. This is implemented through providing an external scan and blanking signal to the microscope optics scan and blanking interface board external scanning port, which controls the blanker dipole and the octupole deflection voltages (see Appendix A). A user will set a desired scan pattern in terms of resolution and HFW which is then provided to the patterning and image acquisition (PIA) by setting an X and Y scan voltage for each image pixel based on the HFW and resolution. At the end of each exposure, the camera on the spectrometer outputs a trigger signal which is taken from the camera output and received on a National Instrument data acquisition modular system (DAQ) to increment to the next X,Y voltage pair. The DAQ control app takes the desired image pixel size in X and Y and creates a scan pattern. To collect an SE signal from the ETD while simultaneously acquiring a spectrum at the pixel, a video out channel on the Acquisition Motherboard (ACQMB) is connected to the DAQ receiving channel and recorded in the application software.

Limited spectrometer control was built into the software since the spectrometer came with its own user interface. Control can be taken by the spectrometer app, but it was simple enough to keep gratings and calibration control within the spectrometer and only control the camera and acquisitions settings from the developed software.

Since each pixel generates a 1024 integer counts from the spectrum, an N x N x 1024 data matrix can take a lot of space. To save memory, the 2D spectral map is saved from the camera as raw data .dat file and with metadata saved as an ASCII .asc file. The .dat file contains the spectral counts as a 3D array of unsigned ints while the .acs file contains the camera setting metadata. Once collected, the data is exported in .h5 formatting, which is then opened later in Python for analysis. Python scripts are used to reshape the raw data into the original resolution shape set in the metadata, while the user can choose which spectral bins of the 1024 pixel columns to analyze based on the spectrometer grating settings. The handling of the data this way not only saves space, but also allows for the freedom of more advanced processing methods and scripts to be used to aid in analysis such as Gaussian peak fitting, filtering, colormap scaling, and background subtraction.

Its important to note that a rough knowledge of the spot size is needed *a priori* in order to ensure a proper scan. Depending on the beam current being used, the FIB probe may end up being much smaller or larger than the pixel size set by the resolution and HFW. If the probe is smaller, then the entirety of the pixel will not be irradiated. If the probe is too large, then beam overlap will occur and result in mixed signals. For example, if a beam with 30 nm spot size is used to image a 10 µm x 10 µm region with a resolution of 100 x 100 pixels, then roughly 70 nm of each pixel will go unirradiated. In this case, one can either increase the resolution to match the spot size (at the cost of total acquisition time N x N x exposure time seconds), or one can defocus the ion beam spot to match the pixel size. The defocus is made by simply applying an offset to the working distance WD between the current spot radius r_1 and the desired spot radius r_2 using the beam image half-angle α (see Appendix A):

$$\tan\alpha = \frac{\mathrm{r}_2 - \mathrm{r}_1}{WD_1 - WD_2} \tag{3.12}$$

or

$$WD_2 = WD_1 - \frac{\mathrm{r}_2 - \mathrm{r}_1}{\tan\alpha} \tag{3.13}$$

α and r_1 were found by running multiple spot burns on silicon while sweeping over a range of working distances and measuring the diameter of the crater for each beam current.

3.5.3 Photon Imaging Mode

The last mode is termed Photon Imaging Mode, and it is the mode that utilizes the PMT. Similar to Hyperspectral Mode, the FIB scan and the PMT acquisition are clocked in sequence, but here the light is directed towards the PMT. This mode was born of the limitations inflicted by the long exposure times of the EMCCD. Since the dwell is linked to the camera frame rate, the minimum exposure time available in Hyperspectral mode is roughly 5 ms. This is very long and can result in massive amounts of damage at a single pixel for moderate beam currents (nanoamps). The PMT allows for nanosecond and microsecond dwell times, resulting in real-time, high-resolution photon imaging and with minimum dose per pixel. When equipped with narrow band filters discussed in the PMT design section, high-resolution individual elemental mapping can be gained in a matter of seconds.

Integration on the FIB is easy since the ETD and ICE detectors on the system already operate using a PMT mechanism. The standard SE detector accelerates secondary electrons using a positively biased grid towards a scintillating material on the surface of light guide or glass. The light generated by the scintillator is directed towards a PMT and the SE image is formed. Therefore, a PMT with the same pin configuration and voltage range was chosen for this mode, except one with a VIS ranged photocathode is chosen instead of the standard 400 nm peaked sensor. The FIB-FS PMT simply borrows the power supply and pre-amp from one of the existing SE detectors and the PMT settings are able to be controlled like a normal SE detector, the microscope being none the wiser.

There are advantages and disadvantages between Hyperspectral Mode and Photon Imaging Mode with the PMT. The most straightforward and clear benefit of Hyperspectral Mode is that spectroscopy can be performed with high sensitivity. Because the EMCCD can collect dispersed light from the grating, a full spectra is captured. The detector array also allows for on-chip binning of charge and electron multiplication, further increasing signal to noise. A disadvantage of this, however, is that frame rate of the camera is relatively slow, resulting in long dwell times of the ion beam at each pixel and large amounts of damage to the sample. When taking maps of low-yield materials or challenging geographies, the use of high primary beam dose to extract a signal can result in excessive damage after a map acquisition. In addition to the large damage induced by the dwell, another factor to consider is the time to data and resolution available for the acquisition. When capturing a pixel map with 20 ms dwell, the total map acquisition time can easily reach an hour for maps of moderate resolution such as 400 x 400 pixels.

When sample damage is to be minimized or high resolution maps are required, the PMT offers the speed of acquisition and flexibility in the dwell to match the FIB scan boards. Single images or multiple frames can be taken with the PMT and averaged together, creating contrast images of FIB-FS signal with resolutions at 3072 x 2048 in a couple minutes. More importantly, the ability to dwell for shorter times has a significant impact on the maximum achievable resolution due to the Gaussian nature of the current density distribution in the FIB spot probe and ion-sample interactions. This concept is discussed in detail later on.

The main disadvantage to this method is that the light directed onto the PMT is not dispersed, so the elemental identification is not given with 100% confidence. The use of various optics in front of the PMT, however, can provide reasonable discernment of the signal, allowing for qualitative elemental mapping. For example, if the spectra is known after an acquisition in Survey Mode, a narrow band-pass filter over the desired transition can be placed in front of the PMT which transmits only the desired wavelength. The result is a high-resolution image containing the elemental information with minimal damage.

In summary, the capabilities of PMT imaging provide access to data that the EMCCD cannot deliver without excessive damage. The resolution achievable far exceed those available with the EMCCD maps with significantly less acquisition times. On its own, the PMT offers an additional source of contrast that is free from charging effects and can provide unique information about the surface. With the flexibility of discriminatory optics to be implemented, it can provide qualitative elemental information with the assumption that a proper spectrum of the region of interest is collected beforehand. While not usable for every application, the simple and inexpensive design offers a new approach to FIB-FS imaging and elemental mapping that is capable of forming powerful images.

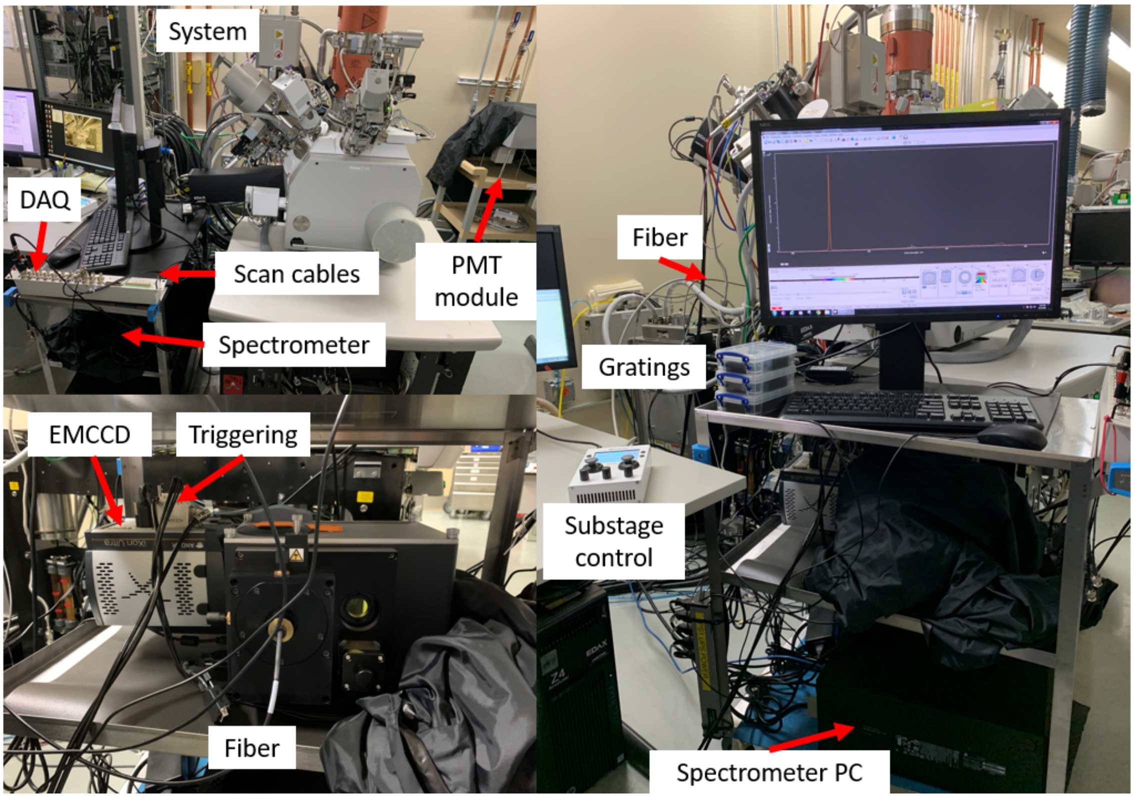

Figure 3.20: The FIB-FS hardware setup. The entire setup fits on a small cart that can be moved from system to system

3.6 Versatility and Upkeep

Every aspect of the hardware is mobile and can be moved easily. The control PC, DAQ card, spectrometer, and detectors are all on a mobile cart, while the mirror has multiple stage mounting hardware/platforms to fit different stages. The mini-lens probe can be mounted on any standard GIS port, making the technique easily transferrable. Figure 3.20 shows the complete setup on the mobile station. The results presented in this dissertation are from both a Ga^+ LMIS FIB-SEM and a multi-ion species plasma FIB-SEM system, where the setup and optics were routinely transferred from one system to the other.

A final note on the hardware is that over time and through repeated use, redeposition of sputtered atoms may occur on the collection hardware. This occurs faster with use of high currents and at the close proximity to the surface. The redeposition of multiple sputtered atoms and materials will develop thin films and amorphous layers like those shown in Figure 3.21. This will degrade the reflectivity and transmission of photons at the imaging end, resulting in worse performance over time. This is unavoidable, so both the mini-probe and the mirror were designed in a way to be consumable. The lens on the mini-probe is separate from the fiber so that it can be replaced when it becomes covered. The lens may be

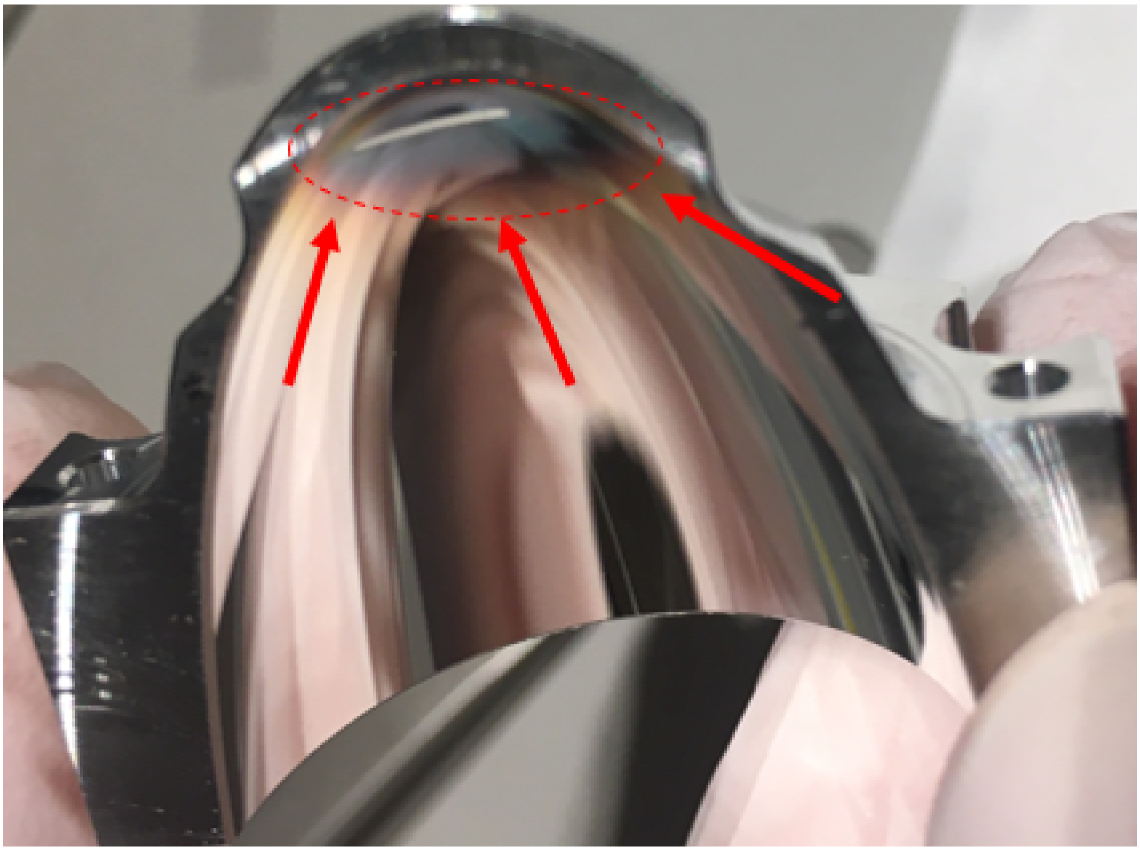

Figure 3.21: Redeposition of sputtered material on elliptical mirror seen as darkening at the nose-end of the mirror near the entrance aperture.

cleaned if desired, but their low cost of around 35 USD is not worth the headache. The mirror is also made separate from the mounting hardware and fiber so that this piece may be removed and replaced as well. Since the internal surface of the mirror is diamond-turned to such a high finish quality, it is not recommended to attempt to clean it. While the mirror replacement is more expensive than the lens, a bulk order was placed and their unit cost is roughly 150 USD. Redeposition rates were not thoroughly investigated, however, experience is that the average lifespan is between 6 months to a year. This number is purely from experience and can change vastly with ion bombardment conditions.

3.7 Conclusions

FIB-FS is a multimodal technique that has been designed to be versatile and capable of performance on any FIB system, while maintaining the sensitivity and requirements demanded by a nanoscale technique. A small insertable probe has been designed that allows for simultaneous use with a variety of detectors and is compatible with almost any application through its low profile. The lens configuration in the probe is unlike a standard fiber coupling system and provides a relatively high collection efficiency through its coupling and solid angle. If more signal is required, an ultra-sensitive, high efficiency collector has been designed in the form of an elliptical mirror. The mirror can be inserted and retracted, and methods have been designed for alignment and operation. Detectors have been specially chosen to match an optimized detection chain to provide multiple modes of operation. Each mode provides a unique form of information through the logic of its function. These modes can be combined, iterated, and repeated to perform complex elemental analysis at the nanoscale and are used throughout the rest of this dissertation to prove out fundamental limits and 3-dimensional nanoscale tomography.

Chapter 4

FIB-FS Characterization

4.1 Introduction

Nanostructures and materials are synthesized and fabricated to higher degrees of precision than ever before, demanding equal performance from the techniques used to characterize them. The interdisciplinary nature of nanotechnology, lack of nanoscale reference materials, and difficulties in sample preparation present many challenges for characterization of nanostructured materials *in situ*. Therefore, the prevalence and usefulness of elemental and chemical analysis techniques begins with basic performance metrics of resolution, accuracy and sensitivity.

The hardware and instrumentation described in the prior chapter have detailed the extensive enhancements to collection efficiency and the enabled methodology that FIB-FS offers compared to its broad ion beam predecessors. These developments and their operation are what uniquely define FIB-FS and make it capable of nanoscale elemental analysis. In the following chapter, these capabilities are tested to their limits. Through 3D tomography of GaAs/AlGaAs quantum wells, nanoscale lateral resolution of semiconductor heterostructures, and detection of trace-level impurities, the FIB-FS technique utility is shown to have high 3D spatial resolution, high sensitivity and the ability to detect light elements. A lateral and depth resolution of 15.5 and 12.8 nm are presented, respectively, and it is demonstrated that its performance is limited fundamentally by ion-solid interactions. In addition, minimum detection on the order parts-per-million (ppm) are reported and shown to be dependent on ion dose and ultimately limited by the volume sputtered.

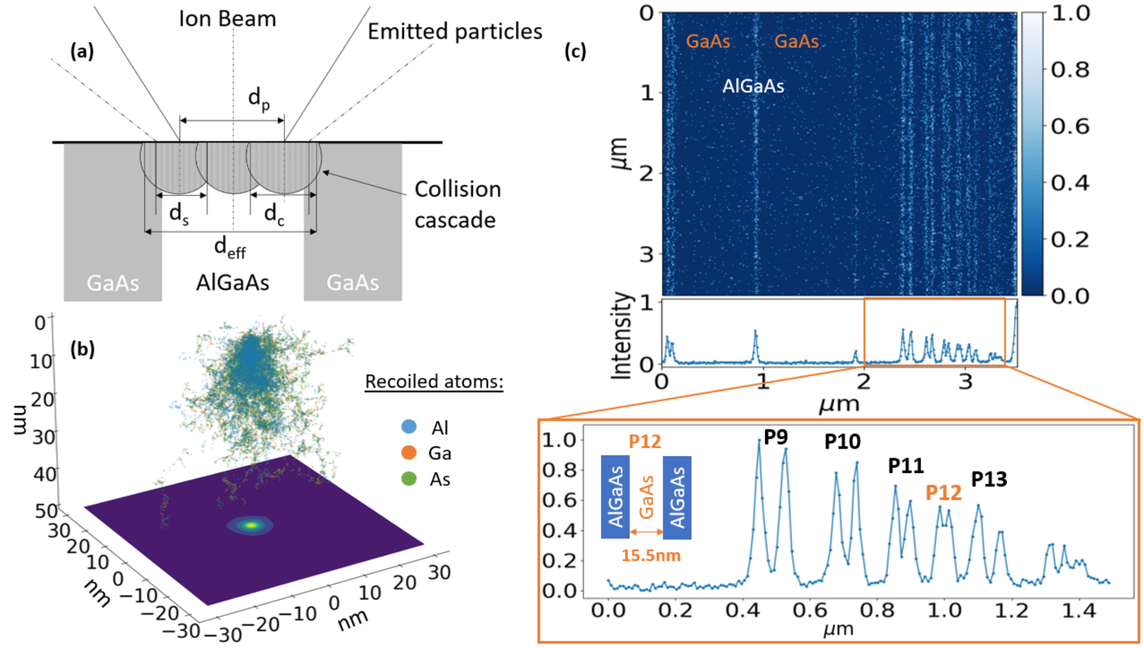

Figure 4.1: Lateral resolution of FIB-FS. **(a)** Cross-sectional schematic of the effective probe diameter $\mathrm{d_{eff}}$, ion beam diameter $\mathrm{d_p}$, sputtered atom range $\mathrm{d_s}$, and collision cascade range $\mathrm{d_c}$. Each circle represents a collision cascade initiated by a single ion. The ion beam is incident onto a GaAs-AlGaAs-GaAs heterostructure. **(b)** Monte Carlo trajectory simulation of 30 kV $\mathrm{Ga^+}$ ions incident onto AlGaAs. The plot shows the distributions of displaced Al, Ga and As atoms which are responsible for intermixing and broadening of interfaces in the sample. **(c)** Aluminum elemental map of the BAM L200 resolution standard – a heterostructure comprised of AlGaAs layers embedded in GaAs (see Appendix B). The bottom panel is the corresponding integrated line spread function, showing a resolution of 15.5 nm through AlGaAs-GaAs-AlGaAs stripe pattern P12, depicted in the inset.

4.2 Lateral Resolution

The FIB-FS technique is based on fluorescence spectroscopy of sputtered particles. Lateral resolution is therefore expected to be limited by the ion beam diameter $(\mathrm{d_p})$ and by ion-induced collision processes in the sample, as is the case in other ion beam techniques [36, 191]. Figure 4.1 **(a)** is a schematic illustration of the three factors that are expected to determine the effective probe diameter $\mathrm{d_{eff}}$ in FIB-FS: the diameter of the ion beam probe $(\mathrm{d_p})$, the diameter of the region from which atoms are sputtered as a result of ion impact $(\mathrm{d_s})$, and the diameter of the volume within which atoms are displaced in the sample $(\mathrm{d_c})$. The latter is a consequence of a collision cascade initiated by each ion and causes intermixing and broadening of interfaces in samples such as the GaAs-AlGaAs-GaAs heterostructure depicted in Figure 4.1 **(a)**. Collision cascades determine the size of the interaction volume, which is shown in Figure 4.1 **(b)** for the case of an ideal (zero diameter) 30 keV Ga$^+$ beam incident onto AlGaAs.

In order to measure lateral resolution and investigate the above-mentioned limitations, a certified standard (BAM L200) that is commonly used to characterize FIB-SIMS performance [36, 37, 192–194] is also used here. The sample is a cross-sectioned, epitaxially-grown AlGaAs-GaAs heterostructure with a range of layer thicknesses and periods down to 1 nm (see Appendix B). Figure 4.1**(c)** shows a FIB-FS image of the standard generated by summing the 394.4 and 396.2 nm Al emissions shown in Appendix B Figure B.2. The image was collected with the PMT imaging mode using UV-VIS fiber optics and a 10nm narrowband filter at center wavelength 396nm to allow only the transmission of the 394.4 and 396.2 nm Al signal to the PMT. The image is a 256 frame average of 7 pA 30 keV Ga$^+$ ion beam scan with 500 ns dwell time and pixel resolution of 512x442. Bright stripes in the map correspond to AlGaAs layers embedded in GaAs. The bottom panel is an integrated line profile of the Al map (i.e., the line spread function), showing AlGaAs-GaAs-AlGaAs stripe patterns P9–P13, in which the GaAs layer thickness ranges from 38.3 nm to 11.5 nm (see Appendix B, Figure B.1, and Table B.1). The thinnest GaAs layer resolved in the line profile is in pattern P12 – it has a thickness of 15.5 nm, which corresponds to the resolution of the FIB-FS map.

To decompose the contributions of $\mathrm{d_{eff}}$ in the 15.5 nm resolution measurement, analysis of the primary spot diameter $\mathrm{d_p}$ is first required. Measuring the primary beam spot diameter directly is difficult due to the Gaussian current distribution in the probe size. De-convolution of the beam width from the dwell is especially difficult at low currents where high dwell times are required to see changes in SEM-SE contrast or remove sufficient surface atoms to measure a crater. As the dwell time increases, the staining from probe spot beam tails and re-deposition

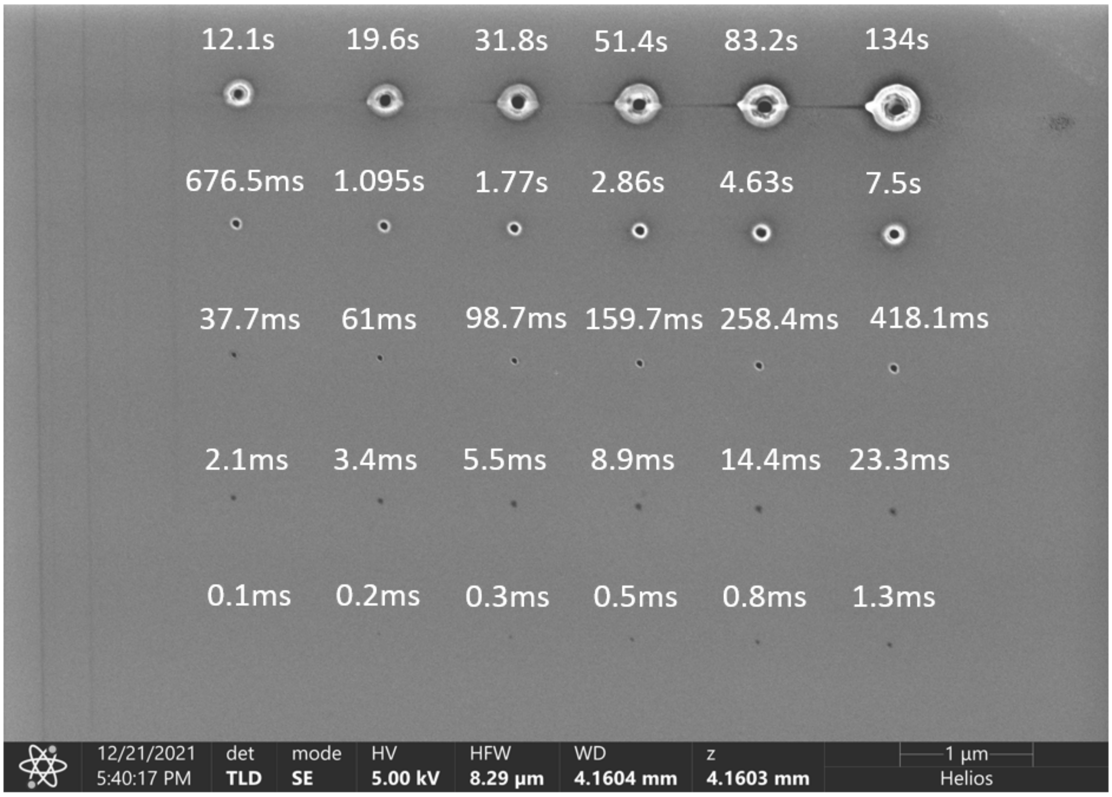

Figure 4.2: Spot burn grid of the 7 pA 30 keV Ga$^+$ FIB beam used in the resolution measurements. The dwell time of the spot burn increases from bottom left to top right as a Fibonacci sequence starting with a 0.1 ms dwell time. At this current, dwell times less than 0.1 ms do not create enough contrast to measure the burn, while longer dwell times result in contrast from beam tails. The longest dwell times result in beam tails milling the sample and sputtered atom re-deposition, enlarging the spot size. The dwell time used in our resolution measurement is 500 ns, too short to be directly measured. Note: the patterning and acquisition framework of this FIB has a maximum allowable dwell time of 100 ms so streaks are seen to the left of the high dwell spots due to ion fly-back during blanking.

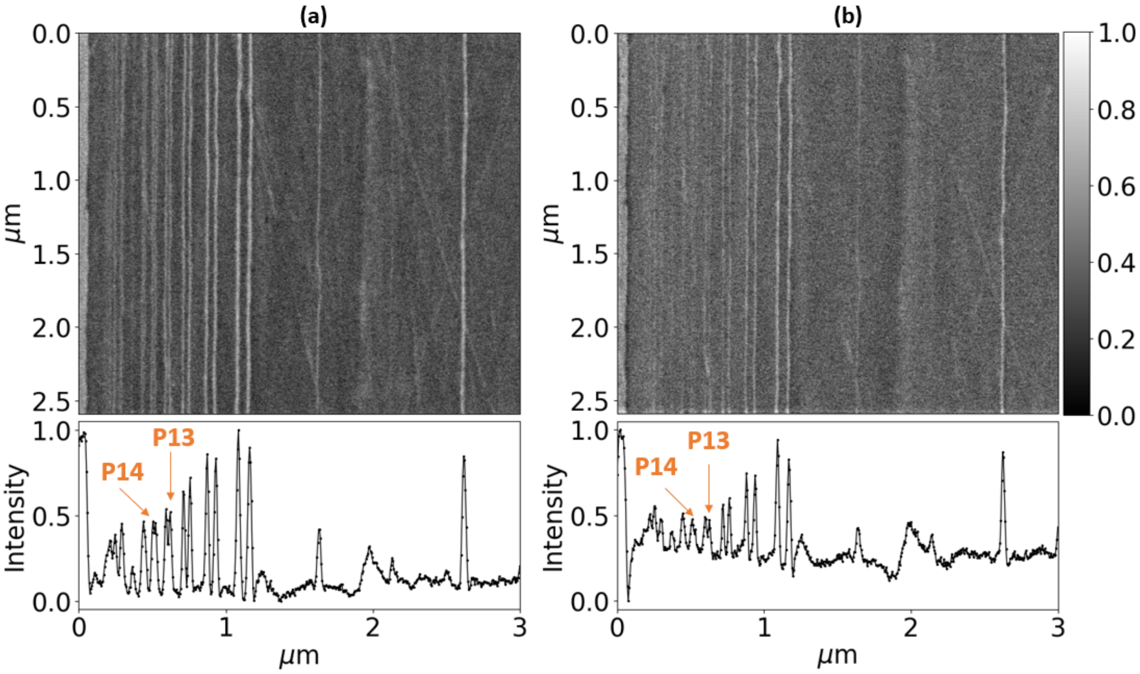

Figure 4.3: SE images of the BAM L200 sample taken with 7 pA 30 keV Ga$^+$ FIB beam used in the resolution measurements. **(a)** SE image and line-spread function of the sample at 3.5 pC/µm^2 showing separation of period P13. The distance between the P13 strips is 11.5 nm, demonstrating the impact of the spot current density contributions to the signal at 500 ns dwell compared to spot burns in Figure 4.2. **(b)** SE image and line-spread function the same region after 7 pC/µm^2 accumulation, showing the broadening of P13 and impact of the collision cascade on the resolution as the beam mills through the surface.

of sputtered atoms increase the apparent spot size (see Figure 4.2). At low dwell times ($\leq$10s of µs), however, signal originating from within the diameter of the beam that contains 50% of the current (d50) dominates due to the highly centralized current distribution in the probe spot. Therefore, measurements of spot profiles from burns made with dwell times long enough to make a stain will always be much larger than the diameter from which the signal arises at low dwell times. As a result, direct measurements of the ion beam probe size are done through image analysis and resolution measurements with secondary electrons.

Resolution of an imaging system is typically measured by the convolution of an object with the point spread function. In nanoscale microscopy, however, well-defined point-like objects are difficult to manufacture or validate so the use of other methods are accepted: knife-edge rise time of a line spread function, modulation transfer function, full width at half-maximum of a delta layer, and strip-to-strip imaging distance. Here, strip-to-strip imaging distance with the BAM-L200 sample is used to determine resolution of the same 7 pA 30 keV Ga$^+$ beam and

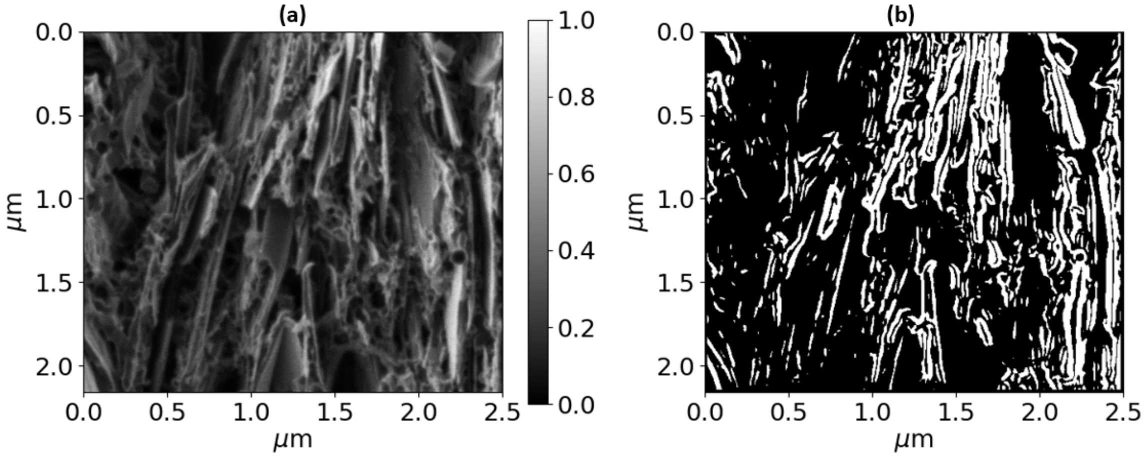

Figure 4.4: SE resolution measurement using graphite pencil lead stalks with the same beam. **(a)** SE image of the graphite lead stalks, which provide numerous suspended flakes to perform knife-edge measurements. **(b)** Thousands of edges along contrast boundaries are found. Contrast transitions that show clipping or delta step transitions are eliminated. The 35-65% rise time is found to be 9.3 nm for 65% of the transitions, and less than 11 nm for 74% of edges.

the same irradiation conditions in Figure 4.3. The SE image from the acquisition shows line grating P13 being resolved, corresponding to $\sim$9 nm d50 spot size (and P14 partially resolved at low dose). This d50 value is also corroborated with knife-edge measurements on a sample of graphite composed of sharp vertical suspended edges as opposed to embedded heterostructures shown in Figure 4.4 (this sample is common for measuring resolution as the suspended edges provide sharp contrast drop off as well to reduce the intermixing between boundaries). Clearly, if the measurements made from the spot-burn profiles in Figure 4.2 were taken as the true probe size at lower dwell time, then separation of P13 would not be possible.

From the analysis on SE resolution, the employed 30 keV ion beam is determined to have a diameter $\mathrm{d_p}$ of roughly 10 nm, which is approximately 6 nm smaller than the measured lateral spatial resolution. To confirm that the difference is caused by ion-induced collision processes in the sample, the Monte Carlo code SRIM is used to simulate the trajectories of the incident Ga$^+$ ions and recoiled atoms in AlGaAs (Figure 4.1 **(b)**) and to deduce the parameters $\mathrm{d_s}$ and $\mathrm{d_c}$. To simulate sputtering and calculate $\mathrm{d_s}$, recoiled atoms are tracked in the sample and their final coordinates are recorded at the surface before ejection, shown in Figure 4.5. A Gaussian kernel density estimate with 1 angstrom bin size to find the distribution sputtered atoms at locations around the center and show that in the case of 30 keV Ga$^+$ ion incident onto AlGaAs, most sputtered atoms are

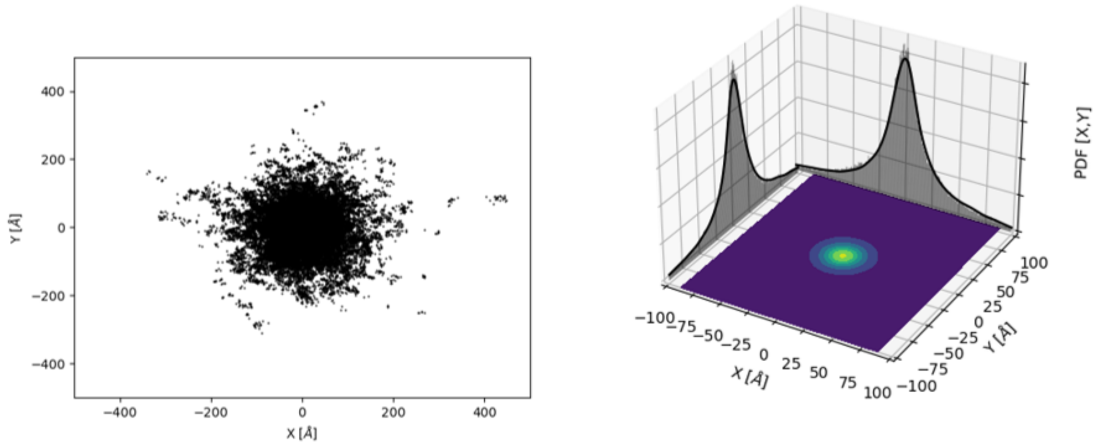

(a) (b)

Figure 4.5: SRIM Monte Carlo simulations of ion bombardment of 10,000 Ga+ ions incident at 30 keV on AlGaAs substrate. For sputtered atoms, the program will track the atoms until they leave the surface and mark the position on the plane of their last location before ejection. (a) Top-down scatter plots of the range of sputtered particle ejection locations. (b) Gaussian kernel density estimation with a bin of roughly 1 angstrom to derive the probability density function which is projected alongside the contoured KDE surface. Here, it is shown that the vast majority sputtered particles are emitted within a 10 nm radius from the point of impact.

ejected from within a 10 nm radius. The standard deviation of the lateral distribution is $\sim 4.3\ \mathrm{nm}$, which corresponds to the sputtered atom range $\mathrm{d_s}$. Similarly, to determine $\mathrm{d_c}$, the Ga ions are tracked and their coordinates are recorded when they come to rest in the sample. The mean lateral range of the implanted ions is given by $\mathrm{r}_l = \sum_i \mathrm{y}_i/N$, where y is the projection of the coordinates in the plane of the sample and N is the number of ions simulated [62]. For 30 keV Ga^+ ions in AlGaAs, r_l ~5.6 nm, which corresponds to the collision cascade range $\mathrm{d_c}$.

Based on the above analysis of 30 keV Ga^+ ions in AlGaAs, the sputtered atom range limits lateral resolution to $\sim 4\ \mathrm{nm}$ and intermixing (which causes broadening of interfaces in the sample) to $\sim 6\ \mathrm{nm}$. Given the ion beam diameter of $\sim 10\ \mathrm{nm}$ in the experiment, this is in excellent agreement with the measured resolution of $\sim 16\ \mathrm{nm}$ seen in Figure 4.1 **(c)**. The same agreement is found using other resolution measurement techniques on the same sample (see Appendix B.2).

This behavior proposes a critical and fundamental relationship between the resolution of any FIB-based technique and the minimum achievable signal or yield. Figure 4.3 **(a)** shows how the d50 probe size dominates the signal contribution at low dwell times allowing for high resolution imaging, but Figure 4.3 **(b)** shows the impact of the cascade on resolution measurement as more ion beam dose is accumulated. Even though the beam tail contributions are minimized through the short 500 ns dwell time at any given pixel, each pass of the beam results in surface removal and the acquired area begins to recede into the region of recoiled atoms of the cascade from the initial passes. At these depths, the atoms have become intermixed and have broadened the boundaries or the effective minimum distance between the two strips, impacting the resolution measurement vis-à-vis primary ion dose. The result from FIB-FS in Figure 4.1 is limited by this effect due to the fundamental yield of the Al atoms and the sensitivity of the hardware. In the measurement, the instrument settings and dwell time allow for probe sizes that should yield resolutions $\sim$10 nm, however, low signal-to-noise at the extreme conditions demand that a higher dose be used (11.6 pC/µm^2) to collect more sputtered atoms and the technique is pushed into a collision cascade-limited regime below the initially irradiated surface.

It is important to note that the ion beam diameter is limited by the virtual size of the ion source and the ion focusing optics (see Appendix A). In general, $\mathrm{d_p}$ increases with ion beam energy and reciprocal current, and it is a function of the ion species. These limitations are technological and continuously improve in modern FIB instruments. Conversely, the limitations imposed by sputtering and intermixing are fundamental. They are determined by the ion mass and energy, and by the masses and binding energies of atoms that make up the sample. However, systematic studies of the effects of ion mass and energy on lateral resolution are complicated by the fact that they affect not only $\mathrm{d_s}$ and $\mathrm{d_c}$, but also $\mathrm{d_p}$. This is, however, not the case for depth resolution, which is independent of $\mathrm{d_p}$. Hence, depth profiling elucidates the fundamental effects of ion species and energy on FIB-FS spatial resolution.

4.3 Depth Resolution

A demonstration of FIB-FS depth profiling using a sample comprised of three GaAs quantum wells embedded in AlGaAs is shown in Figure 4.6. A TEM image of the sample is shown in Figure 4.6 **(a)**. The quantum wells have thicknesses of 3.5, 5 and 8 nm. Figure 4.6 **(b)** is a 3D FIB-FS image of the sample generated by summing, at each pixel, the FIB-FS Al emissions at 394.4 nm and 396.2 nm (see Appendix B.2) excited by a 2 keV, 3.2 nA Ga$^+$ beam collected with the PMT, UV-VIS optics, and Al filter. The 3D image stack consists of 2,467 2D FIB-FS maps, each collected in a single scan lasting 1.13 s and a lateral field width of

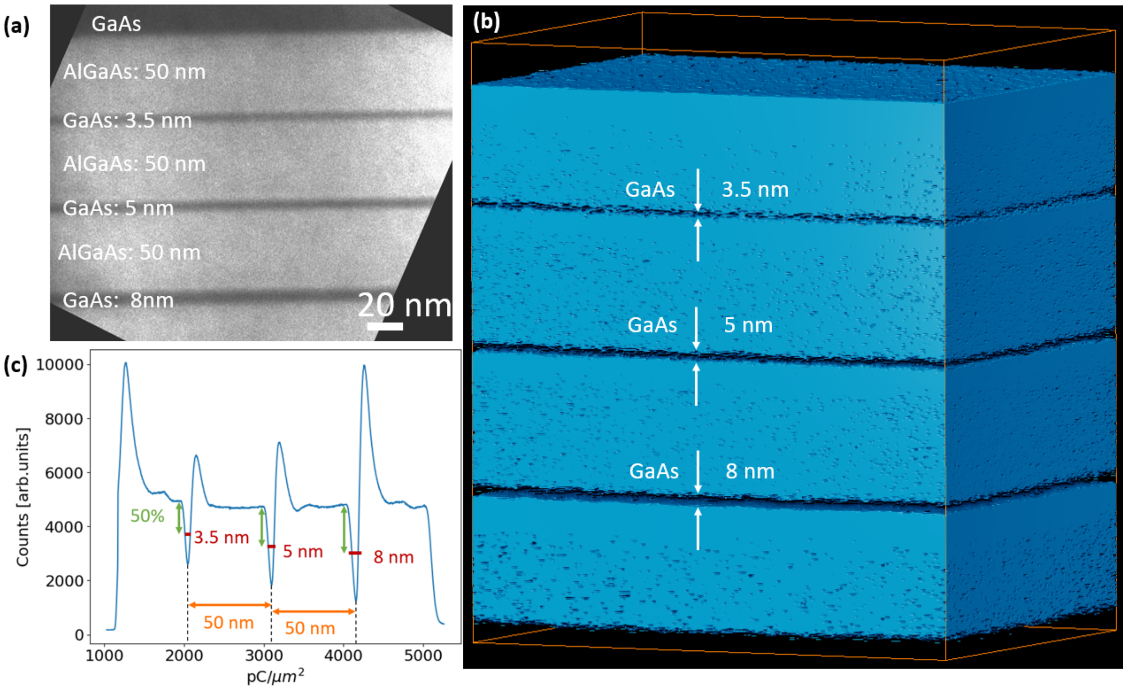

Figure 4.6: FIB-FS depth-profiling and 3D imaging of a layered quantum well structure. **(a)** TEM image of a quantum well heterostructure comprised of three GaAs quantum wells in AlGaAs. The quantum well thicknesses are 3.5, 5 and 8 nm. **(b)** 3D volume reconstruction of the quantum well heterostructure generated by summing, at each pixel, the FIB-FS Al emissions at 394.4 nm and 396.2 nm, excited by a 2 keV Ga^+ beam (1.68 pC/µm^2 per slice). All three GaAs quantum wells are clearly resolved in the image (the lateral field width is 48 µm). **(c)** FIB-FS Al line profiles of the heterostructure in **(b)**. The center-point of the minima of the quantum wells are marked by a dashed line. A scale bar is draw between the first and second minima and is shown to be identical for the second and third. A second scale bar is made at the location of the 50% loss of Al signal and attributed the 3.5 nm thickness of the first quantum well. The bar is scaled according to the thicknesses of the subsequent quantum wells and placed over the respective 50% loss. The difference in perceived width is due to the preferential sputter rate difference between the AlGaAs and GaAs layers that increases with quantum well thickness and ion dose.

50 µm. The first 600 frames are removed to ignore most of the 260 nm GaAs top layer, while each frame is cropped by 1 µm at the outer rim to remove crater edge/wall effects [195]. All three quantum wells are clearly resolved in the 3D FIB-FS image, illustrating qualitatively the outstanding sensitivity and resolving power of the technique.

In order to quantify the depth resolution and measure dependencies on ion mass and energy, the NIST Standard Reference Material (SRM) 2135c is employed [196]. SRM 2135c is a sputter depth calibration standard comprised of alternating Cr and Ni layers (see Appendix C). A 1D depth profile is measured with VIS-NIR optics across a Ni-Cr interface by collecting the Cr FIB-FS signal as a function of the ion dose used to sputter the sample, and resolution is defined as the thickness of the measured interface. Specifically, resolution is the full-width-at-half-maximum (FWHM) of the first derivative of the line spread function corresponding to a Cr FIB-FS signal rise time of 15%–85%. Ion irradiation was performed with Ga^+, Xe^+ and O^+ beams starting at 30 keV and lowering the landing energy at each interval. For each energy, profiling was collected from a 70x70 µm box mill with 1 µs dwell time at 2.2 ± 0.4 pA/µm^2, 3.0 ± 0.6 pA/µm^2 and 15.2 ± 0.5 pA/µm^{2}for Ga^+, Xe^+ and O^+, respectively.

An overview of the analysis is shown in Figure 4.7. The Cr spectral signals are integrated, and their count values are first plotted against the time-accumulated dose of the mill and then normalized. The first transition from Ni to Cr is sliced from the dataset for analysis. Since travel through the elemental layer is variable by the sputtering rate, the line spread profile must be converted from a time/ion dose domain to the spatial depth domain for comparison. The transformation is accomplished under two assumptions: that the midpoint of the Ni and Cr layer of the first transition of the FIB-FS data matches the midpoints of the Ni and Cr layers in the NIST data and that the rate of change through the layer is directly proportional to the percent change in the elemental composition by sputter rate. The sampling rate of the acquisition remains constant throughout the transition, so the transformation results in the Ni data points frequency being spread out in z-space and the Cr being compressed. For consistency of alignment to the midpoint of the layer, a fitting algorithm was used which uses a composite function of a Gaussian and square wave during the peak and valley of the transition. The second derivative of the composite fit is used to determine the edges of the transition and the midpoint between the two minimum values is used as the midpoint of the Cr and Ni layers. The data is then fitted to a standard cumulative density function (CDF) and the derivative is taken both numerically and empirically. The full width at half maximum (FWHM = $2.355 * \sigma$) is found, correlating to a 15%-85% rise time transition between the layer. The same is repeated for the Auger sput-

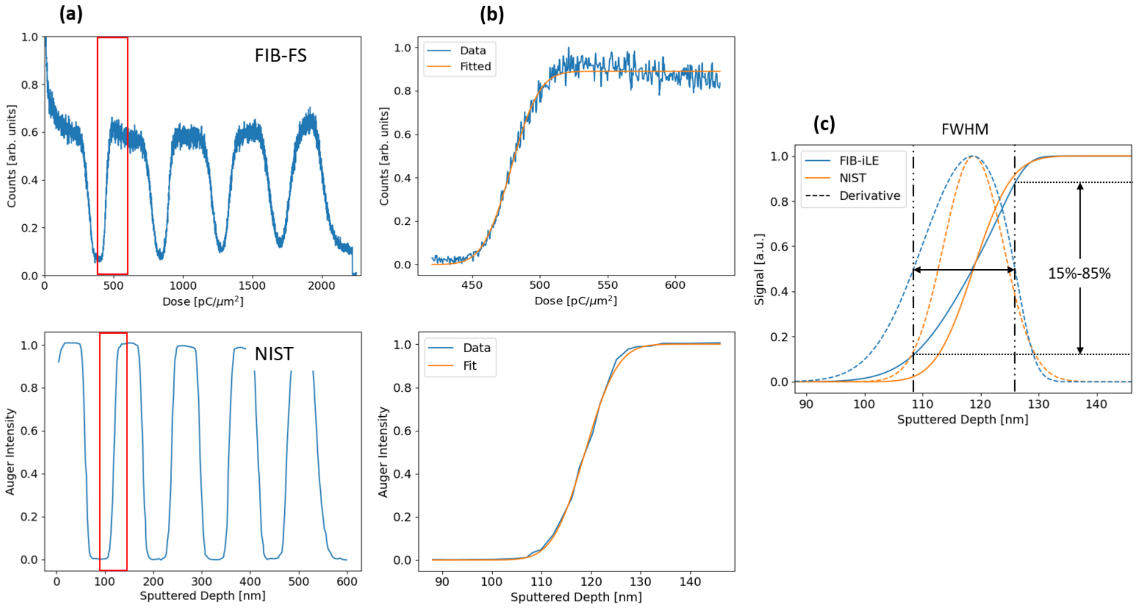

Figure 4.7: Method used to calculate the depth resolution for all primary ions on NIST SRM 2135c, demonstrated using 8 keV Ga$^+$ irradiation dataset. The resolution value is determined by taking the full width at half max of the first derivative of the line spread function **(b)** of the profile of the first Ni-to-Cr layer transition shown in **(a)** and compared to the profile provided by the certificate. The full width at half maximum of the first derivative of the FIB-FS transition profile is found, corresponding to the 85%-15% rise time to give the resolving power of the transition in nm shown in **(c)**. The resolution of the 8 keV profile shown is 18.07nm compared to the 12.2 nm NIST reference (see Appendix C).

ter depth profile given in the SRM 2135c certification [196] for comparison (see Appendix C).

Figure 4.8 shows the results of the depth resolution measurements. Starting with 2 keV Ga$^+$, the FIB-FS depth profile resolution is 12.8 nm. This is in excellent agreement with a reference measurement of 12.2 nm obtained from an Auger electron spectroscopy depth profile generated using 1 keV Ar$^+$ ions (see Figure 4.7). Increasing the Ga$^+$ ion energy to 30 keV reduced the measured depth resolution to 34.8 nm and changing the ion species to 30 keV Xe$^+$ increased it to 25.6 nm. These trends are expected since the ion range increases with energy and decreases with ion mass, unless the implanted ions are chemically active and modify the binding energies of atoms in the sample, as in the case with O$^+$ irradiation [197, 198]. This result confirms that the FIB-FS spatial resolution is limited fundamentally by the volume excited by the ions used to irradiate the sample.

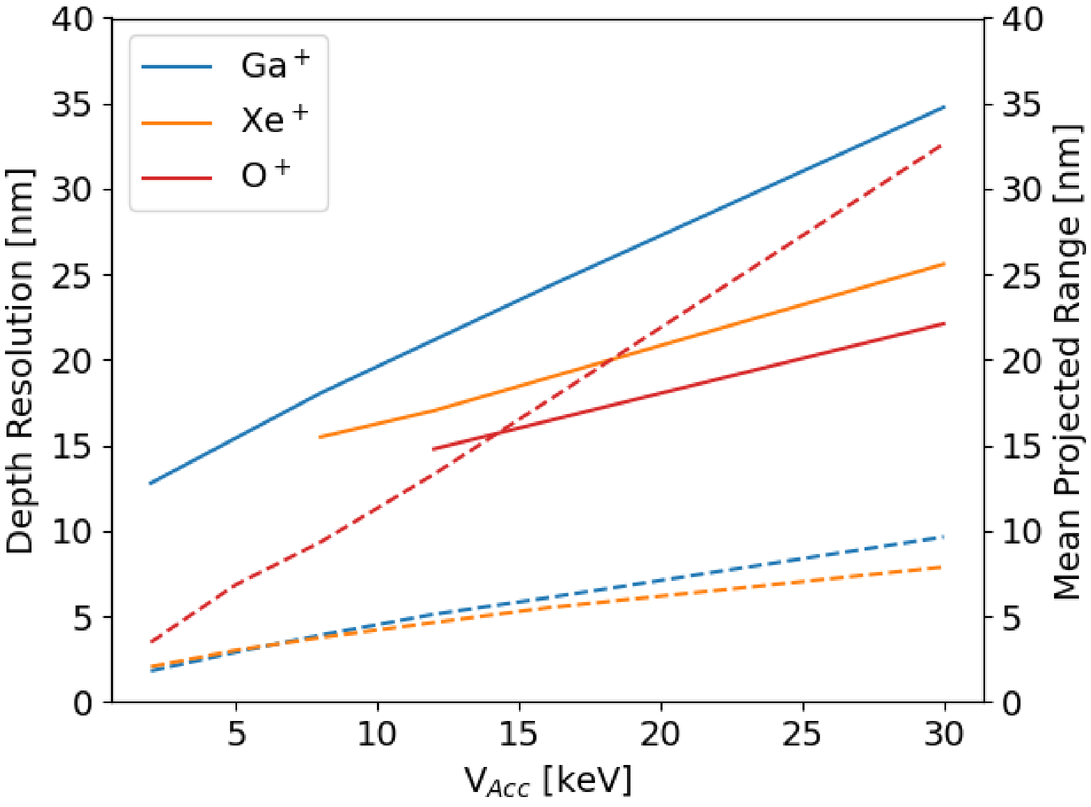

Figure 4.8: Measured FIB-FS depth resolution (solid line) of the transition between the first Ni-to-Cr transition graphed as a function of beam accelerating energy alongside the corresponding mean projected range in Ni (dashed line) predicted by TRIM. The result is in qualitative agreement with sputter profiling studies performed with SIMS showing strong correlation between the incident ion range and the measured resolution. The exception is the O^+ bombardment for which TRIM does not account for chemical effects during irradiation which reduces the range through formation of oxide and increased lattice binding energy.

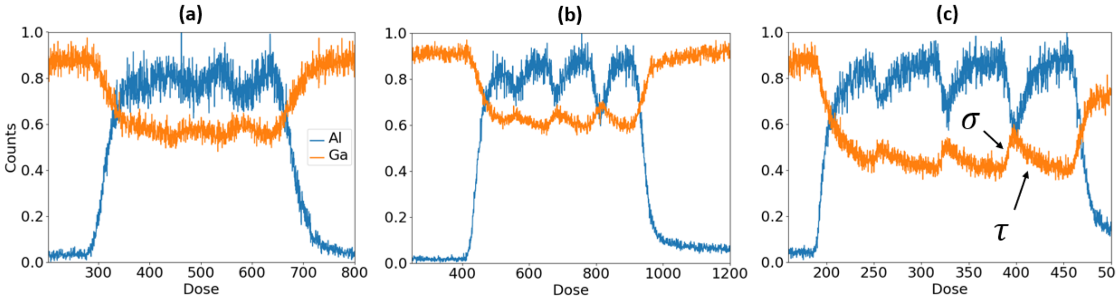

Figure 4.9: Depth profiles of the quantum well structure shown in 4.6 taken at different ion landing energies and ion masses showing the impact of collisional mixing on the ability to resolve the layers. **(a)** Depth profile taken with 30 keV Ga$^+$ and 9 nA. The 3.5 nm and 5 nm are smaller than the interaction volume of the 30 keV beam and the layer is not able to be seen in the profile. **(b)** Depth profile taken with 8 keV Ga$^+$ and 11.2 nA. The 3.5 nm is just barely visible while the others are clearly seen. **(c)** Depth profile taken with 8 keV Xe$^+$ and 6 nA showing all layers. The slope of the profile into and out of each layer marked by σ and τ, respectively, are different for each ion mass and ion energy, demonstrating the complicated interactions of ion-mixing, preferential sputtering, and knock-on effects at the boundary.

4.3.1 Discussion

The depth resolution is limited fundamentally by intermixing caused by ion impacts shown in Figure 4.8, however, this becomes even more evident when trying to resolve layers smaller than the interaction volume of the primary beam. This effect is readily seen in the 1D Al and Ga FIB-FS depth profiles shown in Figure 4.9. Here, the quantum well stack is profiled using different ion beam energies and masses. In the first graph of Figure 4.9 **(a)**, the sample is profiled using the 30 keV Ga$^+$ beam and only the last quantum well is barely able to be seen. When the energy drops to 8 keV in **(b)**, the interaction volume of the ion beam beneath the irradiating surface is decreased and less intermixing along the layer boundary occurs allowing all three quantum wells to be resolved. When the mass is increased by using Xe$^+$ at the same energy in **(c)**, the interaction volume is decreased even further and all three layers are more easily seen in the depth profiles.

An interesting phenomena appears at the interfaces of the AlGaAs and GaAs layers. When entering or exiting each GaAs layer, the leading and trailing line slopes σ and τ (shown in the plot) are non-zero and distinct. Because the range of the ions is greater than the boundary transition of the AlGaAs layers, atomic displacements in the sample and intermixing causes broadening of the interfaces.

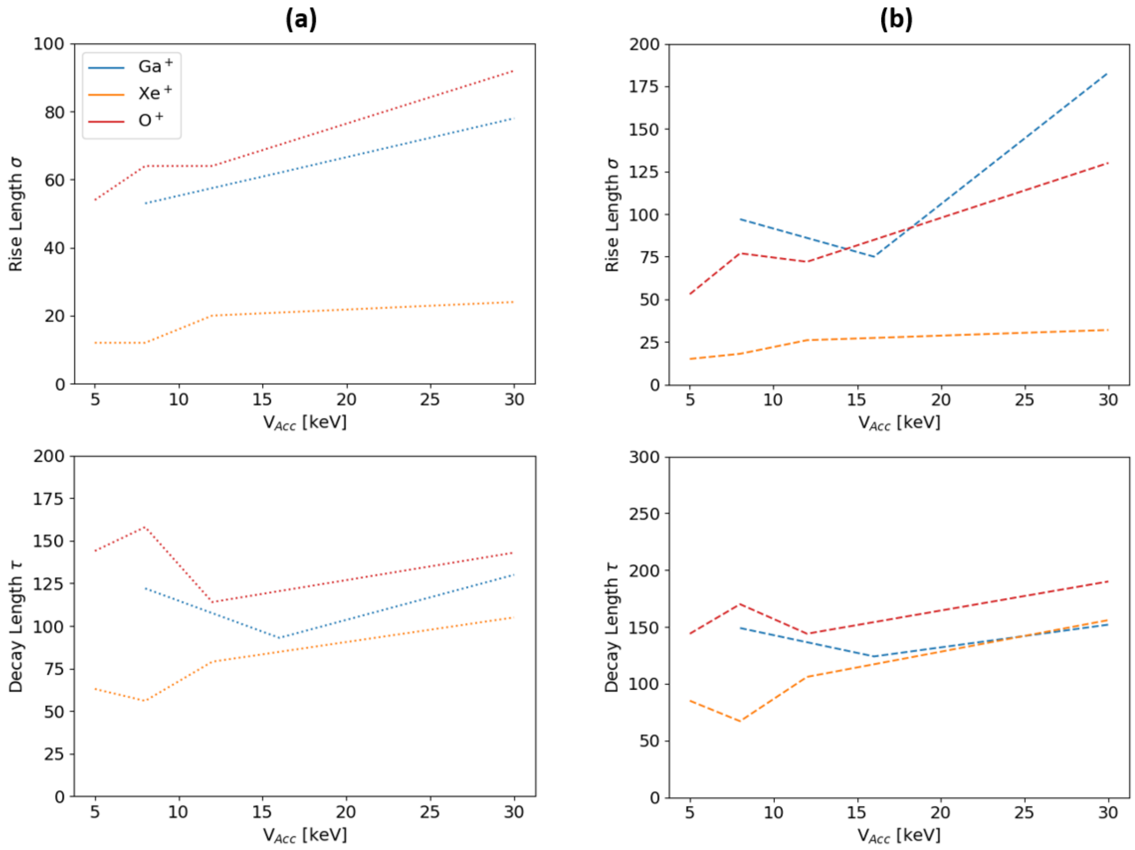

Figure 4.10: Comparison of the rise length factor σ_i and decay length factor τ_i as a function of beam energy across multiple primary ion beams of the 5 nm layer (column **(a)**) and the 8 nm layer (column **(b)**). The marker atom (Ga) being traced through sputter profiling in the AlGaAs layer exhibits different behavior under different systems. The rise and decay profiles both scale with incident primary ion energy, but while the rise length σ_i seems to scale with mass, the decay length factor τ_i is relatively independent of mass.

This is only one factor that contributes the depth profiling analysis capabilities in the FIB.

Altogether, there are 5 main attributes of the ion-solid interactions that can impact the resolving power of a depth profiling technique and result in the differences between primary ions: depth of origin from sputtered atoms emitting photons, ion beam mixing/interface broadening, preferential sputtering, surface texturing/topography formation, and instrumentation. Depth of origin has been studied extensively for sputtered atoms and is known to be in the topmost atomic layers of any material [55]. Instrumentation parameters such as dwell time, sampling frequency, primary ion beam spot size, sputtered signal from the edges, and quantum efficiency are the first order of limitation, but are easily mitigated. This leaves ion beam mixing, surface topography, and preferential sputtering to result in the most fundamental limitations for FIB profiling.

On its own, surface topography will result in increased sputtering at edges and features, leading to the formation of islands or craters that expose signal from layers above or below the target plane and results in mixed/blended signals. In most cases, this is easily resolved with sufficient sample preparation and cleaning or by cropping the edges of the profiled region. Preferential sputtering, however, is a result of the inherent differences in sputtering rates between two different elements from energy transfer mechanisms discussed in section 2.2. In profiling applications, it leads to differences in endpoints for two elements in the same compound, different perceived thicknesses for layers of differing composition when acquired under the same sampling frequency, and can produce artifacts of enhanced or decreased emission at interstitial boundaries [199–203]. An example of this type of artifact is shown in Figure 4.6 **(c)** where an increase in Al signal is seen at the leading edge entrance of the AlGaAs layer where preferential sputtering and matrix effects increase the Al signal at the boundary until a steady state is reached further in the layer. While troublesome, these effects are commonly observed in SIMS and FIB milling applications and can be mitigated through optimized experimental conditions such as primary energy and flux, as well as through computational post processing corrections [204–206].

In cases where both layer thickness and preferential sputtering rates are known and corrected for, only the unavoidable limitation of ion mixing remains. Sputter profiling experiments with SIMS [195,198,207–210] have investigated this behavior using tracer elements and have found that such mixing profiles are determined by the atom dislocation and surface recession rates within the collision cascade. Two major features of the profile that contribute to analysis complications are (i) the rate of change between entering a new layer material described by the leading edge of the profile and (ii) the rate of change when exiting each layer described by the trailing edge. The onset into thin layers is described well with a Gaussian function:

$$G_i(x) = \frac{A}{\sigma_i\sqrt{2\pi}}\exp\left[-(x-\mu t)^2/2\sigma_i^2\right] \tag{4.1}$$

while the trailing edge is typically described by exponential decay of species i:

$$I_i(x) = A\exp\left[-x/\tau_i\right]. \tag{4.2}$$

Contributions from these limitations mark a key difference between sensitivity and resolving power for which Figure 4.9 is an example. Different rates at the leading and trailing edge of the AlGaAs layer are easily seen and mixing of the layers as a result of recoiled atoms appear to extend the 3.5 nm GaAs layer well into the 50 nm AlGaAs layer, making it difficult to know when the layer ends.

Comparisons of the rise length factor σ_i and decay length factor τ_i fitted from equations 4.1 and 4.2 for this sample under different ion species and energies are shown in Figure 4.10 for the 5 nm and 8 nm layer transitions. The results show that both the rise and decay profiles scale with incident primary ion energy, in agreement with prior findings in SIMS [55, 197, 198, 203, 207, 208]. While a similar trend might be expected for primary ion beam mass, such a dependency is only readily observed for the rise length σ_i while the decay length factor τ_i tends to have similar values regardless of mass. Contributions from preferential sputtering to the rise factor followed by the transition to a steady state of removal can help explain this dependence, however, formalization of the complete picture remains an active area of investigation for all FIB profiling applications.

4.4 Detection Limits

All elements in the periodic table are fluorescent, and detection of trace elements present in the parts-per-million range should be feasible based on prior work with broad-beam ion sources [31, 136]. To confirm this, methods established in SIMS [211, 212] are adopted for FIB-FS to demonstrate minimum detection limits of 3.9 ppm and 0.8 ppm for K and Li, respectively.

Two NIST SRM samples with certified mass fractions of dozens of elements were examined using a 30 keV Xe^+ beam to explore the sensitivity and detection limits of the FIB-FS technique.

Reference material SRM 93a [213] consists of 12 compounds embedded homogeneously in a borosilicate glass matrix. The matrix is comprised of 12.56% $\mathrm{B_2O_3}$, 80.8% $\mathrm{SiO_2}$, 3.98% $\mathrm{Na_2O}$, and 2.28% $\mathrm{Al_2O_3}$. However, of interest are trace levels of $\mathrm{K_2O}$ and MgO which have concentrations of 0.014% and 0.005% by weight, respectively. FIB-FS spectra showing K and Mg emissions are shown in Figure 4.11 and 4.12. Both UV-VIS and VIS-NIR optics were used for maximum efficiency, while bandpass filters and high-resolution gratings were employed to resolve the lines and to remove second order peaks and background emissions. Multiple peaks from each element were detected (K: $3p^6 4p\,(^2\mathrm{P}^{\mathrm{o}}_{\frac{3}{2},\frac{1}{2}}) \rightarrow 3p^6 4s\,(^2\mathrm{S}_{\frac{1}{2}})$ at 766.5 nm and 769.9 nm, Mg: $3s3p\,(^1\mathrm{P}^{\mathrm{o}}_1) \rightarrow 2p^6 3s^2\,(^1\mathrm{S}_0)$ at 285.2 nm and $3s3d\,(^3\mathrm{D}_{1,2,3}) \rightarrow 3s3p\,(^3\mathrm{P}^{\mathrm{o}}_{0,1,2})$ at 382.9 nm, 383.23 nm, and 383.83 nm).

Reference material SRM 612 [214] consists of 61 elements embedded homogeneously in a glass matrix, with weight fractions in the range of 10 to 80 mg/kg. The matrix is comprised of 72% $\mathrm{SiO_2}$, 14% $\mathrm{Na_2O}$, 12% CaO, and 2% $\mathrm{Al_2O_3}$. As in the case of SRM 93a, VIS-NIR optics, selective filters, and high-resolution gratings were used to delineate emissions from specific trace elements. This sample is of interest due to the presence of Li at a concentration of ~ 40 ppm. Figure 4.13 shows FIB-FS spectra with lines from Li transitions $1s^2 2p\,(^2\mathrm{P}^{\mathrm{o}}_{\frac{3}{2},\frac{1}{2}}) \rightarrow 1s^2 2s\,(^2\mathrm{S}_{\frac{1}{2}})$ at 670.77 nm and 670.8 nm and $1s^2 3d\,(^2\mathrm{D}_{\frac{3}{2}}) \rightarrow 1s^2 2p\,(^2\mathrm{P}^{\mathrm{o}}_{\frac{3}{2},\frac{1}{2}})$ at 610.35 nm and 610.36 nm.

For SIMS, detection limits and sensitivity (detected atoms/cm^3) are typically quantified by converting secondary ion counts to atomic density using calibration standards [211,212]. Following an analogous approach, the atomic concentration n_i (cm^{-3}) of analyte i in matrix m can be defined by:

$$n_i = \frac{P_i}{P_m}(\mathrm{RSF})_i \tag{4.3}$$

where P_i and P_m are the photon counts from analyte i and matrix m, respectively. RSF is a relative sensitivity factor that relates photon counts to atomic density. It can be determined from a calibration sample with a known atomic density n_m (cm^{-3}) by comparing the ratio of photon yields β (photons/sputtered atom) of analyte i and matrix m such that (RSF) $= n_m(\beta_m/\beta_i)$. Equation (4.3) can then be written in terms of fractional concentrations C_i and C_m:

$$\frac{C_i}{C_m} = \frac{P_i}{P_m}\frac{\beta_m}{\beta_i} \tag{4.4}$$

or for minimum concentrations:

$$\frac{C_{i(\mathrm{min})}}{C_m} = \frac{P_{i(\mathrm{min})}}{P_m}\frac{\beta_m}{\beta_i} \tag{4.5}$$

Hence, by using a standard of known composition, β_m/β_i can be found by comparing P_i to P_m where P_m is the photon count rate from matrix element m present at fractional concentration C_m.

For SRM 612, the photon count rates from Li transitions $1s^2 2p\,(^2\mathrm{P}^{\mathrm{o}}_{\frac{3}{2},\frac{1}{2}}) \rightarrow 1s^2 2s\,(^2\mathrm{S}_{\frac{1}{2}})$ at 670.77 nm and 670.8 nm are compared to those of Ca transitions $3p^6 3d4p\,(^3\mathrm{F}^{\circ}_2) \rightarrow 3p^6 3d4s\,(^3\mathrm{D}_{1,2})$ at 649.38 and 649.96 nm. Substituting the conversion rate from equation (4.4) into (4.5), where $P_{\mathrm{Li(min)}}$ is determined by the limit of detection defined as the sum of the limit of the background and $1.645 * \mathrm{std}(P_{\mathrm{Li}})$, yields $C_{\mathrm{Li(min)}} = 0.8$ ppm.

For SRM 93a, the photon count rates from K transitions $3p^6 4p\,(^2\mathrm{P}^{\mathrm{o}}_{\frac{3}{2},\frac{1}{2}}) \rightarrow 3p^6 4s\,(^2\mathrm{S}_{\frac{1}{2}})$ at 766.5 nm are compared to that of the Si transition $3s^2 3p4s\,(^1\mathrm{P}^{\mathrm{o}}_1) \rightarrow 3s^2 3p^2\,(^1\mathrm{S}_0)$ at 390.55 nm observed as the second order at 781.1 nm. Given the fractional concentrations $C_{\mathrm{K}} = 0.0116\%$ and $C_{\mathrm{Si}} = 37.77\%$, $C_{\mathrm{K(min)}} = 3.9$ ppm.

The Mg detection limit was not quantified due to the presence of the intense broadband emission seen in Figure 4.12. The spectrum is shown to illustrate qualitatively the ability of FIB-FS to detect Mg present at a concentration of 50 ppm.

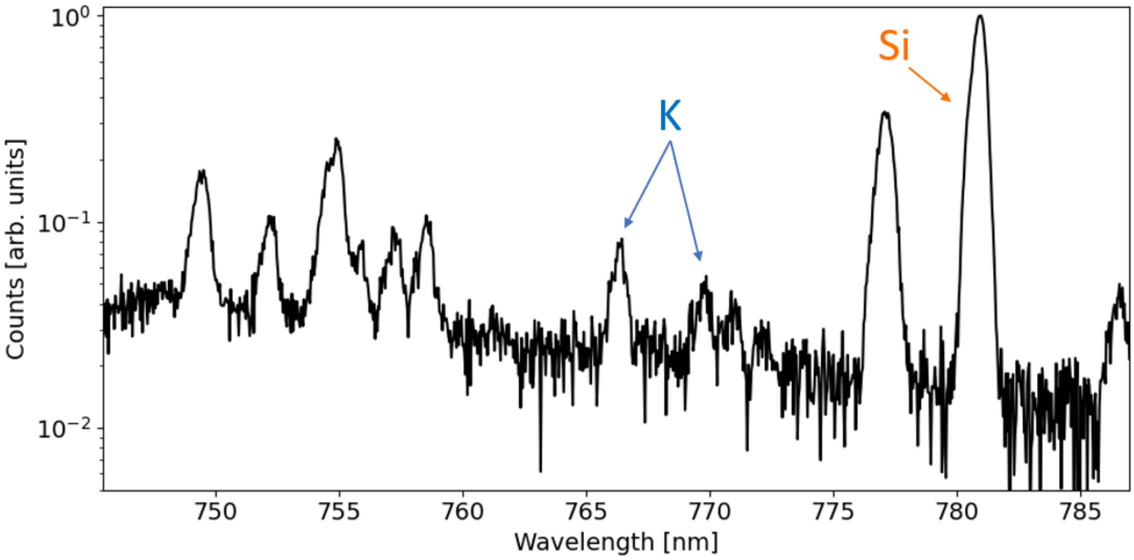

Figure 4.11: FIB-FS spectrum collected from NIST SRM 93a showing the detection of potassium (peaks at 766.5 nm and 769.9 nm) present at a relative concentration of 140 ppm (30 keV Xe^+ 375 pC/µm^2).

For matrices in which the atomic density n_m is known, n_i can be found and written as a function of the sputtered volume V [36]:

$$n_i = \frac{P_i}{V\beta_i} \tag{4.6}$$

That is, sensitivity and sputtered volume (i.e., the achievable spatial resolution) are inter-related. In the case of nanostructured materials, sensitivity is limited by the volume that contains the analyte of interest. Moreover, since sensitivity is inversely proportional to the volume removed by sputtering, it is therefore a function of the required spatial resolution.

A useful characteristic of FIB-FS is the dynamic range and modularity of the detection system compared to mass spectrometers. The spectral response can be modified with filters and gratings to preferentially increase or decrease the effective dynamic range, and a sputtered atom can emit photons at a number of wavelengths and efficiencies. This can be beneficial for comparing concentrations by providing multiple opportunities to compare matrix and analyte peaks if a particular pair are beyond the dynamic range of the detector.

In general, ultimate FIB-FS sensitivity will be determined by the collection efficiency of the detection chain, the experimental conditions available (beam current, exposure time, filters, etc.), the concentration of elements with nearby spectral peaks (dynamic range), the required spatial resolution, and the inherent photon yield (photons/sputtered atom) of the element to be detected. In the case of FIB-FS, the highest photon yields occur in light alkali and alkaline earth

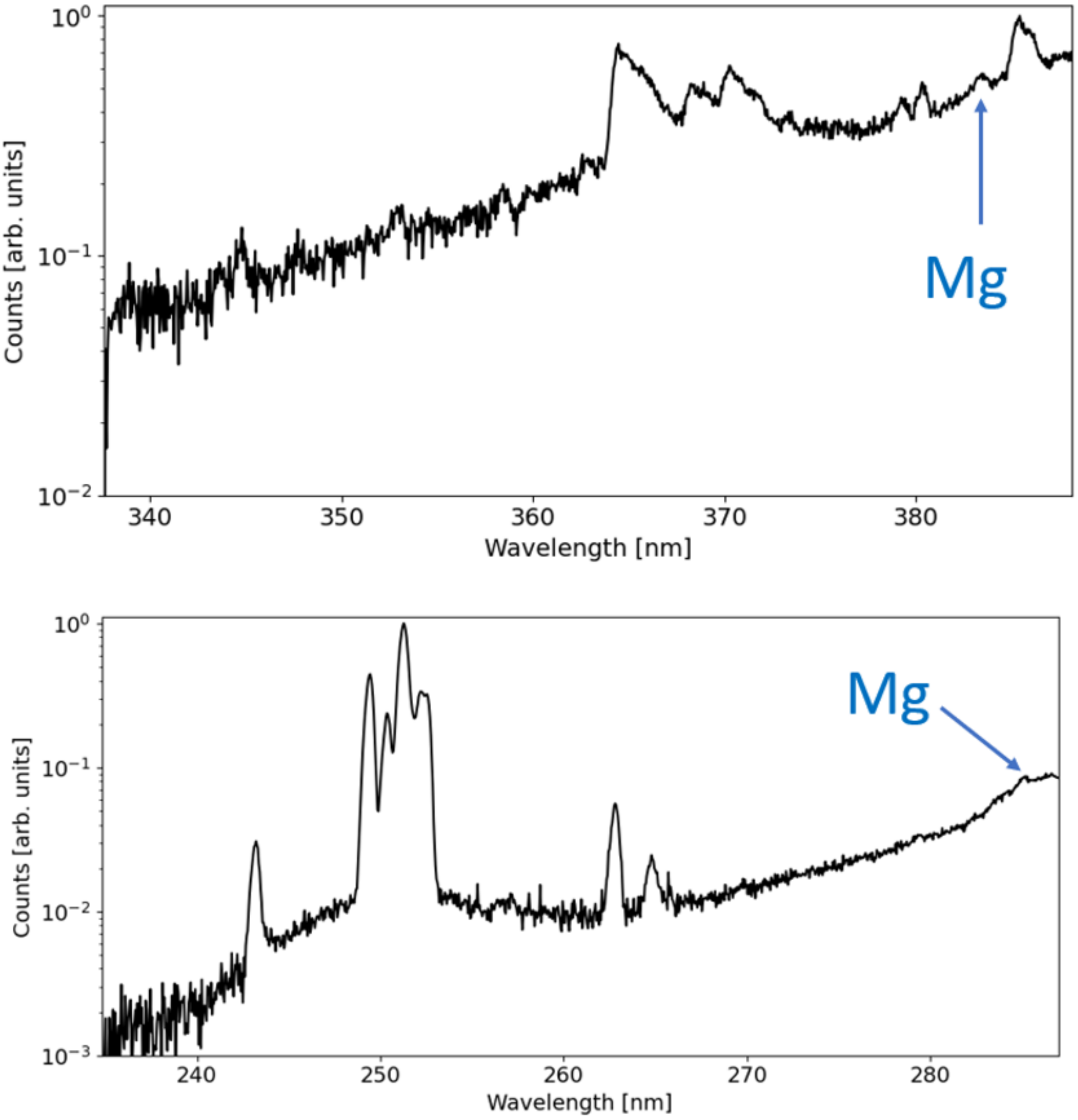

Figure 4.12: FIB-FS spectrum collected from NIST SRM 93a showing the detection of magnesium (peaks at 383 nm and 285 nm) present at a relative concentration of 50 ppm (30 keV Xe^+ 375 pC/µm^2).

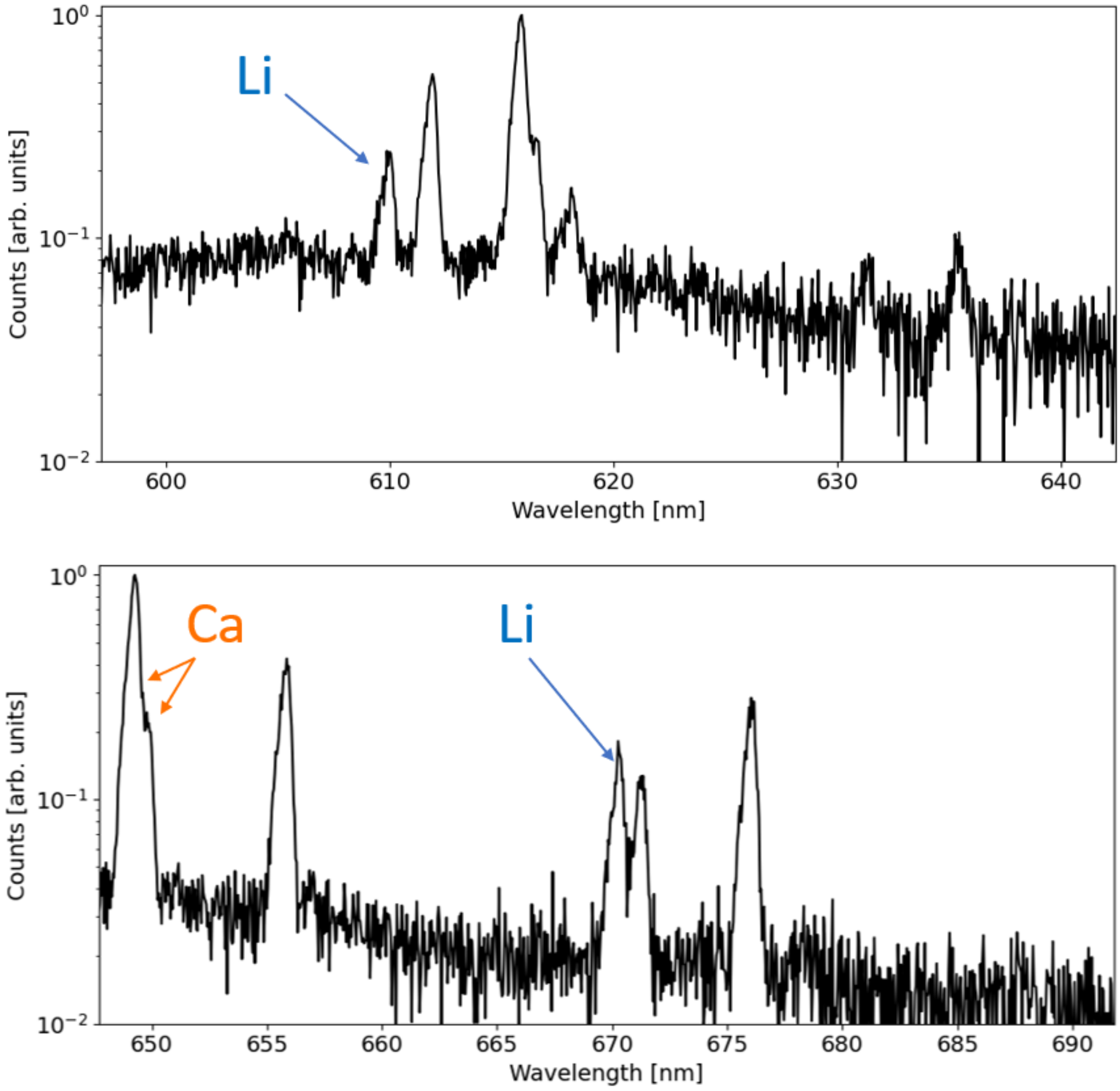

Figure 4.13: FIB-FS spectrum collected from NIST SRM 612 showing the detection of lithium (peaks at 610 nm and 670 nm) present at a relative concentration of 40 ppm (30 keV Xe^+ 37.5 and 18.7 pC/µm^2 for the top and bottom spectra, respectively).

metals [136], making the technique favorable for applications like Li ion battery research and complementary to techniques such as EDX. However, these values are not universal - the emission efficiencies are influenced by sample matrix effects and electron transfer processes that vary with surface electronic structure, vacuum pressure, incident ion energy, angle, and flux [27, 79, 89, 163] discussed in Chapter 2. In nanostructured materials, sensitivity also depends on ion dose, and is limited ultimately by sputtering as it removes the material that is being analyzed.

4.5 Conclusions

A new technique of elemental analysis has been developed in FIB-FS. The capabilities of the technique enabled by the optical design and implementation onto a FIB make it suitable for 3D tomography and elemental analysis at the nanoscale. High spatial resolution, depth resolution, and sensitivity to detect trace level-impurities have reinvented the way photons may be used in ion beam and charged particle microscopy. Moreover, the analysis shows that, fundamentally, the resolution capabilities of the FIB-FS technique are not limited by processes other than ion-solid interactions. This makes FIB-FS highly appealing as a nanoscale analysis technique that is intrinsically compatible with FIB-based nanofabrication methods.

Chapter 5

FIB-FS Application: Li Ion Batteries

5.1 Introduction

Detection of lithium, hydrogen, and trace metal dopants is critical to battery research and development, yet existing analytical methods such as energy dispersive x-ray spectroscopy (EDX), electron energy loss spectroscopy (EELS), or atom probe tomography (APT) fall short in providing a practical, streamlined solution. The nature of the low energy characteristic x-ray emission from Li K at 55eV [215] combined with its low fluorescence yield ω_K of 1.06x10^{-4} photons per ionization [216] render traditional EDX virtually useless since any signal is either absorbed before leaving the sample or absorbed in the window of the detector. The recent rollout of sensitive windowless EDX detectors has enabled detection of lithium [217], although with difficulty and confusion around the emission mechanism behind the Li K lines [215] while hydrogen detection remains physically impossible. Furthermore, trace elements and contaminants - particularly those confined to the surface or topmost layers of the region of interest - can go undetected by EDX due to the large interaction volume of the electron beam and depth of origin of the x-ray generation.

Time of flight secondary ion mass spectroscopy (ToF-SIMS) has emerged as a powerful solution in this field with impressive analysis on $LiCoO_2$ [17,18,218–221], $Li_xMn_yCo_zO_2$ [222,223], and $LiFePO_4$ [224], although it is not without its own challenges. Large and complex data collection [36, 225] with mass interferences and overlaps [226] often require experienced operators or spectrometrist oversight, while matrix effects and sample charging complicate signal collection and acquisition [227]. Hence, there is continued interest in new characterization techniques, particularly ones that are cheaper and compatible with processing methods and non-destructive sample preparation [18–20].

The FIB-FS technique has high 3D spatial resolution, high sensitivity and the ability to detect light elements. Moreover, the technique is inherently compatible with FIB nanofabrication and processing techniques, which have matured into versatile methods used broadly for direct-write processing of nanostructured materials [21–26]. FIB-FS is complementary to electron beam techniques such as EDX which are often employed on FIB-SEM systems, where its versatility in high resolution imaging and sensitivity for Li and H detection allow it to bridge the gap that exists for detection of these elements. The following sections demonstrate these capabilities, deploying a novel method in the coupling of traditional EDX with FIB-FS that enables full battery characterization not otherwise found with existing techniques.

5.2 Cathode Analysis

The first sample analyzed is a lithium-nickel-manganese-cobalt-oxide (NMC) cathode, of form Li(Ni$_x$Mn$_y$Co$_z$M'$_m$)O$_2$ where M' denotes dopants of Fe, Al, Zr, and Mg at 0.02 at.% with $x + y + z + m = 1$. EDX yields a good understanding of the Ni/Mn/Co/O bulk chemical composition and its spectral signals present a general understanding of the base metal structure. Maps of the sample are shown in Figure 5.1. The map was taken with an EDAX Octane Elite Plus SSD detector with a silicon nitride window, using a SEM energy of 20 keV and a total dose of 573 pC/µm^2. Unfortunately, the most important features of interest are missed: namely Li, H, and trace metal dopant distributions. Lithium mobility and transfer between electrodes is the core process for generating electric power in the battery, so visualizing the lithium distribution within cathode and anode structures becomes critical to study its interaction during development and failure analysis. Similarly, detection and distribution of hydrogen in NMC cathodes is of interest when pointing towards sites of electrolytic infiltration and decomposition. Ni$^+$ sites in particular have been shown to cause solvent hydrolysis from (OH)$^-$, leading to cracking and cation mixing and resulting in capacity fading and ultimate battery failure [228, 229]. EDX remains fundamentally blind to H detection and without a windowless detector is unable to detect Li. FIB-FS, however, shows the results from Li 2D and 3D maps as well as H from a cross-section of the NMC cathode with ease in Figure 5.2. Of interest is the FIB-FS H map showing a particle is rich in H which could likely be a candidate site for electrolytic decomposition or compromised Ni$^+$ site.

The maps in Figure 5.2 are generated from the Li doublet $1s2p(^2\mathrm{P}^o_{\frac{1}{2},\frac{3}{2}}) \rightarrow 1s2s(^2\mathrm{S}_{\frac{1}{2}})$ transition at $\lambda = 670.776\mathrm{nm}$ & $\lambda = 670.791\mathrm{nm}$ shown in Figure 5.3. The hydrogen map was made from the first transition H-α in the Balmer series at

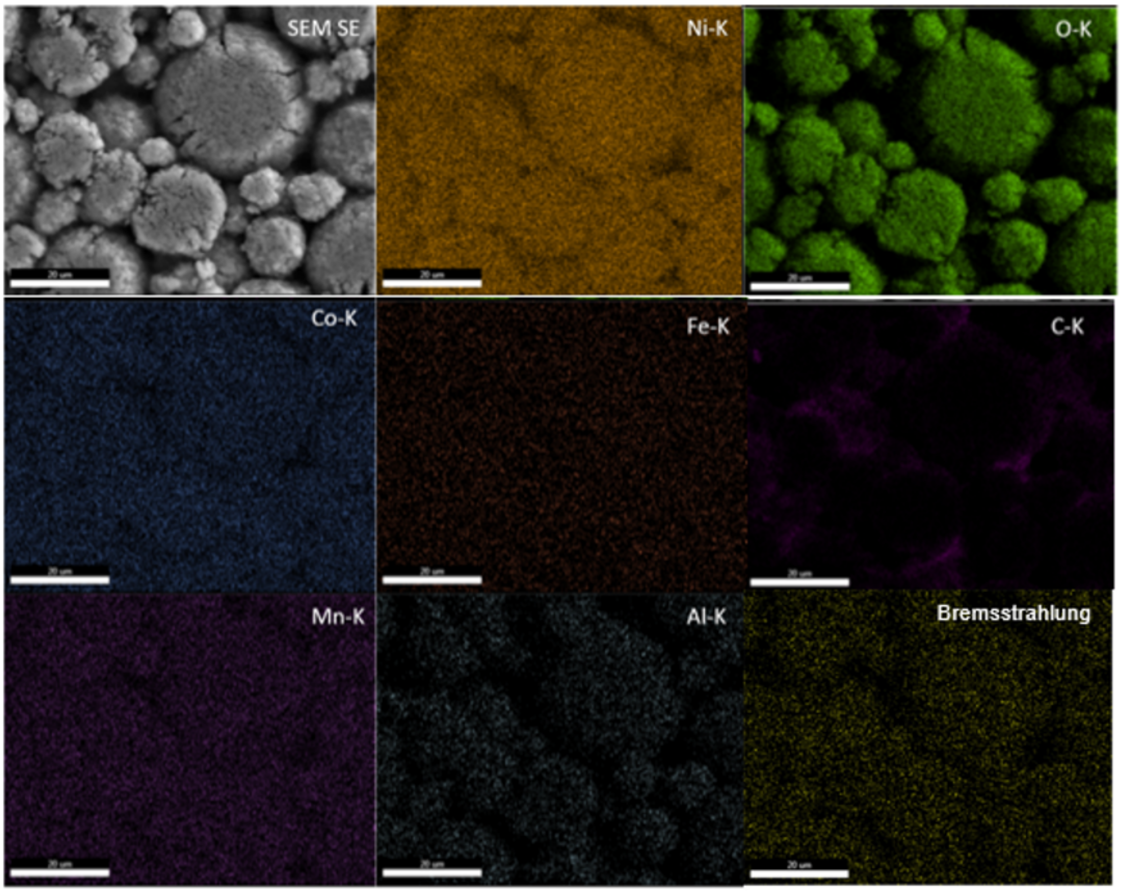

Figure 5.1: EDX maps of a Li ion battery NMC cathode from 573 pC/µm^2 20 keV SEM. Some bulk chemical properties of Ni, Mn, and Co can be seen in the cathode under EDX, but the spatial resolution under the imaging conditions are limited compared to the FIB-FS maps of the same sample. The increased performance of the FIB-FS at the same dose is attributed to the surface sensitivity of the ions, which maintains an interaction volume up to order of magnitude smaller than that of the SEM at these energies. A background Bremsstrahlung map is provided for comparison.

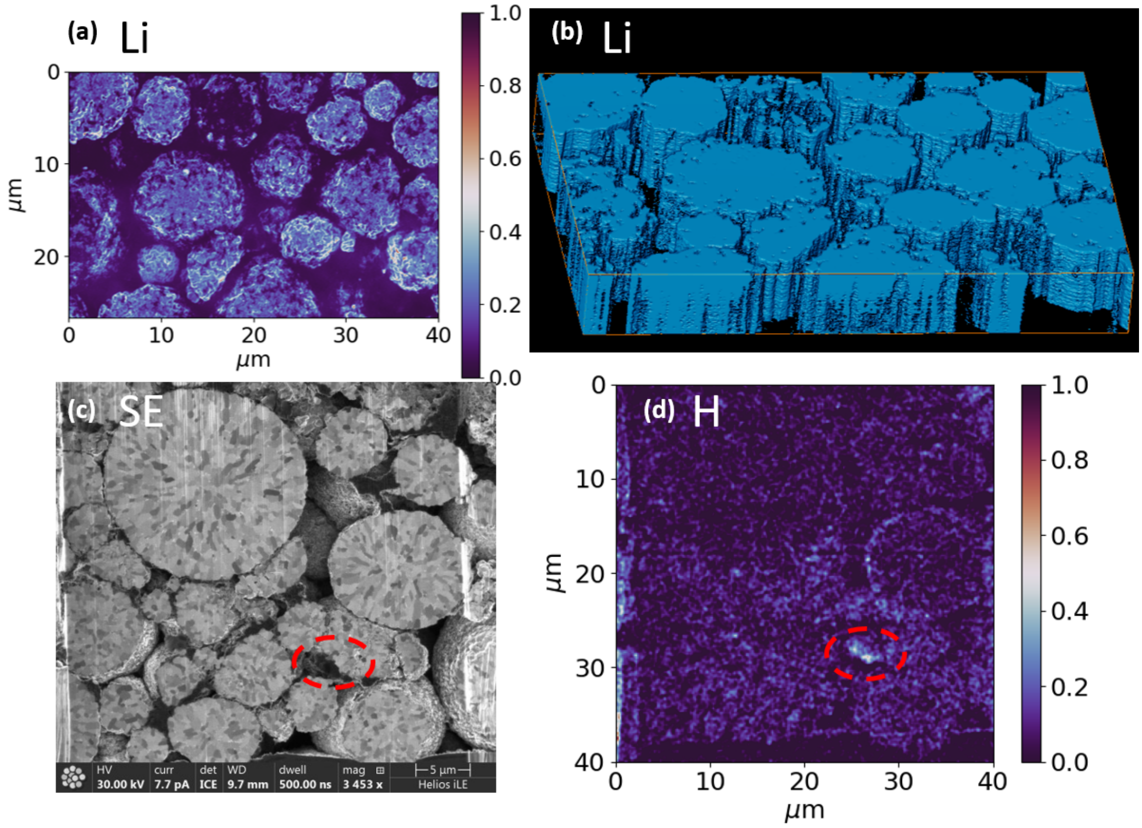

Figure 5.2: Li and H distributions in an NMC cathode collected with FIB-FS. **(a)** Top-down high resolution Li map of the NMC cathode showing Li distributions and **(b)** subsequent 3D volume rendering from the same images under 30 keV Ga^+ irradiation (276 pC/µm^2 total, 0.55 pC/µm^2 per frame) on the FIB-SEM system. **(c)** Cross-sectional secondary electron view of the inside of the cathode prepared by the Ga^+ beam showing the crystal grains and a particle of interested on the surface of the LiNiMnCoO crystal. **(d)** H map of the area taken with FIB-FS showing the particle is rich in H and a candidate site for electrolytic decomposition or compromised Ni site (30 keV Ga^+, 1.07 nC/µm^2). The cross-section is cut with the same beam used for FIB-FS, allowing for *in situ* analysis.

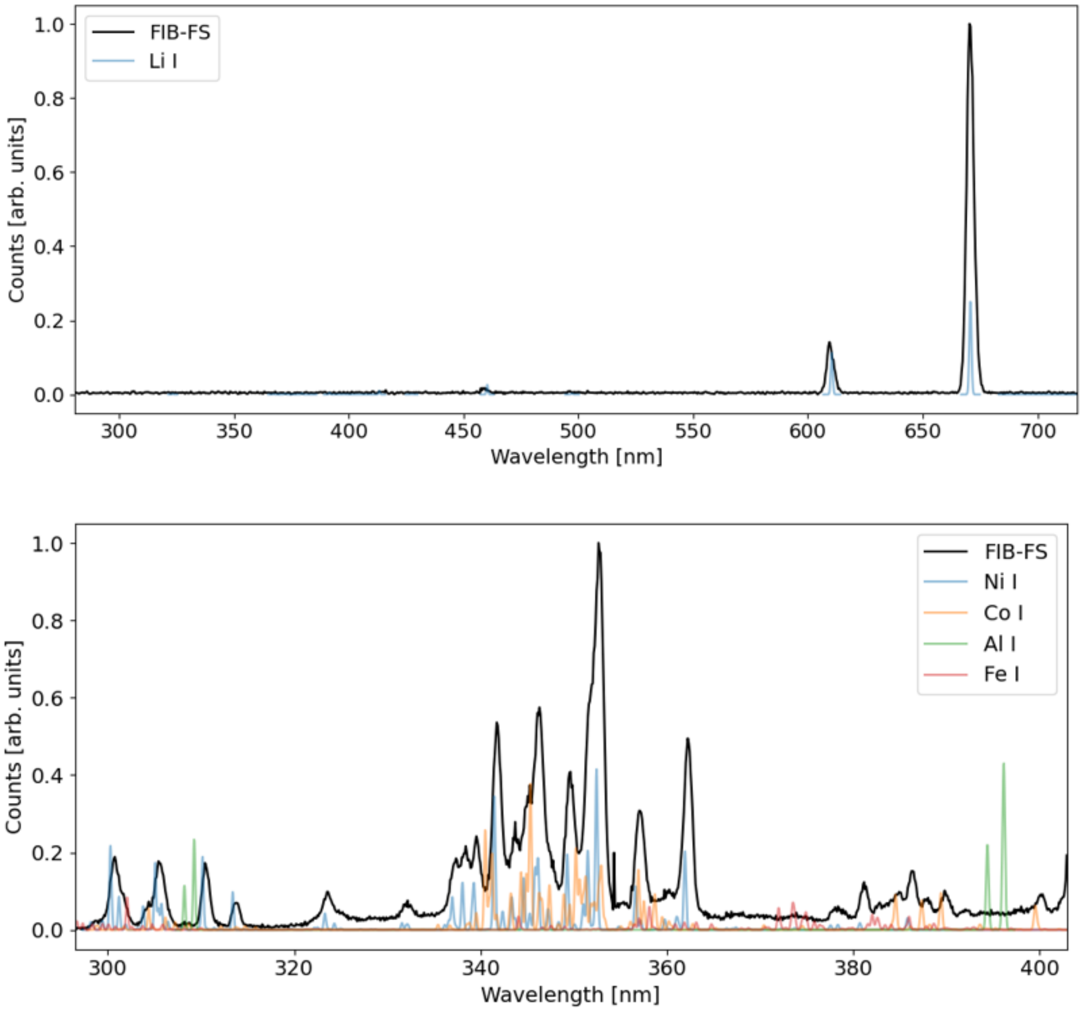

Figure 5.3: FIB-FS spectra of the NMC cathode collected in Survey Mode. Lithium detection is much more efficient due to both its concentration, inherent photon yield, and emission in the visible range of the spectrum where the quantum efficiency of the optics is optimized.

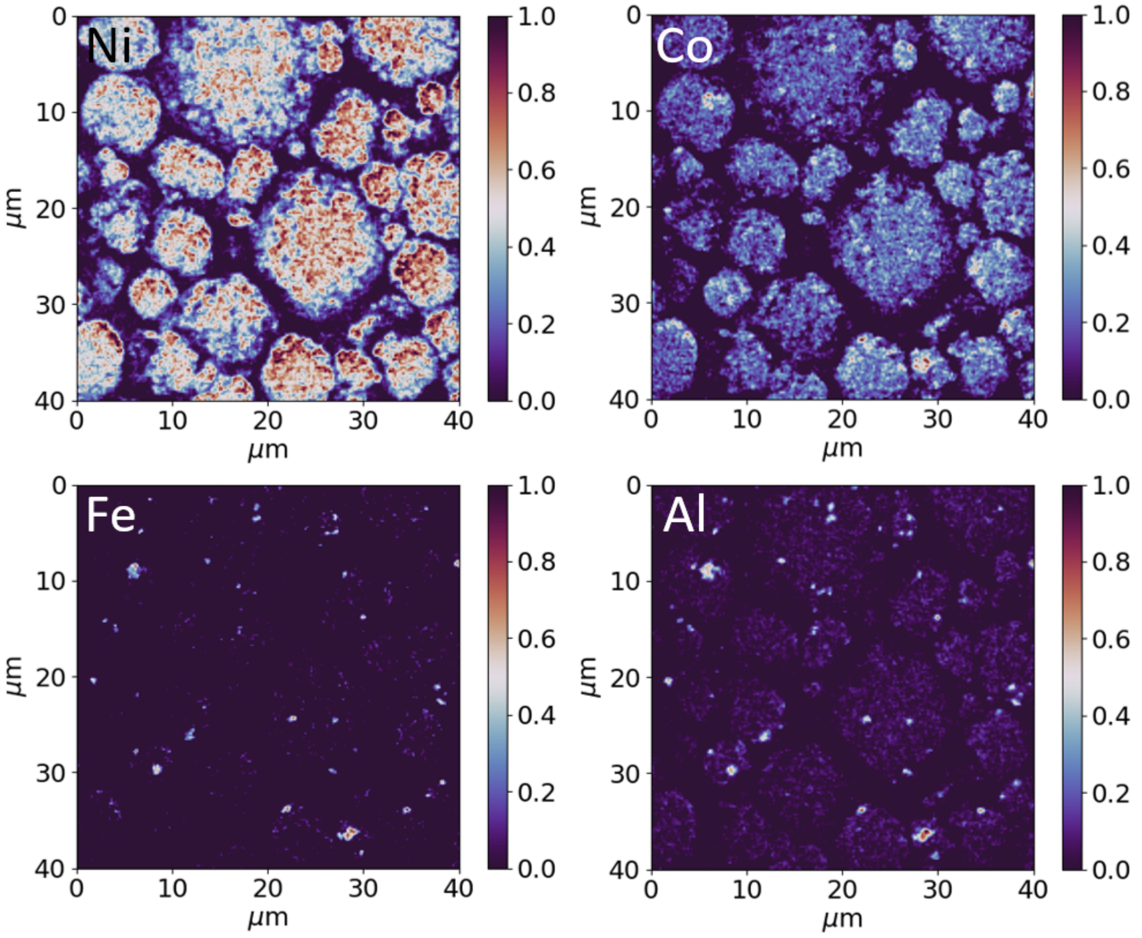

Figure 5.4: FIB-FS Hyperspectral maps of NMC lithium-ion battery cathode. Distributions of the mixed metal base (Ni and Co) as well as the trace metal dopants (Fe and Al) are shown under 30 keV Ga^+ bombardment (518 pC/µm^2). The Ni and Co maps show significant improvement to the resolution and clarity of the chemical maps over EDX maps due to the surface sensitivity of FIB-FS and the higher detection limits of the trace metal dopants at these conditions allow for Al and Fe detection when EDX fails.

656.279 nm (see Appendix 5.3). Figure 5.3 shows an example of how different parts of the spectra and different acquisition times result in detection of different elements. In the case of Li, the emission occurs in the VIS range, near 671 nm, where the Ni/Co/Mn occur closer to the UV range between 300 nm and 400 nm. Because of the spectral response of the optics, two different gratings – one blazed at 500 nm and one blazed at 300 nm – and two different transmission optics – VIS-NIR and UV-VIS – are used to improve the efficiency of the collection in their respective dynamic ranges.

The NiMnCo mixed metal forms the base of the cell, but it is not uncommon for developers to dope the structure with trace amounts of other metals for performance and longevity improvements. Aluminum presence will lend to a heighten

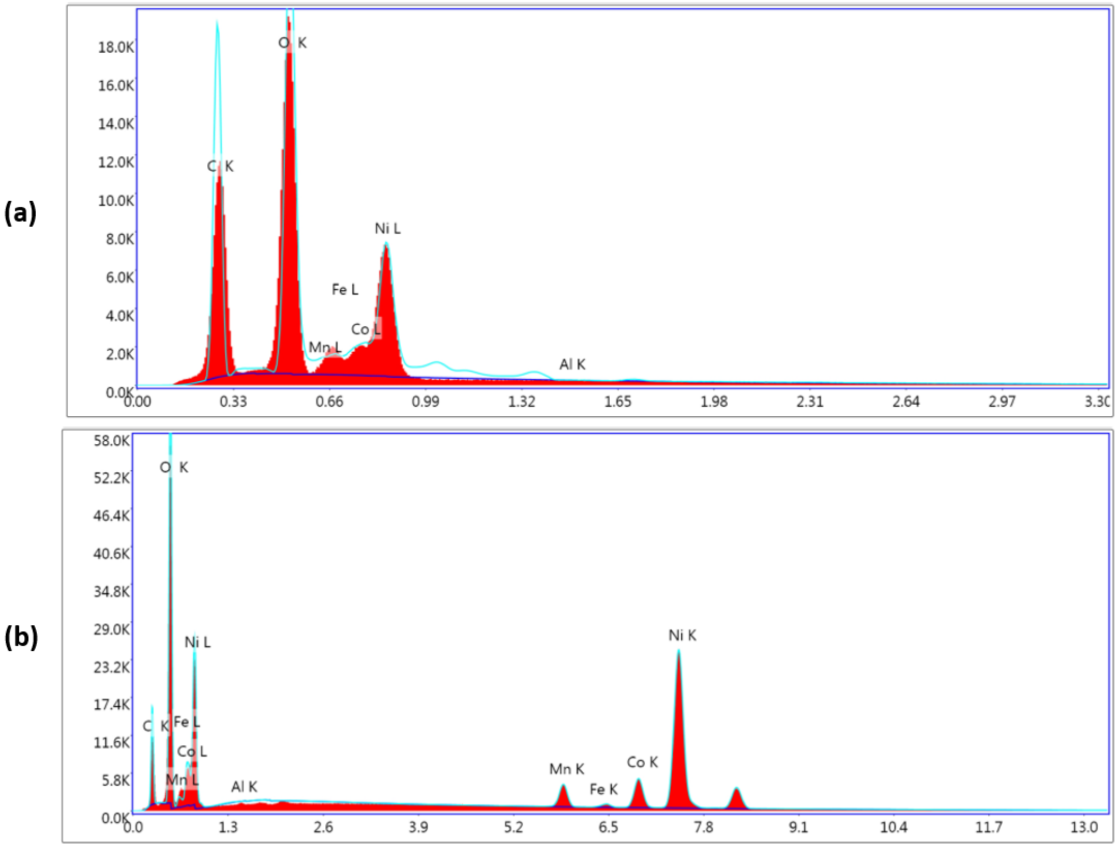

Figure 5.5: EDX summed spectra of a Li ion battery NMC cathode from 573 pC/μm^2 at 5 keV **(a)** and 20 keV **(b)** SEM energies. Higher SEM energies result in detection of the Kα major transitions, but lower spatial resolution while 5 keV yields higher spatial resolution at the expense of spectral identification. Al and Fe are force-identified and we note that the peak at 6.5 eV is the Mn Kβ_1 transition and not the Fe Kα_1 and Kα_2.

initial capacity, while iron denotes anti-site defects, and structural stability is generally associated with magnesium [230, 231]. As is the case with Li, the distribution of these dopants is important to gain an understanding of their reactivity during the charge and discharge cycles. Figure 5.4 are the results of a map taken with 30 keV Ga$^+$ at 518 pC/μm^2. Compared to the EDX maps, it is easy to see an increase in the signal to noise, increased spatial resolution, and the ability to detect the trace metals Al and Fe. In order to ensure the conclusion, the mapping of the Al and Fe spectral bins are forced and compared to the background Bremsstrahlung signal. In this case, the map will plot the raw counts of the spectral signal located at 1.87 keV for the Al Kα and 6.4 keV for Fe Kα to demonstrate that any contributions to the map are mostly fluctuations of the background Bremsstrahlung signal.

Comparison of the detection limits and spatial resolution between FIB-FS and

EDX highlights a common trade-off experienced with EDX. For the energies required to detect the most efficient Kα transitions of the Ni, Co, Fe and Mn, the interaction volume of the SEM limits the EDX spatial resolution to $\sim$1 µm, whereas the energy of the FIB yields an interaction volume $\sim$30 nm allowing for high surface sensitivity and higher resolution images. When the landing energy of the electrons is lowered to 10 keV or 5 keV, an increase in the spatial resolution is observed for Ni and Co, but the excitation energy is no longer able to efficiently excite the Kα transitions. Figure 5.5 shows the sum spectra of the sample under 5 keV and 20 keV SEM energies at the same dose. While a much improved spatial resolution is realized at 5 keV, the excitation of the sample elements is limited to the lower energy Lα transitions and is more subject to spectral overlaps and decreased signal to noise and confidence compared to the Kα major transitions enabled at higher energy. At the higher energy the Fe Kα transition *appears* to be observed, however, upon closer examination the peak is slightly shifted towards 6.5 keV instead of 6.4 keV indicating that it is more likely the Mn Kβ_1 transition at 6.49 keV as opposed to the Fe Kα_1 and Kα_2 peaks at 6.4 keV and 6.39 keV, respectively. This is further evidenced by its lack of appearance in the map and that we force the software to look for Fe and Al trace concentrations (see Al label in Figure 5.5(a)).

Depth profiles of the dopants were also taken to confirm that the distributions are not a surface artifact or contamination, but a structural dopant persistent through the NCM crystal body(see Figure 5.6). It is worth noting that this process is not possible with EDX alone, as EDX is not a depth-profiling technique.

The distributions of the trace elements in Figure 5.4 are interesting since it appears that the dopants are concentrated in specific lattice sites on the bulk Ni-Co crystal. In order to confirm that the maps are consistent with the true form and to benchmark the performance of FIB-FS to an established technique, the sample was analyzed with a ToF-SIMS system. The results are in Appendix 5.3 and are in excellent agreement with the distributions found with FIB-FS.

5.3 Li Ion Battery Validation

5.3.1 Hydrogen Detection Validation

Additional post process analysis can easily be done on the pixels in Hyperspectral FIB-FS maps to confirm conclusions about local concentrations. One method is averaging only the spectra of pixels contained in a region of interest to ensure the map or count value is not an artifact or background noise. This process is used

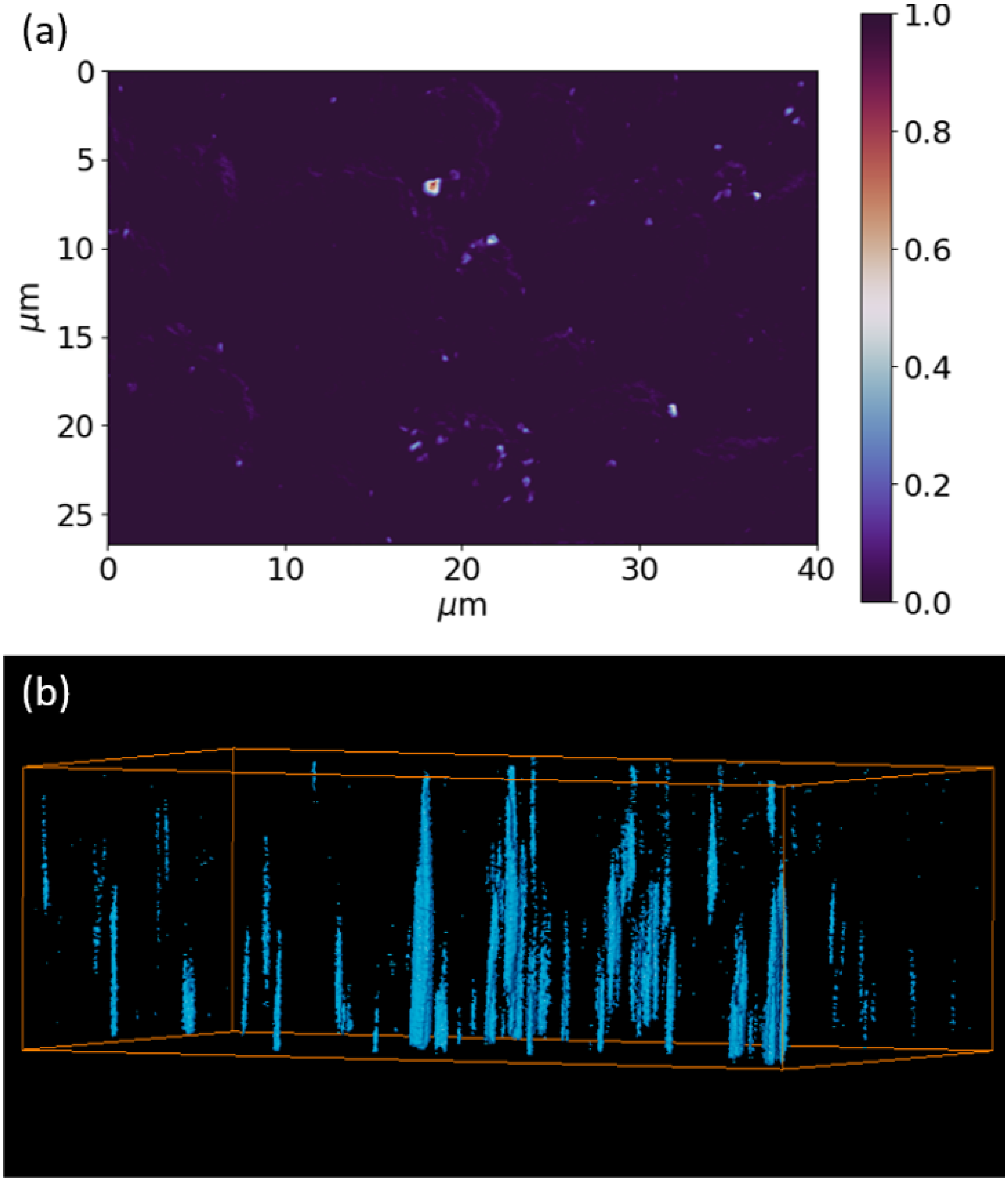

Figure 5.6: FIB-FS depth profile of Mg trace metal dopant distributions in NMC lithium-ion battery cathode from 30 keV Ga^+. (a) 2D frame averaged FIB-FS map of the Mg dopant taken top-down (1.3 nC/µm^2). (b) 3D volume of the same data showing that dopants are implanted throughout the sample volume (2.7 pC/µm^2 per frame).

in Figure 5.7 in order to confirm the presence of H in the questionable particle. Here, the spectra contained in the orange box are averaged together to show the hydrogen spectral peak located at 656.3 nm and confirm the spectral composition of the region as opposed to any artifacts or broadband emission which might appear in a simple raw count analysis.

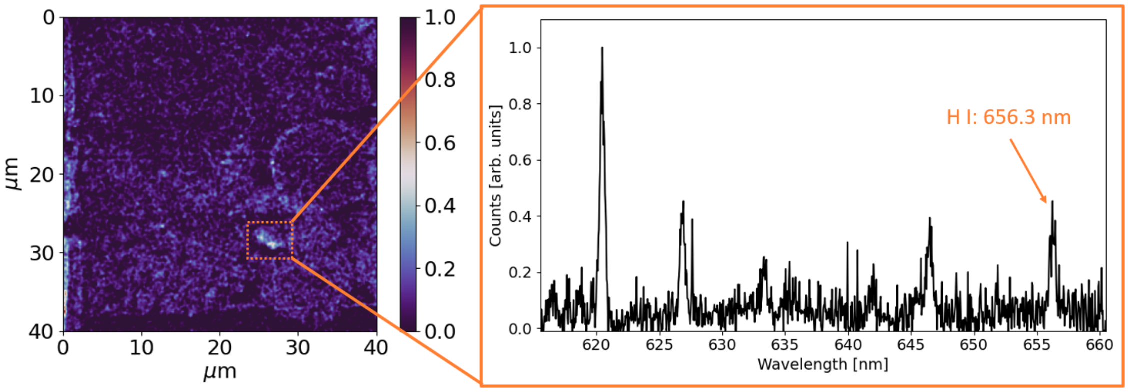

Figure 5.7: FIB-FS Hyperspectral map of NMC cathode and regional average spectrum showing clear hydrogen concentration within the cross-sectional area. Only the pixels contained in the orange square are considered.

5.3.2 ToF-SIMS Validation

With any new technique, it is important to cross-reference and benchmark the claims with existing and established techniques. Since EDX was unable to verify the trace element, Li, and H results found with FIB-FS in the battery sample, it was tested with a Ga^+ FIB ToF-SIMS in a different lab. The following Figures D.1, 5.9, 5.10 show the results from the ToF-SIMS measurements, providing the supporting evidence that the results garnered from FIB-FS in Chapter 5 show the true form of the sample structure.

5.4 Anode Analysis

In addition to analyzing an NMC cathode, a graphite/silicon (Si-C) anode was examined. Analysis of these materials for their elemental distributions is important to make interpretations of Li mobility back and forth from cathode to anode during the cycling process or to determine production recipes based on the trace element location in the binder. In particular, this anode is comprised of SiO_2 and graphite particles suspended in a mixed CMC and PVDF binder, which during production is baked at a temperature that allows the binder to distribute evenly throughout the graphite particles and set. The temperature of this binder is critical to allow the binder to set without separating the two components, which severely degrades the operation of the anode if not properly set and distributed. The only way to view the binder distribution is to map the chemical differences in the cross-section to show uniformity and distribution. Since the chemical composition of the two binders overlap and are complicated by the bulk reference material in

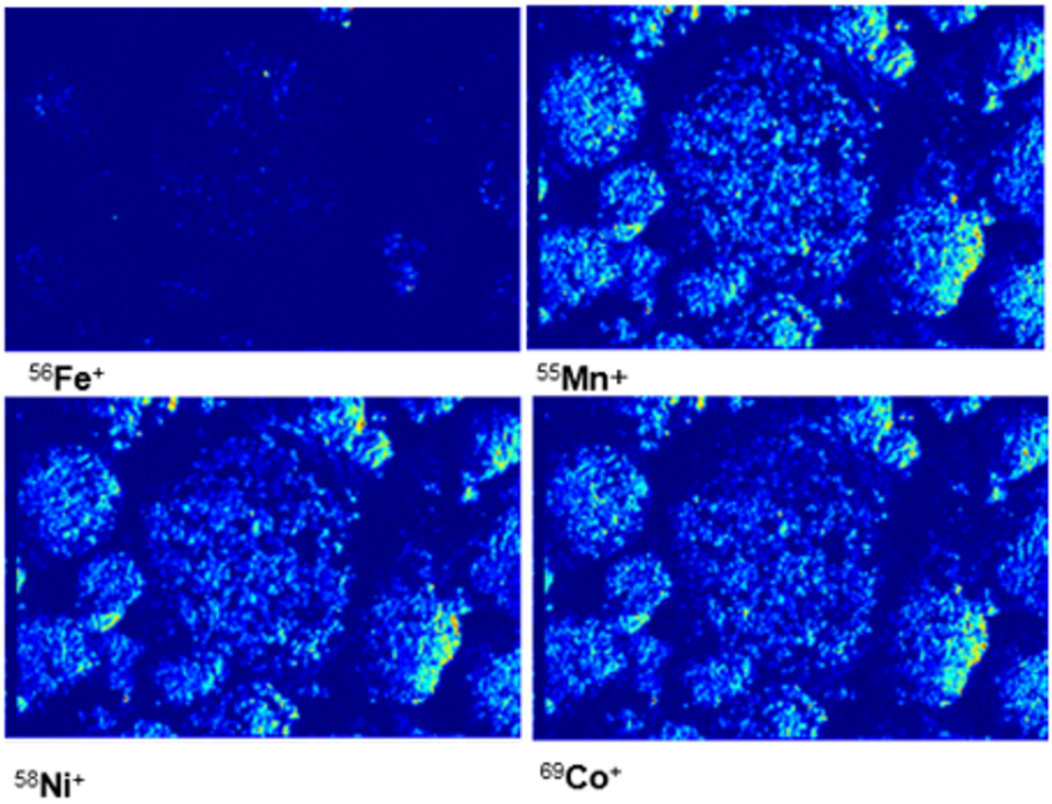

Figure 5.8: Ga^+ FIB ToF-SIMS elemental maps of the NMC cathode used in this report taken with 30 keV 147 pC/µm^2 conditions. Qualitative comparisons of the chemical maps to those collected with FIB-FS confirm the elemental distributions.

graphite, the only way to visualize the binder is through the trace sodium in the CMC binder ($C_8H_{12}NaO_8$). Tackling of this problem with EDX and FIB-FS provides an excellent solution that echoes the results of the cathode: FIB-FS picks up the trace Na (1-2 wt.%) and the Li, while EDX picks up the C, O, and Si, making the two techniques highly complementary.

Figure 5.11 shows the graphite/silicon anode cross section alongside the Li I map at 670 nm and the Na I $2p^6 3p(^2\mathrm{P}^o_{\frac{1}{2},\frac{3}{2}}) \rightarrow 2p^6 3s(^2\mathrm{S}_{\frac{1}{2}})$ maps. Silicon and graphite particles are suspended in a CMC and PVDF binder and are identified with the EDX results shown in Figure 5.12. Utilization of both EDX and FIB-FS in this example reveal how correlative images are used to play to the strengths and weaknesses of each technique.

Detection of sodium distributions within the sample is significant due to its low concentration in the electrode (1 -2% for CMC). Despite its low presence, its distribution shows a strong concentration at and around SiO_2 particles with a mostly uniform displacement through the height of the binder. Since both Li and Na show high concentration around the SiO_2 particles, which might indicate that mobility of Li is reduced in these regions. If so, both the Na and Li can undergo a

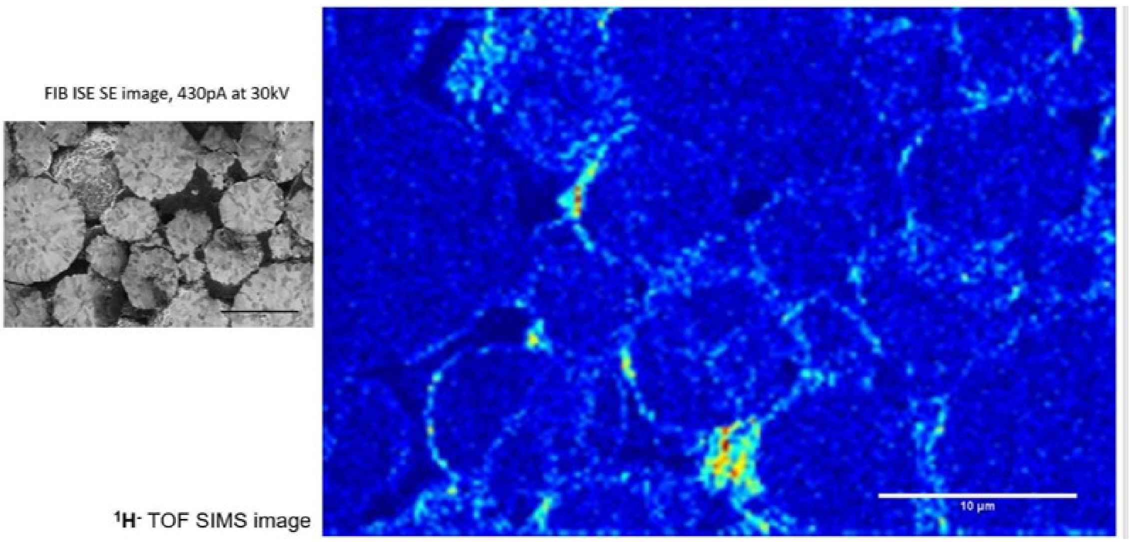

Figure 5.9: H^- maps of the NMC cathode collected from ToF-SIMS for comparison. 30 keV Ga^+, 317 pC/µm^2 conditions.

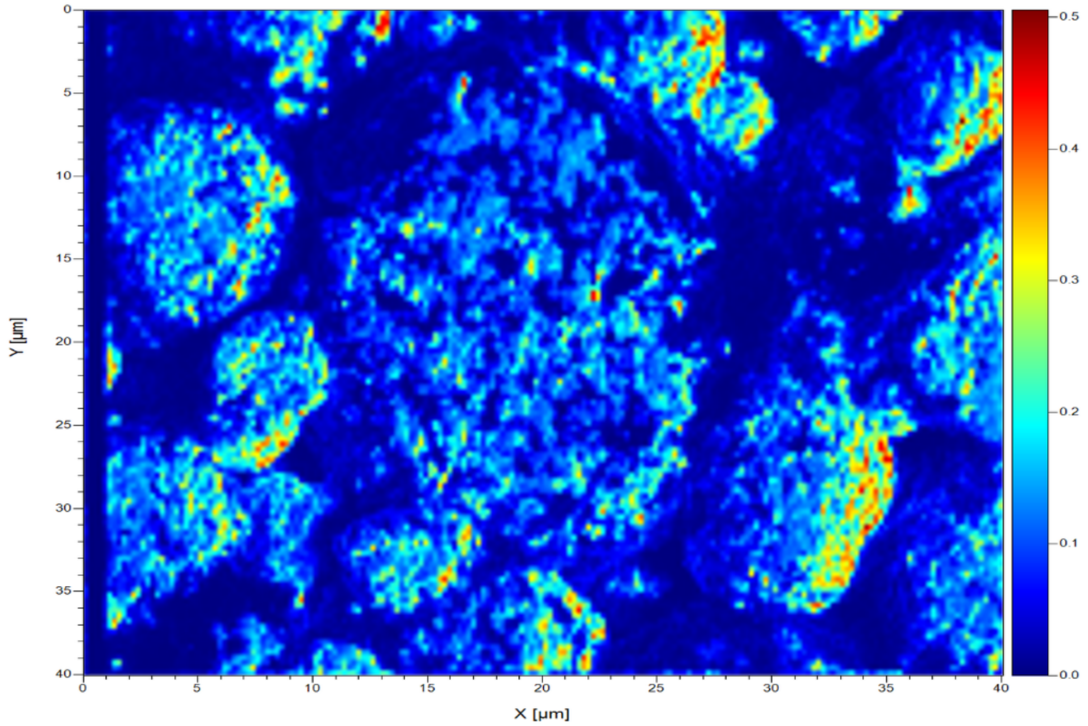

Figure 5.10: Li^+ map of the NMC cathode collected from ToF-SIMS for comparison. 30 keV 147 pC/µm^2 conditions comparable to the FIB-FS Li map.

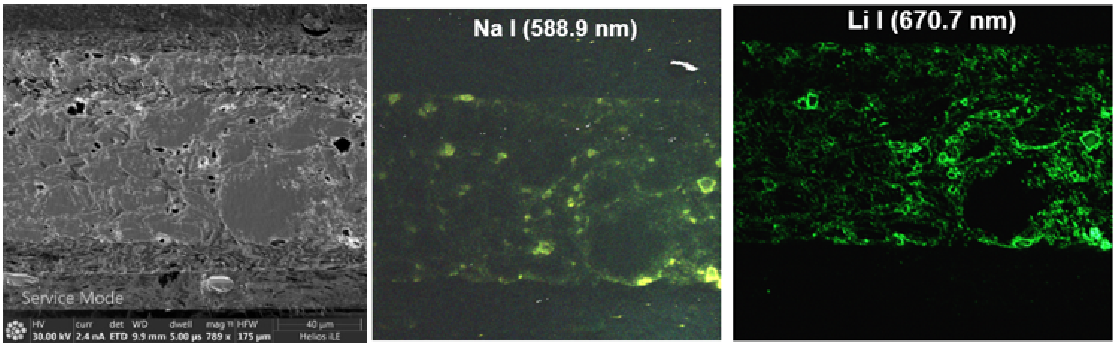

(a) (b) (c)

Figure 5.11: Cross-sectional FIB-FS analysis of Si-C anode. (a) Secondary electron image. (b) FIB-FS map of Na at 588.9 nm showing the Na distribution throughout the sample. (c) FIB-FS map of Li at 670.7 nm. The cross-section is cut with the same beam used for FIB-FS.

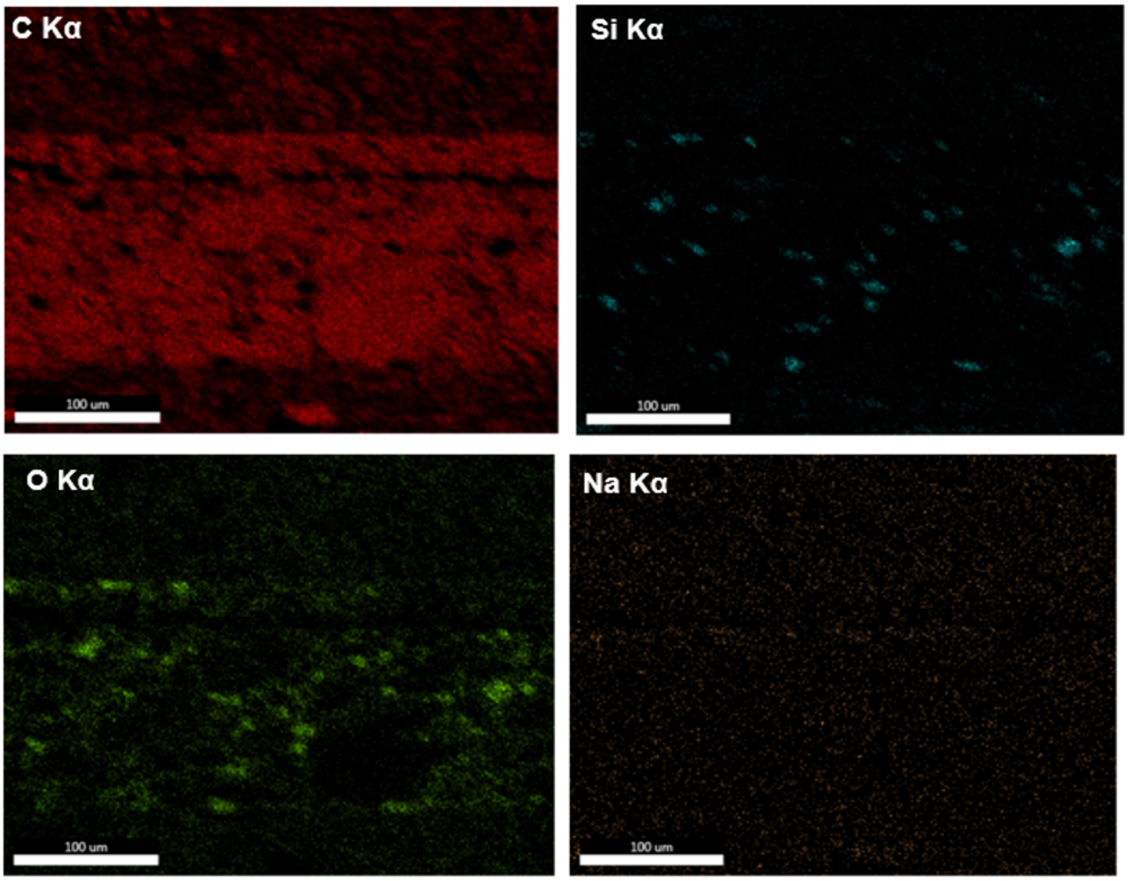

Figure 5.12: EDX maps of the Si-C anode cross-section showing C graphite, SiO_2 particles, and a Na map for comparison.

performance-reducing chemical process in which the oxidized surface becomes terminated and contributes to the growth of insulating films on the anode which ultimately impede charge transfer and reduce lifetime [224, 232, 233]. The image is also surprising as the sample has been cycled and discharged, so little lithium is expected to be present within the anode since most should return to the cathode. Some lithium presence is expected at the surface where the anode is in direct contact with the electrolyte, however, large distributions within the cross section suggest local trapping sites along SiO_2.

5.5 Conclusions

To develop better performing batteries, understanding of failure mechanisms and the effects of various dopants or chemistries on performance is critical. The mobility of lithium from cathode to anode is what drives performance while its immobility is what leads to degradation. Formation of defects through electrolysis and hydrogen interactions lead to cracking, film development, and capacitance degradation. Therefore, the ability to visualize lithium, hydrogen, and trace element distributions within both cathode and anode is fundamentally needed to draw conclusions about battery performance and characterization. The results presented here have demonstrated the capabilities of the FIB-FS technology to be applied to battery applications and have been compared to existing techniques of EDX and SIMS.

The biggest takeaway is not that FIB-FS is a catch-all technique, but rather that it is an ideal complement to EDX. FIB-FS plays to its strengths by excelling at areas of weakness for EDX. While EDX will easily detect heavy and electronegative elements in bulk quantities without sample damage or destruction, FIB-FS provides excellent light element detection like lithium and hydrogen as well as trace element mapping and extreme surface sensitivity leading to higher spatial resolution. Like the ToF-SIMS, FIB-FS enables multimodality of the FIB, yet the nature of spectroscopy with high resolution gratings and short bandpass filters avoid mass/charge overlap challenges, sample charging, and provides a simple, cost-effective, analysis add-on to FIB-SEM systems.

Chapter 6

Fundamental Insight from FIB-FS

6.1 Introduction

When a beam of charged atoms bombards the surface of a material, a variety of particles will be ejected from the surface. Elastic collisions between the incident ions and substrate surface atoms may cause some of the incident ions to be backscattered, while inelastic collisions will cause the ejection of electrons (secondary electrons or SEs) and substrate atoms in a process called sputtering described in section 2.2. While the vast majority of sputtered substrate atoms will be ejected into a neutral state, a fraction of the population may be ejected in an ionized state in the form of secondary ions (SIs), which can then be collected and separated by mass to perform elemental analysis in a process called secondary ion mass spectrometry (SIMS) [16, 36–38]. A still smaller fraction of the sputtered atoms will be ejected into an electronically excited state, whereby upon deexcitation, will release a photon with energy indicative of its electronic structure in processes described in section 2.3. These photons can be collected and separated through spectroscopic techniques for elemental analysis in methods outlined in Chapter 3 and with the high-performance metrics in the nanoscale regime presented in Chapter 4.

The limitations described in Chapter 4 are fundamental and depend directly on the interaction of the incident ions with the substrate in the collision cascade. Through the implantation volume and the probe size, the limitations are inherently coupled to the photon emission yield (see section 4.2) and present another fundamental limitation to the performance of FIB-FS. In other words, strength of signal will determine the minimum amount of ion dose required to collect a spectrum, which subsequently determines the magnitude of ion-sample interactions. Therefore, a deeper understanding of the mechanisms at play in the formation of excited states in sputtered atoms is desired to establish the role of FIB-FS and its modes of operation in the workflow of modern FIB systems.

Despite a large body of literature surrounding photon and ion emission from sputtered atoms, a unified understanding of the mechanisms that govern the both the formation processes of sputtered ions and excited atoms has yet to come forward. By the nature of their emission, secondary ion and photons are often compared and models proposed to describe the mechanism of ionization have been adopted and prescribed to photon emission. Two models – resonant electron tunneling [134, 145] and molecular bond-breaking [55, 156] – have had success in their application to secondary ion emission by describing a delocalized and localized interaction of the particles, respectively. Still, these two models fail to describe all experimental observations, and SIMS remains subject to the dynamic changes in the bombarding region and matrix effects inherent to each unique sample [234, 235].

When used to describe the mechanism leading to the excited state population of sputtered atoms prior to the emission of photons (see section 2.3), each has fallen short in accurately describing the body of experimental data for photons. Bond-breaking models are unable explain the excitation of states with energies that lie above the maximum energy allowed in the adiabatic to diabatic transformation [96, 118, 125, 155], while reports on population distributions are widely varied and provide conflicting evidence for resonant electron tunneling models [79, 80, 161–164, 164–174].

The capabilities of FIB-FS enable the exploration of the excitation mechanisms in new ways. The high efficiency collection allows for observation of low-yield photon and ion emission at current and ion flux scales previously unexplored, while the integration on a FIB allows for direct-write and controlled modification of the sample surface at the nanoscale to probe local chemical impacts on the photon emission. The following presents a study of both excited sputtered magnesium neutrals (Mg I) and excited sputtered magnesium ions (Mg II) in different oxygen environments and under various primary ion species bombardment conditions. Changes to the population distributions of excited states are reported by comparing relative photon yields and find them to be dependent on primary ion mass, energy, and flux regimes. By comparing signals from SIs, Mg I, and Mg II in such environments, it is shown that their emission cannot be explained with the existing resonant electron transfer or other previously proposed models, and that different mechanisms may exist for each species. Furthermore, the photon yield behavior of Mg I and Mg II signals under different primary ion energies and fluxes provide evidence that these mechanistic effects contribute to the photon yield in all measurements and that an optimization condition exists to maximize the absolute photons yields. The results are discussed in the context of adsorbed and implanted oxygen concentration, and its impact on the analytical applications of the FIB-FS technique.

6.2 Method

The experiments reported in this work have been performed on a Thermo Fisher Scientific Hydra multi-ion species FIB-SEM system that has been outfitted with both optical detection systems described in Chapter 3 and is outlined in Figure 6.1. The FIB originates from a plasma source and delivers ions at energies from 500 eV to 30 keV described in Appendix A. The system is equipped with Xe, Ar, O, and N gases (99.999%) that can be interchanged in a matter of minutes through vacuum systems in the plasma source cell and without venting the main chamber sample region. The ions are focused to a spot on the order of 10s-100s of nanometers (beam energy and mass dependent) through a series of electrostatic lenses and precisely scanned across the sample surface. The main specimen chamber pressure maintains 1.5 x 10^{-6} Torr, consistent with operating vacuums of Thermo Fisher systems.

The elliptical mirror depicted in Figure 6.1 **(a)** and the insertable mini-probe described in section 3.3.1 with UV-VIS optics are used in two different schemes to test the photon emission under different environments. The mirror is used to collect photons with high efficiency for implantation and steady state irradiation while the insertable mini-probe is used to collect photons in a variable gas environment modulated by an insertable gas injection system (GIS). The mirror is retracted via the substage system to allow the insertable mini-probe to be pneumatically inserted and retracted from a port on the side of the main specimen chamber. By mounting the insertable mini-probe body at a different angle to the coincident point, the GIS nozzle is inserted past the optic and placed microns away from the target surface. Oxygen gas is delivered through the nozzle, allowing for photon transient behavior to be observed *in situ*. The detection chain is absolute irradiance-calibrated with NIST-certified deuterium-tungsten and halogen lamps for each grating and grating acquisition angle, which is used to correct for the spectral response of the system and deliver an absolute photon yield measurement [photons/sputtered atom].

Two different modes of photon collection are used: Hyperspectral Mode and Kinetic Survey Mode. In Hyperspectral Mode, a predefined region and resolution is set for the FIB to scan and the EMCCD exposure time is linked to the dwell time through a NIST data acquisition card that interfaces with the FIB deflection board such that a complete photon spectrum is collected at each pixel. A typical Mg

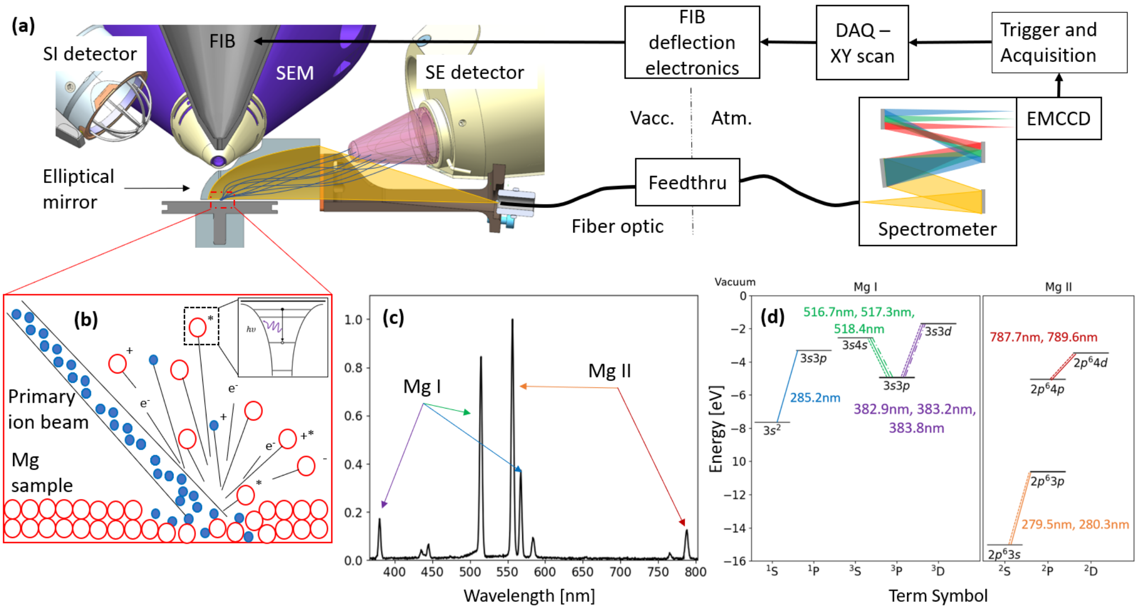

Figure 6.1: Overview of the concepts involved in the emission of Mg I and Mg II and their detection with FIB-FS. **(a)** Schematic illustration of the high efficiency hardware developed and used to perform spectroscopic analysis on sputtered particles. Photons emitted by the ejected atoms are coupled to a fiber optic by positioning an elliptical mirror above the incident point, which is then transmitted through a vacuum/atmosphere interface and into a spectrometer which is linked to the FIB scan to collect spatially resolved spectra in a region of interest. **(b)** Depiction of the various types of particles emitted during the ion bombardment process. The majority of ejected particles consists of secondary electrons (SEs) and sputtered neutral atoms, while smaller populations of backscattered primary ions, positively and negatively charged secondary ions (SIs), excited sputtered neutrals (Mg I), and excited sputtered ions (Mg II) are ejected. When an excited sputtered atom or excited sputtered ion leaves the surface, it can relax to a lower state through emission of a photon with energy $h\nu$. **(c)** Typical spectrum from the deexcitation process collected from Mg under 30 keV Xe$^+$ bombardment showing Mg I and Mg II transitions. **(d)** Grotrian diagram of the transitions observed in this study and indicated in the preceding spectrum. The energy scale is referenced to vacuum = 0 and the ionization energy of the ground state of Mg neutral and Mg ion, respectively.

spectrum is shown in Figure 6.1 **(c)**. In post processing, these spectra are aligned to the shape of the scan pattern and the spectral lines of interest are integrated. The resulting integrated count value is displayed in each pixel resulting in spatially resolved maps of the integrated peak or transition (i.e. chemical map). In Kinetic Survey Mode, the scan rate of the FIB and the exposure time of the EMCCD camera are decoupled such that multiple spectra are acquired in series over a defined length of time while the FIB continuously scans a region of interest with a set of independent scanning parameters. The spectra are similarly analyzed, yielding a time-resolved measurement of the integrated peaks/transitions.

Single crystal magnesium $\langle 0001 \rangle$ was chosen due to its relatively simple electronic structure: only a handful of transitions are allowed, being bound by strong spin-orbit coupling and minimized cascade emission through the existence of the $3s3p$ $^3\mathrm{P}^0$ metastable state shown in Figure 6.1 **(d)**. For each measurement, the magnesium is sputter-cleaned with 1 µA of 30 keV Xe$^+$ for 2 to 3 minutes to remove the native oxide layer and to equally amorphize the crystal structure prior to irradiation, thereby reducing contributions from initial transients, channeling, or time evolution of an amorphized layer. Sputter rates are empirically measured at each energy and for each ion species by milling multiple boxes on the cleaned region and measuring the volume removed with the SEM.

The absolute photon yields as a function of ion flux and incident ion beam energy reported here are performed in the Kinetic Acquisition Mode once a steady state has been achieved under ion irradiation. Ion flux is controlled by tuning the surface area of irradiation with the scan parameters of the ion beam for a given ion beam current. Since different ion accelerating voltages and primary ion sources can lead to different currents for the same aperture, the currents are adjusted to keep the ion flux range and respective surface area of irradiation within the maximum field of view determined by the collection optics. Each box mill is serpentine patterned with 1 µs dwell and 50% beam pitch overlap, such that each spectrum contains hundreds to thousands of passes over the surface area. The spectra are then averaged together to give the final yield value for a given exposure time and repeated two more times and averaged again. Photon yields are calculated by fitting the spectral peak to a composite Gaussian model and integrating the resulting form. The photon counts are then corrected by the spectral response of the detection chain and adjusted by the volume removed during the exposure time. The atoms removed is determined by the empirically measured volume removed and assumed Mg density of 1.74 g/cm^3, yielding photons/sputtered atom unit.

6.3 Results

The sensitivity and accuracy of the FIB combined with its switchable source chemistry allows for direct writing and implantation of oxygen atoms into the magnesium surface at predefined areas. This is to investigate photon emission behavior on a localized, site selective basis. Figure 6.2 shows a region of magnesium that was first cleaned with a Xe^+ plasma FIB, followed by irradiation with the O^+ FIB in a pattern, then switched back to Xe^+ for a hyperspectral map. After sputter cleaning with the Xe^+ plasma FIB, the ion source chamber is quickly pumped of Xe gas with a turbomolecular pump, then filled with O gas and ignited to form an O plasma. A bitmap of the UTS logo is loaded into the patterning engine and the image is patterned into the region using the O^+ beam at 30 keV and 100 pA for 3 minutes. The source is then changed back to Xe^+, and a 2D elemental map is taken of the area in Hyperspectral Mode. The resulting spectra are integrated over the Mg I $3s3d\ ^3\mathrm{D}_{1,2,3} \rightarrow 3s3p\ ^3\mathrm{P}_{0,1,2}$ triplet and the Mg II $2p^6 4d\ ^2\mathrm{D}_{\frac{3}{2},\frac{5}{2}} \rightarrow 2p3p\ ^2\mathrm{P}_{\frac{1}{2},\frac{3}{2}}$ doublet peaks to create the chemical maps of the region from the same acquisition. The enhancement of the Mg I signal is clearly seen through the depiction of the logo in the Mg I map, demonstrating a localized effect of the implanted oxygen. The spectra in the regions defined by **(a)** and **(b)** of the figure are averaged together and graphed below the image to further display the preferential enhancement of the Mg I yield at 383 nm/384 nm (observed as second order spectral lines at 766 nm/768 nm) as opposed to the Mg II yield at 787 nm/789 nm at the same pixel location, which sees no enhancement.

Time-resolved measurements of Mg I and Mg II signals under increased oxygen adsorbate concentrate through the injection of O_2 at the surface of the substrate show similar increases in the Mg I yield, but a decrease in the Mg II yield. Figure 6.3 shows the transient behavior of the Mg I triplet from the $3s4s\ ^3\mathrm{S}_1$ state, the Mg II doublet from the $2p^6 4d\ ^2\mathrm{D}_{\frac{3}{2},\frac{5}{2}}$ state, the O I triplet from the $2s^2 2p^3(^4\mathrm{S}^\circ)3p\ ^5\mathrm{P}_{3,2,1}$ state, and secondary ion signal under 30 keV Ar^+ irradiation at normal incidence. Oxygen gas is injected during the 45-95 second timeframe and the counts are normalized to give relative yields. In the first 45 seconds, the Ar^+ beam removes the native oxide layer present at the surface and an inverse relationship between the Mg I and Mg II emission is observed as it approaches the steady state. Oxygen gas is introduced at 45 seconds and an order of magnitude enhancement occurs in Mg I echoing the results of Figure 6.2, until the yields reach a new steady state determined by O_2 gas arrival and removal. When the precursor is shut off around 95 seconds, a similar process to the initial transient is observed through the removal of surface oxide and knock-on implanted oxide during the exposure.

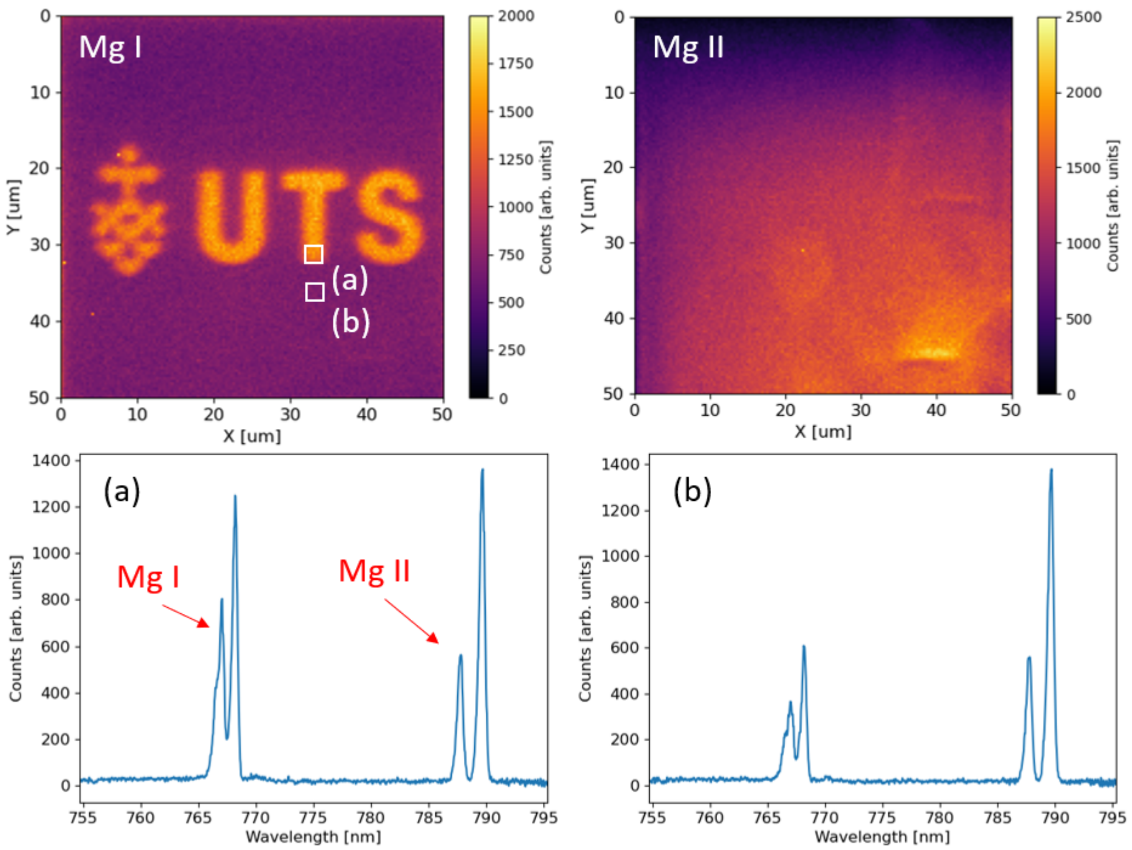

Figure 6.2: 2-D Hyperspectral maps of the excited magnesium neutral (Mg I) emission at 766 nm & 768 nm (second order of 383 nm/384 nm) and the excited magnesium ion (Mg II) emission at 787 nm & 789 nm from a region patterned with the University of Technology Sydney logo using direct-write O^+ implantation. Oxygen atoms are implanted by the FIB only in the region defined by the UTS logo and the letters “UTS”. Two regions are marked in the hyperspectral map **(a)** and **(b)** where the spectra contained in those pixels are averaged and displayed below. The spectra contained in region **(a)** show preferential enhancement of the Mg I emission with no enhancement seen for region **(b)**, showing a direct influence of the localized implanted oxygen on the excitation mechanism for Mg I and not Mg II.

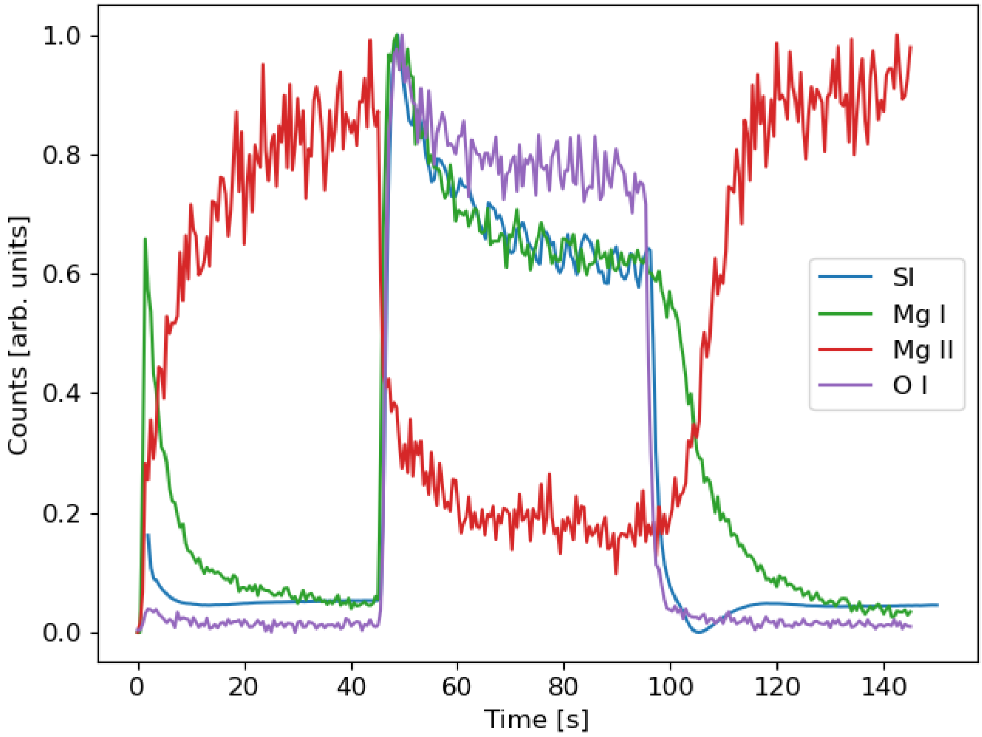

Figure 6.3: Transient measurements of the secondary ion emission (SI) and photon emission from excited Mg neutrals (Mg I), excited Mg ions (Mg II), and excited oxygen neutrals (O I) sputtered under 30 keV Ar^+. The SI collection is not mass-separated and includes detection of all positively charged ions leaving the surface. Oxygen gas is introduced to the sample surface at the 45 second mark and an immediate enhancement is observed in the Mg I and SI signals, however, a sharp decrease is seen in the Mg II signal, demonstrating a reliance only on the decreased sputtering yield as a result of the oxidized surface. Despite the decrease in sputtering yield, the SI and Mg I signals increase by an order of magnitude – a result of a chemical enhancement preferential to Mg I and SIs.

Surprisingly, an inverse behavior in the relative yield between the SI emission recorded by the ion detector and the Mg II emission recorded by the spectrometer. During oxygen exposure, an enhancement in the SI emission is observed in agreement with common observations for secondary ion emission in similar experiments [100, 155, 236], but a decrease in Mg II is observed. It is commonly known that O_2 gas on Mg and other metals will induce a decrease in the sputtering rate between 2-5x [98, 100, 101]. The influence of the oxygen gas on the Mg I and SI yield has a mechanistic enhancement that is exponentially greater than the decrease in the sputter rate, so an increase in signal is still readily observed despite the lower sputtering yield. It is clear by Figures 6.2 and 6.3, however, that no such chemical enhancement mechanism exists for Mg II. Instead, the behavior of Mg II in Figure 6.3 is explained simply by the O_2 gas presence inducing a decrease in the overall sputter rate that is subsequently observed and uncorrected for in the Mg II relative photon plot.

While Figure 6.3 shows two extremes of oxygen concentration, Figure 6.4 explores a gradient of oxygen coverage through photon emission in the steady state of various primary ion fluxes and mass. Three difference Mg I transitions are monitored along with two Mg II transitions to record the behavior at each condition. The transitions lie at different energies relative to the vacuum as depicted in Figure 6.1 **(d)**. A clear decrease in the Mg I signal is observed with increasing ion flux while only a slight decrease is seen in Mg II under all primary ion species except O^+.

When put into the context of oxygen absorbate concentration, the results can be compared to Figures 6.2 and 6.3 through the rate of removal at the surface. For a given ion flux, the volume removal rate will increase with ion mass, while for a given mass it increases with ion flux. A crossover point at roughly 3 pA/µm^2 shows more efficient photon yield for Mg II at these conditions with Xe^+, while the same condition does not occur until 10 pA/µm^2 for incident Ar^+ at the same energy. Comparing to N^+ and O^+, it is easy to see that the same level of flux dependence is not achieved, and that a more consistent photon yield is maintained. In the case of N^+, the sputtering rate is so low that high fluxes are required to overcome adsorbate rates. In the case of O^+, a regime is never achieved due to the continual replenishment of implanted oxygen from primary ion beam. Therefore, the results are consistent with the behavior associated with the charge state of the sputtered atoms from Figures 6.2 and 6.3, extending the observation to other excited states of the neutral and ionic species.

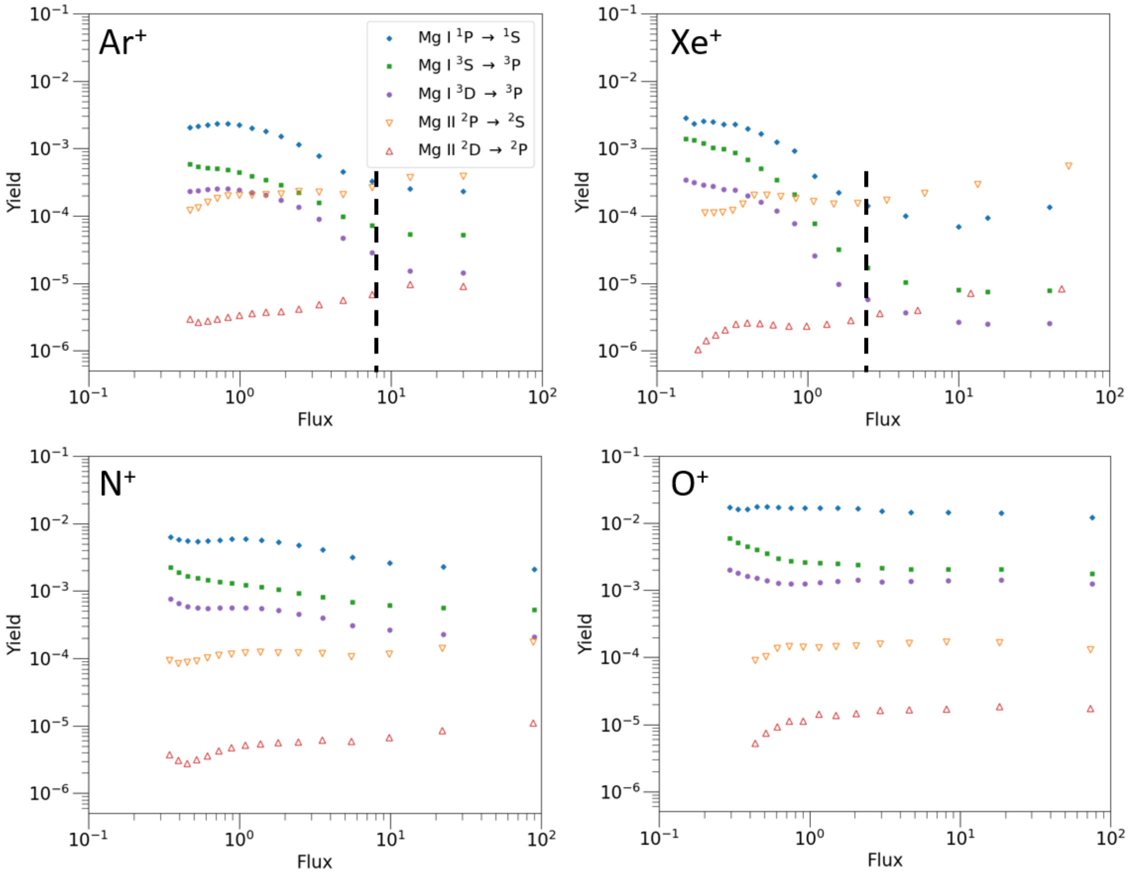

Figure 6.4: Absolute photon yields [photon/sputtered atom] of sputtered magnesium neutrals (Mg I) and sputtered magnesium ions (Mg II) plotted as a function of incident ion flux [pA/µm^2] for 30 keV Ar$^+$, Xe$^+$, O$^+$, and N$^+$. Two different regimes are observed with a crossover point marked by the dashed line: adsorbed oxygen-depleted and oxygen-rich surface composition. In the oxygen-rich regions at low flux, Mg I is dominated by the chemical enhancement from the oxygen presence while Mg II is only impacted by the reduced sputtering rate. In oxygen-depleted regimes, Mg I yield undergoes exponential decrease by the reduced concentration of oxygen and its impact on the chemical enhancement via the flux.

6.4 Discussion

While it is well known that the presence of O_2 gas can lead to an order of magnitude increase in both Mg I and SIs, there are very few accounts of excited secondary ions under such conditions. The vast majority of prior research observe metastable and short-lived excited states of sputtered neutral atoms, while only a handful of authors ever report seeing photons from excited sputtered ions [89, 91, 92, 103, 108, 111, 115, 158–160]. Qualitatively, the behavior of Mg I reported here is consistent with prior reports that show enhancement of the photon signal from neutrals with increased oxygen presence through oxygen chamber pressure and in comparisons between metals and their metal oxides counterparts [89, 98, 100, 101, 103, 108, 155, 158–160, 236]. The response of the Mg II signal, however, is surprising and doesn't show any mechanistic dependence on the oxygen presence outside of pedestrian kinetic dependencies on the sputtering rate. If it is believed that the population of electrons into excited states is inherently a fundamental process of a departing particle, then it is expected that the core mechanism of excitation should be the same between departing neutrals (Mg I) and ions (Mg II). As such, any model used to successfully describe Mg I, must also describe the dissimilar behavior of Mg II based on some characteristic difference between Mg I and Mg II that acts as a variable to the probability for excitation.

Looking to prior research, one variable that may be considered is the oxygen adsorbate concentration that increases the yield through a molecular bond-breaking process. The bond breaking model described by Yu [156] and extended for photons by others [155], describes a charge exchange process at the crossing of diabatic covalent potential-energy curves of the dissociation of a metal (M) oxide (O) molecule M-O into $M^+ + O^-$ when the atoms are moving away from each other. The potential energy curve that describes the transition from its fundamental state of M-O will cross multiple potential energy curves that describe excited states $M^* + O$, see Section 2.3.3.

There are two natural consequences of this model. The first is an upper limit of the excitation energy of the metal atom being bound by the ionization energy I of the metal atom and the electronegativity EA of oxygen: $\Delta E = I - EA$. The second is that for simple wavefunctions, the transition matrix decays exponentially with increasing energy (i.e. interatomic distance R), making population into high lying excited states very unlikely. The bond-breaking model is well known to be successful in describing SI enhancement from oxygen, so it is no surprise that the SI and the Mg I behavior in Figures 6.2 and 6.3 agree qualitatively. The existence of Mg II, however, prohibits the application of this model by the imposed upper limit while the proclivity for Mg II emission over Mg I in oxygen depleted regimes in Figure 6.3 all but invalidate it.

Electron tunneling models describe these differing yield behaviors based on the departing atom's velocity and the electronic structure resonance with the bulk valence and conduction bands. There are two channels that describe the probability of the atom leaving in an excited state: electron transfer from an excited atom to empty states in the surface conduction band in a non-radiative resonant ionization process proposed by van der Weg [105]

$$P(v) = \text{exp}\left(-\frac{A}{av_{\perp}}\right) \tag{6.1}$$

and resonant electron transfer from loosely bound electrons near the Fermi level of the surface to an outgoing ionic core proposed by Veje [158]

$$P(v) = 1 - \text{exp}\left(-\frac{A}{av_{\perp}}\right) \tag{6.2}$$

where A and a are constants for transition rates of radiative transfer above the surface and $v_{\perp}$ is the departing perpendicular velocity. Constant a is determined by the overlap of the atomic and bulk metallic electron wave functions with A being constant rate.

In the first expression (6.1), excitation is described as a static or constant rate determine by the natural evolution of the collision cascade where only the subsequent deexcitation of the atom may occur by resonant ionization to available states above the Fermi level, followed by resonant neutralization into the ground state or Auger-neutralization. In this situation, the sputtered atom's probability to escape without losing its excited electron through nonradiative transfer is determined by its normal velocity component – i.e. if the atom is moving away from the surface faster, then the atom has less time to interact with the surface and can escape the region, being forced to deexcite radiatively. The total photon emission can then be described as being proportional to the maximum velocity v_m [91, 92, 127]:

$$Y \propto J\ S\ \text{exp}\left(-\frac{A}{av_m}\right) \tag{6.3}$$

where J is the ion current density and S is the sputtering yield. When the maximum velocity v_m corresponds to the maximum energy transferred from the ion of mass M_1 and energy E to target atom M_2:

$$v_m = \left(\frac{7.72\text{x}10^{12}\ M_1\ E_1}{(M_1 + M_2)^2}\right)^{1/2} \text{(cm/s)} \tag{6.4}$$

then the transfer rate of A/a can be found by fitting ln $[Y/(JS)]$ vs $1/v_m$. When measuring photon yields with varying incident ion energy E_1 (or v_m), an exponential decrease is found at low energies and values for A/a are extrapolated [87, 89, 91, 92, 127, 148].

When used to describe enhancement from oxygen, non-radiative transfer determined by A/a is blocked by the existence of a forbidden band gap in the case of metal oxides or by a modified work function that raises or lowers the occupied states at the surface in and out of resonance with the departing atom's excited state electronic structure [30, 93–95, 97, 109, 125, 128, 237, 238]. Together, the enhancement of oxygen along with the lower yields at low ion energy bombardment have led the model to be used numerous times to describe neutral atom photon emission.

The second expression (6.2) describes the reverse process in which the electron is transferred from the bulk/surface into the departing atom's excited state. It was proposed in order to explain disparity of results with the van der Weg model. For example, the transition rates A/a found when changing ion bombardment energy in [91, 92, 127] are all almost identical despite the several eV differences in the excited states and their positions above and below the Fermi level. While Veje did not look at velocity explicitly when first proposing the model, he observed preferential population of Mg ion excited states over the excited neutral atoms. He related this distribution to the fact that the surface electronic structure was in more in resonance with the final excited states of the ionic species than the neutral states, attributing it to transfer from the surface to the atom by A/a. Others report similar preferential populations in sputtered metastables and found that excited states were actually travelling *slower* than the ground state atoms for any given bombardment energy [79, 161–164, 164–170, 173, 174]. Furthermore, higher velocity distributions of excited states from oxidized surfaces were reported [98, 101, 141, 163], contrary to expectations from equation (6.1). In other words, if the non-radiative pathways are blocked by oxygen, then slower particles should be expected to survive. Thus, under the van der Weg model clean metals should see faster velocity distributions while oxidized metals should see slower. Under Veje's model, however, the effect is alternatively explained by a lowering of the work function that increases the rate of population into the faster moving species [163].

Comparison of the current data to these models needs to consider all of these prior observations. It is clear from Figures 6.2 and 6.3 that oxygen has a direct and preferential enhancement of the Mg I state and not the Mg II. When the model proposed by van der Weg and described in Equation (6.1) is applied in these experiments, it does not agree. If the work function of the Mg surface is taken to be 3.64 eV [239–241], then the excited states of the $3d$ and $4s$ Mg I states in Figure 6.2 and 6.3 are 1.94 eV and 1.1 eV above the Fermi energy, respectively, while the $4d$ Mg II state is only 0.714 eV. Therefore, if a decrease in the work function or a forbidden gap is introduced to block non-radiative transfer of the Mg I states to the conduction band, it must also block the non-radiative transfer of the Mg II state so a relative enhancement of this transition is expected. This is not the case and the reverse behavior is actually observed.

In fact, it appears as though Veje's model might be a good fit. On the clean Mg surface, the $4d$ Mg II state is in resonance with the Fermi level of the bulk and sees higher population than the higher lying Mg I $3d$ and $4s$ states. As oxygen is introduced to specific sites in Figure 6.2, the electronic structure is locally modified through a decrease in the work function around 1-2 eV such that the resonance is matched with the Mg I $3d$ state, enhancing the photon emission while the Mg II state is then out of resonance. The same effect is experienced globally in Figure 6.3 to enhance the $4s$ state of Mg I.

Unfortunately, the model begins to fall apart when observing multiple states of Mg I and Mg II in oxygen-depleted and oxygen-rich environments like those shown in Figure 6.4, which shows the enhancement of Mg I states by oxidation from the ambient chamber pressure as function of ion flux. The adsorbate concentration N_a of adsorbate a in the steady state of a given pressure, temperature, and sputtering rate is inversely proportional to the bombarding particle flux $N_\mathrm{a} \propto 1/f$ [242].

By modifying the incident ion flux in the steady state in Figure 6.4, moderate adsorbate concentration environments are probed. If a modification to the electronic structure of the surface is imposed as a function of adsorbate concentration, then the states may be seen as going in and out of resonance with the sputtered particle's electronic structure. When considering the two Mg II states with respect to the Fermi level, there are two key observations that contradict a tunneling effect: (i) the fact that *both* $4d$ and the $3p$ states are inversely proportional to the Mg I states despite their large difference in resonance with the bulk structures and (ii) the Mg I $3p$ and the Mg II $4d$ state are only separated by 0.16 eV and are both near resonance with the clean Mg Fermi level, but respond inversely to the same perturbations. Even if the states prior electronic configuration instead of the final configuration is considered - i.e. Mg I $3s3p$ is treated as Mg II $2p^6 3p$ and Mg II is Mg III $2p^5 3p$ - then all the states adjust by the respective ionization energy and fall well below resonance level so the same argument holds. Any argument made in favor of resonant transfer under the conditions of oxygen concentration, work function changes, and resonances with the bulk electronic structure may hold for one case in Mg I, but do not hold for both Mg I and Mg II. In other words, either resonant electron transfer is not a dominant process in any excitation mechanism or there exists an entirely separate mechanism that populates the Mg II states.

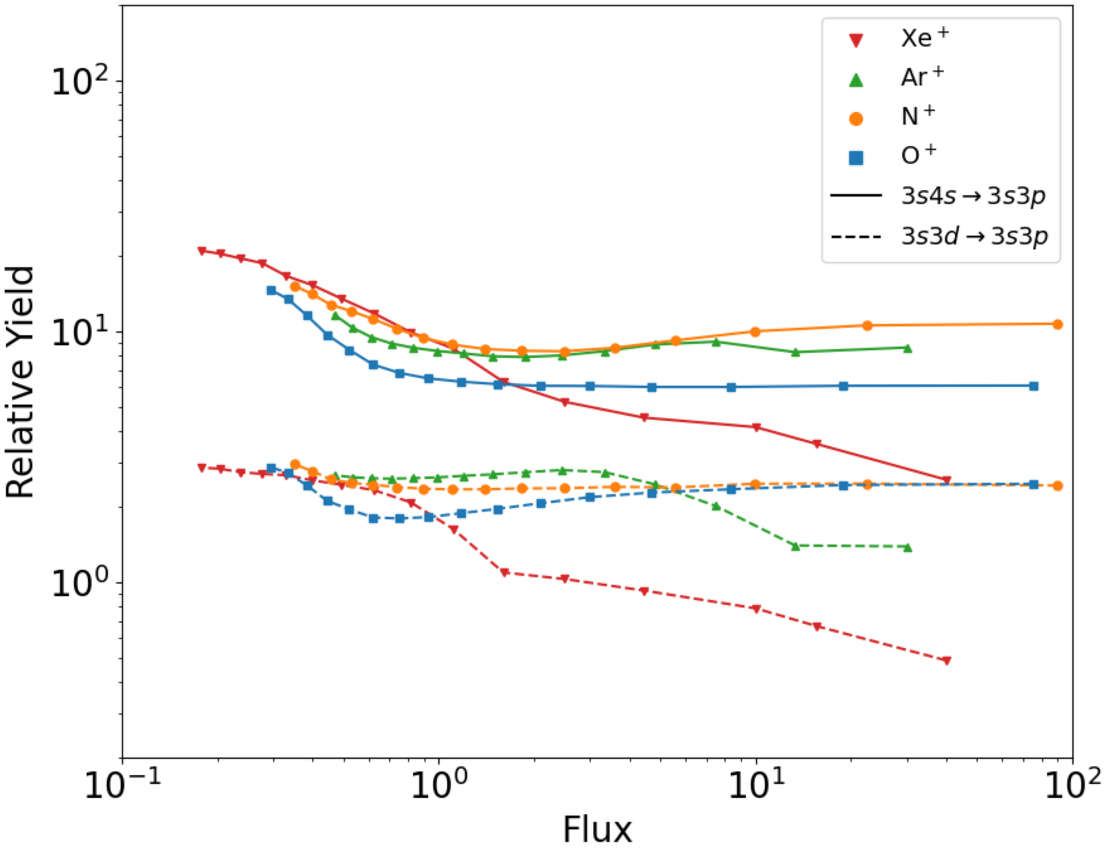

Figure 6.5: Mg I peak ratios of the measured excited states relative to the singlet ground state transition, showing a change in the population distribution of excited states as a function of incident ion beam flux and ion mass. Since all each data is taken in the same acquisition, the peaks are simply divided by the integrated counts. Note that higher lying $3d$ state plateaus at higher flux (lower oxygen coverage) than the $4s$ state when decreasing ion flux.

A closer examination on the states of Mg I can reveal further inconsistencies with the resonant transfer model. By taking the data in Figure 6.4 and graphing the raw photon counts relative to the ground state transition $3s3p^1$P to $3s^2$, a relative population distribution of the $4s$ and $3d$ excited Mg I states can be found. Figure 6.5 shows the Mg I states relative to the ground state transition for each of the primary ion masses. An interesting observation is the plateau of the $3d$ state before the $4s$ state with decreasing ion flux. This is surprising considering that the work function should be decreasing from 3.64 eV with increasing oxygen at lower ion fluxes. Since the $3d$ state lies roughly 0.84 eV above the $4s$ state, it is expected that the $3d$ state population should continue to increase with more oxygen coverage and that the $4s$ state should begin to plateau at a higher flux value, but the opposite is observed.

It is important to note that the results presented above do not contradict prior results. In fact, Veje observed the preferential population of Mg II excited states over the Mg I atoms and related this distribution to the surface electronic structure in order to develop the resonant electron transfer model [158–160]. The key differences are that Veje performed his experiments in the steady state at a single ion flux and that he did not observe all Mg II emissions (specifically he did not measure the $4d$ state), using a snapshot to build the model. Figure 6.4 shows just how variable the population of excited states can be at any given flux or current density and highlights the importance of vacuum conditions. In later reports, Veje was able to measure the Mg I and Mg II vs oxygen pressure and his results are mixed [103]; some transitions are enhanced with others are suppressed. While Veje's observation of the Mg II $3p$ population matches the behavior shown here, again the $4d$ state was not observed and the mixed results between the differences in the ionic vs the neutral species are left without discussion [89, 103, 108].

The results also don't immediately conflict evidence in prior reports related to the photon yield as a function of incident ion landing energy. The reports mentioned earlier show exponential decrease in photon emission with decreasing incident ion landing energy. Figure 6.6 shows the results of the Mg I and Mg II absolute emission yields of the as a function of incident ion energy ($3s3p\ ^1\mathrm{S} \rightarrow 3s^2\ ^1\mathrm{P}$ and $2p^63p\ ^2\mathrm{P} \rightarrow 2p^63s\ ^2\mathrm{S}$, respectively). The results for Mg I show a complete reversal at low energies, favoring emission. When the result is put into context by the above data, the supposed discrepancy is explained as an artifact of the oxygen concentration from the reduced sputtering rate at low ion landing energies. The same argument applies: as the sputtering rate decreases with ion landing energy, the adsorbate concentration will increase, resulting the enhanced Mg I and decreased Mg II. Thus, the same conclusion is made that either resonant electron transfer is not a dominant process or there are two different mechanisms at play. Furthermore, these effects are present at all stages of sputtering such that other kinetic influences such as incident angle, edge-effects, and channeling can impose shifts in the excited state population.

Still, the exponential decrease in photon emission at low incident ion energy in prior reports is interesting, especially for experiments performed in UHV or with non-oxidizing metals. Neither electron transfer model can explain both the Mg results here and the reported experiments that have negligible oxygen effects, indicating that other velocity dependent mechanisms may be dominant. A possible alternative explanation may be that the Mg II may have vastly different velocities than Mg I. In this case, any modifications to the electronic structure that are experienced by Mg I may not be experienced by Mg II since the probability for population is dominated by a high velocity component $v_\perp$. The velocity distri-

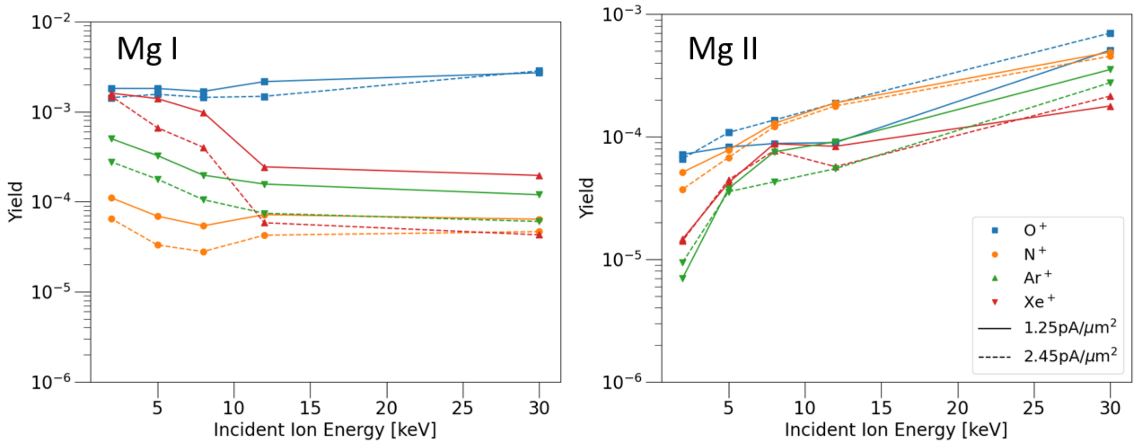

Figure 6.6: Absolute photon yields of Mg I and Mg II vs primary ion energy. The left graph shows the photon yields from the $3s4s$ ^{3}S $\rightarrow 2s3p$ ^{3}P transition of Mg I while the right graph shows the yields from $2p^6 3p$ ^{2}P $\rightarrow 2p^6 3s$ ^{2}S transition of Mg II.

butions of the sputtered species were not measured in this experiment, but this explanation seems unlikely due to the known measured velocities of secondary ions and due to the population distributions in Figure 6.5.

Consideration of the first point is simple in that secondary ions tend to be emitted in velocities similar to the ones recorded for excited atoms: most peak between 1-8 eV [74, 243–245]. To examine the second point, it is helpful to consider the treatment of resonant transfer under the current logic. It is described well in Cortona [163] as a probability function that acts on a velocity distribution of the entire sputtered atom population for a given set of ion beam irradiation conditions. In other words, the ion beam sputters all kinds of particles resulting in a total velocity distribution and the probability of population into an excited state is determined by the state's resonance with the bulk through factors A and a in Equation (6.2). When the velocities of this state are measured, the result is a distribution or subset of the original distribution - resonance only determines where along the original distribution the current excited state's velocity distribution lands. When the resonance is changed, such as through the work function, the original distribution doesn't change, but only where the resonant transfer probability function acts on it changes.

In the case being proposed, two separate velocity distributions on which the resonant transfer probability function could act are needed. Generation of these two separate distributions requires an ionization mechanism *a priori* with a velocity distribution dependent on excited state energy or charge state. Mg I is sputtered with velocity distribution X and Mg II is sputtered with velocity distribution Y. The probability function is then free to act separately on distributions X and

Y based on their resonance since the velocities themselves don't change with the ion flux. While the existence of an ionization mechanism as a prerequisite to deliver separate velocity distributions might be possible, yet another subset would be required to explain the plateau of the higher lying $3s3d$ state before the $3s4s$ state in 6.5. Since the lower level should saturate based on the same resonance mechanism as the work function decrease, this would require $v_\perp$ to be inherently different between excited states within Mg I as well as within Mg II. It would be difficult to know where such a mechanism would end (e.g. fine, hyperfine), and a much deeper consideration is needed than the simple models proposed so far. One way to explore this would be to perform the same measurements above at UHV to extract resonant transfer components A/a vs $v_\perp$ and compare to the yields of the excited states to the electronic structure. This way, the states may be compared without interference from the chemical effects of the background chamber pressure and oxidation.

6.5 Conclusions and Impact to FIB-FS

To conclude, excited sputtered Mg neutrals and excited sputtered Mg ions are influenced by the oxygen concentration at the point of emission. From an application standpoint, the results are extremely pertinent given the experimental conditions of modern FIB and SEM systems. The advancement in the optics of charged particles has pushed the probe size of the ion beam to the nanometer scale with high current density and high landing energy (30 keV) irradiation regimes. While these conditions are optimized for milling and high resolution imaging, the results shown here (particularly Figures 6.4 and 6.6) show that these conditions may be less optimal from an efficiency standpoint for photon and SI signal collection in FIB-FS. Therefore, an optimization problem exists to maximize signal, reduce sample damage, and minimize acquisition time for a given resolution and current flux. These conditions are ultimately determined by the sample chemistry, primary ion beam kinetics, and specimen chamber pressure, which the user can control to balance the tradeoffs between resolution and signal-to-noise. Based on Figure 6.3, these conditions also exist for ToF-SIMS applications that operate in the same regimes.

Furthermore, by comparison of Mg I, Mg II, and SI signals under different oxygen environments and primary ion irradiation conditions, it is shown that the existing models of molecular bond breaking and electron resonant transfer that have been applied in both secondary ion formation and in excited state formation cannot adequately describe the experimental data presented. Instead a different mechanism must be developed to describe the population of electrons into excited states of sputtered atoms under these conditions. Such a model must take into consideration the kinetic response of the surface under the ion from changes in sputtering rate, surface oxide removal, and the electronic structures of the surface and the departing atom.

Duvenbeck et al. [246, 247] have provided the framework for a molecular dynamics model that may prove promising in this discussion. Their model expresses the excitation of excited atoms and production of ions in an electronic stopping power dominated regime where the excitations are characterized by the energy density of electron-hole pairs and a conduction band that rapidly thermalizes, creating a local electronic temperature in the sp band. They show that these local electronic temperatures can reach values high enough to form excited states and ions. Such a model may qualitatively describe the different population distributions of Mg I and Mg II seen here through the development of different electronic "temperatures" that are dependent on the perturbations from the primary beam kinetics. These are only building blocks and for now, the results presented here serve to progress the knowledge of excitation mechanisms by opening opportunities for experiments on modern FIB systems and by provide a framework for operation of the FIB-FS technique in potential applications.

Chapter 7

Conclusions and Outlook

The work described in this thesis has shown that FIB-FS can be placed among the few techniques capable of overcoming inherent difficulties of nanoscale material analysis. It has been done so by developing and implementing a novel optical hardware and instrumentation scheme onto a FIB-SEM system with new methodologies and in demonstrating both 3D nanoscale applications and new fundamental insights. The capabilities of FIB-FS not only the meet the requirements of multidisciplinary applications of nanotechnology, but in some cases feature the technique as an ideal method. It is important, however, to consider what FIB-FS is and what it is not. FIB-FS is not a catch-all technique capable of detecting every element on the periodic table with excellent sensitivity or at trace concentrations. It is not reliably quantifiable and it is not a simple plug-and-play solution for every situation that requires minimal to no interpretation or oversight. On the other hand, FIB-FS is excellent at detecting certain groups of periodic elements like alkali, alkline earth, an rare-earth despite being poor at detecting halogens and non-metals. While not reliably quantifiable, its surface sensitivity, spatial resolution, and qualitive aspects position it as a powerful tool that is compatible with other techniques on the FIB-SEM platform. While not fool-proof, the instrumentation was intentionally and deliberately designed to be modular and versatile, with plug-and-play solutions available in some applications (e.g. filter + PMT). These same design decisions allow FIB-FS to maintain both a wide range of applications as well as a low cost of ownership.

While the most desirable next step for FIB-FS is in the form of quantifiable detection, the understanding of the complex mechanisms of excitation is simply not there yet. Therefore, the first integrations of FIB-FS are likely to be as a marriage to EDX and as plug-and-play single element or PMT imaging modules while its standalone power is continues as a lower-cost and affordable alternative to SIMS. These employments can be improved with new imaging modules and detectors to form new contrast and signal mixing under any FIB imaging or milling procedures to gain free information.

Other areas of research involve the detection of molecules and isotopes from sputtered species. Like atoms, molecules can be electronically excited during sputtering and deexcited by the release of a photon. Unlike atoms, however, the many rotational and vibrational states present a family of sub-levels for transition and result in a broad spectral peak. While some molecular emission was observed during this project such as C-H, B-H, Be-H, and C_2, molecular emission is relatively rare compared to atomic emission. Isotopes, however, are only as rare as their abundancies. In most cases, the shift in the transition energy from the hyperfine splitting from the different nuclear mass is so small that only the highest spectral resolution instruments are able to detect it. Further research and development of the technique in these areas will only improve and expand the reach of FIB-FS.

The future of FIB-FS is entirely and completely open. It stands before a field of applications that only continues to grow in its complexity and shrink in its scale. Despite the performance shown here, FIB-FS is in its infancy with the majority of its potential unrealized. What remains clear, however, is that the progress made here has set the stage for FIB-FS to be a powerful and versatile technique, to be kept in the company of modern nanoscale microscopy techniques.

Appendices

Appendix A

Focused Ion Beams

A.1 Introduction

The foundation of focused ion beam-induced fluorescence spectroscopy (FIB-FS) is built upon the operation and interaction of focused ion beams with matter. In particular, the work presented in this dissertation discusses the photons that are emitted when ions bombard the surface of a sample and compares excited state populations and transient behaviors of the emission to the various other types of particles emitted in the same event. Performance metrics of FIB-FS as well as evaluation of physical mechanisms of the signal are directly coupled to the hardware operation, instrument performance, and optical limitations of the FIB column through the ion probe. In order to contextualize FIB-FS on the FIB-SEM system, this appendix provides an overview of focused ion beams, their operation, and architecture.

There are several comprehensive reviews of FIB technology and its application [46, 47, 248–252] which elaborate in much greater detail than the following overview. Each author reserves their own approach - some favoring optics, others focusing on application or ion-sample interactions. It is from these references that this general summary is sourced from.

A.2 FIB Architecture

The FIB is a multifaceted tool that delivers a steady beam of positively or negatively charged particles to the surface of a substrate in a tightly focused spot on the order of tens of nanometers. In essence, the FIB is a microscope that demagnifies a source object to a small probe, but instead of transmitting and manipulating a beam of photons, the lenses are made to control ions. A FIB column will consist of (at a minimum) a source, an extractor, an aperture (or apertures), a condensing or collimating lens, a deflection assembly typically consisting of octupoles or quadrupoles, and a final focusing lens. A typical system architecture is shown in Figure A.1.

There are many different types of FIB microscopes, but the two used throughout this report are those which transmit ions from a liquid metal ion source (LMIS) and ions from a plasma cell (PFIB). The LMIS consists of a liquid metal on the surface of a needle-like support base from which ions are drawn out by field-induced ion formation at the tip. When high electric fields on the order of 10 V/nm are applied to the tip of the needle, a conical body of liquid metal forms. Ion formation occurs and a liquid metal jet emits from the surface, while the liquid metal thin film on the base of the needle acts as reservoir source for continual source replenishment. The resulting jet is a high current density ($\sim 10^{11}$ A/m^2), high-brightness (current per steradian per unit area per volt), source with properties of a virtual source size 50 nm in diameter, allowing for projection and demagnification to nanoscale probe sizes with the appropriate optics. The gallium LMIS is used for experimental work in this thesis and is widely implemented in the field of FIB technology because of its low melting point, unreactive nature with the tungsten needle, the mass of Ga, and its low vapor pressure. A typical Ga$^+$ LMIS is shown in Figure A.2. Source contamination and gas scattering is preserved through a series of ion getter pumps (IGPs) and differential pumping apertures that maintain vacuum pressures around 10^{-8} to 10^{-9} Torr that separate the column and source regions from the main specimen chamber, which typically operates at 10^{-6} to 10^{-7} Torr.

Plasma ion beams have been used in broad ion beam (BIB) experimentation for nearly 100 years, however, the integration into a FIB has only been more popularized in recent years. This is mainly due to the limitations inherent in the source end imparted on the optics, which make nanoscale probe sizes difficult compared to the high-brightness LMIS sources. These source regions consist of a chamber (cell) in which either an inductively coupled or capacitively coupled plasma is ignited and maintained. The plasma cell is fitted with an aperture typically 100s of microns in diameter from which to extract the plasma ions. As a result of the large extraction aperture and angular intensity from which the ions are extracted, the overall brightness of the source is lower than LMIS and this limits its demagnification. The versatility of the plasma source chamber, however, allows for a range of gases to be used: xenon, argon, and oxygen plasmas being most common. Each of these ion sources provide a unique aspect to be lent to different applications.

After extraction, the ions are accelerated and follow a trajectory along the optical axis of the column whose goal is imaging the virtual source onto the image plane. Like any optical microscope, this is achieved through lensing, however, in

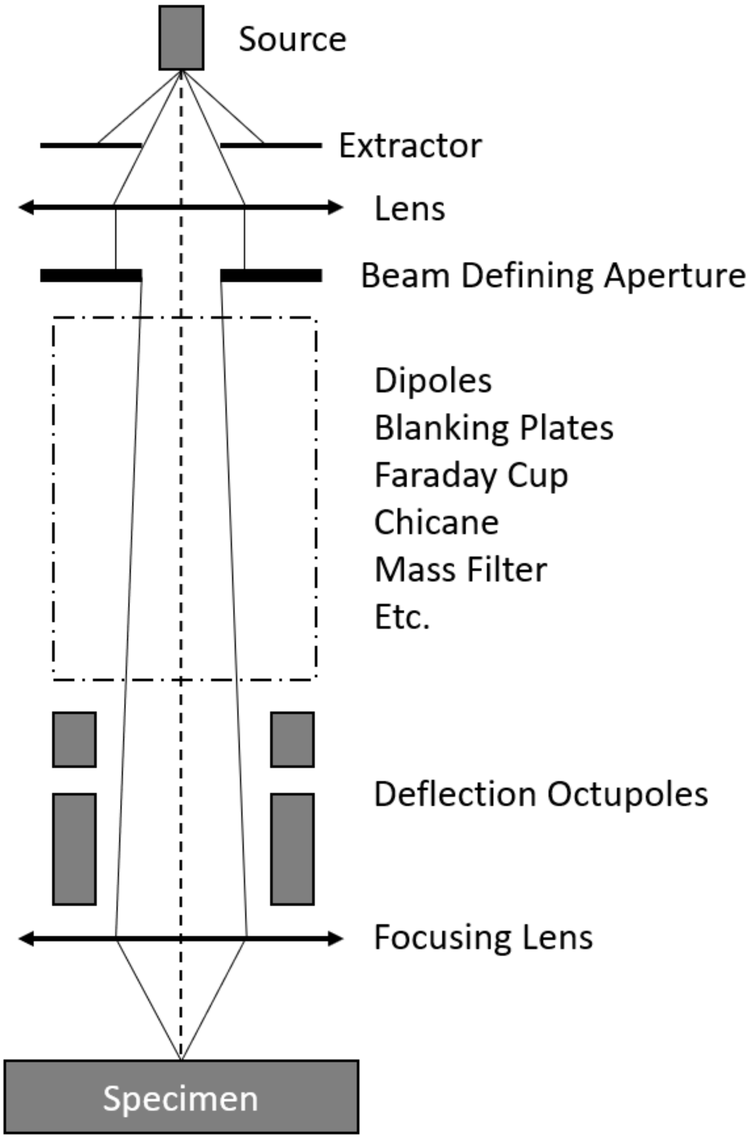

Figure A.1: Basic system architecture of the FIB. The components and orientation of a modern FIB will vary from manufacturer and model, but contain the main core elements of a source, extractor, lensing, and scanning components. Other common elements include blanking dipoles, Faraday cups for beam current measurements, chicane or mass filters, and dipoles for aberration optimization.

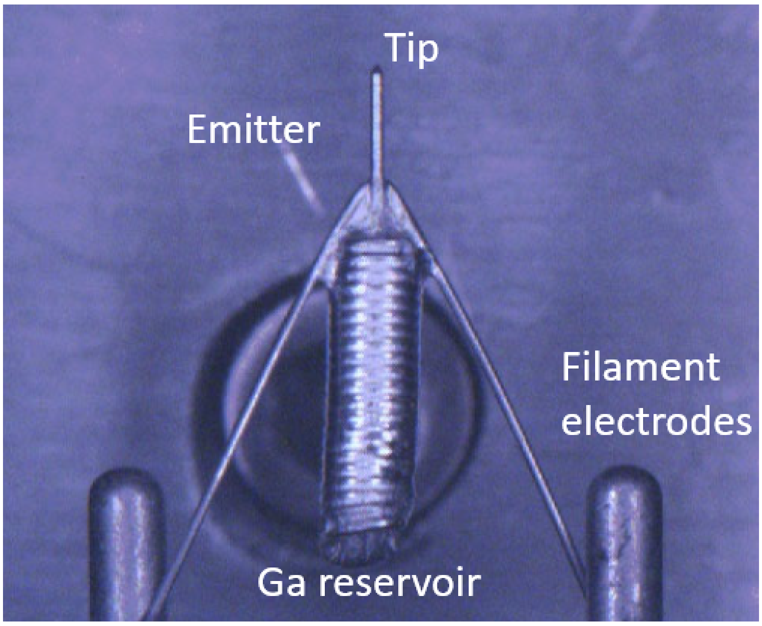

Figure A.2: A typical A typical Ga^{+} LMIS. The assembly is placed in an extraction region in which strong electric fields applied at the tip of of the emitter cause field-ionization of the liquid metal for which ions may be extracted. Figure courtesy of Thermo Fisher Scientific.

the case of charged particles these lenses are electrostatic or magnetic in nature as opposed to being based on index of refraction. The most common electrostatic lens is the Einzel lens or unipotential lens: a three-electrode lens in which the energy of the ions are maintained in the image and object plane, while the middle element performs the acceleration or deceleration of the ions. Depending on the source extraction characteristics, 2 or 3 lenses may be used, each with a unique voltage applied to the middle electrode to manipulate the beam envelope at a given energy. In the case of a 2-lens system, the first lens may collimate or focus the beam from its divergent emission cone through the defining aperture, while the last lens focuses the beam on the final plane. For a 3-lens system, the first and second lenses can operate together to focus and collimate (or vice versa) in different modes to form a cross-over point.

Cross-over points are used in charged particle optics to either reduce the size of the source object to be projected at the sample plane or to focus more ions through an aperture to increase the ion beam current. Similar to ray optics, reducing the source object will allow for a smaller image, however, unlike ray optics trajectories of charged particles are implicitly affected by fields generated by the neighboring charged particles. Grouping a bunch of charged particles close in proximity (in a cross-over) and allowing them to interact for longer amounts of time (e.g. at low landing energy) will introduce space charge and energy broadening due to the Boersch effect - both degrading performance. Trajectory displacement through space charge interactions will vary with the type of beam distribution (Gaussian, Holtsmark, pencil beam, etc.), but all are highly influenced by current I, beam radius r_0 and potential V where the lateral FWHM distribution of a cylindrical slice can be described as:

$$C_H \frac{I^{2/3} L}{V^{4/3} r_0^{4/3}} \tag{A.1}$$

for a Holtzmark distribution, or

$$C_P \frac{I^3 r_0 L}{V^{5/3}} \tag{A.2}$$

for a pencil beam, where C_i is the spherical aberration coefficient and L is the length of the segment. The Boersch effect, described as the change in axial velocity resulting from the same ion-ion interactions can be described as:

$$\frac{\Delta E_H}{E} = 0.891 \frac{m^{1/3}}{\varepsilon_0} \frac{I^{2/3}}{r_0^{1/3} \alpha_0 V^{4/3}} \tag{A.3}$$

for a Holtsmark distribution, or

$$\frac{\Delta E_P}{E} = 0.642 \frac{m}{\varepsilon_0 e^2} \frac{I^2 L}{V^2} \tag{A.4}$$

for a pencil beam, where α_0 is the beam semi-angle and m is the ion mass. Therefore, there exists a tradeoff between these contributions and a subsequent optimized setting depending on the beam current and landing energy desired. For the case of the high-brightness LMIS, a two-lens system minimizes space charge and Boersch effect by increasing the volume over which the charge acts and maintaining a collimated beam throughout the column.

Any lensing that will collimate or focus introduces both spherical and chromatic aberrations that become limitations to the current distribution in the beam. The beam parameters (brightness B, energy V and energy spread δE) and the application settings (current I and image angle α_i) combine to impose these limitations to the probe size via the Barth and Kruit [253] method. The diameter of the beam containing 50% of the beam can be written as a function of these aberrations:

$$d_{50} = \left((d_{Sph}^{1.3} + d_{Src}^{1.3})^{2/1.3} + d_{Chr}^2 \right)^{1/2} \tag{A.5}$$

Demagnified source: $d_{Src} = \frac{2}{\pi} (\frac{I}{B * V})^{\frac{1}{2}} \frac{1}{\alpha_i}$

Chromatic aberration: $d_{Chr} = 0.34 C_c (\frac{\delta E}{V}) \alpha_i$

Spherical aberration: $d_{Sph} = 0.18 C_s {\alpha_i}^3$

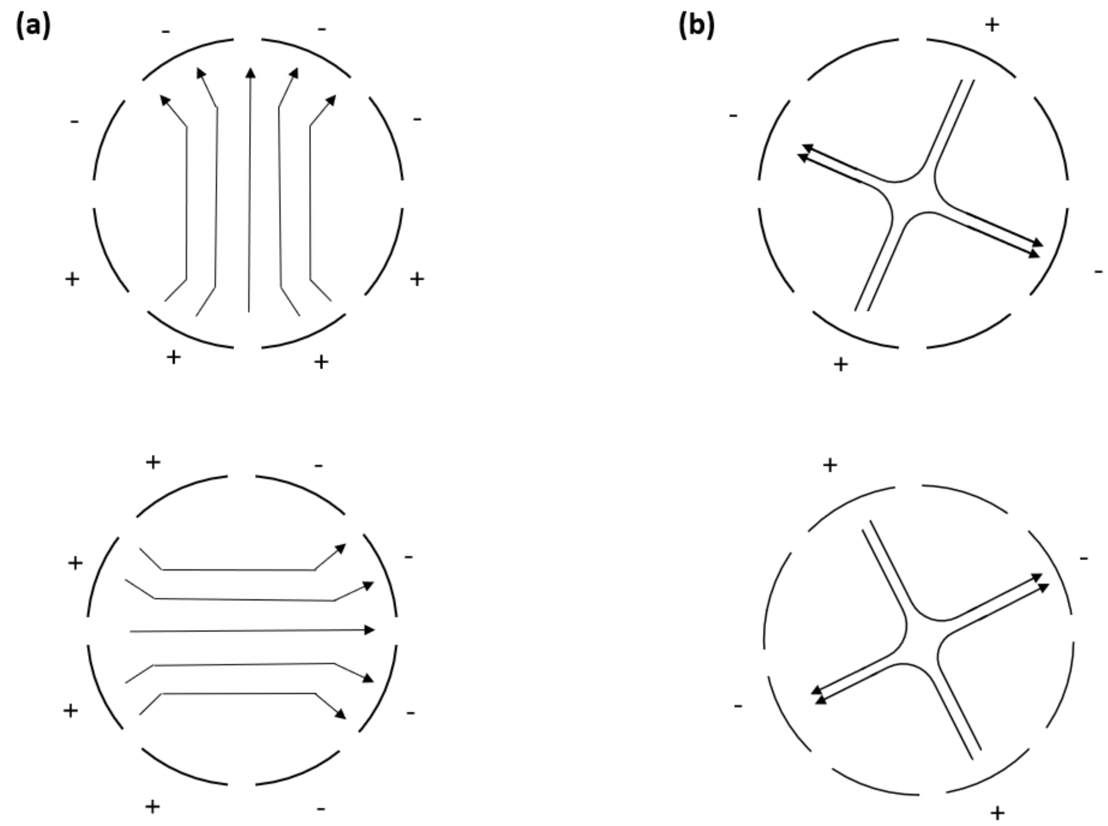

Figure A.3: Fields generated by the octupole electrode plates to enable deflection and stigmation. **(a)** Deflection dipole fields for scanning and beam shift. **(b)** Quadrupole fields for astigmatism corrections.

Therefore, by limiting the image angle through aperturing, beam acceleration, and focusing with lens elements, the demagnified image of the virtual source is achieved at the sample plane. It is important to note that for different types of ion sources and operation modes, different aberrations may dominate. For example, in the plasma FIB space charge and Coulombic interaction between the ions may contribute more and require different lens and column geometries to minimize aberrations, reduce source size, or limit charge exchange with gas molecules in the column. These finer details, however, go beyond the scope of this brief overview.

After the first condensing lens, it is common to find architectures consisting of dipoles, apertures, Faraday cups, and drift tubes. Apertures are used to block ions from the emission cone and deliver a specific beam current. Steering dipoles may be used to keep the ion beam on-axis through the center of the column to correct for misalignments and minimize aberrations, while drift tubes might accelerate the beam to reduce Coulombic interactions. The Faraday cup is coupled with a dipole to blank the beam during transitions from beam modes, to protect

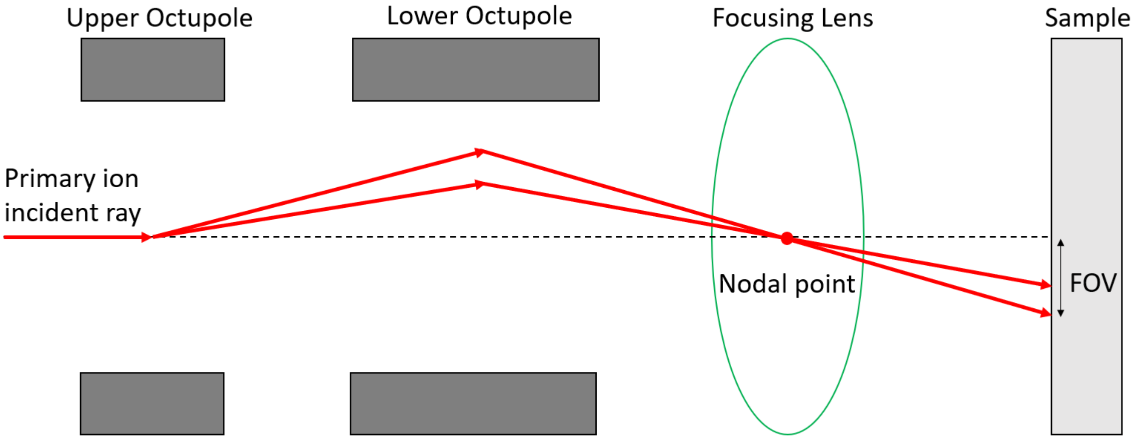

Figure A.4: Ray diagram of the primary ion beam deflection in the lower column. The dipole fields generated in Figure A.3 rock the beam about the lens nodal point to enable scanning while reducing aberrations through the focusing element.

the sample from constant irradiation, and to provide a source of current measurements. The blanking dipole is coupled with lower scanning and deflection in a fast beam blanking regime in order to blank the beam when the scan pattern begins a new scan line, is needed to avoid specific regions of interest, or returns to the beginning of the pattern mill.

The last features of the column are the scanning and deflection determined by the octupole plates and the focusing lens. The deflection is handled by a series of electrodes that form fields to deflect the beam about the focusing lens nodal point (where an incoming ray leaves the lens with the same angle as it enters). Two sections of 8 electrode plates form the two octupoles. Each octupole plate has voltages applied (up to $\sim$100 V) which form quadrupole and dipole fields that are superimposed to both scan the beam in accordance with its deflection angle and to correct for beam astigmatism. Figure A.3 shows an example of the fields generated by the octupole section and Figure A.4 demonstrates how incident rays are deflected about the focusing lens nodal point for a given field of view (FOV) to produce an aberration-limited spot.

There is not a one-size fits all schematic when it comes to the FIB, and its development is constantly improving with companies like Thermo Fisher Scientific, Hitachi, and Tescan all with their own unique performance and designs. In the end, however, these handful of components provide the foundation on which ion beam technology has transitioned from broad ion beam irradiation and beam foil scattering experiments to focused beams with spots on the order of a few nanometers to enable nanoscale precision and advanced material processing.

Appendix B

BAM-L200 Certified Reference Sample

B.1 BAM-L200 Structure

The BAM-L200 sample is accepted as a standard certified resolution sample for sputter-based measurements [36, 192–194]. It consists of strip widths W, grating periods P, and strip distances D, each of which to be used for different resolution measurement techniques: knife-edge, image modulation of a square wave grating, full width at half maximum (FWHM) of a single strip, or strip-to-strip distance. A SEM SE image alongside the illustrative pattern map is shown in Figure B.1 and depicts the orientation of the sample used to measure the spatial resolution in this study. The metrics corresponding to the various patterns and periods are reported in Table B.1.

Resolution measurements were performed with the FIB-FS hardware through detection of the Al $3s^2 4s$ $(^2\mathrm{S}_{\frac{1}{2}})$ excited state to the ground state $3s^2 3p$ $(^2\mathrm{P}^{\mathrm{o}}_{\frac{1}{2},\frac{3}{2}})$ which are located at 394.4 nm and 396.2 nm, respectively and are shown in the spectrum in Figure B.2 – a typical spectrum of an AlGaAs sample.

B.2 Resolution From FWHM of Delta Strip

It is not uncommon to return different resolution metrics for the same beam conditions under different analysis methods and therefore there is no official singular universal method for reporting lateral resolution, but rather reporting of resolution using any or multiple of the above-mentioned techniques. In a practical sense, the ultimate test is the user's eyeball and ability to look at an image and confidently say that two features are separate and distinguished. In ToF-SIMS literature that characterize the performance of lateral resolution [36–38] on the standard sam-

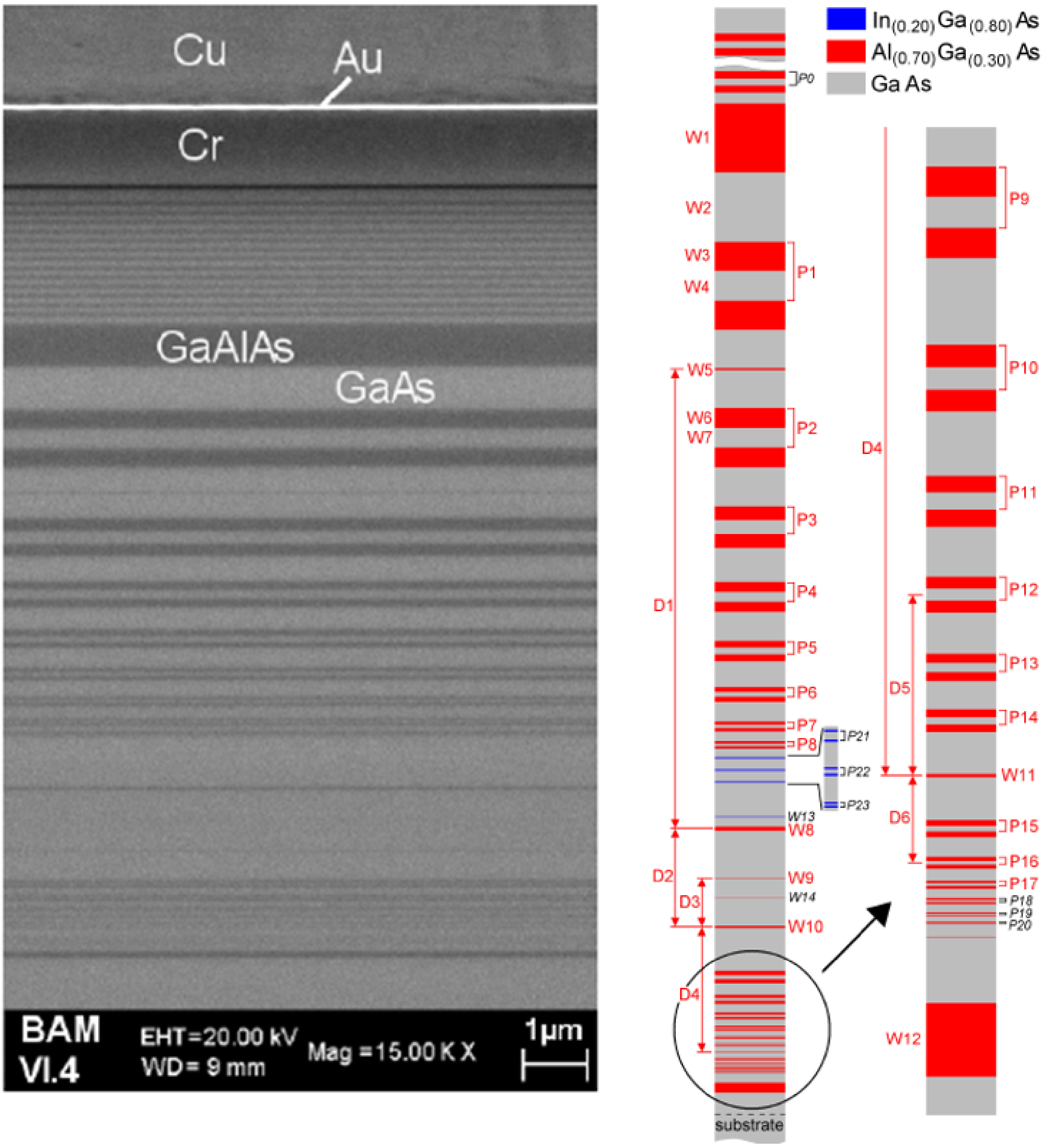

Figure B.1: Structure and schematic of the BAM L200 resolution calibration sample. The BAM-L200 sample consists of nanoscale stripe patterns with gratings of alternating GaAs and AlGaAs with varying periods for lateral resolution testing and calibration. The layer stack is grown by Metal Organic Vapor Phase Epitaxy and layer thickness certified by high resolution X-ray diffraction, optical reelection spectroscopy, and transmission electron microscopy. Image provided in the certification data sheet [254].

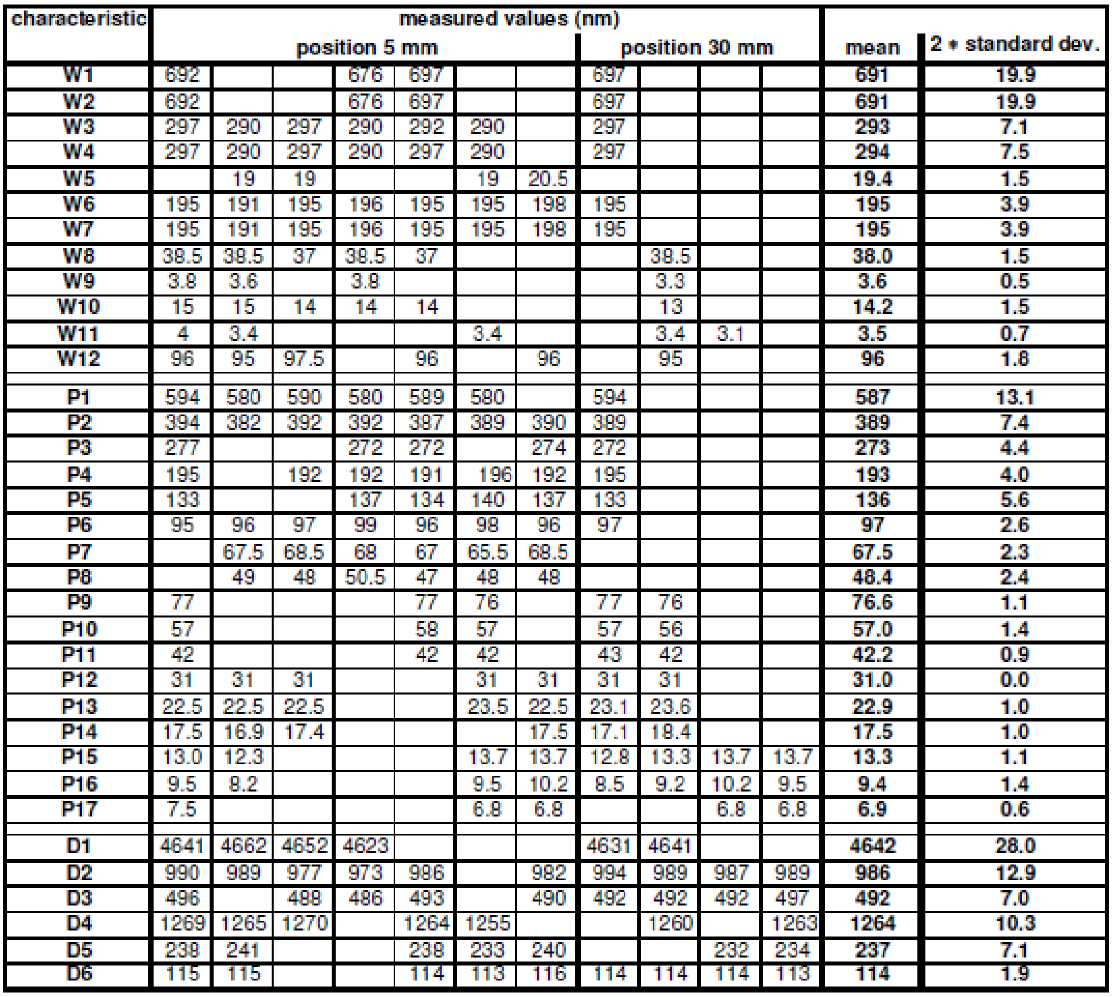

characteristic	measured values (nm)												
	position 5 mm							position 30 mm				mean	2 * standard dev.
W1	692			676	697			697				**691**	**19.9**
W2	692			676	697			697				**691**	**19.9**
W3	297	290	297	290	292	290		297				**293**	**7.1**
W4	297	290	297	290	297	290		297				**294**	**7.5**
W5		19	19			19	20.5					**19.4**	**1.5**
W6	195	191	195	196	195	195	198	195				**195**	**3.9**
W7	195	191	195	196	195	195	198	195				**195**	**3.9**
W8	38.5	38.5	37	38.5	37				38.5			**38.0**	**1.5**
W9	3.8	3.6		3.8					3.3			**3.6**	**0.5**
W10	15	15	14	14	14				13			**14.2**	**1.5**
W11	4	3.4				3.4			3.4	3.1		**3.5**	**0.7**
W12	96	95	97.5		96		96		95			**96**	**1.8**
P1	594	580	590	580	589	580		594				**587**	**13.1**
P2	394	382	392	392	387	389	390	389				**389**	**7.4**
P3	277			272	272		274	272				**273**	**4.4**
P4	195		192	192	191	196	192	195				**193**	**4.0**
P5	133			137	134	140	137	133				**136**	**5.6**
P6	95	96	97	99	96	98	96	97				**97**	**2.6**
P7		67.5	68.5	68	67	65.5	68.5					**67.5**	**2.3**
P8		49	48	50.5	47	48	48					**48.4**	**2.4**
P9	77				77	76		77	76			**76.6**	**1.1**
P10	57				58	57		57	56			**57.0**	**1.4**
P11	42				42	42		43	42			**42.2**	**0.9**
P12	31	31	31			31	31	31	31			**31.0**	**0.0**
P13	22.5	22.5	22.5			23.5	22.5	23.1	23.6			**22.9**	**1.0**
P14	17.5	16.9	17.4				17.5	17.1	18.4			**17.5**	**1.0**
P15	13.0	12.3				13.7	13.7	12.8	13.3	13.7	13.7	**13.3**	**1.1**
P16	9.5	8.2				9.5	10.2	8.5	9.2	10.2	9.5	**9.4**	**1.4**
P17	7.5					6.8	6.8			6.8	6.8	**6.9**	**0.6**
D1	4641	4662	4652	4623				4631	4641			**4642**	**28.0**
D2	990	989	977	973	986		982	994	989	987	989	**986**	**12.9**
D3	496		488	486	493		490	492	492	492	497	**492**	**7.0**
D4	1269	1265	1270		1264	1255			1260		1263	**1264**	**10.3**
D5	238	241			238	233	240			232	234	**237**	**7.1**
D6	115	115			114	113	116	114	114	114	113	**114**	**1.9**

Table B.1: Table of certified values in nanometers for the features on BAM-L200 sample reported in the certificate and their corresponding location on the sample. In the experiment, the region of the sample imaged contains strip periods P7 through single line W12. Table is provided in the BAM-L200 certification report [255].

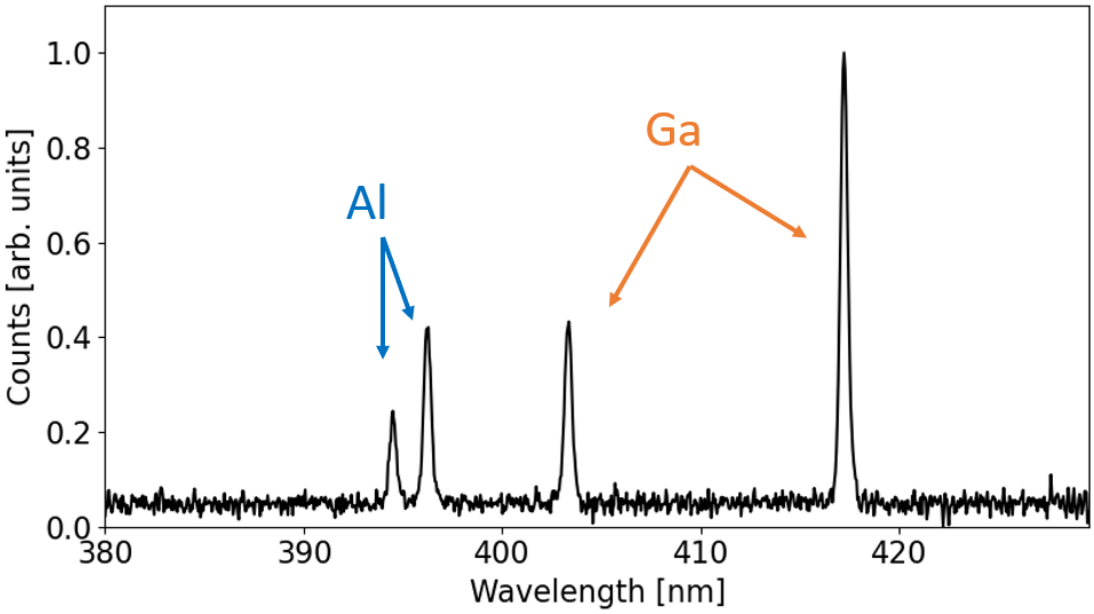

Figure B.2: FIB-FS spectrum of AlGaAs showing the Al doublet transition from the $4s$ excited state to the $3p$ ground state at 394.4 nm and 396.2 nm and the Ga doublet transition from the $5s$ excited state to the $4p$ ground state at 403.3 nm and 417.2 nm. Due to the Ga presence in each heterostructure as well as the primary ion beam, only the Al signal is used for chemical mapping in both the lateral resolution and depth profiling measurements.

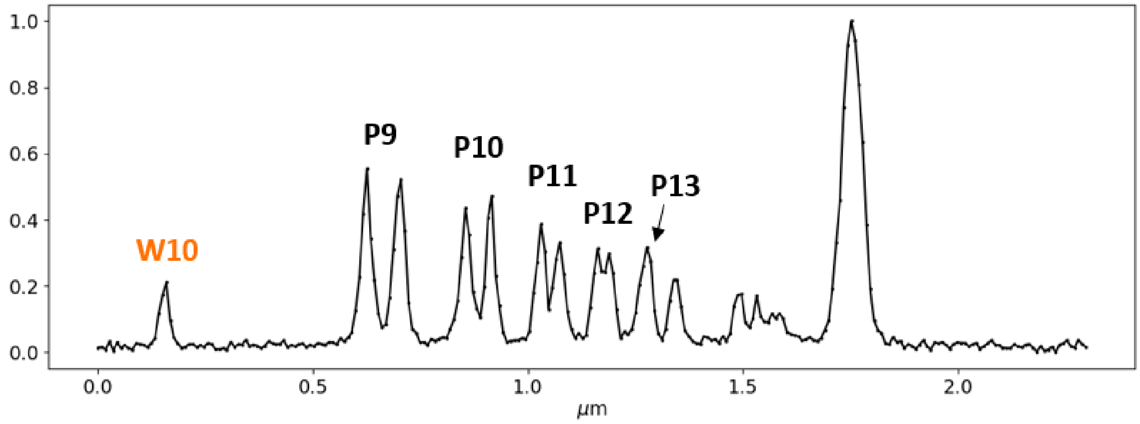

Figure B.3: Line spread profile of the BAM-L200 sample with delta strip W10. Here, the W10 strip has a given width of 14.2 nm from Table B.1, but is measured to have a FWHM of 27 nm in the FIB-FS profile. The broadening of this line from its original size is attributed to the same collision cascade intermixing effects discussed in 4.2.

ple, strip-to-strip distance is the most reported alongside images of the strips for visual confirmation as in Figure 4.1 in the 4.2. In any case, the same conclusion of lateral resolution limitations from the collision cascade is returned by different measurement methods. For example, the FWHM of the W10 single line width returns a value of 27 nm (broadening from 14.2 nm) in Figure B.3, in agreement with the reported collision cascade-limited effective probe size presented in section 4.2.

Appendix C

Depth Resolution of NIST SRM 2135c

C.1 SRM 2135c Structure

Depth resolution measurements were performed on the NIST certified depth profiling sample Standard Reference Material (SRM) 2135c depicted in Figure C.1. The sample consists of alternating layers of Ni and Cr deposited thin-films with certified thicknesses of 57 nm and 56 nm. Three different ion beams were tested at different landing energies using a top-down box mill and a decoupled FIB-FS spectrometer acquisition in Kinetic Survey Mode to record the Ni and Cr signals as the ion beam raster-scan milled through the layered structure for which an example is provided in Figure C.2. Knife-edge measurements of the transition from a Ni to a Cr layer is used to determine the depth-resolution. To avoid contributions from the surface oxide which can enhance the photon yield chemically [27, 100, 101, 130] as well as to avoid the development of non-planar delayering as a result of the different sputter rates between Cr and Ni, only the first transition from Ni to Cr is considered.

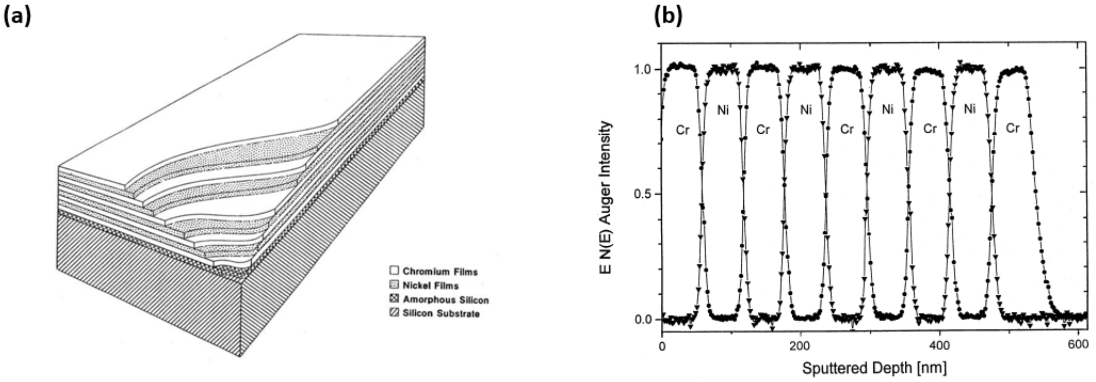

Figure C.1: Structure and layout of NIST SRM 2135c certified sputter depth profiling standard of multilayered Ni/Cr alternating thin films. **(a)** Sectional view the thin-film structure. The nominal thickness of each Cr layer is 57 nm and each Ni layer is 56 nm. **(b)** Normalized Auger sputter depth profile obtained using 1 keV Ar^{+} bombardment. Images are provided with the SRM certification data sheet [196].

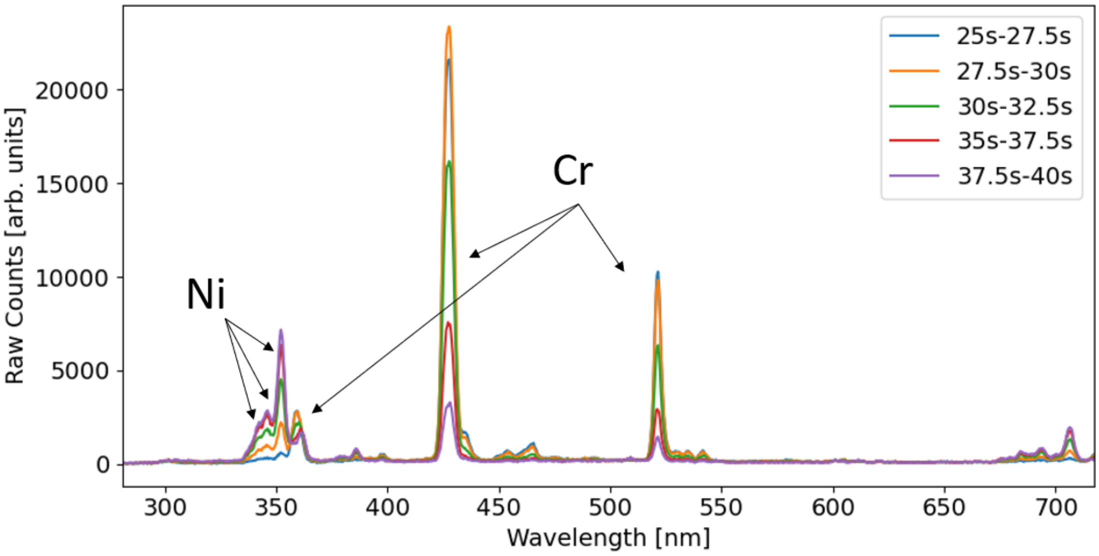

Figure C.2: FIB-FS spectra of the SRM 2135c sample going from the first Cr layer into the Ni layer showing the Ni and Cr signals in raw counts. Each spectrum is an average of the frames over the time interval of the mill listed in the legend. The main Cr signals observed are: $3d^4(^5\mathrm{D})4s4p(^3\mathrm{P}^\mathrm{o})$ y $^7\mathrm{P}^\mathrm{o}_{2,3,4}$ excited state triplet to the ground state $3d^5(^6\mathrm{S})4s$ a $^7\mathrm{S}_3$ at 357.9 nm, 359.35 nm, and 360.5 nm, the excited state triplet $3d^5(^6\mathrm{S})4p$ z $^7\mathrm{P}^\mathrm{o}_{2,3,4}$ to the ground state at 425.4 nm, 427.5 nm, 428.97 nm, and lastly the $3d^5(^6\mathrm{S})4p$ z $^5\mathrm{P}^\mathrm{o}_{1,2,3}$ excited state triplet to the $3d^5(^6\mathrm{S})4s$ a $^5\mathrm{S}_2$ excited state at 520.45 nm, 520.6 nm, and 520.84 nm. The main Ni signals observed are a mix of various transitions from the $3d^9(^2\mathrm{D})4p$ $(^3\mathrm{P}^\mathrm{o}_{0,1,2})$ and $(^3\mathrm{F}^\mathrm{o}_{2,3})$ excited states to the $3d^9(^2\mathrm{D})4s$ $(^3\mathrm{D}_{1,2,3})$ excited states between 340 nm and 352 nm. Due to the large spectral distance between the Ni and Cr signals, a large bandwidth-low resolution grating (∼8 nm resolution) was used to capture both signals, so the triplets and transition arrays are not able to be resolved at these settings.

Appendix D

Periodic Table of Emission

When it comes to elemental identification, optical detection spectral range, or simply knowing what to look for it would be beneficial to have a table summarizing what elements can be identified, under which conditions and at what energies. As previously stated, all elements can be detected by their fluorescence and the energies of emission used for identification are found from well-known spectroscopic databases. Unfortunately, ideal conditions under which some elements are more fluorescent than others or knowing all conditions one can expect to see one element more than another one is still an area of investigation and heavily dependent on the experimental conditions used (see Chapter 6). Instead, knowing what to expect for a set of standard conditions might be more benefitial. Be is a graphic of the periodic table for a large list of elements taken under a set of standard conditions defined by a 30 keV Ga^+ irradation at 6.5 pA/µum^2 showing the intensity of the most easily detectable emission lines to provide a basis for elemental identification and methodology of the technique.

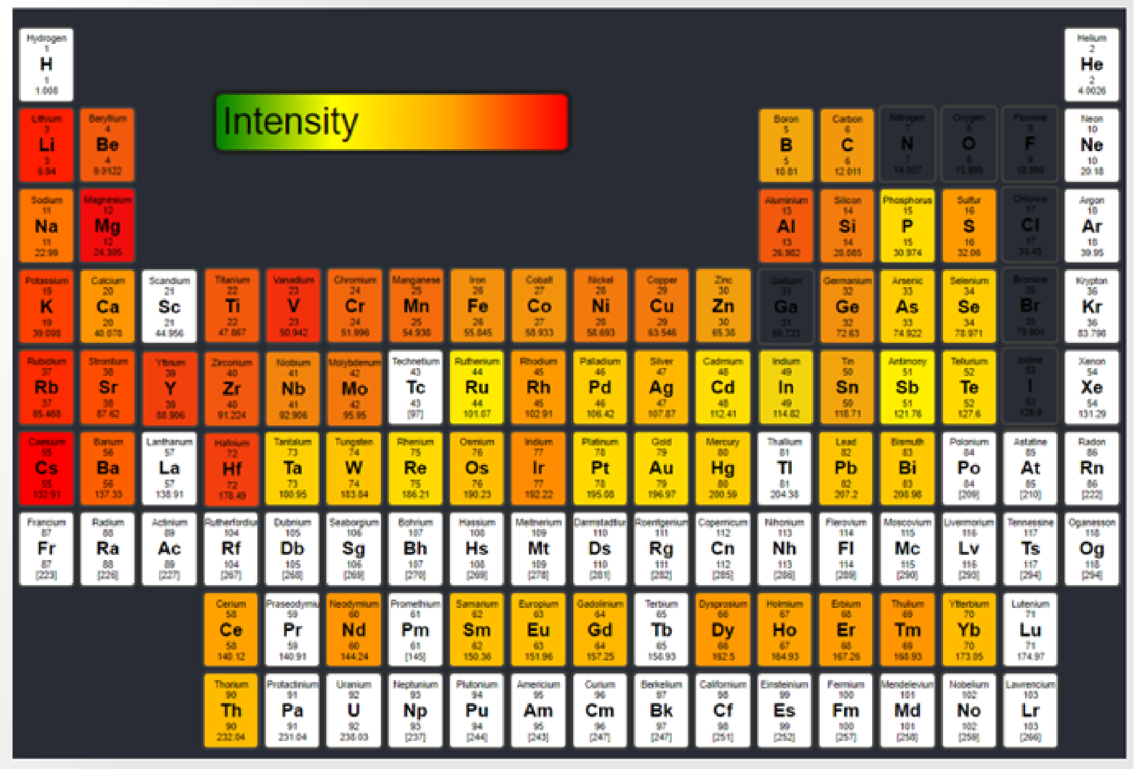

Figure D.1: Periodic table showing relative intensity of the elements strongest peak corrected for exposure time under the same irradiation conditions of 30 keV Ga^+ irradiation. White tablets have not been collected and grey tablets are omitted due to the nature of samples coming in compound form.

Bibliography

[1] Fernando A. Lasagni and Andrés Lasagni, editors. *Fabrication and Characterization in the Micro-Nano Range*. Advanced Structured Materials. Springer, Berlin, 2011.

[2] Yang Leng. *Materials Characterization: Introduction to Microscopic and Spectroscopic Methods*. John Wiley & Sons, 2 edition, 2013.

[3] Stefanos Mourdikoudis, Roger M. Pallares, and Nguyen T. K. Thanh. Characterization techniques for nanoparticles: comparison and complementarity upon studying nanoparticle properties. *Nanoscale*, 10:12871–12934, 2018.

[4] Romano Rinaldi and Xavier Llovet. Electron probe microanalysis: A review of the past, present, and future. *Microscopy and Microanalysis*, 21(5):1053–1069, 2015.

[5] Ondrej L Krivanek, Matthew F Chisholm, Valeria Nicolosi, Timothy J Pennycook, George J Corbin, Niklas Dellby, Matthew F Murfitt, Christopher S Own, Zoltan S Szilagyi, Mark P Oxley, et al. Atom-by-atom structural and chemical analysis by annular dark-field electron microscopy. *Nature*, 464:571–574, 2010.

[6] Jaysen Nelayah, Mathieu Kociak, Odile Stéphan, F Javier García de Abajo, Marcel Tencé, Luc Henrard, Dario Taverna, Isabel Pastoriza-Santos, Luis M Liz-Marzán, and Christian Colliex. Mapping surface plasmons on a single metallic nanoparticle. *Nature Physics*, 3(5):348–353, 2007.

[7] Naoyuki Nakagawa, Harold Y Hwang, and David A Muller. Why some interfaces cannot be sharp. *Nature Materials*, 5:204–209, 2006.

[8] A. Pattammattel, R. Tappero, M. Ge, Y. S. Chu, X. Huang, Y. Gao, and H. Yan. High-sensitivity nanoscale chemical imaging with hard x-ray nanoxanes. *Science Advances*, 6(37):3615, 2020.

[9] Anne Sakdinawat and David Attwood. Nanoscale x-ray imaging. *Nature Photonics*, 4:840–848, 2010.

[10] Ke Bian, Christoph Gerber, Andreas J Heinrich, Daniel J Müller, Simon Scheuring, and Ying Jiang. Scanning probe microscopy. *Nature Reviews Methods Primers*, 1(36), 2021.

[11] Baptiste Gault, Ann Chiaramonti, Oana Cojocaru-Mirédin, Patrick Stender, Renelle Dubosq, Christoph Freysoldt, Surendra Kumar Makineni, Tong Li, Michael Moody, and Julie M. Cairney. Atom probe tomography. *Nature Reviews Methods Primers*, 1(51), 2021.

[12] Zhisen Liang, Shudi Zhang, Xiaoping Li, Tongtong Wang, Yaping Huang, Wei Hang, Zhilin Yang, Jianfeng Li, and Zhongqun Tian. Tip-enhanced ablation and ionization mass spectrometry for nanoscale chemical analysis. *Science Advances*, 3(12):eaaq1059, 2017.

[13] Albert Polman, Mathieu Kociak, and F Javier García de Abajo. Electron-beam spectroscopy for nanophotonics. *Nature Materials*, 18:1158–1171, 2019.

[14] Chenfei Shen, Mingyuan Ge, Langli Luo, Xin Fang, Yihang Liu, Anyi Zhang, Jiepeng Rong, Chongmin Wang, and Chongwu Zhou. In situ and ex situ TEM study of lithiation behaviours of porous silicon nanostructures. *Scientific Reports*, 6:31334, 2016.

[15] R F Egerton. Electron energy-loss spectroscopy in the TEM. *Reports on Progress in Physics*, 72(1):016502, dec 2008.

[16] Amanda Rae Buchberger, Kellen DeLaney, Jillian Johnson, and Lingjun Li. Mass Spectrometry Imaging: A Review of Emerging Advancements and Future Insights. *Analytical Chemistry*, 90(1):240, 2018.

[17] Yufan Zhou, Mao Su, Xiaofei Yu, Yanyan Zhang, Jun-Gang Wang, Xiaodi Ren, Ruiguo Cao, Wu Xu, Donald R Baer, Yingge Du, et al. Real-time mass spectrometric characterization of the solid–electrolyte interphase of a lithium-ion battery. *Nature Nanotechnology*, 15:224–230, 2020.

[18] Jun Lu, Tianpin Wu, and Khalil Amine. State-of-the-art characterization techniques for advanced lithium-ion batteries. *Nature Energy*, 2:17011, 2017.

[19] Danna Qian, Cheng Ma, Karren L More, Ying Shirley Meng, and Miaofang Chi. Advanced analytical electron microscopy for lithium-ion batteries. *NPG Asia Materials*, 7:e193, 2015.

[20] Alok M. Tripathi, Wei-Nien Su, and Bing Joe Hwang. In situ analytical techniques for battery interface analysis. *Chem. Soc. Rev.*, 47:736–851, 2018.

[21] Kedar Narayan and Sriram Subramaniam. Focused ion beams in biology. *Nature Methods*, 12:1021–1031, 2015.

[22] Ahmet F Coskun, Guojun Han, Shambavi Ganesh, Shih-Yu Chen, Xavier Rovira Clavé, Stefan Harmsen, Sizun Jiang, Christian M Schürch, Yunhao Bai, Chuck Hitzman, et al. Nanoscopic subcellular imaging enabled by ion beam tomography. *Nature Communications*, 12:789, 2021.

[23] Yara Haridy, Markus Osenberg, André Hilger, Ingo Manke, Donald Davesne, and Florian Witzmann. Bone metabolism and evolutionary origin of osteocytes: Novel application of fib-sem tomography. *Science Advances*, 7(14):9113, 2021.

[24] Marie Fuest, Miroslava Schaffer, Giovanni Marco Nocera, Rodrigo I Galilea-Kleinsteuber, Jan-Erik Messling, Michael Heymann, Jürgen M Plitzko, and Thomas P Burg. In situ microfluidic cryofixation for cryo focused ion beam milling and cryo electron tomography. *Scientific Reports*, 9:19133, 2019.

[25] TL Burnett, SA McDonald, A Gholinia, R Geurts, M Janus, T Slater, SJ Haigh, C Ornek, F Almuaili, DL Engelberg, et al. Correlative tomography. *Scientific Reports*, 4:4711, 2014.

[26] Shingo Hirashima, Keisuke Ohta, Tomonoshin Kanazawa, Satoko Okayama, Akinobu Togo, Naohisa Uchimura, Jingo Kusukawa, and Keiichiro Nakamura. Three-dimensional ultrastructural analysis of cells in the periodontal ligament using focused ion beam/scanning electron microscope tomography. *Scientific Reports*, 6:39435, 2016.

[27] Thomas G.E. Bombardment-induced light emission. *Surf. Sci.*, 90 (2):381–416, 1979.

[28] Malgorzata Suchańska. Ion-induced photon emission of metals. *Progress in Surface Science*, 54(2):165–209, 1997.

[29] E Veje. Ion-induced sputtering as a light source for atomic spectroscopy. *Vacuum*, 39(2):319–321, 1989. Special Issue Ion Beam Interactions with Matter.

[30] I. S. T. Tsong. Photon emission from sputtered particles during ion bombardment. *physica status solidi (a)*, 7(2):451–458, 1971.

[31] C. W. White, D. L. Simms, and N. H. Tolk. Surface composition determined by analysis of impact radiation. *Science*, 177(4048):481–486, 1972.

[32] Norman H. Tolk, Ignatius S. T. Tsong, and C. Woody White. In situ spectrochemical analysis of solid surfaces by ion beam sputtering. *Analytical Chemistry*, 49, 1977.

[33] Robert H. Reuss, Damon Morgan, Ann Goldenetz, William M. Clark, David B. Rensch, and Mark Utlaut. Fabrication of bipolar transistors by maskless ion implantation. *Journal of Vacuum Science & Technology B: Microelectronics Processing and Phenomena*, 4(1):290–294, 1986.

[34] J. Fröch, Alan Bahm, Mehran Kianinia, Zhao Mu, Vijay Bhatia, Sejeong Kim, Julie M. Cairney, Weibo Gao, Carlo Bradac, Igor Aharonovich, and Milos Toth. Versatile direct-writing of dopants in a solid state host through recoil implantation. *Nature Communications*, 11(1):5039, 2020.

[35] A.J. De Marco and J. Melngailis. Maskless fabrication of jfets via focused ion beams. In *International Semiconductor Device Research Symposium, 2003*, pages 426–427, 2003.

[36] Lex Pillatsch, Fredrik Östlund, and Johann Michler. Fibsims: A review of secondary ion mass spectrometry for analytical dual beam focussed ion beam instruments. *Progress in Crystal Growth and Characterization of Materials*, 65(1):1–19, 2019.

[37] James A. Whitby, Fredrik Östlund, Peter Horvath, Mihai Gabureac, Jessica L. Riesterer, Ivo Utke, Markus Hohl, Libor Sedlacek, Jaroslav Jiruše, Vinzenz Friedli, Mikhael Bechelany, and Johann Michler. High spatial resolution time-of-flight secondary ion mass spectrometry for the masses: A novel orthogonal tof fib-sims instrument with in situafm. *Advances in Materials Science and Engineering*, 2012, 2011.

[38] Mathias Senoner and Wolfgang E. S. Unger. Sims imaging of the nanoworld: applications in science and technology. *J. Anal. At. Spectrom.*, 27:1050–1068, 2012.

[39] John Melngailis. Focused ion beam lithography. *Nuclear Instruments and Methods in Physics Research Section B: Beam Interactions with Materials and Atoms*, 80-81:1271–1280, 1993.

[40] Tariq Mahbub and Md Enamul Hoque. Chapter 1 - introduction to nanomaterials and nanomanufacturing for nanosensors. In Kaushik Pal and Fernando Gomes, editors, *Nanofabrication for Smart Nanosensor Applications*, Micro and Nano Technologies, pages 1–20. Elsevier, 2020.

[41] Tadatsugu Itoh, editor. *Ion Beam Assisted Film Growth*. Elsevier, Amsterdam, 1989.

[42] Shinji Matsui, Takashi Kaito, Jun-ichi Fujita, Masanori Komuro, Kazuhiro Kanda, and Yuichi Haruyama. Three-dimensional nanostructure fabrication by focused-ion-beam chemical vapor deposition. *Journal of Vacuum Science & Technology B: Microelectronics and Nanometer Structures Processing, Measurement, and Phenomena*, 18(6):3181–3184, 2000.

[43] J J Cuomo, S M Rossnagel, and H R Kaufman. *Handbook of ion beam processing technology*. American Society of Mechanical Engineers, 1989.

[44] Rointan Bunshah, editor. *Handbook of Deposition Technologies for Films and Coatings*. William Andrew, 1994.

[45] ST Davies and B Khamsehpour. Focused ion beam machining and deposition for nanofabrication. *Vacuum*, 47(5):455–462, 1996.

[46] K. Nikawa. Applications of focused ion beam technique to failure analysis of very large scale integrations: A review. *Journal of Vacuum Science & Technology B: Microelectronics and Nanometer Structures Processing, Measurement, and Phenomena*, 9(5):2566–2577, 1991.

[47] Lucille Giannuzzi and Fred Stevie, editors. *Introduction to Focused Ion Beams*. Springer, Boston, 2005.

[48] Peter Sigmund. Theory of sputtering. i. sputtering yield of amorphous and polycrystalline targets. *Phys. Rev.*, 184:383–416, Aug 1969.

[49] P. Sigmund. Collision theory of displacement damage. iv. ion range and sputtering. *Revue Roumaine De Physique*, 17(8):969–1000, 1972.

[50] Peter Sigmund. Mechanisms and theory of physical sputtering by particle impact. *Nuclear Instruments and Methods in Physics Research Section B: Beam Interactions with Materials and Atoms*, 27(1):1–20, 1987.

[51] J. Lindhard and M. Scharff. Energy dissipation by ions in the kev region. *Phys. Rev.*, 124:128–130, Oct 1961.

[52] J Lindhard, M Scharff, and H E Schioett. Range concepts and heavy ion ranges (notes on atomic collisions, ii). *Kgl. Danske Videnskab. Selskab. Mat. Fys. Medd.*, Vol: 33: No. 14, 1963.

[53] J Lindhard, V Nielsen, and M Scharff. Approximation method in classical scattering by screened coulomb fields. *Kgl. Danske Videnskab. Selskab. Mat. Fys. Medd.*, 1968.

[54] Peter Sigmund. Stopping power in perspective. *Nuclear Instruments and Methods in Physics Research Section B: Beam Interactions with Materials and Atoms*, 135(1):1–15, 1998.

[55] H Gnaser. *Low-Energy Ion Irradiation of Solid Surfaces*. Springer, Berlin, 1999.

[56] J.F. Ziegler. *Stopping Range of Ions in Matter*. Pergamon, 1977.

[57] J. F. Ziegler. Stopping of energetic light ions in elemental matter. *Journal of Applied Physics*, 85(3):1249–1272, 1999.

[58] Rainer Behrisch and Wolfgang Eckstein, editors. *Sputtering by Particle Bombardment*. Springer, Berlin, 2007.

[59] Niels Bohr. Xxii. the penetration of atomic particles through matter. In Jens Thorsen, editor, *The Penetration of Charged Particles through Matter (1912–1954)*, volume 8 of *Niels Bohr Collected Works*, pages 423–568. Elsevier, 1987.

[60] Sir E. Rutherford F.R.S. Lxxix. the scattering of α and β particles by matter and the structure of the atom. *The London, Edinburgh, and Dublin Philosophical Magazine and Journal of Science*, 21(125):669–688, 1911.

[61] Sir E. Rutherford F.R.S. Lvii. the structure of the atom. *The London, Edinburgh, and Dublin Philosophical Magazine and Journal of Science*, 27(159):488–498, 1914.

[62] James F. Ziegler, M.D. Ziegler, and J.P. Biersack. Srim – the stopping and range of ions in matter (2010). *Nuclear Instruments and Methods in Physics Research Section B: Beam Interactions with Materials and Atoms*, 268(11):1818–1823, 2010. 19th International Conference on Ion Beam Analysis.

[63] C. J. Richmond. Ion implantation. H. Ryssel and I. Ruge. Wiley, Chichester, 1986, 478 pages, £48, ISBN 0471-10311 X. *Surface and Interface Analysis*, 10(4):221–221, 1987.

[64] Mark T. Robinson and Ordean S. Oen. Computer studies of the slowing down of energetic atoms in crystals. *Phys. Rev.*, 132:2385–2398, Dec 1963.

[65] J. Lindhard. Motion of swift charged particles, as influenced by strings of atoms in crystals. *Physics Letters*, 12(2):126–128, 1964.

[66] E. Bøgh and E. Uggerhøj. Orientation dependence of rutherford scattering yields in single crystals. *Physics Letters*, 17(2):116–118, 1965.

[67] Peter Jung. Average atomic-displacement energies of cubic metals. *Phys. Rev. B*, 23:664–670, Jan 1981.

[68] P. Jung. Atomic displacement functions of cubic metals. *Journal of Nuclear Materials*, 117:70–77, 1983.

[69] W. Eckstein and R. Preuss. New fit formulae for the sputtering yield. *Journal of Nuclear Materials*, 320(3):209–213, 2003.

[70] C. García-Rosales, W. Eckstein, and J. Roth. Revised formulae for sputtering data. *Journal of Nuclear Materials*, 218(1):8–17, 1995.

[71] Martin Vičánek, J.J.Jimenez Rodriguez, and Peter Sigmund. Depth of origin and angular spectrum of sputtered atoms. *Nuclear Instruments & Methods in Physics Research Section B-beam Interactions With Materials and Atoms*, 36:124–136, 1989.

[72] Jochen P. Biersack and Wolfgang Eckstein. Sputtering studies with the monte carlo program trim.sp. *Applied Physics A*, 34:73–94, 1984.

[73] Helge L. Bay. Laser induced fluorescence as a technique for investigations of sputtering phenomena. *Nuclear Instruments and Methods in Physics Research Section B: Beam Interactions with Materials and Atoms*, 18(1):430–445, 1986.

[74] H.L. Bay, B. Schweer, P. Bogen, and E. Hintz. Investigation of light-ion sputtering of titanium using laser-induced fluorescence. *Journal of Nuclear Materials*, 111-112:732–737, 1982.

[75] R.B. Wright, M.J. Pellin, D.M. Gruen, and C.E. Young. Laser fluorescence spectroscopy of sputtered uranium atoms. *Nuclear Instruments and Methods*, 170(1):295–302, 1980.

[76] D.M. Gruen, W.F. Calaway, M.J. Pellin, C.E. Young, D.R. Spiegel, R.N. Clayton, A.M. Davis, and J.D. Blum. Selectivity, specificity and sensitivity in the photoionization of sputtered species. *Nuclear Instruments and Methods in Physics Research Section B: Beam Interactions with Materials and Atoms*, 58(3):505–511, 1991.

[77] H. F. Arlinghaus, M. T. Spaar, T. Tanigaki, A. W. McMahon, and P. H. Holloway. Sputter-initiated resonance ionization spectroscopy: An analytical technique for quantitative and sensitive measurements of impurities and ultra-shallow doping profiles in semiconductors. *Journal of Vacuum Science & Technology B: Microelectronics and Nanometer Structures Processing, Measurement, and Phenomena*, 12(1):263–268, 1994.

[78] F.M. Kimock, J.P. Baxter, and N. Winograd. Detection of sputtered neutrals by multi-photon resonance ionization. *Nuclear Instruments and Methods in Physics Research*, 218(1):287–292, 1983.

[79] W. Berthold and A. Wucher. Energy- and angle-dependent excitation probability of sputtered metastable silver atoms. *Phys. Rev. B*, 56:4251–4260, Aug 1997.

[80] C. Staudt, A. Wucher, J. Bastiaansen, V. Philipsen, E. Vandeweert, P. Lievens, R. E. Silverans, and Z. Sroubek. Sputtering of Ag atoms into metastable excited states. *Physical Review B*, 66(8):085415, August 2002.

[81] Peter D. Brewer. Two-photon laser-induced fluorescence and “2+1” multiphoton ionization of silicon atoms. *Chemical Physics Letters*, 136(6):557–561, 1987.

[82] Boden S. A., Franklin T.M., Scipioni L., Bagnall D.M., and Rutt N.H. Ionoluminescence in the helium ion microscope. *Microsc. Microanal.*, 18 (6):1253–1262, 2012.

[83] I.S Sharodi, Yu.A Bandurin, and S.S Pop. Ion–photon emission during ion bombardment of beryllium surface. *Nuclear Instruments and Methods in Physics Research Section B: Beam Interactions with Materials and Atoms*, 193(1):699–704, 2002.

[84] White C.W., Tolk N.H., Kraus J., and Van Der Weg W.F. Continuum optical radiation produced by low-energy heavy particle bombardment of metal targets. *Nucl. Instrum. Methods*, 132:419–425, 1976.

[85] Vasilisa Veligura and Gregor Hlawacek. *Ionoluminescence*, pages 325–351. Springer International Publishing, Cham, 2016.

[86] Calvo del Castillo H., Ruvalcaba J.L., and Calderon T. Some new trends in the ionoluminescence of minerals. *Anal. Bioanal. Chem.*, 387 (3):869–878, 2007.

[87] Martel J.G. and Olson N.T. Ion bombardment induced photon and secondary electron emission. *Nuc. Instrum. Meth.*, 105:296–275, 1972.

[88] V. V. Ovchinnikov and K. V. Shalomov. The independence of the emission spectra of metal targets from the energy and mass of the implanted ions. *AIP Conference Proceedings*, 2174(1):020252, 2019.

[89] Veje E. Atomic excitations in sputtering as functions of the projectile energy. *Nuclear Instruments and Methods in Physics Research Section B: Beam Interactions with Materials and Atoms*, 33:543–546, 1988.

[90] Veje E., H. Winter, and H. Hagedorn. Electron transfer to excited projectile states after grazing ion-surface scattering. *Radiation Effects and Defects in Solids*, 109:47–54, 1989.

[91] R.B. Wright and D.M. Gruen. Secondary photon emission studies of ion bombarded beryllium. *Nuclear Instruments and Methods*, 170:577–583, 1980.

[92] R.B. Wright, M.J. Pellin, D.M. Gruen, and C.E. Young. Incident ion energy dependence of the secondary photon emission of ion bombarded beryllium. *The Journal of Chemical Physics*, 73:664–672, 1980.

[93] Roger Kelly and C.B. Kerkdijk. Bombardment-induced photon emission from al and al2o3 targets. *Surface Science*, 46(2):537–557, 1974.

[94] A.R. Bayly, P.J. Martin, and R.J. MacDonald. Inelastic collisions at ion bombarded surface: I. studies in secondary ion and photon excitation. *Nuclear Instruments and Methods*, 132:459–466, 1976.

[95] C.W. White, D.L. Simms, N.H. Tolk, and D.V. McCaughan. Effects of non-radiative de-excitation of excited sputtered atoms near silicon and silicon dioxide surfaces. *Surface Science*, 49(2):657–663, 1975.

[96] G.E. Thomas and E.E. De Kluizenaar. A chemical effect on light emission from ion-bombarded copper and aluminum surfaces. *International Journal of Mass Spectrometry and Ion Physics*, 15(2):165–179, 1974.

[97] Martin P. J., Bayly A. R., Macdonald R. J., Tolk N. H., and G. J. Clark. De-excitation processes near the surface of ion bombarded sio$_2$ and si. *Surf. Sci.*, 60 (2):349–364, 1976.

[98] G. Betz and W. Husinsky. Sputtering of insulators. *Nuclear Instruments and Methods in Physics Research Section B: Beam Interactions with Materials and Atoms*, 32(1):331–340, 1988.

[99] Ghose D. and Battacharyya S.R. Light emission from an ion bombarded copper single crystal. *Phys. Lett. A*, 227:133–137, 1997.

[100] Betz G. and Husinsky W. Sputtering of metal targets under increased oxygen partial pressure. *Nucl. Instrum. Meth. Phys. Res. B: Beam Interactions with Materials and Atoms*, 13 (1-3):343–347, 1986.

[101] Betz G. Electron excitation in sputtered atoms and the oxygen effect. *Nucl. Instrum. Methods B*, 27 (1):104–118, 1987.

[102] P.J. Martin and R.J. MacDonald. The spectroscopy of ion-induced photon emission and its application to quantitative surface analysis. *Surf. Sci.*, 62:551–566, 1977.

[103] E. Veje. Study of the role of oxygen in atomic excitation processes in sputtering and in secondary electron emission. *Nuclear Instruments and Methods in Physics Research Section B: Beam Interactions with Materials and Atoms*, 33(1):497–501, 1988.

[104] C.M. Loxton, R.J. MacDonald, and P.J. Martin. The influence of non-radiative transitions on bombardment induced photon emission from ti and ti oxide. *Surface Science*, 93(1):84–106, 1980.

[105] W.F. van der Weg and P.K. Rol. On the excited state of sputtered particles. *Nuclear Instruments and Methods*, 38:274–276, 1965.

[106] I.S.T Tsong. The excitation efficiency of atoms ejected during ion-beam sputtering. *Surface Science*, 69:609–618, 1977.

[107] JS Colligon. Surface compositional analysis using low energy ion bombardment induced emission processes. *Vacuum*, 24(9):373–388, 1974.

[108] Veje E. Atomic excitations in sputtering studied with the use of composite targets. *Zeitschrift für Physik B Condensed Matter*, 70:55, 1988.

[109] Van Der Weg W. F. and Bierman D. J. Excitation of cu atoms by ar ions and subsequent radiationless deexciation of scattered particles near a cu surface. *Physica*, 44 (2):206–218, 1969.

[110] C Snoek, W.F. van der Weg, and P.K. Rol. Photon emission by ionically bombarded copper surfaces. *Physica*, 30:341–344, 1964.

[111] T. Andersen, K. A. Jessen, and G. Sorensen. Beam-foil excitation studies of aluminum with a heavy-ion accelerator. *J. Opt. Soc. Am.*, 59(9):1197–1201, Sep 1969.

[112] T. Andersen, O. H. Madsen, and G. Sørensen. Radiative lifetimes in sn i and bi i. *J. Opt. Soc. Am.*, 62(9):1118–1118, Sep 1972.

[113] T. Andersen. Beam-foil spectroscopy with low-energy accelerators. *Nuclear Instruments and Methods*, 110:35–42, 1973.

[114] T. Andersen, S. Worre Jørgensen, and G. Sørensen. Radiative lifetimes in as i and sb i. *J. Opt. Soc. Am.*, 64(6):891–892, Jun 1974.

[115] Thomas Vestergaard Andersen, Aleksander P. Petkov, Aleksander P. Petkov, and Gunnar Sorensen. Lifetimes of excited levels in mgiii, caiii, kiv–v, cav, and ge i. *Physica Scripta*, 12:283–286, 1975.

[116] M Braun, B Emmoth, and I Martinson. Optical radiation emitted at heavy-ion bombardment of solids. *Physica Scripta*, 10(3):133–138, sep 1974.

[117] M. D. Havey, L. C. Balling, and J. J. Wright. Direct measurements of excited-state lifetimes in mg, ca, and sr†. *J. Opt. Soc. Am.*, 67(4):488–491, Apr 1977.

[118] K. Jensen and E. Veje. An experimental study of optical radiation from sputtered species. *Zeitschrift fur Physik*, 269(3):293–300, September 1974.

[119] N.A. Yusuf and I.S.T. Tsong. Kinetic energies of excited atoms ejected from ion-bombarded surfaces. *Surface Science*, 108(3):578–586, 1981.

[120] C. W. White and N. H. Tolk. Optical radiation from low-energy ion-surface collisions. *Phys. Rev. Lett.*, 26:486–489, Mar 1971.

[121] Homer D. Hagstrum. low energy de-excitation and neutralization processes near surfaces. In N.H. TOLK, J.C. TULLY, W. HEILAND, and C.W. WHITE, editors, *Inelastic Ion–Surface Collisions*, pages 1–25. Academic Press, 1977.

[122] R. Hippler, W. Krüger, A. Scharmann, and K.-H. Schartner. Line shape measurements of atoms sputtered from polycrystalline cu, zn, and al by 300 kev ar+ bombardment. *Nuclear Instruments and Methods*, 132:439–444, 1976.

[123] V. V. Gritsyna, T. S. Kijan, A. G. Koval', and Ya. M. Fogel'. An investigation of the velocity spectrum of excited particles by fast ions from a solid as a means to study its electronic level structure. *Radiation Effects*, 14(1-2):77–79, 1972.

[124] I.S.T. Tsong and A.G. McLaren. An ion beam spectrochemical analyser with application to the analysis of silicate minerals. *Spectrochimica Acta*, 30(9):343–351, 1975.

[125] C.B. Kerkdijk and Roger Kelly. Photon emission from a bombarded al target and its dependence on oxygen. *Surface Science*, 47(1):294–300, 1975.

[126] A.H. Dogar and A. Qayyum. Study of the cascading effect on photon emission from sputtered excited carbon atoms and ions. *Nuclear Instruments and Methods in Physics Research Section B: Beam Interactions with Materials and Atoms*, 248(2):259–263, 2006.

[127] A.H. Dogar and A. Qayyum. Atomic excitations during ion beam sputtering of yba2cu3o7 targets. *Nuclear Instruments and Methods in Physics Research Section B: Beam Interactions with Materials and Atoms*, 247(2):290–294, 2006.

[128] Kaddouri A., Ashraf I., Ait El Fqih M., Targaoui H., El Boujlaïdi A., and Berra K. Photon emission from clean and oxygenated si and sio2 surfaces bombarded by 5 kev krypton ions. *Appl. Surf. Sci.*, 256:116–119, 2009.

[129] G.E. Thomas, E.E.De Kluizenaar, and M. Beerlage. Light emission from excited molecules sputtered from chemisorption layers on silicon. *Chemical Physics*, 7(2):303–309, 1975.

[130] R.J MacDonald and P.J Martin. A study of the interaction of oxygen with chromium using ion bombardment induced photon and secondary ion emission. *Surface Science*, 67(1):237–250, October 1977.

[131] R. Behrisch, J. Roth, J. Bohdansky, A.P. Martinelli, B. Schweer, D. Rusbüldt, and E. Hintz. Dependence of light-ion sputtering yields of iron on ion fluence and oxygen partial pressure. *Journal of Nuclear Materials*, 93-94:645–655, 1980.

[132] R.J. MacDonald, E. Taglauer, and W. Heiland. The effect of co adsorption on ion and photon yields from ion bombarded metal surfaces. *Applications of Surface Science*, 5(2):197–211, 1980.

[133] G.E. Thomas and E.E. de Kluizenaar. The effect of adsorption of cs and coadsorption of cs and o2 on bombardment-induced light emission from cu and al surfaces. *Nuclear Instruments and Methods*, 132:449–452, 1976.

[134] Ming L. Yu and N. D. Lang. Direct evidence of electron tunneling in the ionization of sputtered atoms. *Phys. Rev. Lett.*, 50:127–130, Jan 1983.

[135] Roger Kelly. Statistical model for the formation of excited atoms in the sputtering process. *Phys. Rev. B*, 25:700–712, Jan 1982.

[136] I.S.T Tsong and N.A. Yusuf. Absolute photon yields in the sputter-induced optical emission process. *Applied Physics Letters*, 33 (12):999–1002, 1983.

[137] R. B. Wright, M. J. Pellin, and D. M. Gruen. Velocity distribution of sputtered U atoms as determined by laser induced fluorescence spectroscopy*1. *Nuclear Instruments and Methods*, 182-183:167–178, May 1981.

[138] R. B. Wright, C. E. Young, M. J. Pellin, and D. M. Gruen. High resolution continuous wave laser induced fluorescence spectroscopy of sputtered zr atoms. *Journal of Vacuum Science and Technology*, 20(3):510–514, 1982.

[139] M. J. Pellin, R. B. Wright, and D. M. Gruen. Laser fluorescence spectroscopy of sputtered zirconium atoms. *The Journal of Chemical Physics*, 74(11):6448–6457, 1981.

[140] D M Gruen, M J Pellin, C E Young, M H Mendelsohn, and A B DeWald. Outer shell excitation mechanisms and static mode laser fluorescence spectroscopy of sputtered atoms. *Physica Scripta*, T6:42–53, jan 1983.

[141] W. Husinsky, G. Betz, and I. Girgis. Ground state and excited state sputtering doppler-shift laser-fluorescence studies of cr and ca targets. *Journal of Vacuum Science & Technology A*, 2(2):698–701, 1984.

[142] W. Berres, D. Rusbüldt, E. Hintz, and H. L. Bay. An investigation of laser-induced fluorescence for measuring velocity distributions of neutral atoms using a cw dye laser. *Applied Physics B*, 35(2):83–93, 1984.

[143] P. Bogen, H.F. Döbele, and Ph. Mertens. Measurement of velocity distributions of sputtered carbon atoms using laser-induced fluorescence in the vacuum uv. *Journal of Nuclear Materials*, 145-147:434–437, 1987.

[144] C.A. Andersen and J.R. Hinthorne. Thermodynamic approach to the quantitative interpretation of sputtered ion mass spectra. *Analytical Chemistry*, 45(8):1421–1438, 1973.

[145] Ming L. Yu. *Charged and excited states of sputtered atoms*, pages 91–160. Springer Berlin Heidelberg, Berlin, Heidelberg, 1991.

[146] R.J. MacDonald and P.J. Martin. Quantitative surface analysis using ion-induced secondary ion and photon emission. *Surface Science*, 66(2):423–435, 1977.

[147] R.J. MacDonald and R.F. Garrett. A method of quantitative analysis based on ion bombardment induced secondary ion and photon emission. *Surface Science*, 78(2):371–385, 1978.

[148] Andersen Niels, Andresen Bjarne, and Veje Erling. Atomic excitations in sputtering processes. *Radiation Effects*, 60(1-4):119–127, 1982.

[149] I.S.T. Tsong. Reply to “photon emission from sputtered atoms — the observation of apparent local thermodynamic equilibrium in the excitation” by r.j. macdonald, r.f. garrett and p.j. martin. *Surface Science*, 75(1):159–160, 1978.

[150] K. J. Snowdon. A fundamental analysis of the validity of thermodynamic models of ionized and excited particle production during sputtering. *Radiation Effects*, 40(1-2):9–18, 1979.

[151] K. J. Snowdon. Relation of the photon yield from a sputtering source to the population distribution and excitation function. *Radiation Effects*, 42(3-4):185–190, 1979.

[152] K. J Snowdon, B. Andresen, and E. Veje. Conditions for the indistinguishability of thermal equilibrium and single atomic collision relative level populations. *Radiation Effects*, 43(4-5):205–210, 1979.

[153] K. J. Snowdon, B. Andresen, and E. Veje. An evaluation of the methods of determining excited state population distributions from sputtering sources. *Radiation Effects*, 40(1-2):19–22, 1979.

[154] G. E. Thomas. Letter to the editor. *Radiation Effects*, 31(3):185–186, 1977.

[155] G Blaise. Similarities in photon and ion emissions induced by sputtering. *Surface Science*, 60(1):65–75, 1976.

[156] Ming L. Yu. A bond breaking model for secondary ion emission. *Nuclear Instruments and Methods in Physics Research Section B: Beam Interactions with Materials and Atoms*, 18(1):542–548, 1986.

[157] Ming L. Yu and Norton D. Lang. Mechanisms of atomic ion emission during sputtering. *Nuclear Instruments and Methods in Physics Research Section B: Beam Interactions with Materials and Atoms*, 14(4):403–413, 1986.

[158] E. Veje. Atomic excitations in sputtering studied with group two element targets. *Surface Science*, 110(2):533–542, 1981.

[159] E. Veje. Study of atomic excitations in sputtering with the use of mg, al, ca, and cd targets. *Phys. Rev. B*, 28:5029–5036, Nov 1983.

[160] E. Veje. Study of atomic excitations in sputtering with the use of be, b, and c targets. *Phys. Rev. B*, 28:88–94, Jul 1983.

[161] C. He, Z. Postawa, S. W. Rosencrance, R. Chatterjee, B. J. Garrison, and N. Winograd. Band structure effects in ejection of ni atoms in fine structure states. *Phys. Rev. Lett.*, 75:3950–3953, 1995.

[162] E. Vandeweert, V. Philipsen, W. Bouwen, P. Thoen, H. Weidele, R. E. Silverans, and P. Lievens. Anomalous sputtering behavior observed by quantitative measurements of the population partition of metastable ni atoms. *Phys. Rev. Lett.*, 78:138–141, Jan 1997.

[163] A. Cortona, W. Husinsky, and G. Betz. Influence of adsorbates, crystal structure, and target temperature on the sputtering yield and kinetic-energy distribution of excited ni atoms. *Phys. Rev. B*, 59:15495–15505, Jun 1999.

[164] Peter Lievens, Vicky Philipsen, Erno Vandeweert, and Roger E Silverans. Emission of ground and metastable state ni and co atoms during ion-beam sputtering: Quantitative measurements of population and kinetic energy distributions. *Nuclear Instruments and Methods in Physics Research Section B: Beam Interactions with Materials and Atoms*, 135(1):471–476, 1998.

[165] E. Vandeweert, J. Bastiaansen, V. Philipsen, P. Lievens, and R.E. Silverans. Resonant electron transfer during ion-beam sputtering of metals studied by double-resonant laser ionization. *Nuclear Instruments and Methods in Physics Research Section B: Beam Interactions with Materials and Atoms*, 164-165:795–802, 2000.

[166] E. Vandeweert, P. Lievens, V. Philipsen, J. Bastiaansen, and R. E. Silverans. Measurements of the population partitions and state-selected flight-time distributions of kev ion-beam-sputtered metastable atoms. *Phys. Rev. B*, 64:195417, Oct 2001.

[167] J. Bastiaansen, V. Philipsen, P. Lievens, R. E. Silverans, and E. Vandeweert. Influence of the atomic structure on the quantum state of sputtered ir atoms. *Phys. Rev. A*, 70:052902, Nov 2004.

[168] J. Bastiaansen, V. Philipsen, F. Vervaecke, E. Vandeweert, P. Lievens, and R. E. Silverans. Velocity dependent electron transfer during emission of ion-beam sputtered cu atoms. *Phys. Rev. B*, 68:073409, Aug 2003.

[169] W. Berthold and A. Wucher. Electronic excitation during sputtering of silver atoms. *Phys. Rev. Lett.*, 76:2181–2184, Mar 1996.

[170] W. Berthold and A. Wucher. Population of sputtered metastable silver atoms. *Nuclear Instruments and Methods in Physics Research Section B: Beam Interactions with Materials and Atoms*, 115(1):411–414, 1996.

[171] Z. Sroubek, F. Sroubek, A. Wucher, and J. A. Yarmoff. Formation of excited ag atoms in sputtering of silver. *Phys. Rev. B*, 68:115426, Sep 2003.

[172] Barbara J. Garrison, Nicholas Winograd, Reema Chatterjee, Zbigniew Postawa, Andreas Wucher, Erno Vandeweert, Peter Lievens, Vicky Philipsen, and Roger E. Silverans. Sputtering of atoms in fine structure states: a probe of excitation and de-excitation events. *Rapid Communications in Mass Spectrometry*, 12(18):1266–1272, 1998.

[173] Ming Tan and Bruce V. King. Population inversion of metastable ni atoms sputtered from $\mathrm{Ni}(100)$, $\mathrm{ni_3Al}(100)$, and $\mathrm{NiAl}(110)$. *Phys. Rev. B*, 73:075414, Feb 2006.

[174] A. Wucher and Z. Sroubek. Formation of metastable excited states during sputtering of transition metals. *Phys. Rev. B*, 55:780–786, Jan 1997.

[175] I.S.T. Tsong, A.C. Mclaren, and B.E. Hobbs. Determination of hydrogen concentration in silicates using ion-beam spectrochemical analysis (ibsca), 1976.

[176] Ampere Tseng. Recent developments in nanofabrication using focused ion beams. *Small*, 1(10):924–939, 2005.

[177] Ivo Utke, Patrik Hoffmann, and John Melngailis. Gas-assisted focused electron beam and ion beam processing and fabrication. *Journal of Vacuum Science & Technology B: Microelectronics and Nanometer Structures Processing, Measurement, and Phenomena*, 26(4):1197–1276, 2008.

[178] Warren J. MoberlyChan, David P. Adams, Michael J. Aziz, Gerhard Hobler, and Thomas Schenkel. Fundamentals of focused ion beam nanostructural processing: Below, at, and above the surface. *MRS Bulletin*, 32(5):424–432, 2007.

[179] A. Brahm, A. Wilms, M. Tymoshchuk, C. Grossmann, G. Notni, and A. Tünnermann. Optical effects at projection measurements for terahertz tomography. *Optics & Laser Technology*, 62:49–57, 2014.

[180] Toon Coenen, Benjamin J.M. Brenny, Ernst Jan Vesseur, and Albert Polman. Cathodoluminescence microscopy: Optical imaging and spectroscopy with deep-subwavelength resolution. *MRS Bulletin*, 40(4):359–365, 2015.

[181] Toon Coenen and Jacob Jan de Boer. Sparc: a cathodoluminescence platform for nanoscale plasmonics in a scanning electron microscope. *Microscopy and Microanalysis*, 21(S3):2051–2052, 2015.

[182] A.D. Trigg. A high efficiency cathodoluminescence system and its application to optical materials. *Scanning Electron Microscopy*, 3, 1985.

[183] J Brückner and R Brenn. Detection limits in ion induced photon emission measurements achieved by an intensity optimized optical system. *Measurement Science and Technology*, 8(3):272–278, mar 1997.

[184] C.G.H. Walker, M.M. El-Gomati, A.M.D. Assa'd, and M. Zadrazil. The secondary electron emission yield for 24 solid elements excited by primary electrons in the range 250-5000 ev: a theory/experiment comparison. *Scanning*, 30(5):365–380, 2008.

[185] Dai Zhang, Xiao Wang, Kai Braun, Hans-Joachim Egelhaaf, Monika Fleischer, Laura Hennemann, Holger Hintz, Catrinel Stanciu, Christoph J. Brabec, Dieter P. Kern, and Alfred J. Meixner. Parabolic mirror-assisted tip-enhanced spectroscopic imaging for non-transparent materials. *Journal of Raman Spectroscopy*, 40(10):1371–1376, 2009.

[186] Jian Liu, Cien Zhong, Jiubin Tan, Tong Wang, and Tony Wilson. Elliptical mirror based imaging with aperture angle greater than $\pi/2$. *Opt. Express*, 20(17):19206–19213, Aug 2012.

[187] M. A. Lieb and A. J. Meixner. A high numerical aperture parabolic mirror as imaging device for confocal microscopy. *Opt. Express*, 8(7):458–474, Mar 2001.

[188] J. Stadler, C. Stanciu, C. Stupperich, and A. J. Meixner. Tighter focusing with a parabolic mirror. *Opt. Lett.*, 33(7):681–683, Apr 2008.

[189] Jian Liu, Min Ai, He Zhang, and Jiubin Tan. Focusing properties of elliptical mirror with an aperture angle greater than π. *Optical Engineering*, 53(6):1 – 7, 2013.

[190] Andor. ixon ultra 897: Hardware guide, 2015.

[191] G. Betz and F. Rüdenauer. Collision cascade limit to spatial resolution in focused ion beam processes. *Applied Surface Science*, 51(1):103–112, 1991.

[192] M. Senoner, Th. Wirth, W. Unger, W. Österle, I. Kaiander, R. L. Sellin, and D. Bimberg. Bam-l002—a new type of certified reference material for length calibration and testing of lateral resolution in the nanometre range. *Surface and Interface Analysis*, 36(10):1423–1426, 2004.

[193] M. Senoner, A. Maassdorf, H. Rooch, W. Osterle, M. Malcher, M. Schmidt, F. Kollmer, D. Paul, V. D. Hodoroaba, S. Rades, and W. E. Unger. Lateral resolution of nanoscaled images delivered by surface-analytical instruments: application of the bam-l200 certified reference material and related iso standards. *Anal Bioanal Chem.*, 407(11):3211, 2015.

[194] M. Senoner and W. E. S. Unger. Lateral resolution of secondary ion mass spectrometry–results of an inter-laboratory comparison. *Surface and Interface Analysis*, 39(1):16–25, 2007.

[195] C. W. Magee and R. E. Honig. Depth profiling by sims—depth resolution, dynamic range and sensitivity. *Surface and Interface Analysis*, 4(2):35–41, 1982.

[196] Rance A. Velapoldi and Thomas E. Gills. Standard Reference Material 2135c Ni/Cr Thin Film Depth Profile Standard certificate, 1999.

[197] K. Wittmaack and D.B. Poker. Interface broadening in sputter depth profiling through alternating layers of isotopically purified silicon: I. experimental results. *Nuclear Instruments and Methods in Physics Research Section B: Beam Interactions with Materials and Atoms*, 47(3):224–235, 1990.

[198] K. Wittmaack. Towards the ultimate limits of depth resolution in sputter profiling: Beam-induced chemical changes and the importance of sample quality. *Surface and Interface Analysis*, 21(6-7):323–335, 1994.

[199] H. De Witte, T. Conard, W. Vandervorst, and R. Gijbels. Ion-bombardment artifact in tof-sims analysis of zro2/sio2/si stacks. *Applied Surface Science*, 203-204:523–526, 2003. Secondary ion mass spectrometry SIMS XIII.

[200] Kyung Joong Kim, David Simons, and Greg Gillen. Quantitative depth profiling of an alternating pt/co multilayer and a pt–co alloy multilayer by sims using a buckminsterfullerene (c60) source. *Applied Surface Science*, 253(14):6000–6005, 2007.

[201] K. Wittmaack, E. Hammerl, I. Eisele, and S. B. Patel. Peak or centroid — which parameter is better suited for quantifying apparent marker locations in low-energy sputter depth profiling with reactive primary ion beams? *Surface and Interface Analysis*, 31(9):893–896, 2001.

[202] K. Wittmaack and I. W. Drummond. Transient phenomena and impurity relocation in sims depth profiling using oxygen bombardment: Pursuing the physics to interpret the data [and discussion]. *Philosophical Transactions: Mathematical, Physical and Engineering Sciences*, 354(1719):2731–2764, 1996.

[203] P C Zalm. Ultra shallow doping profiling with SIMS. *Reports on Progress in Physics*, 58(10):1321–1374, oct 1995.

[204] Kyung Joong Kim, Jong Shik Jang, Dae Won Moon, and Hee Jae Kang. A method to determine the interface position and layer thickness in SIMS depth profiling of multilayer films. *Metrologia*, 47(3):253–261, apr 2010.

[205] R. Havelund, M. P. Seah, M. Tiddia, and I. S. Gilmore. Sims of organic materials—interface location in argon gas cluster depth profiles using negative secondary ions. *J Am Soc Mass Spectrom*, 29:774–785, 2018.

[206] M.G. Dowsett, J.H. Kelly, G. Rowlands, T.J. Ormsby, B. Guzmán, P. Augustus, and R. Beanland. On determining accurate positions, separations, and internal profiles for delta layers. *Applied Surface Science*, 203-204:273–276, 2003. Secondary ion mass spectrometry SIMS XIII.

[207] K. Wittmaack. Assessment of the extent of atomic mixing from sputtering experiments. *Journal of Applied Physics*, 53(7):4817–4820, 1982.

[208] Klaus Wittmaack. Beam-induced broadening effects in sputter depth profiling. *Vacuum*, 34:119–137, 1984.

[209] B.V. King and I.S.T. Tsong. Deconvolution of atomic mixing effects from SIMS depth profiles. *Nuclear Instruments and Methods in Physics Research Section B: Beam Interactions with Materials and Atoms*, 7-8:793–797, 1985.

[210] B.V. King and I.S.T. Tsong. The depth resolution of sputter profiling. *Ultramicroscopy*, 14(1):75–78, 1984.

[211] P. Chakraborty. Secondary ion mass spectrometry for quantitative surface and in-depth analysis of materials. *Promana - J Phys*, 50:617–640, 1998.

[212] Luisa Ottolini, Piero Bottazzi, and Riccardo Vannucci. Quantification of lithium, beryllium, and boron in silicates by secondary-ion mass spectrometry using conventional energy filtering. *Anal. Chem.*, 65:1960–1968, 1993.

[213] William P. Reed. Standard Reference Material 93a Borosilicate Glass ($12.5\% B_2O_3$), 1991.

[214] Stephen A. Wise and Robert L. Watters. Standard Reference Material 612 Trace Elements in Glass, 2012.

[215] P. Hovington, V. Timoshevskii, S. Burgess, H. Demers, P. Statham, R. Gauvin, and K. Zaghib. Can we detect li k x-ray in lithium compounds using energy dispersive spectroscopy? 38:571–578, 2016.

[216] K. Feser. K-shell fluorescence yield of metallic lithium and other light elements. 29:901–903, 1972.

[217] S. Burgess, L. Xiaobing, and J. Holland. High spatial resolution energy dispersive x-ray spectrometery in the sem and the detection of light elements including lithium. 27:S8–S12, 2013.

[218] C. Dellen, H. G. Gehrke, S. Möller, C. L. Tsai, U. Breuer, S. Uhlenbruck, O. Guillon, M. Finsterbusch, and M. Bram. Time-of-flight secondary ion mass spectrometry study of lithium intercalation process in licoo2 thin film. 321:241–247, 2016.

[219] Miwa Ohnishi, Osamu Matsuoka, Hidenobu Nogi, and Tetsuo Sakamoto. Observation of a licoo$_2$ cathode material of a li-ion battery by high spatial resolution tof-sims. 10:207–209, 2012.

[220] Yang Lu, Chen-Zi Zhao, Rui Zhang, Hong Yuan, Li-Peng Hou, Zhong-Heng Fu, Xiang Chen, Jia-Qi Huang, and Qiang Zhang. The carrier transition from li atoms to li vacancies in solid-state lithium alloy anodes. *Science Advances*, 7(38):5520, 2021.

[221] Xu Xu, Chengge Jiao, Kexue Li, Min Hao, Katie.L. Moore, Timothy.L. Burnett, and Xiaorong Zhou. Application of high-spatial-resolution secondary ion mass spectrometry for nanoscale chemical mapping of lithium in an al-li alloy. *Materials Characterization*, 181:111442, 2021.

[222] Stéphanie Bessette, Andrea Paolella, Chisu Kim, Wen Zhu, Pierre Hovington, Raynald Gauvin, and Karim Zaghib. Nanoscale lithium quantification in lixniycowmnzo2 as cathode for rechargeable batteries. *Scientific Reports*, 8:17575, 2018.

[223] Chengge Jiao, Lex Pillatsch, Johannes Mulders, and David Wall. Three-dimensional time-of-flight secondary ion mass spectrometry and dualbeam fib/sem imaging of lithium-ion battery cathode. 25:876–877, 2019.

[224] Jiajun Wang, Yongji Tang, Jinli Yang, Ruying Li, Guoxian Liang, and Xueliang Sun. Nature of lifepo4 aging process: Roles of impurity phases. 238:454–463, 2013.

[225] Daniel J. Graham, Matthew S. Wagner, and David G. Castner. Information from complexity: Challenges of tof-sims data interpretation. 252:6860–6868, 2006.

[226] Thomas Stephan. Tof-sims in cosmochemistry. 49:859–906, 2001.

[227] V. R. Deline, William Katz, C. A. Evans, and Peter Williams. Mechanism of the sims matrix effect. 33:832–835, 1978.

[228] Tianyu Li, Xiao-Zi Yuan, Lei Zhang, Datong Song, Kaiyuan Shi, and Christina Bock. Degradation mechanisms and mitigation strategies of nickel-rich NMC-based lithium-ion batteries. *Electrochemical Energy Reviews*, 3(1):43–80, 2020.

[229] Enrico Trevisanello, Raffael Ruess, Gioele Conforto, Felix H. Richter, and Jürgen Janek. Polycrystalline and single crystalline NCM cathode materials—quantifying particle cracking, active surface area, and lithium diffusion. *Advanced Energy Materials*, 11(18):2003400, 2021.

[230] Ahmed M. Hashem, Ashraf E. Abdel-Ghany, Marco Scheuermann, Sylvio Indris, Helmut Ehrenberg, Alain Mauger, and Christian M. Julien. Doped

nanoscale nmc333 as cathode materials for li-ion batteries. *Materials*, 12(18), 2019.

[231] Albert L. Lipson, Jessica L. Durham, Michael LeResche, Ismael Abu-Baker, Michael J. Murphy, Timothy T. Fister, Lixin Wang, Fu Zhou, Lei Liu, Kitae Kim, and Derek Johnson. Improving the thermal stability of NMC 622 li-ion battery cathodes through doping during coprecipitation. *ACS Applied Materials & Interfaces*, 12:18512–18518, 2020.

[232] Stevie F.A., Zhou C., Zhang Z., and Turansky A. Sims measurement of hydrogen and deuterium detection limits in silicon: Comparison of different sims instrumentation. 34, 2016.

[233] Tan Sui, Bohang Song, Jiri Dluhos, Li Lu, and Alexander M. Korsunsky. Nanoscale chemical mapping of li-ion battery cathode material by fib-sem and tof-sims multi-modal microscopy. *Nano Energy*, 17:254–260, 2015.

[234] V. R. Deline, C. A. Evans, and Peter Williams. A unified explanation for secondary ion yields. *Applied Physics Letters*, 33(7):578–580, 1978.

[235] M.P. Seah and A.G. Shard. The matrix effect in secondary ion mass spectrometry. *Applied Surface Science*, 439:605–611, 2018.

[236] G. Blaise and M. Bernheim. Adsorption of gases studied by secondary ion emission mass spectrometry. *Surface Science*, 47(1):324–343, 1975. Proceedings of the Third Symposium on Surface Physics University of Utrecht, The Netherlands 26-28 June 1974.

[237] C.W. White. Ion induced optical emission for surface and depth profile analysis. *Nuclear Instruments and Methods*, 149(1):497–506, 1978.

[238] Stefan Reinke, Dieter Rahmann, and Rainer Hippler. Light emission from sputtered atoms following ion bombardment of polycrystalline al and cu targets. *Vacuum*, 42(13):807–810, 1991.

[239] M. Maazouz, A. G. Borisov, V. A. Esaulov, J. P. Gauyacq, L. Guillemot, S. Lacombe, and D. Teillet-Billy. Effect of metal band characteristics on resonant electron capture:h^- formation in the scattering of hydrogen ions on mg, al, and ag surfaces. *Phys. Rev. B*, 55:13869–13877, May 1997.

[240] M. Maazouz, L. Guillemot, T. Schlatholter, S. Ustaze, and V.A. Esaulov. Electron capture and loss in the scattering of oxygen atoms and ions on mg, al and ag surfaces. *Nuclear Instruments and Methods in Physics Research*

Section B: Beam Interactions with Materials and Atoms, 125(1):283–287, 1997. Inelastic Ion-Surface Collisions.

[241] M Maazouz, S Ustaze, L Guillemot, and V.A Esaulov. Electron capture and loss in the scattering of fluorine and chlorine atoms and ions on metal surfaces. *Surface Science*, 409(2):189–198, 1998.

[242] Milos Toth, Charleen Lobo, Vinzenz Friedli, Aleksandra Szkudlarek, and Ivo Utke. Continuum models of focused electron beam induced processing. *Beilstein Journal of Nanotechnology*, 6:1518–1540, 2015.

[243] I.F. Urazgil'din. Secondary ion emission from metal surfaces. *Nuclear Instruments and Methods in Physics Research Section B: Beam Interactions with Materials and Atoms*, 78(1):271–277, 1993.

[244] D.V. Klushin, M.Yu. Gusev, and I.F. Urazgil'din. Velocity dependence of ionization probability of secondary ions emitted from metal surfaces. *Nuclear Instruments and Methods in Physics Research Section B: Beam Interactions with Materials and Atoms*, 100(2):316–321, 1995. Proceedings of the Tenth International Workshop on Inelastic Ion-Surface Collisions.

[245] Fumihiro Honda, Gerald M. Lancaster, Yasuo Fukuda, and J. Wayne Rabalais. Sims study of the mechanism of cluster formation during ion bombardment of alkali halides. *The Journal of Chemical Physics*, 69(11):4931–4937, 1978.

[246] A. Duvenbeck, F. Sroubek, Z. Sroubek, and A. Wucher. Computer simulation of low-energy electronic excitations in atomic collision cascades. *Nuclear Instruments and Methods in Physics Research Section B: Beam Interactions with Materials and Atoms*, 225(4):464–477, 2004.

[247] A. Duvenbeck, Z. Sroubek, and A. Wucher. Electronic excitation in atomic collision cascades. *Nuclear Instruments and Methods in Physics Research Section B: Beam Interactions with Materials and Atoms*, 228(1):325–329, 2005. Proceedings of the Seventh International Conference on Computer Simulation of Radiation Effects in Solids.

[248] John Orloff, Mark Utlaut, and L. Swanson. *High Resolution Focused Ion Beams: FIB and Its Applications*. Kluwer Academic/Plenum Publishers, 2003.

[249] John Orloff. High-resolution focused ion beams. *Rev. Sci. Instrum.*, 64(5):1105–1130, 1993.

[250] John Orloff, editor. *Handbook of Charged Particle Optics*. Taylor & Francis Group, Boca Raton, 2 edition, 2009.

[251] P.D. Prewett and G.L.R. Mair. *Focused Ion Beams from Liquid Metal Ion Sources*. Wiley, New York, 1991.

[252] Nan Yao, editor. *Focused Ion Beam Systems*. Cambridge University Press, Cambridge, 2007.

[253] JE Barth and P Kruit. Addition of different contributions to the charged particle probe size. *Optik*, 101(3):101–109, 1996.

[254] G Reiners and W Unger. Nanoscale stripe pattern for testing of lateral resolution and calibration of length scale BAM-L200 certificate, 2007.

[255] M Senoner. Nanoscale stripe pattern for testing of lateral resolution and calibration of length scale BAM-L200 certification report, 2007.